Exploring New and Enhanced Optical Functionalities in Coupled Nano-Systems

A PhD Thesis

by:

John J. Gough

Supervisor:

Prof. Louise Bradley

School of Physics

Trinity College Dublin

2018

Declaration

I declare that this thesis has not been submitted as an exercise for a degree at this or any other university and it is entirely my own work with the exception of assistance and collaboration recognised in the acknowledgements and throughout the thesis where applicable.

I agree to deposit this thesis in the University's open access institutional repository or allow the library to do so on my behalf, subject to Irish Copyright Legislation and Trinity College Library conditions of use and acknowledgement.

I have read and I understand the plagiarism provisions in the General Regulations of the University Calendar for the current year, found at http://www.tcd.ie/calendar.

I have also completed the Online Tutorial on avoiding plagiarism “Ready Steady Write”, located at http://tcd-ie.libguides.com/plagiarism/ready-steady-write.

____

John Gough

Summary

In this thesis, a variety of novel emerging systems were chosen to explore new and enhanced optical functionalities in coupled nano-systems. The coupling of novel nanomaterials with complimentary properties paves the way for enhanced performance and functionality for future device applications. Near-field interactions between nano-systems can lead to a variety of interesting mechanisms, such as, modification of the emission properties of a fluorescent species, and nonradiative energy transfer (NRET) *via* dipole-dipole coupling.

A coupled nano-system of quantum dots (QDs) and chiral Ag nanohelices is investigated with a view towards optical antennas. The chiral Ag nanohelices are nanoscale analogues of traditional helical antennas. It is shown that there is a strong interaction between the QDs and the Ag nanohelices, demonstrating an interaction efficiency of (82 ± 2)%. The far-field emission pattern from the QDs when coupled to the Ag nanohelices is found to exhibit greater directionality than the emission pattern from the QDs on a planar substrate. The far-filed emission pattern is also shown to fit with an ordinary end-fire emission pattern, a characteristic radiation pattern exhibited by traditional antennas. Similarly, the coupling between the QDs and the chiral Ag nanohelices leads to circular polarisation of the QD emission, with the emission polarised in the same handedness as the nanohelices, with a maximum value of (17.7 ± 3.0)% circularly polarised emission.

A composite structure of Ag nanoparticle (NP) decorated graphene oxide (GO) is studied to investigate the influence of the composite substrate on the emission and Raman scattering signals of three organic dyes; Rhodamine 6G (R6G), Rhodamine B (RhB), and Sulforhodamine 101 (SR101). The interactions between each of the dyes and the Ag NPs, GO, and the Ag NP decorated GO (AgGO) were studied to investigate the relationship between fluorescence quenching and surface enhanced Raman scattering (SERS) enhancements. The SERS enhancements of R6G were found to be influenced most strongly by the fluorescence quenching by the GO, while SR101 was more strongly influenced by the field enhancement associated with the Ag NPs. RhB was shown to have the weakest SERS enhancements and also the weakest coupling to the Ag NP decorated GO substrate.

Colloidal Ag NPs and lithographically defined arrays of Ag NPs were used to demonstrate plasmon mediated NRET from QDs to quantum wells (QWs). This is the first experimental demonstration of plasmon mediated NRET from QDs to QWs. Plasmon mediated NRET efficiencies as large as ~25% are observed. The colloidal Ag NPs were used

to study the distance dependence of the plasmon mediated NRET, where it was found to follow the same d^{-4} dependence as the direct NRET from the QD to the QW. In the case of the plasmon mediated NRET, there is evidence of an increased interaction distance, indicating that the process follows a Förster-type NRET model, with the coupled QD-Ag NP acting as an enhanced donor dipole. The lithographically defined arrays of Ag NPs display plasmon mediated NRET efficiencies of ~17% and demonstrate the tunability of the interaction, going from a situation of overall quenching to an enhancement of the QW emission, simply by changing the geometry of the Ag NPs.

Coupled system of QDs and MoS_2 devices are studied to investigate the influence of the MoS_2 film quality on the photocurrent enhancements due to NRET from the QDs. The MoS_2 film quality is found to be critically important in order to achieve large photocurrent enhancements. Multiple devices with varying film quality are studied, including pristine monolayers, mixed monolayer/bilayer, and polycrystalline bilayer devices. NRET efficiencies of over 90% are measured on each device, however, photocurrent enhancements of ~14 fold are found for pristine monolayer devices, with modest enhancements of ~2.5 fold on mixed layer devices. The polycrystalline bilayer and bulk-like thickness devices show no enhancement of the photocurrent.

A spectral dependence study of NRET and photocurrent enhancements in coupled QD-monolayer MoS_2 devices is presented. This is the first demonstration of the spectral dependence of NRET in these coupled systems and also the first demonstration of the spectral dependence of the photocurrent enhancements. Three spectrally separated QDs with peak emission wavelengths of 450 nm, 530 nm, and 630 nm, were chosen for the study in order to identify the optimal spectral location for the sensitizing species in a hybrid QD-sensitized MoS_2 device. The largest photocurrent enhancements and NRET efficiencies were found for the 630 nm QD-monolayer MoS_2 system. Good agreement is found between the spectral overlap, NRET efficiency and photocurrent enhancement for each device, which indicates that the NRET drives the photocurrent enhancement in each hybrid device.

Acknowledgements

Firstly, I would like to thank my supervisor, **Prof. Louise Bradley** for all her advice and guidance.

Most importantly, I would like to thank my wife **Gillian**, my son **Adam**, and my daughter **Alexa**, for their love, encouragement, and support.

List of Publications

1. **J. J. Gough**, N. McEvoy, M. O'Brien, J. McManus, A. P. Bell, D. McCloskey, G. S. Duesberg, and A. L. Bradley. "*Spectral Dependence of Photocurrent Enhancements in Hybrid Quantum Dot-MoS_2 Devices*". Submitted February 2018.

2. J. Jadwiszczak, C. O'Callaghan, Y. Zhou, D. S. Fox, E. Weitz, D. Keane, C. P. Cullen, I. O'Reilly, C. Downing, A. Shmeliov, P. Maguire, **J. J. Gough**, C. McGuinness, M. S. Ferreira, A. L. Bradley, J. J. Boland, G. S. Duesberg, V. Nicolosi, and H. Zhang. "*Oxide-mediated recovery of field-effect mobility in plasma-treated MoS_2".* Sci. Adv. 4 (2018)

3. **J. J. Gough**, N. McEvoy, M. O'Brien, A. P. Bell, D. McCloskey, J. B. Boland, J. N. Coleman, G. S. Duesberg, and A. L. Bradley. "*Dependence of Photocurrent Enhancements in Quantum Dot (QD)-Sensitized MoS_2 Devices on MoS_2 Film Properties*". Advanced Functional Materials, 1706149 (2018)

4. **J. J. Gough**, N. McEvoy, M. O'Brien, A. P. Bell, D. McCloskey, J. B. Boland, J. N. Coleman, G. S. Duesberg, and A. L. Bradley. "*Enhancing the electrical properties of MoS_2 through nonradiative energy transfer*". Advanced Electromagnetic Materials in Microwaves and Optics (METAMATERIALS). IEEE, 124-126 (2017)

5. **J. J. Gough**, K. E. Siewerska, S. Mehigan, D. Hanlon, C. Backes, Z. Gholamvand, B. M. Szydłowska, W. J. Blau, E. McCabe, and A. L. Bradley. "*Influence of Graphene Oxide/Ag Nanoparticle Composites on the Fluorescence Properties of Organic Dyes*". Journal of Nanoscience and Nanotechnology, *17,* 8901-8911 (2017)

6. L. J. Higgins, C. A. Marocico, J. A. Garcia Coindreau, V. D. Karanikolas, A. P. Bell, **J. J. Gough**, G. P. Murphy, P. J. Parbrook, and A. L. Bradley. "*Influence of plasmonic array geometry on non-radiative energy transfer from a quantum well to a quantum dot layer*". Transparent Optical Networks (ICTON). IEEE, 1-4 (2017)

7. G. P. Murphy, **J. J. Gough**, L. J. Higgins, V. D. Karanikolas, K. M. Wilson, J. A. Garcia Coindreau, V. Z. Zubialevich, P. J. Parbrook, and A. L. Bradley. "*Ag colloids and arrays for plasmonic non-radiative energy transfer from quantum dots to a quantum well*". Nanotechnology, *28,* 115401 (2017)

8. B. D. Jennings, D. McCloskey, **J. J. Gough**, T. Hoang, N. Abadía, C. Zhong, E. Karademir, A. L. Bradley, and J. F. Donegan. "*Characterisation of multi-mode propagation in silicon nitride slab waveguides*". Journal of Optics, *90,* 015604 (2016)

9. **J. J. Gough**, K. E. Siewerska, S. Mehigan, D. Hanlon, C. Backes, Z. Gholamvand, B. M. Szydłowska, W. J. Blau, E. McCabe, and A. L. Bradley. "*Ag nanoparticle decorated graphene oxide: Fluorescence quenching and surface enhanced raman scattering*". Advanced Electromagnetic Materials in Microwaves and Optics (METAMATERIALS). IEEE, 121-123 (2016)

10. L. J. Higgins, C. A Marocico, V. D. Karanikolas, A. P. Bell, **J. J. Gough**, G. P. Murphy, P. J. Parbrook, and A. L. Bradley. "*Influence of plasmonic array geometry on energy transfer from a quantum well to a quantum dot layer*" Nanoscale, *8,* 18170-18179 (2016)

11. **J. J. Gough**, D. McCloskey, J. M. Caridad, V. Krstic, M. Müller, N. Gaponik, and A. L. Bradley. "*Chiral Ag nanostructure arrays as optical antennas*". Advanced Electromagnetic Materials in Microwaves and Optics (METAMATERIALS). IEEE, 88-90 (2015)

Conference Contributions

Oral Presentations:

1. **J. J. Gough**, N. McEvoy, M. O'Brien, A. P. Bell, D. McCloskey, J. B. Boland, J. N. Coleman, G. S. Duesberg, and A. L. Bradley. "*Enhancing the electrical performance of MoS_2 through non-radiative energy transfer*". Photonics Ireland 2017. 13th-15th September 2017, Galway, Ireland.

2. **J. J. Gough**, N. McEvoy, M. O'Brien, A. P. Bell, D. McCloskey, J. B. Boland, J. N. Coleman, G. S. Duesberg, and A. L. Bradley. "*Enhancing the electrical properties of MoS_2 through nonradiative energy transfer*". Advanced Electromagnetic Materials in Microwaves and Optics. METAMATERIALS 2017. 28th-31st August 2017, Marseille, France.

3. **J. J. Gough**, K. E. Siewerska, S. Mehigan, D. Hanlon, C. Backes, Z. Gholamvand, B. M. Szydłowska, W. J. Blau, E. McCabe, and A. L. Bradley. "*Ag nanoparticle decorated graphene oxide: Fluorescence quenching and surface enhanced raman scattering*". Advanced Electromagnetic Materials in Microwaves and Optics. METAMATERIALS 2016. 19th-22nd September 2016, Chania, Crete.

4. **J. J. Gough**, D. McCloskey, J. M. Caridad, V. Krstic, M. Müller, N. Gaponik, and A. L. Bradley. "*Chiral Ag nanostructure arrays as optical antennas*". Advanced Electromagnetic Materials in Microwaves and Optics. METAMATERIALS 2015. 7th-10th September 2015, Oxford, England.

5. **J. J. Gough**, D. McCloskey, J. M. Caridad, V. Krstic, M. Müller, N. Gaponik, and A. L. Bradley. "*Helical Nanostructures as Optical Antennas*". Photonics Ireland 2015. 2nd-4th September 2015, Cork, Ireland.

Poster Presentations:

1. **J. J. Gough**, D. McCloskey, J. M. Caridad, V. Krstic, M. Müller, N. Gaponik, and A. L. Bradley. "*Circularly Polarised Quantum Dot Emission via Coupling with Chiral Ag Nanostructures*". NanoMeta 2015. 5th-8th January 2015, Seefeld (Tirol), Austria.

Contents

Chapter 1

Motivation

“***There’s Plenty of Room at the Bottom***”. This is the title of the talk given by Nobel laureate, Richard Feynman, to the American Physical Society in Caltech in 1959 and is considered the inaugural lecture in the history of nanotechnology. In this talk, Feynman evoked a scientific field of research that had remained undeveloped, the field of nanotechnology. It was 15 years later in 1974 when Norio Taniguchi at the University of Tokyo, penned the term ‘nanotechnology’, when describing the research involving the synthesis and study of nanoscale objects with ‘new’ properties. As a result of the reduced size of nanomaterials, typically 1 – 100 nm in at least one dimension, the chemical and physical properties of the nanomaterial can differ significantly from the atomic, molecular, or bulk counterpart of the same elemental composition.[1] These nanomaterials offer an exotic intermediate between the basic building blocks of matter; atoms and molecules, and the macroscopic, bulk-matter. This intriguing situation gives rise to dynamics and properties that differ vastly from the macroscopic and molecular systems that prevail at larger scale.

Over the past 50 years or so, scientific advancements in material growth and fabrication techniques have paved the way for the fabrication and synthesis of many novel nanomaterials. These advancements have come in the form of both ‘top-down’ and ‘bottom-up’ approaches to the fabrication of nanomaterials. The ‘top-down’ approach involves the fabrication of nanostructures through processing of the bulk material, examples of which include; photolithography and electron beam lithography (EBL), focused ion beam (FIB) milling, nano-imprint lithography (NIL) and the mechanical exfoliation of 2D materials, to name but a few. In contrast, the ‘bottom-up’ approach is driven by the self-assembly of molecules and atoms. These ‘bottom-up’ approaches have gained significant momentum due to improved chemical synthesis techniques, some examples are; epitaxial growth methods such as metal-organic-vapor-phase-epitaxy (MOVPE), molecular beam epitaxy (MBE), and chemical and physical vapor deposition techniques, (CVD and PVD), respectively. Following the emergence of these techniques came the fabrication and synthesis of novel nanostructures and nanomaterials.

Some of the relevant milestones that relate directly to the work in this thesis include the growth of the first quantum well (QW) using MBE techniques in 1974.[2] In 1976, Broers *et al.* demonstrated the first use of EBL to pattern nanostructures, these structures consisted of 8 nm lines of Au/Pd film (10 nm thick) on carbon foil.[3] Quantum dots (QDs) were first discovered in 1981 by the Russian physicist Ekimov in a glass matrix[4] and in colloidal solutions in 1983 by Brus *et al.* at Bell labs.[5] Brus followed up on his discovery with derivations to describe the relationship between the size of the QD and the bandgap energy.[6,7] More recently came the discovery of atomically thin 2D materials in 2004 when Novoselov *et al.* isolated graphene from bulk graphite for the first time.[8]

Another promising property associated with nanomaterials is the ability of metallic nanoparticles (NPs) to support localised surface plasmons (LSPs). Surface plasmons are collective oscillations of conduction electrons between a metal and dielectric surface/interface.[9] The existence of surface plasmons in thin metallic films was first predicted in the 1950s by Rufus Ritchie.[10] Following this prediction, the 1960s saw an extensive body of experimental research in terms of propagating surface plasmon polaritons (SPPs).[11,12] LSPs which differ from the SPPs in that the LSPs are confined to the surface of plasmonic NPs, unlike SPPs that can propagate along the metallic surface at the metal-dielectric interface in thin metal films.[9]

Due to the perpetual advances in the fabrication of nanostructures, there has been a big focus on the realisation of fully functional optical antennas for many years now. The ability to control and manipulate light at the nanoscale unlocks endless potential for a variety of commercial applications including sensing,[13] lighting,[14] display,[15] and photodetection technologies.[16] However, while there has been significant progress in this field, we are yet to see full commercial application of optical antennas. As a consideration, one must appreciate the relationship between the antenna operation wavelength and the antenna dimensionality, which leads to antennas (ideally 3D) with structural dimensions ≤ 100 nm, when considering operation at optical frequencies. The performance of the antenna is also strongly influenced by fabrication related defects and as such there is little room for error in the fabrication stage as dimensions should be accurate to just a few nanometres. While traditional radio-wave antennas are fed by electrical generators, the majority of optical antennas in the literature are driven by light or active materials which are coupled to the antennas.[17–21]

One specific form of antenna that is of particular interest in this thesis is that of a helical antenna. Helical antennas can operate over a large bandwidth and have the added ability to polarise the radiation in accordance to the 'handedness' of the helix. Given that a helical antenna has a 'handedness' this gives rise to an inherent chirality associated with the antenna. Chirality is a property of asymmetry, and as a result of this asymmetry, a chiral object cannot be superimposed on its mirror image. While chirality is typically a property associated with sugars, proteins, and DNA, being of specific interest in the chemical and biological sciences,[22,23] there have been significant theoretical and experimental advances in terms of chiral nanostructures in recent years.[24–27] The coupling of active materials such as QDs to antennas provides a promising route towards increased directionality of the QD emission pattern and also the ability to polarise the QD radiation through the imparting of the antenna properties.[28–33]

When considering coupling in these nano-systems, particularly with fluorescent materials, an important mechanism to consider is that of nonradiative energy transfer (NRET). NRET is an efficient dipole-dipole coupling mechanism and provides a route for the transfer of energy between donor-acceptor pairs over limited distances, typically on the order of ~ 10 nm with a d^{-6} distance dependence for individual donor-acceptor pairs and a distance dependence of d^{-4} for 2D planes of donor-acceptor species. This short interaction range is a notable disadvantage regarding the exploitation of this mechanism in device applications. Nonetheless, there is a significant effort in the research community aimed towards increasing this interaction distance.[34] One specific area of interest which has gained substantial momentum is the interaction between emitters and plasmonic metal nanoparticles (NPs).

The early work regarding the interaction between emitters, such as QDs and organic dyes, and plasmonic materials, either thin films or NPs, revealed that the optical properties of the emitters could be significantly modified in the presence of a plasmonic material.[35–39] These modifications come in the form of enhanced Raman scattering signals due to the large electromagnetic field enhancement provided by the plasmonic material,[35] and reduced fluorescence lifetime and intensity due to an enhanced excitation rate, enhanced radiative rate and non-radiative energy transfer from the emitter to the plasmonic material which can result in emission quenching *via* Joule heating or scattered radiation.[36–39] Additionally, NRET from an emitter to a plasmonic NP has been demonstrated to have longer interaction distances than the traditional donor-acceptor pairs of emitters.[40] The promise of this interaction has prompted many theoretical studies of plasmon mediated NRET, predicting large enhancements of the NRET rate, efficiency, and range of the interaction.[41–43] In agreement with the theoretical predictions there have been a number of experimental studies demonstrating enhanced NRET rates, efficiencies, and range using a variety of different geometries, emitters, and plasmonic NPs.[44–53]

As mentioned above, the first QW was grown in 1974,[2] and since then there has been a substantial body of research regarding the characterisation and application of these materials.[54,55] However, there is a lesser body of work regarding the use of QWs coupled to nanostructures. The coupling between QDs and QWs allows for further device implementation such as nanoscale lasers, tunable solid state lighting, and solar cells.[56–59] However, in contrast to QWs, QDs have poor carrier transport properties and typically require additional charge transport layers for device implementation.[60] One obvious method to circumvent the poor carrier transport in the QDs is to utilise NRET from the QDs to the QWs. A hybrid system consisting of both QDs and QWs is advantageous for many device applications including LEDs and light harvesting systems as the hybrid system combines the excellent optical properties of the QDs with the electrical properties of the QWs.

More recently, the area of 2D materials has emerged and has had a significant impact on the scientific community. These 2D materials exhibit a plethora of exciting and exotic properties, including extremely high carrier mobilities in graphene,[8] and the transition from indirect bandgap at few layer thickness to direct bandgap at monolayer thickness in the Transition Metal Dichalcogenide (TMD) family of materials.[61–63] These 2D materials are also of interest in NRET studies and they have been shown to be exceedingly good acceptors in donor-acceptor pairs,[64–67] and have even been dubbed as ‘exciton sinks’.[64,68] These 2D materials also possess good electrical properties. While graphene exhibits unparalleled carrier mobilities, graphene lacks a direct optical bandgap. TMDs, however, possess a direct optical bandgap at monolayer thickness and display modest carrier mobilities, which leads to promising applications in photodetection and light harvesting devices. Similarly, given the ‘exciton sink’ behaviour of these TMD materials, it is of significant interest to utilise these materials as acceptors in donor-acceptor pairs to study the extraction of electrical current due to NRET. QDs are the optimal choice of donor in such a system given the advantages in terms of broadband absorption and high photostability in contrast with fluorescent dyes. These coupled QD-2D material systems provide an exciting route towards photodetection and light harvesting applications.

Much of the early work with these nanomaterials and nanostructures has focused on the growth, characterisation, and understanding of the individual, stand-alone materials or structures. In this thesis, a number of novel emerging systems were chosen as test beds for the exploration of coupled nano-systems. These materials are briefly mentioned above and include, QDs, QWs, plasmonic nanostructures and chiral plasmonic nanostructures, and 2D materials. However, it is the combination of these individual elements in coupled nano-systems that incite curiosity and offer a wealth of intriguing ‘what ifs’ that has provided the motivation for the work in this thesis. As such, each chapter in this thesis will be briefly outlined below.

Chapter 2 will focus on the introduction of the general topics discussed throughout this thesis. These topics include the optical properties QDs and QWs, the basics of NRET theory and the distance dependences of the process for different sample geometries, and also the impact of LSPs on emitters and the NRET process. Different energy transfer mechanisms are also briefly described. Traditional antenna theory with a focus on helical antennas is concisely explained and the basic properties of chiral systems outlined in the following section. The origin and benefits of Raman scattering and surface enhanced Raman scattering (SERS) are also described. This chapter also includes discussion of the most relevant literature reports and state-of-the-art for each of the coupled nano-systems studied in this thesis and their individual components.

In Chapter 3, all the sample preparation and characterisation techniques used in this thesis will be described. This chapter will include specific details on all the materials and techniques used to fabricate, synthesize, and measure the samples. The custom built experimental set-ups are also discussed in detail. Descriptions of the analysis of samples using absorption, photoluminescence (PL), and time-resolved photoluminescence (TRPL) are also provided.

Chapter 4 will focus on the coupling of QDs to Ag nanohelices. The Ag nanohelices are grown in an array and behave as an optical antenna array. This system was chosen to investigate whether the coupled system could behave as a single entity with the QDs acting as the feed for the antennas with the antennas influencing the radiation properties of the QDs. In particular, the interaction strength between the QDs and the Ag nanohelices is quantified using TRPL measurements. The far-field emission properties of the QDs when coupled to the Ag nanohelices were found to exhibit greater directionality in the far field emission pattern and circular polarisation of the emission in accordance with the handedness of the helices. The near-field coupling between the QDs and the Ag nanohelices was found to allow for the antenna properties of the Ag nanohelices to influence the emission properties of the QDs.

In Chapter 5, the influence of a Ag NP decorated graphene oxide (GO) composite on the fluorescence and SERS of three fluorescent dyes; Rhodamine 6G (R6G), Rhodamine B (RhB), and Sulforhodamine 101 (SR101) is investigated. This coupled nano-system was chosen to investigate the underlying physics in such a system. Previous reports using similar systems had shown large enhancements of the SERS signals from fluorescent dyes but it was unclear whether the major contribution to these enhanced signals was due to quenching of the dye fluorescence by the GO or enhancement of the SERS signal due to the large electromagnetic field enhancements from the Ag NPs. The interactions between the dyes and the Ag NP decorated GO, and each individual constituent; Ag NPs and GO are investigated using spectral PL, TRPL, and SERS. It was found that the SERS enhancements of R6G were influenced most strongly by the quenching of the PL by the GO, while SR101 was more strongly influenced by the Ag NPs. RhB was found to have the weakest SERS enhancements and also the weakest coupling to the Ag NP decorated GO substrate.

Chapter 6 focusses on the plasmon mediated NRET from QDs to QWs. Two systems were studied in this chapter, a system utilising colloidal Ag NPs and a system utilising lithographically defined arrays of Ag NPs. This coupled system consisting of colloidal Ag NPs was chosen to investigate the distance dependence of the NRET from the QDs to 2D QWs with different barrier thicknesses. The distance dependence was found to follow a d^{-4} dependence, with and without the Ag NPs, in agreement with theoretical predictions. This was also the first experimental demonstration of this distance dependence utilising a QW as an acceptor. The coupled QD-QW system utilising lithographically defined arrays of Ag NPs as the plasmonic elements was studied to investigate the tunability of the interaction using two different NP geometries, namely nanoboxes and nanodiscs. The nanodisc arrays lead to a stronger interaction but ultimately quenches the QD and QW intensity, whereas the nanobox array gives weaker interaction strengths but leads to enhancement of the QW emission.

Chapter 7 will focus on coupled systems of QDs and MoS_2 devices of varying film quality. This coupled nano-system was chosen to investigate the influence of the MoS_2 film quality on the photocurrent enhancements due to the NRET from the QD sensitizing layer. The interaction between the QDs and the MoS_2 was monitored using TRPL measurements and the enhancements in device performance were quantified using photocurrent measurements. Large enhancements were found for pristine monolayer MoS_2 devices with modest enhancements observed in devices consisting of mixed monolayer/bilayer films. There was no enhancement in devices consisting of polycrystalline films and also devices consisting of MoS_2 of bulk-like thickness.

In Chapter 8, a spectral dependence of NRET and photocurrent enhancements in coupled QD-monolayer MoS_2 devices is presented. Three QD samples with emission wavelengths of 450 nm, 530 nm, and 630 nm, spanning the visible spectrum were chosen for this study with the aim of identifying the optimal spectral location for a sensitizing species for hybrid QD-MoS_2 devices. Largest NRET efficiencies and photocurrent enhancements are found for the 630 nm QD-MoS_2 system. Good agreement is found between the spectral overlap, NRET efficiency and photocurrent enhancement for each device, indicating that the NRET drives the photocurrent enhancement in each hybrid device.

The main conclusions of this work and some outlook regarding the future work are given in Chapter 9.

Chapter 2

Background

2.1 Semiconductor Nanocrystal Quantum Dots

Semiconductor nanocrystal quantum dots (QDs) are quasi 0-dimensional (0D) structures that have spatial confinement in 3 dimensions. This spatial confinement is possible as an electrons de Broglie wavelength, λ_e, is greater than one order of magnitude larger than the lattice constant of many crystals, thus allowing for the confinement of the electrons while keeping the crystal lattice structure relatively unperturbed. As an illustration, consider the de Broglie wavelength, λ_e, and assuming the effective mass of an electron in a real crystal at room temperature ($k_B T = 26.7\ meV$) as an estimate of the electrons kinetic energy, the de Broglie wavelength is given by[9,69]

$$\lambda_e = \frac{h}{\sqrt{2m_e^* k_B T}} \tag{2.1}$$

As an example, consider CdTe, a semiconductor material comprising the nanocrystal QDs presented in Chapter 4 of this thesis. CdTe has an effective electron mass, $m_e^* = 0.1m_0$, which gives $\lambda_e = 23\ nm$ while the lattice constant is $a_L = 0.647\ nm$. As a result of this quantum confinement, the electronic structure of the QD can be described by discrete energy levels.[9,69] This can be understood by applying the quantum mechanical 'particle in a box' description to excitons (bound electron and hole states). The formation of an exciton occurs when a photon excites an electron from the valence band (VB) to the conduction band (CB) in a semiconductor material, thus leaving a positively charged hole in the VB. Due to the strong Coulombic attraction between the electron and the hole, an exciton is formed with an energy slightly less than that of the unbound electron and hole. This exciton can then be described using a quantum mechanical treatment as an exotic hydrogenic atom.

Excitons have an average physical separation between the electron and hole, denoted as the exciton Bohr radius, a_B^*, similar to the electron and proton in a hydrogen atom. However, in terms of the exciton, this Bohr radius, a_B^*, will vary depending on the material. The exciton Bohr radius is expressed as $a_B^* = \varepsilon_r(m/\mu)a_B$, where $a_B = 4\pi\varepsilon_0\hbar^2/m_e e^2$ is the Bohr radius, ε_r is the relative permittivity, m is the mass, and μ is the reduced mass. In bulk semiconductor crystals the energy levels can be treated as continuous as the physical dimensions are much larger than a_B^*. However, when the dimensions of the semiconductor material become comparable to a_B^* then the excitonic energy levels must be treated as discrete. The term quantum confinement is used to describe the situation of discrete energy levels. The band gap energy of QDs in such a strong confinement regime, where $r \ll a_B^*$ is approximated by[9,69]

$$E_g^{QD} = E_g^{Bulk} + \left[\frac{\hbar^2\pi^2}{2r^2}\left(\frac{1}{m_e} + \frac{1}{m_h}\right)\right] - 1.786\left(\frac{e^2}{\varepsilon_r}\right)0.248E_{Ry}^* \qquad (2.2)$$

where E_g^{Bulk} is the band gap energy of the bulk material, r is the radius of the QD, m_e and m_h are the effective masses of the electron and hole, respectively, ε_r is the dielectric constant of the material, and E_{Ry}^* is the Rydberg energy for the electron-hole pair. The first term in Equation 2.2 is the band gap energy of the bulk material, the second term arises from the effect of the ‘particle in a box’ and the third term is due to the Coulombic interaction between the electron and hole, and the last term is a spatial correlation term. This expression reveals that as the radius of the QD decreases, the band gap energy increases, thus leading to the tunability of the QD emission wavelength *via* the control of the QD size. A schematic illustration of the bulk material bandgap and the splitting (and tunability) of the QD bandgaps are shown in Figure 2.1.

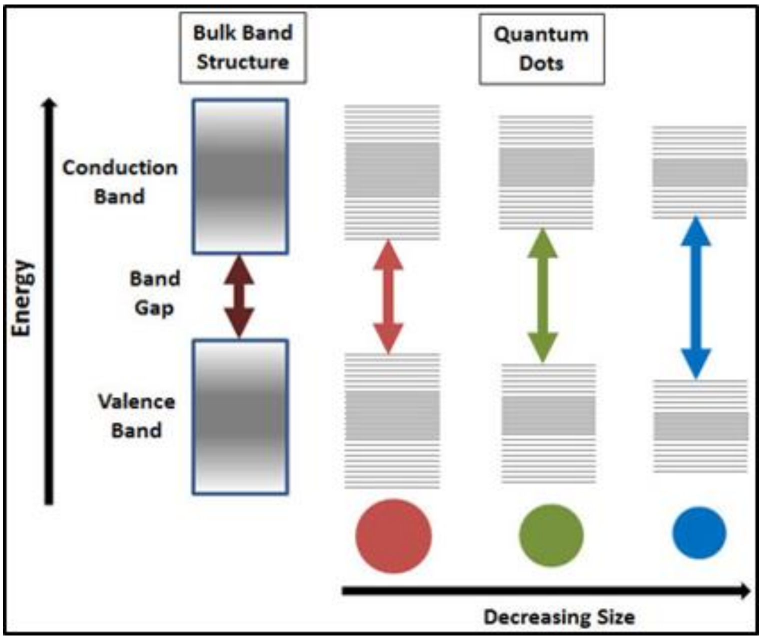

Figure 2.1: Schematic diagram of the splitting and increasing energy of the QD bandgap as the QD diameter decreases.

A significant benefit of QDs as compared to organic dyes is the ability to tune the emission wavelength through the size of the nanocrystal. QDs offer broadband absorption which permits a wide range of excitation wavelengths, and as such, a single excitation wavelength can be used to excite a variety of QD samples. This is in contrast to organic dyes which have narrow absorption bands where multiple excitation sources would be needed to excite various dyes. QDs also have greater photostability, a higher resilience to photobleaching, and recent advances in the chemical synthesis of colloidal nanocrystal QDs have led to improved quantum yields,[70–73] further demonstrating the substantial benefits of QDs over organic dyes, as a fluorescent species. These intriguing characteristics of semiconductor QDs have given rise to significant interest in the research community and also in applications such as display technology,[74] biomedical applications,[75,76] photodetectors[77–79] and photovoltaic devices.[80]

A QD will absorb a photon if the photon energy, E_{Ph}, is greater than the bandgap energy, E_g. As a result of quantum confinement in QDs, decreasing (increasing) the QD diameter will result in a blue-shift (red-shift) of the absorption onset corresponding to the first electronic transition. This can is expected as the $E \propto 1/L^2$ is evident from the 'particle in a box' description.[81] This photo induced energy can then be re-emitted as a photon through radiative recombination leading to photoluminescence (PL). The rapid optical excitation and de-excitation that leads to PL is commonly referred to as fluorescence. The photoemission (radiative) rate, k_r, of QDs is on the order of 10^8 Hz, and as such, the fluorescence lifetimes, τ, of QDs are ~10 ns, where $\tau = 1/k_{r}$.[9] The fluorescence lifetime of a fluorophore is defined as the average time between the excitation of an electron to the excited state and the return of this electron to the ground state *via* the emission of a photon. Theoretically, the time-resolved PL (TRPL) decay of a QD should be of mono-exponential form, illustrative of the intrinsic exciton recombination rate, k_r. However, given that solution processed QDs are not 'ideally' monodisperse, a given solution of QDs will contain an ensemble of QDs with deviating diameters, this in combination with surface defects leads to the observation of a multi-exponential TRPL decay for QDs.

To illustrate the tunability of the QD emission wavelength *via* the size of the nanocrystal, the absorption and PL spectra of three CdTe QDs are shown in Figure 2.2. Each of the QD solutions has a size distribution of 7-10%. It is clear from Figure 2.2 that the QD absorption and PL spectra blue-shifts (red-shifts) as the QD diameter decreases (increases). The PL spectra of the QDs have quite a broad distribution with full-width at half-maximum (FWHM) values between 40–50 nm. In terms of a single QD, one would expect to observe a narrow profile, similar to that of a delta function, however, due to the size distribution of the solution processed QDs in combination with scattering at surfaces and defects, a homogeneous broadening is observed and leads to a Gaussian-like PL distribution.[9,69]

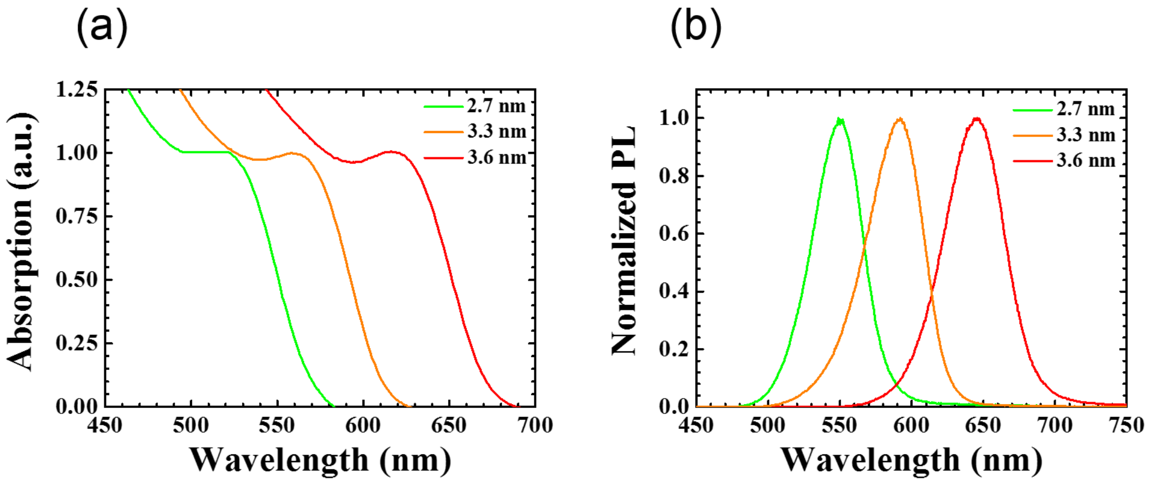

Figure 2.2: (a) Absorption spectra of three different sized CdTe QDs. The absorption spectra have been normalized to the peak absorption value of the first electronic transition. (b) Normalized PL spectra of the three CdTe QDs shown in a. The legend in each plot gives the QD diameter.

Consider the smallest QDs presented in Figure 2.2 in green, comparison between the peak wavelength of the first absorption peak (520 nm) and the peak of the PL spectrum (550 nm) reveals a red-shift of 30 nm. This difference in energy is known as the Stokes shift. The Stokes shift arises due to exciton-phonon interactions as the electron relaxes to the lowest vibrational level in the excited state, this is commonly referred to as internal conversion. The transition resulting in photon emission is usually from the lowest energy excited state to an excited vibrational level of the ground state. The electron then further relaxes *via* exciton-phonon interactions to the lowest energy ground state, which further increases the energy difference between the absorbed and emitted photon.[82]

The semiconductor nanocrystal QDs used in this thesis were solution processed, thioglycolic acid (TGA) stabilised CdTe core-only QDs and oleic acid functionalised alloyed CdSeS/ZnS core-shell QDs. The CdTe QDs were prepared and supplied in aqueous form from our collaborators in the Gaponik group, TU Dresden, Germany. The alloyed

CdSeS/ZnS QDs were purchased from Sigma-Aldrich in toluene at a concentration of 1 mg/mL.

2.2 Nonradiative Energy Transfer

Nonradiative energy transfer (NRET) is an efficient dipole-dipole coupling mechanism which occurs due to the Coulombic interaction between confined excitons in the donor and acceptor species.[68,82,83] The acceptor may be a non-emitting species, (e.g.) a metal (quenching species). NRET is commonly dubbed as Förster-type resonance energy transfer (FRET), named after the German physical chemist, Theodor Förster, who outlined the first theoretical description of the process.[84] With this process, the optical excitation of the donor species generates an oscillating transition dipole and if the donor and acceptor have resonant states in the excited (S_1) and ground (S_0) states, this oscillating donor dipole can induce a transition dipole in the acceptor, and this dipole-dipole interaction can mediate the transfer of energy from the donor to the acceptor.

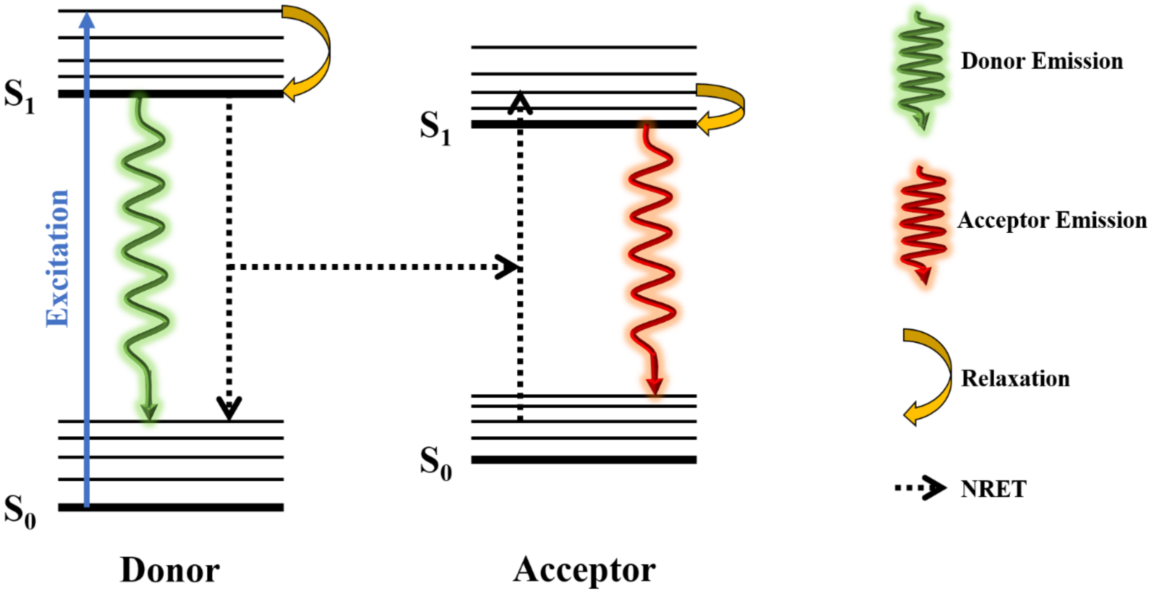

Figure 2.3: Schematic illustration of the NRET process.

A schematic representation of the process is given in Figure 2.3. The donor species is optically excited and an electron is promoted from the lowest energy ground state (S_0) to a vibrational level of the excited state (S_1), indicated by the blue line. This electron then relaxes to the lowest energy excited state *via* exciton-phonon interactions (internal conversion), indicated by the yellow arrow. If the donor is isolated, this electron can return to the ground state *via* radiative recombination of the exciton leading to photon emission, having a lifetime of $\tau_D = 1/(k_r + k_{nr})$, where k_r and k_{nr} are the radiative and nonradiative decay rates, respectively. The photon emission by the donor is indicated by the green line. However, if the donor is in close proximity to an acceptor species (typically within a distance of < 10 nm),[82,85] and the acceptor species has available states that are in resonance with the donor, this exciton energy can be transferred to the acceptor *via* NRET, with a rate, k_{NRET}, indicated by black dotted lines. The electron in the acceptor then relaxes to the lowest energy level in the excited state (yellow arrow) and the exciton undergoes radiative recombination, resulting in a photon emission from the acceptor.

This process leads to an increased decay rate, $k_{DA} = k_r + k_{nr} + k_{NRET}$, in the donor species due to the introduction of an alternative decay pathway in the presence of an acceptor. This increased decay rate can be measured experimentally as a reduced lifetime, τ_{DA}, given that $k_{DA} = 1/\tau_{DA}$. A decrease in the donor lifetime in the presence of an acceptor is the key fingerprint of NRET, as well as a reduction of the donor PL intensity.

2.2.1 Nonradiative Energy Transfer Theory

There are four underlying properties that determine the rate, k_{NRET}, and consequently, the efficiency, η_{NRET}, of the NRET process. These are; (i) the degree of spectral overlap, J, between the donor PL spectrum and the acceptor absorption spectrum, which accounts for the coupled oscillator strength of the donor and acceptor dipoles, (ii) the donor quantum yield, (iii) the relative orientation between the donor and acceptor dipoles, and (iv) the centre-to-centre distance, d, between the donor and acceptor species.

The rate of NRET, k_{NRET}, between a donor and acceptor species at a given centre-to-centre separation, d, is given by[82,85]

$$k_{NRET} = \frac{1}{\tau_D}\left(\frac{R_0}{d}\right)^6 \tag{2.3}$$

where R_0 is the characteristic distance at which the NRET efficiency, η_{NRET}, is 50%, and as mentioned earlier, $\tau_D = 1/(k_r + k_{nr})$, is the lifetime of the isolated donor. It should be noted that k_{nr} is the nonradiative decay rate to decay pathways other than NRET, such as exciton traps at defect states and internal conversion. Taking consideration of the four prerequisites mentioned above, the NRET rate, k_{NRET}, can be simplified as[68]

$$k_{NRET} = \frac{1}{\tau_D}\left(\frac{QY \cdot \kappa^2 \cdot J(\lambda)}{d^6}\right) \tag{2.4}$$

where QY is the quantum yield of the donor, κ^2 is a factor that describes the relative orientation between the donor and acceptor dipoles and $J(\lambda)$ is the spectral overlap between the donor emission spectrum and the acceptor absorption spectrum. The orientation factor, κ^2, is typically assumed to be 2/3 arising from the random orientations of both donor and acceptor dipoles.[82] The spectral overlap, $J(\lambda)$, is given by

$$J(\lambda) = \int_0^\infty I_D(\lambda) \cdot \varepsilon_A(\lambda) \cdot \lambda^4 d\lambda \tag{2.5}$$

where $I_D(\lambda)$ is the dimensionless, area normalized donor PL spectrum, $\varepsilon_A(\lambda)$ is the acceptor extinction coefficient spectrum in units of M^{-1} cm^{-1}, and given that λ is in units of nm, $J(\lambda)$ has units of M^{-1} cm^{-1} nm^4.

The characteristic distance at which the NRET process is 50% can be expressed by[68,82]

$$R_0 = \left(\frac{9000 \cdot ln(10) \cdot \kappa^2 \cdot QY \cdot J(\lambda)}{128 \cdot N_A \cdot \pi^5 \cdot n^4}\right)^{\frac{1}{6}} \tag{2.6}$$

where N_A is Avogadro's number and n is the refractive index. This expression can be further simplified by grouping the physical constants, where R_0 has units of nm

$$R_0 = 0.0211\left(\frac{\kappa^2 \cdot QY \cdot J(\lambda)}{n^4}\right)^{\frac{1}{6}} \tag{2.7}$$

The NRET efficiency, η_{NRET}, which represents the percentage of photo-generated excitons in the donor that transfer their energy to the acceptor is given by

$$\eta_{NRET} = \frac{k_{NRET}}{k_r + k_{nr} + k_{NRET}} \tag{2.8}$$

The NRET efficiency is typically extracted from the measured donor PL lifetimes and the integrated donor PL spectra when the donor is isolated (τ_D and I_D) and when the donor is in the presence of the acceptor (τ_{DA} and I_{DA}).[82] Therefore

$$\eta_{NRET} = 1 - \frac{\tau_{DA}}{\tau_D} \tag{2.9}$$

$$\eta_{NRET} = 1 - \frac{I_{DA}}{I_D} \tag{2.10}$$

where $\tau_{DA} = 1/(k_r + k_{nr} + k_{NRET})$ and $\tau_D = 1/(k_r + k_{nr})$. Substituting these lifetime relations into Equation 2.9 and rearranging gives Equation 2.8. Similarly, the energy transfer rate, k_{NRET}, can be calculated from the measured lifetimes as

$$k_{NRET} = \tau_{DA}^{-1} - \tau_D^{-1} \tag{2.11}$$

It should be noted that the rate equations described above have been derived for a single donor-acceptor pair. However, in the situation where a donor can interact with multiple, i, acceptors, then the NRET rate, k_{NRET}, of the single donor is the sum of all NRET rates, k_i, with respect of the NRET to the i^{th} acceptor at a centre-to-centre separation, d_i, from the donor, then the NRET rate is given by

$$k_{NRET} = \sum_i k_i = \tau_D^{-1} \cdot \sum_i \left(\frac{R_0}{d_i}\right)^6 \tag{2.12}$$

This expression indicates that increasing the number of acceptors surrounding a donor leads to an increased NRET rate and an increased probability of the NRET process occurring. Substituting Equation 2.12 into Equation 2.8 gives

$$\eta_{NRET} = \frac{\sum_i \left(\frac{R_0}{d_i}\right)^6}{1 + \sum_i \left(\frac{R_0}{d_i}\right)^6} = \frac{1}{1 + \left[\sum_i \left(\frac{R_0}{d_i}\right)^6\right]^{-1}} \tag{2.13}$$

In terms of the NRET in separated layers of donors and acceptors, analytical solutions can also be obtained.[86] Considering the homogenous distribution of acceptors in a plane layer, Equation 2.12 can be converted to a surface integral, given by

$$k_{NRET} = \tau_D^{-1} \cdot c_{Acc} \cdot \int_0^\infty \left(\frac{R_0}{d}\right)^6 dS \tag{2.14}$$

where c_{Acc} is the acceptor concentration. The integration limit can be extended to infinity given the NRET rate decreases rapidly as d increases. Carrying out the integration leads to the expression[87]

$$k_{NRET} = \frac{c_{Acc} \cdot \pi \cdot R_0^6}{2 \cdot d_{Plane}^4 \cdot \tau_D} \tag{2.15}$$

where d_{Plane} is the separation between the donor and acceptor planes. After carrying out the integral in Equation 2.14 it can be seen that the typical d^{-6} dependence of the NRET changes to a d_{Plane}^{-4} for the interaction of between a donor and a plane of acceptors. Substituting Equation 2.15 into Equation 2.8, gives the NRET efficiency as

$$\eta_{NRET} = \frac{1}{1 + \left[\frac{2 \cdot d_{Plane}^4}{c_{Acc} \cdot \pi \cdot R_0^6}\right]} \tag{2.16}$$

While the aforementioned theory was originally developed for molecular systems, previous studies have shown that the NRET in QD systems is described appropriately with a Förster-type NRET theory.[87–89]

2.2.2 Other Energy Transfer Mechanisms

When studying interactions in coupled nano-systems it is of paramount importance to distinguish NRET from other energy transfer mechanisms. These similar mechanisms are that of Dexter energy transfer,[68,90] charge transfer,[64,91–93] and radiative energy transfer.[94] In NRET processes, following the excitation of the donor, the excited donor species (D^*) relaxes to the ground state (D) as the excited state energy is transferred to the acceptor species (A^*), which was originally in the ground state (A) before the energy was transferred. The overall NRET process, which is a single-step process, can be represented as[68]

$$D^* + A \xRightarrow{k_{NRET}} D + A^* \tag{2.17}$$

The process of radiative energy transfer, however, is two-step. A photon which has been emitted by the donor is then absorbed by the acceptor, with the photon mediating the transfer of energy. In comparison to NRET, this has a longer interaction range, with a distance dependence of d^{-2}.[95] This two-step process can be represented by

$$(i)\ D^* \to D + hv \quad (ii)\ A + hv \to A^* \tag{2.18}$$

Similar to NRET, Dexter energy transfer is a nonradiative process which involves the exchange of electrons between the donor and acceptor species, this process occurs due to the overlapping charge wavefunctions in the donor and acceptor.[68,90] Given the reliance of the process on the overlap of charge wavefunctions, this process has a much more stringent distance dependence (~ 1 nm)[96] as compared with NRET. The rate of Dexter energy transfer, k_{Dex}, decreases exponentially as a function of distance, d, given by

$$k_{Dex} = K \cdot J_{Norm}(\lambda) \cdot e^{-\frac{2d}{L}} \tag{2.19}$$

where K is a factor that is related to specific orbital interactions, $J_{Norm}(\lambda)$ is the normalized spectral overlap term, and L is the characteristic wave-function decay length (van der Waals radius). $J_{Norm}(\lambda)$ is different to $J(\lambda)$ for the NRET calculation because the oscillator strength of the acceptor (accounted for by $\varepsilon(\lambda)$ in the NRET calculation) is not important for Dexter energy transfer.

Charge transfer, on the other hand is similar to Dexter energy transfer given that they both rely on the orbital overlap between the donor and acceptor species, however, the energy transfer range is slightly extended in the case of this mechanism (~ 2 – 3 nm).[64,91–93] Contrary to NRET and Dexter energy transfer, this mechanism does not require the spectral overlap between the donor and the acceptor, however, it does require an electron or hole donor and an acceptor species. The rate of charge transfer process, k_{CT}, similar to Dexter energy transfer, decreases exponentially with distance, given by

$$k_{CT} = K_0 \cdot e^{-\beta d} \tag{2.20}$$

where K_0 is a pre-exponential factor and β characterises the energy transfer.

For all of the coupled systems in this thesis, in terms of NRET, the minimum centre-to-centre separation between the donor and acceptor was greater than 3 nm. In Chapter 4, the CdTe core-only QDs have a diameter of 2.6 nm and a TGA ligand of ~ 0.5 nm. Multiple layers of QDs were deposited onto the Ag nanohelices and the first layer of QDs were separated from the Ag nanohelices by a PE buffer layer of ~ 7.5 nm. In Chapter 6, the alloyed core-shell CdSeS/ZnS QDs have a diameter of 6 nm and an oleic acid ligand of ~ 0.5 nm.

These were deposited on top of the GaN barrier/capping layer of the InGaN QWs. The active region of the InGaN QW is 2 nm and the GaN barrier thicknesses were 3 nm, 5 nm, and 7 nm, thus excluding Dexter energy transfer or charge transfer as the energy transfer process. Similarly, in Chapters 7 and 8, the QD donors used to study the NRET to MoS_2 devices were alloyed core-shell CdSeS/ZnS QDs with a diameter of 6 nm with an oleic acid ligand of ~ 0.5 nm. The monolayer MoS_2 has a thickness of ~ 0.65 nm. Once again, ensuring that the centre-to-centre distance between the donor and acceptor is greater than 3 nm. Therefore, the NRET in each of the systems studied is Förster-type NRET, which will just be referred to as NRET throughout the rest of the thesis.

2.2.3 Distance Dependence of Nonradiative Energy Transfer

NRET has a well-defined distance dependence and the distances over which this process can occur extend beyond the limits of Dexter energy transfer and charge transfer to ~10 nm.[82,85] In conventional NRET, single donor-acceptor pairs are considered, in which case, the efficiency and rate of the NRET has been proven to follow a traditional d^{-6} distance dependence.[83] However, consideration of the dimensionality of the donor-acceptor pair can lead to a range of different distance dependences which is ultimately governed by the acceptor dimensionality,[83,97,98] as illustrated in Section 2.2.1 for a 2D plane of 0D acceptors. The influence of the acceptor dimensionality on the distance dependence of the NRET is driven by the degree of quantum confinement in the acceptor species. These distance dependences of NRET have been proven as d^{-6}, d^{-5}, d^{-4}, and d^{-3} for QDs (confined in three dimensions), nanowires (NWs) (confined in two dimensions), QWs (confined in one dimension), and bulk materials (no confinement), respectively.[83] The NRET efficiency between a point dipole donor (QDs) to 0D QDs, 1D NWs, 2D QWs and 3D bulk materials, as a function of distance, is given in Figure 2.4 to illustrate the difference in these regimes.

For qualitative purposes and simplicity, R_0 has been set to 5 nm for each case. It is clear from Figure 2.4 that as the confinement decreases from three dimensions in the QD acceptor to no confinement in the bulk acceptor, that the range over which the NRET process can occur is increased but the efficiency at shorter distances falls off more quickly.

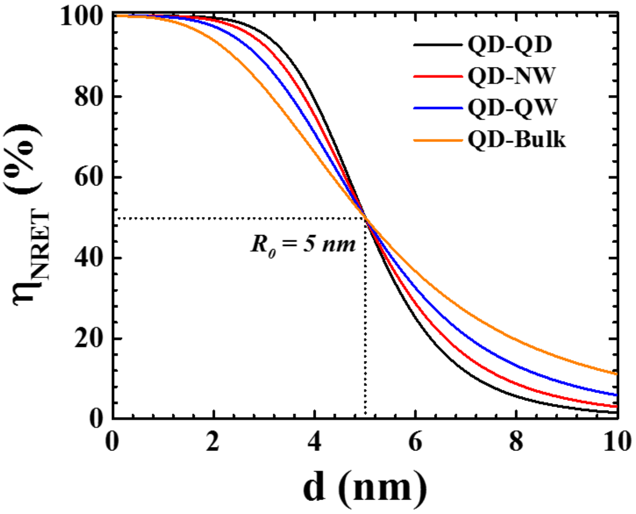

Figure 2.4: NRET efficiency as a function of distance showing the variation in the distance dependence due to the acceptor dimensionality.

2.3 Surface Plasmons

Surface plasmons are bound electromagnetic oscillations of conduction electrons at a metal/dielectric interface. There are two fundamental excitations of surface plasmons: Localised Surface Plasmon Resonance (LSPRs) and Surface Plasmon Polaritons (SPPs). LSPRs are non-propagating excitations of the conduction electrons in metallic nanoparticles (NPs) which are coupled to an electromagnetic field, these LSPRs are confined to the surface of the NP. LSPRs give rise to an enhanced near-field amplitude at sub-wavelength dimensions when excited at the resonance wavelength. This enhanced near-field amplitude decays rapidly into the surrounding dielectric medium. SPPs are propagating electromagnetic waves that propagate along metal/dielectric interfaces in planar structures.[9,99,100] The confinement of these waves to the surface requires that the dielectric permittivity of the metal, ε_m, and the dielectric, ε_d, are of opposite sign. The result of which reveals that these surface waves can only exist at the interface between a conducting medium and an insulating medium. The frequency at which $\varepsilon_m = -\varepsilon_d$ is known as the surface plasmon frequency, ω_{SP}.

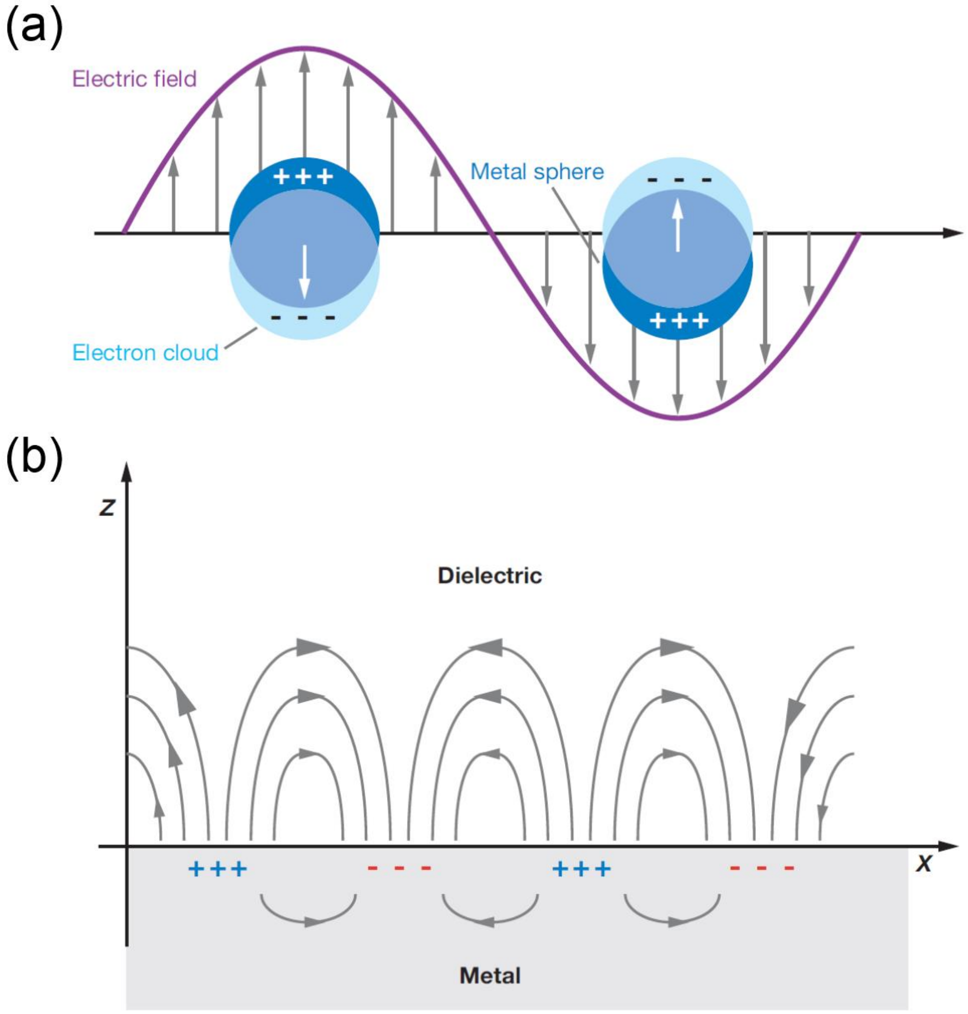

Figure 2.5: (a) Schematic illustration of LSPR in metallic NPs. (b) Schematic of SPP at a metal/dielectric interface.[101]

A schematic representation of LSPRs and SPPs is given in Figure 2.5. The work in this thesis in involving surface plasmons focusses solely on LSPRs of colloidal and lithographically defined arrays of plasmonic NPs. There are many benefits that arise from the inclusion of NPs that support LSPRs in coupled systems, such as, emitter-NP systems. Optical excitation of a plasmonic NP induces a coherent oscillation of electrons on both sides of the NP (assuming spherical geometry). Two specific light-matter interactions can occur here; (i) absorption of the incident light at or close to the peak LSPR wavelength and (ii) scattering of the incident light on the red (low energy) side of the LSPR. The sum of the absorption and scattering contributions gives the extinction. In terms of the light-matter interaction with a plasmonic NP, it is important to consider the NPs effective cross-section. The extinction cross-section, σ_{Ext}, is given by[102]

$$\sigma_{Ext} = \sigma_{Abs} + \sigma_{Sca} \tag{2.21}$$

where σ_{Abs} and σ_{Sca} are the absorption and scattering cross-sections, respectively. As mentioned above the electromagnetic excitation of the plasmonic NP causes a large electromagnetic field enhancement around the NP and this results in larger absorption and scattering cross-sections and consequently a larger extinction cross-section.[103] The relative contributions of absorption and scattering to the overall extinction is strongly dependent on the material, shape and size of the plasmonic NP. The effective cross-section of a plasmonic NP can be as much as 10 times larger than the actual NP size. This strong light-matter interaction has led to significant interest in implementation of plasmonic NPs in a variety of optical systems.

In coupled systems of emitters and plasmonic NPs, there can be modifications of the emitter’s properties which can result in a reduced fluorescence lifetime and reduced or increased fluorescence intensity. These modifications of the emitter’s florescence properties when coupled to plasmonic NPs can include an enhanced excitation rate, enhanced radiative rate and NRET from the emitter to the plasmonic NPs which can lead to emission quenching *via* Joule heating or scattered radiation from the plasmonic NPs.[37–39,52] A large body of work regarding the energy transfer to metals was contributed by Sibley, Chance and Prock in the late 1970's.[36] Such work has been more recently applied within a Nanometal Surface Energy Transfer (NSET) formalism.[40] Previous work in this group focussed on a complete study of the wavelength, concentration and distance dependence of NRET from QDs to a plane of Au NPs.[52] The experimental findings of this study revealed that while there is a good agreement between the calculated R_0 values using a Förster-type NRET model, and the experimentally obtained values for QDs emitting close to the peak wavelength of the LSPR (on-resonance) of the Au NPs, in terms of the QDs emitting at wavelengths longer than the peak LSPR (off-resonance) of the Au NPs, much better agreement is found for fitting with an NSET model which gives a characteristic distance, d_0, value. The data suggests that the NSET formalism gives a better approximation of the NRET to a plane of plasmonic NPs (non-emitting acceptors). More recently further theoretical work using the Greens tensor formalism has shown that in fact a range of distance dependences can be observed in emitter-plasmon coupled systems and that d^{-4} and d^{-2} dependences will only be observed under certain conditions.[43]

2.3.1 Plasmon Mediated Nonradiative Energy Transfer

As mentioned above, NRET is a dipole-dipole coupling mechanism with a well-defined distance dependence, typically < 10 nm in conventional systems.[82,85] However, the modification of Förster-type NRET in a donor-acceptor pair (point dipoles) *via* the inclusion of a plasmonic NP as a mediator of the NRET process was theoretically predicted in the 1980s.[41,104] The enhancement of the NRET depends on the distance between the donor/acceptor and the plasmonic NP, the geometry of the plasmonic NP, and also the orientation of the molecules donor/acceptor dipole transitions in terms of the location of the plasmonic NP. This enhanced NRET process could potentially increase the effective distance of the process from the conventional 10 nm by as much as 7 fold,[42] thus increasing the viability of NRET in future applications. Similarly it was found that the optimal geometry for plasmonic enhancement of NRET was to place the plasmonic NP between the donor and acceptor with a 180° separation between the donor and acceptor species.[42] Recent work carried out in this group has also found that the plasmon mediated NRET depends on a variety of factors, including the emission wavelength and quantum yield of the donor, and the size of the plasmonic NP (Au NPs were used in the aforementioned study).[43] It was found that the small Au NPs which have a negligible scattering component, can greatly reduce the emission intensity of the donor *via* an enhanced quenching rate, whereas increasing the diameter of the Au NP increases the scattering cross section and gives rise to a larger scattering component which can lead to increases in the donor emission intensity. Similarly, it was found that in the case of NRET in a donor-acceptor pair mediated by plasmonic Au NPs, that the donor-NP separation was much more influential in the process than the acceptor-NP separation. Interestingly, in the small Au NP limit, it was found that the interaction between the donor and the Au NP was, in essence, that of a single dipole-dipole interaction (d^{-6}), with the interaction strength increased over that of the free-space counterpart. Consideration of this enhanced donor-Au NP interaction indicates that the coupled donor-Au NP can be considered as an enhanced donor dipole that then couples with the acceptor dipole leading to an enhancement of the NRET process.

There have been numerous experimental observations of the enhanced NRET rate, efficiency, and characteristic interaction distance using a variety of emitters and plasmonic materials, either plasmonic films or NPs. In 2003, Lackowicz *et al*. revealed that the close proximity of Ag islands to donor-acceptor pairs bound to DNA led to an enhancement of the Förster radius, R_0, from 3.5 nm in the absence of the Ag islands to 16.6 nm.[105] Work carried out by the same group in 2007 demonstrated that the NRET rate in donor-acceptor pairs that were bound to a single Ag NP was enhanced by 21 fold while the Förster radius was consequently increased by 60%.[44,106] It should be noted that the NRET studies carried out by the Lackowicz group were carried out using dyes and not QDs. These previous reports demonstrated that the enhancement of the NRET depends on the size of the plasmonic NP and also the distance between the donor-acceptor pair and the surface of the plasmonic NP. Similarly, it is worth mentioning that the first experimental demonstration of plasmon enhanced NRET in mixed monolayers of CdTe core-only QDs was carried out in this group in 2006.[49] A study of the NRET from a conjugated polymer to an emitting, multilayer core-shell NP revealed an increase of over 50% of the Förster radius, a 13 fold enhancement in the NRET efficiency and a 173 fold increase in the NRET rate.[48] Work carried out by de Torres *et al.* demonstrated long range, plasmon mediated NRET using Ag nanowires (NWs) as the plasmonic element, which allows for propagating plasmons, where they found NRET efficiencies as large as 17% for a donor-acceptor separations of 1.3 μm.[107] However, the process involving SPPs as the NRET mediator is technically a two-step process while the LSP mediated NRET of interest to this thesis is a single-step process. In addition to these single NP or NW reports, NP dimers and resonators have also been demonstrated as effective plasmonic mediators of the NRET process.[45,108] A variety of other plasmon mediated NRET reports include the use of Ag prisms as the plasmonic element with donor ZnO NPs and acceptor core-shell CdSe/ZnS QDs in a mixed spincast layer;[46] and other layered configurations such as a mixed layer of core-only CdSe QDs and Ag NPs;[109] mixed core-shell CdSe/ZnTe and CdSeS/ZnS QDs with Au NPs;[110] and a separated layer structure of donor core-only CdTe QDs, Au NPs, and acceptor core-only CdTe QDs[50] reflective of the theoretically proposed optimal geometry for NRET.[42] Similarly, there are number of reports regarding the influence of the plasmonic NP concentration,[51] size,[111] distance,[53] and the selective coupling between the NP and the donor or the acceptor.[112]

Regarding the control of the NRET process *via* the plasmonic NPs, variation of the spectral position of the LSPR in terms of the donor and acceptor absorption allows the ability to switch the NRET process ‘on and off’, this was achieved by studying the core-shell arrangement of Au-Ag core-shell nanocrystals where the donors and acceptors were in the shell.[47] Competition between the plasmon mediated NRET rate and the modified decay rates of the donor and acceptor in the presence of the plasmonic elements has also been proven to either quench or enhance the PL intensity.[113–118]

Previous work in this group had focussed extensively on plasmon mediated NRET.[49–51,53] These studies revealed that the signatures of plasmon mediated NRET depend strongly on the positioning and concentration of the plasmonic NPs. The greatest enhancements in the NRET rate and efficiency were found for systems with higher plasmonic NP concentration, and those with the shortest separations between the donor and the plasmonic NP, and the acceptor and the plasmonic NP. As mentioned earlier, the separation between the donor and the plasmonic NP has a much larger influence on the NRET than the separation between the acceptor and the plasmonic NP.[53] It was also shown that the distance of the plasmon mediated NRET had the same d^{-4} distance dependence as conventional Förster-type NRET. The dominant coupling of the donor to the plasmonic NP indicates that in the tri-layer structure, where the Förster radius is independent of the separation between the acceptor and the plasmonic NP, the coupled donor-plasmon behaves as an enhanced donor dipole, in agreement with theoretical studies performed in this group.[43]

2.4 Antenna Theory

The IEEE Standard Definitions of Terms for Antennas (IEEE Std 145–1983) gives the definition of an antenna or aerial as “a means for radiating or receiving radio waves”.[119] That being said, the antenna is the traditional structure between free-space and a guiding device (receiver) or source (transmitter).[120] In Chapter 4, the free-space component is that of far-field propagating electromagnetic radiation and the source is the emission from the QDs.

Plasmonic nanostructures are commonly referred to as antennas due to their ability to convert the propagating far-field energy to localised near field energy.[121]

Helical antennas have many important uses; they are broadband antennas so they can operate across a broad frequency range and they have the added ability to circularly polarise the emitted radiation according to the handedness of the helix itself.[120] This is beneficial in two senses as the antenna can be used to transmit signals of a given circular polarisation and receive only signals that are polarised in the same handedness.[120] A traditional helix antenna is usually connected to a central conductor or coaxial cable (transmission line) at the feed point while the outer conductor is attached to a ground plane. For the work performed in Chapter 4, the source (feed) will be the CdTe QDs and the transmission line will be the near field of the excited QDs whilst the chiral Ag nanohelices will act as the antennas.

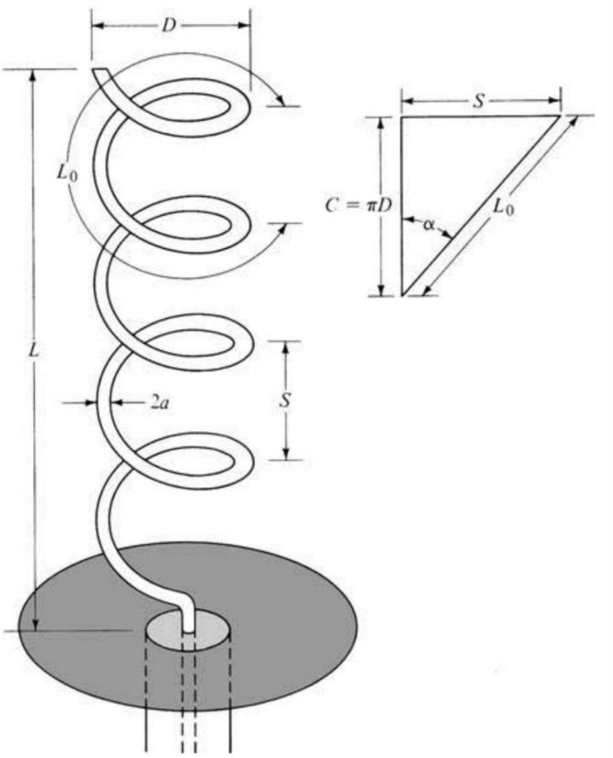

Figure 2.6: Schematic diagram of a traditional helical antenna.[120]

The traditional helical antenna can be seen in Figure 2.6. The geometrical parameters are labelled in the figure, whereby the helix has N turns, a diameter, D, and a pitch or spacing, S, between consecutive turns. The antenna has a total length, L, given by

$$L = NS \tag{2.22}$$

The total length of the 'wire', L_W, is given by

$$L_W = NL_0 = N\sqrt{S^2 + C^2} \tag{2.23}$$

where the length of the wire between turns, L_0, is given by

$$L_0 = \sqrt{S^2 + C^2} \tag{2.24}$$

The circumference of the structure is given by

$$C = 2\pi r = \pi D \tag{2.25}$$

The pitch angle, α, is the angle formed by a tangent line between the helix axis and the plane perpendicular to the same axis, given by

$$\alpha = tan^{-1}\left(\frac{S}{2\pi r}\right) = tan^{-1}\left(\frac{S}{C}\right) \tag{2.26}$$

The radiation characteristics of these helical antennas can be tailored by tuning the dimensions of the helix compared to the wavelength of operation. For helical antennas, the standard output polarisation is elliptical, but linear and circular polarisations can be achieved over varying frequency ranges. These helical antennas generally transmit in two modes/patterns; normal (broadside) and axial (end-fire). The broadside emission pattern has its maximum power radiating outwards, normal to the helix axis whereas the axial emission pattern has its maximum power radiating along the axis of the helix. The axial (end-fire) mode is the most practical mode for the system studied in Chapter 4 and can achieve circular polarisation over a large bandwidth.[120]

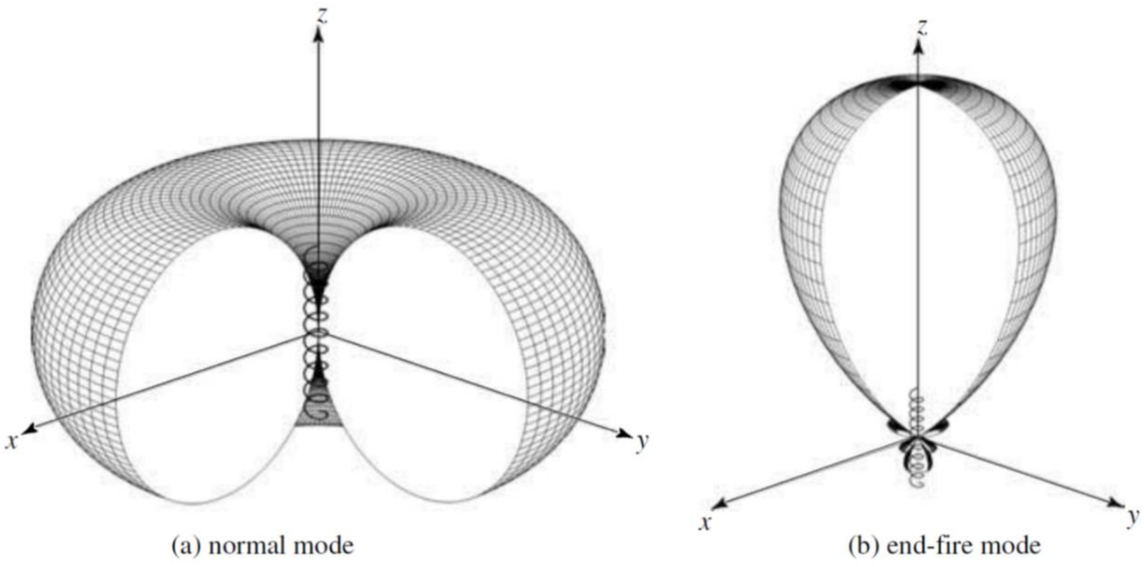

Figure 2.7: Three dimensional radiation patterns for helical antennas.[120]

The standard emission patterns for helical antennas can be seen in Figure 2.7. Herein, only the axial (end-fire) mode will be discussed as this is the emission pattern we wish to exploit. This mode displays just one main lobe with highly supressed side lobes. As can be seen from Figure 2.7, the maximum radiation intensity is along the helix axis. In order to excite the end-fire mode, the diameter and pitch of the helix must be large fractions of the operating wavelength, and circular polarisation in the main lobe is achieved when the circumference of the helix is in the range

$$\frac{3}{4} < \frac{C}{\lambda} < \frac{4}{3} \tag{2.27}$$

The optimum condition being $C/\lambda = 1$. The pitch should also be close to $S = \lambda/4$. Yet, this all relates to the antenna being fed from a coaxial line. Other feeds such as waveguides or dielectric rods are used more specifically at microwave frequencies. Here the dimensions of the helix are not as important for the end-fire mode and a greater bandwidth is achieved.[120]

In order to achieve an ordinary end-fire emission pattern using traditional antennas the relative phase, ϕ, throughout the turns of the antenna must be considered. This phase is given by

$$\phi = k_0 Scos(\theta) + \beta \tag{2.28}$$

Achieving an end-fire emission pattern requires that the radiation from each turn of the helix along $\theta = 0°$ is in phase, thus there is no phase difference ($\beta = 0$). The angle $\theta = 0°$ is along the helix axis, whereas $\theta = 90°$ is perpendicular to the helix axis. Therefore the wave along each turn of the helix travels a distance L_0 and the desired radiation direction is along $\theta = 0°$. In which case the phase is given by

$$\phi = (k_0 S\cos(\theta) - kL_0)_{\theta=0°} = -2\pi m \qquad m = 0,1,2,3\ldots \tag{2.29}$$

where $m = 0$ corresponds to that of a linear wire, and $m = 1$ corresponds to the first transmission mode of a helix and so on. To achieve maximum directionality, such as that of the Hansen-Woodyard pattern, the phase is given by

$$\phi = -\left(2\pi m + {}^{\pi}/_{N}\right) \qquad m = 0,1,2,3\ldots \tag{2.30}$$

Therefore, the normalized far-field emission pattern can be given by

$$E = sin\left({}^{\pi}/_{2N}\right)\cos(\theta)\left[\frac{sin\left({}^{N}/_{2}\right)\phi}{sin\left({}^{\phi}/_{2}\right)}\right] \tag{2.31}$$

The $\cos(\theta)$ term in the above equation represents the field pattern from one turn on the helix and the bracketed term represents the array factor for the uniform array of N elements. Multiplication of both terms gives the total field pattern.[120] It should be noted that Equations 2.30 and 2.31 are valid provided that $N > 3$.

The antennas studied in Chapter 4 are not that of the traditional model and may be more or less sensitive to certain aspects of the above given theory. The antennas used in this project are those of a plasmonic nature and have been shown to support a longitudinal LSPR which decays radiatively along the helical axis.[122,123]

2.4.1 Optical Antennas

Over the past two decades there has been significant interest in the premise of optical antennas.[16,17,32,123–128] These optical antennas are devices that efficiently couple the energy of free-space propagating radiation to a confined region of sub-wavelength dimensions. The majority of optical antenna demonstrations in recent years have utilised light as the driving force to manipulate the transmission/receiving of radiation.[17–19] Similarly, indirectly fed antennas have been demonstrated *via* excited states in active media close to the antennas.[20,21] These driving methods for optical antennas are unlike radio-wave antennas, which are fed by electrical generators. In 2015, Hecht *et al.* demonstrated the first electrically driven optical antenna.[129] The electrically driven device consists of a lateral tunnel junction and operates based on the quantum shot-noise of electrons tunnelling across the feed gap. Interestingly, the authors also find that the spectrum of emitted radiation can be tuned through the antenna geometry and the applied voltage. However, it is important to appreciate the dimensions of these devices. Radio antennas operating at radio frequencies generally have dimensions of ~ 1 m or less. Whereas dielectric waveguides, a technology that utilises planar structures to confine radiation to sub-micron dimensions, have been well established for decades. These devices generally operate at IR and microwave frequencies, and have structural dimensions of 1 – 10 µm. Now consider optical antennas, whereby the wavelength range of operation is between 400 – 700 nm, the dimensional requirements of these structures are sub 100 nm and must be accurate to tens of nanometres. This stringent requirement over the structural dimensions has been the main hurdle regarding the progress and commercial application of optical antennas. Some of the more promising characteristics of antennas are the ability to control the polarisation of the emitted radiation and the emission pattern.[120] These properties have attracted significant interest in recent years and there have been many reports of the influence of optical antennas on the emission patterns and polarisation of photoluminescence of emitters coupled to the antennas.[28–33] The advantageous properties of optical antennas and the efforts in the scientific community that are paving the way for the complete control of these antennas have led to the extensive application of optical antennas for photodetection,[16] sensing,[13] lighting,[14] and display technologies.[15]

2.5 Chirality

Chirality is in essence, a property of asymmetry. Chiral objects lack mirror symmetry and as a result of this the chiral object and its mirror image cannot be superimposed on top of each other. The signature characterisation technique for chiral objects is circular dichroism (CD) spectroscopy, a technique which is of great importance in chemistry,[22] biology,[23] and more recently nanoscience.[122,130–135] Chiroptical effects such as CD or optical rotary dispersion (ORD) arise due to a difference in the refractive indices and extinction coefficients which are experienced by incident light of either left- or right-circularly polarisation, LCP or RCP, respectively.[27] The refractive index difference, Δn, is responsible for ORD, which is a rotation of the plane of linearly polarized light upon interacting with chiral molecules or structures. The difference between extinction coefficients, $\Delta\varepsilon$, is responsible for CD effects,[27] and is measured from the difference in transmission of LCP and RCP light through the chiral molecules or structures. An example of a chiral structure's lack of mirror symmetry and a typical CD spectrum for an array of 'right-handed' Ag nanohelices is given in Figure 2.8.

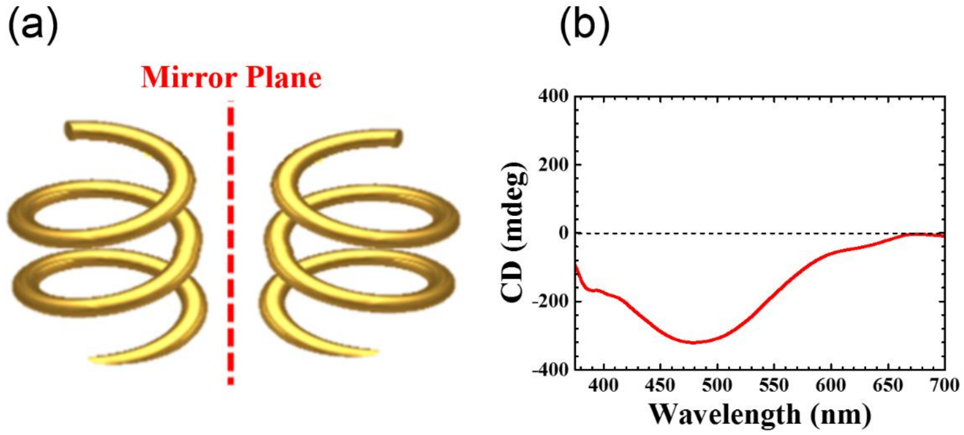

Figure 2.8: (a) Schematic representation of helix and its mirror image.[136] (b) CD spectrum of an array of 'right handed' Ag nanohelices.

Plasmonic metal nanostructures displaying chiroptical effects in the visible spectrum either intrinsically or *via* coupling to chiral molecules have been the subject of intensive theoretical investigation in recent years.[24–26] There have been several demonstrations of chiroptical effects in the infrared[134,137,138] and microwave[139] regimes of the spectrum. More recently, following the theoretical prediction of chiroptical effects in the visible spectrum, a variety of experimental displays of induced,[134] enhanced,[133] and intrinsic/structural[122,130,132,135,140,141] chirality have emerged in the literature. The emergence of these demonstrations is largely due to advances in molecular self-assembly,[135] lithographic, and deposition techniques which have allowed for the growth of three dimensional anisotropic structures.[122,130,132,140,141]

2.6 Raman Scattering

Raman scattering is a process which occurs due to the inelastic scattering of photons by molecules which have been excited to a higher energy vibrational or rotational level,[142] this leads to the scattered photons having different energies than that of the incident photons.

However, this form of inelastic scattering typically only occurs for 1 in every 10^7 incident photons. A much more common scattering process when photons interact with molecules is that of Rayleigh scattering, which is an elastic process, by which, the scattered photons have the same energy as the incident photons. There are two types of Raman scattering; Stokes Raman scattering, and Anti-Stokes Raman scattering. In the case of Stokes Raman scattering, the scattered photon energy is of lower energy than the incident photon energy. This loss of energy is due to the absorption of some the incident energy by the molecule, this loss of energy typically corresponds to a particular vibrational or rotational transition in the molecule, and as such, identification of the scattering peaks can be used as a 'fingerprint' technique to identify particular molecules.[143,144] In terms of Anti-Stokes Raman scattering, the scattered photon energy is greater than that of the incident photon. This process requires that the molecule is in an excited vibrational level of the ground state prior to the interaction with the incident photon. While Stokes Raman scattering is a $1/10^7$ event, Anti-Stokes Raman scattering is a much more unlikely process which is rarely observed under standard excitation conditions. Given the low probability of the Raman scattering of incident photons, the measured signals are very weak and require long integration times during measurements. A schematic representation of these scattering processes in terms of the energy loss and gain is shown in Figure 2.9.

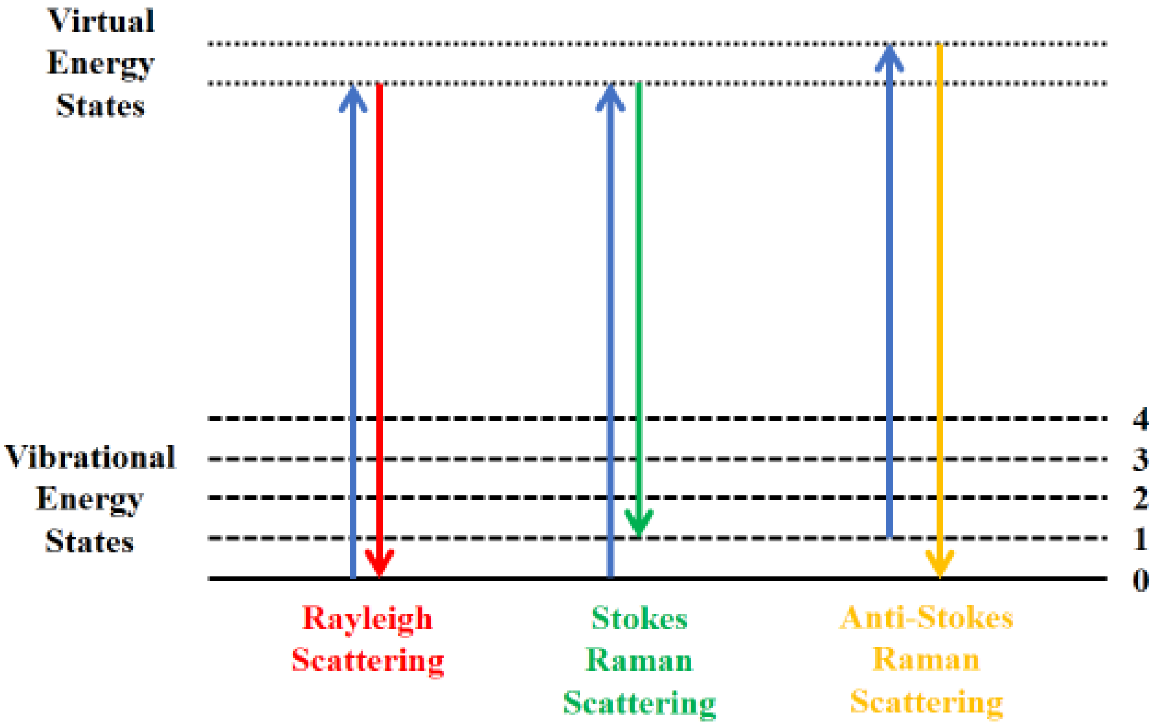

Figure 2.9: Schematic representation of elastic and inelastic scattering processes.

2.6.1 Surface Enhanced Raman Scattering

A significant breakthrough in the field of Raman spectroscopy was the discovery of Surface Enhanced Raman Scattering (SERS). SERS was first discovered in the 1970's and the process was attributed to two mechanisms, local electromagnetic field enhancement and the chemical enhancement, due to the presence of a roughened metal surface.[35,145,146] These large localized electromagnetic fields can be experienced by analytes located close to the surface of a metal, particularly nanostructured or roughened surfaces due to the occurrence of 'hot spots', regions of very high electromagnetic field. The enhancement of SERS by nanostructured metals has been an intense area of research over the past number of years as has been reviewed in the literature.[147–149] The most common materials utilised for SERS studies are those of noble metallic NPs, such as Au or Ag, given the relatively straight forward synthesis which provides control over size and shape of the NPs.[150,151]

Over the past few years, graphene and its derivatives, graphene oxide (GO) and reduced-graphene oxide (rGO), have been investigated as SERS substrates. These monolayer materials have been shown to produce strong chemical enhancement, which is attributed to charge transfer from the graphene substrate.[152–154] The atomically flat graphene substrate provides ideal conditions which allow for sufficiently close proximity of the analytes to the substrate to achieve efficient charge transfer. SERS enhancements as large as 10^3 have been reported for Rhodamine B (RhB) dye on rGO substrates.[155] Combined structures of metallic NPs on graphene and GO/rGO substrates have also been shown to provide significant SERS enhancements.[156–161]

2.7 Quantum Wells

QWs are 2D semiconductor materials that have their charge carriers confined in only one dimension, in comparison to the 3D confinement of charge carriers in semiconductor QDs. This means that the charge carriers in QWs are free to move in a 2D plane in the active region, confined only in the vertical direction. QWs are fabricated in a layered structure where the active QW is sandwiched between two layers of higher bandgap material. The QWs used in this study consist of an active layer of 2 nm thick InGaN sandwiched between GaN layers. Decreasing the thickness of the active layer leads to strong confinement of the charge carriers in 1D and this gives rise to the quantisation of energy levels,[9,162] which leads to the band structure that can be seen in Figure 2.10.

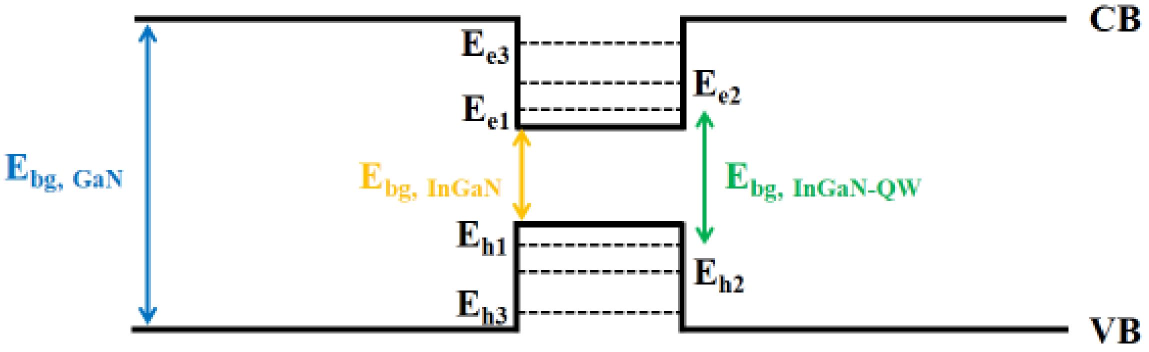

Figure 2.10: Band diagram of InGaN/GaN QW showing the conduction band (CB) and valence band (VB).

In comparison to their bulk crystal 3D counterparts, QWs display many interesting properties. One notable property is that of the exciton binding energy in the QW, which can be as large as four times that observed in the 3D bulk crystal.[9] The result of this manifests into many more exotic excitonic properties at higher temperatures. The absorption spectra of QWs also demonstrates a strong sensitivity to applied electric fields. This heightened sensitivity of the absorption spectra to applied electric fields allows for the integration of QWs with well-established CMOS techniques.[163,164] Regarding the InGaN/GaN QWs studied in Chapter 6, there are significant benefits regarding the use of these types of QWs for applications such as LEDs,[165–167] lasers,[9,168,169] and light harvesting devices.[170,171] In a similar vein, combining QDs and QWs in hybrid architectures has led to promising applications in photovoltaic devices,[59,172–174] colour conversion,[57,175–177] and white light generation.[178,179]

2.8 Summary

This chapter has provided a glimpse into the extensive work that has been carried out with QDs, NRET, plasmonic NPs, optical antennas, chiral nanostructures, and QWs. This chapter has also provided some of the basic theory that will be used throughout this thesis. In Chapter 4, the antenna properties of a coupled system of chiral Ag nanohelices and QDs are investigated for the first time. The influence of a Ag NP decorated graphene oxide composite on the fluorescence and SERS properties of organic dyes is studied in Chapter 5. The first experimental demonstration of plasmon mediated NRET from QDs to QWs is presented in Chapter 6. NRET from QDs to 2D MoS_2 devices will be the focus of Chapters 7 and 8. Chapter 7 investigates the role of MoS_2 film quality on the photocurrent enhancements in QD-sensitized MoS_2 devices. The first experimental demonstration of the spectral dependence of NRET and photocurrent enhancements in QD-sensitized MoS_2 devices is presented in Chapter 8.

Chapter 3

Sample Preparation and Characterisation

A variety of materials and structures were investigated in this work. In Chapter 4, the coupled structure of quantum dots (QDs) and Ag nanohelices was realised using the Layer-by-Layer (LbL) deposition technique.[180,181] The arrays of Ag nanohelices were grown using a room temperature glancing angle vapour deposition (GLAD) technique[122] and supplied by our collaborators in the Krstić group, TCD. The core only CdTe QDs were synthesized according to well documented standard procedures[71,182,183] and supplied by our collaborators in the Gaponik group, TU Dresden, Germany. The LbL deposition technique works on the basis of electrostatic attraction, whereby the deposition of alternating layers of oppositely charged species leads to the formation of complex and multi-layered structures. This simple and versatile technique allows for nanometre precision and control of the structure simply through the immersion of a substrate in solutions containing different charged molecules. This well-established technique has been extensively used to investigate the nonradiative energy transfer (NRET) process[53,184–187] and has been implemented in a variety of applications, such as, sensors and detectors,[79,188,189] photovoltaic devices,[190–193] and biomedical devices.[194,195] A detailed description of this technique and the materials used for the samples studied in Chapter 4 is given in Section 3.1.1.

The hybrid composites of Ag nanoparticles (NPs) and graphene oxide (GO), AgGO, studied in Chapter 5 were synthesized using a one-pot synthesis according to the method proposed by Zhang *et al.*[156] The GO was synthesized using a modified Hummers' method[196] and supplied by our collaborators in the Coleman group, TCD. The three fluorescent dyes used in the study; Rhodamine 6G (R6G), Rhodamine B (RhB) and Sulforhodamine 101 (SR101), were all obtained from Sigma-Aldrich. The dyes were optically characterised using

UV-Vis absorption, photoluminescence (PL), and time-resolved PL (TRPL) spectroscopy. A detailed description of the synthesis of the AgGO composite is given in Section 3.1.4 and the optical characterisation is of the composite is described in Section 3.2.4.

The hybrid QD-quantum well (QW), QD-QW, structures studied in Chapter 6 were realised using a spin coating technique. The alloyed CdSeS/ZnS QDs were purchased from Sigma-Aldrich and the Ag NPs were purchased from Plasmachem. The InGaN/GaN QWs were grown using a metal organic vapour phase epitaxy (MOVPE) technique[197] and supplied by our collaborators in the Parbrook group, TYNDALL. GaN buffer layers were grown on sapphire substrates, followed by the growth of a 2 nm InGaN QW. The 2 nm InGaN QW was then capped with GaN barrier layers of 3 nm, 5 nm, and 7 nm. The colloidal samples of QDs and Ag NPs, both in toluene, were dispersed in 0.1% wt. poly(methyl methacrylate) (PMMA) in toluene and spincast onto the QWs of different GaN barrier thicknesses. A detailed description of the sample characterisation is given in Section 3.1.5. The lithographically defined arrays of Ag NPs presented in the Chapter 6.3 were fabricated using electron beam lithography (EBL).

The QD-sensitized MoS_2 devices studied in Chapters 7 and 8 were realised using a spin coating technique. The mono- and few-layer MoS_2 was grown on Si/SiO_2 and quartz substrates using a chemical vapour deposition (CVD) technique[198] and supplied by our collaborators in the Duesberg group, TCD. The electrodes and the electrical contact pads were fabricated on the MoS_2 samples using EBL. The QDs were dispersed in 0.1% wt. PMMA and spincast onto the devices. The alloyed CdSeS/ZnS QDs used in both chapters were purchased from Sigma-Aldrich.

3.1 Sample Preparation

3.1.1 Layer-by-Layer: Materials and Sample Description

The samples described in this section were used to investigate the interaction between QDs and optical antennas, in the form of Ag nanohelices. With semiconductor nanocrystal QDs the optically excited exciton is formed in the core of the QD, whereby core-shell type QDs incorporate a shell layer of higher bandgap semiconducting material to passivate surface trap states, thus increasing the quantum yield of the QD and permitting for tighter confinement of the exciton to the core. However, core-shell type QDs are typically stabilised with organic ligands and only soluble in organic solvents which are not compatible with our LbL deposition process. The core only CdTe QDs and the chosen polyelectrolytes (PEs) are water soluble. The CdTe QDs are stabilized by a thioglycolic acid (TGA) functional group, giving the QDs a negative charge. The PEs used to form spacer layers were; positively charged Poly(diallyldimethylammonium chloride) (PDDA), and negatively charged Poly(sodium 4-styrene sulfate) (PSS). Both PEs were purchased from Sigma-Aldrich. The PDDA was purchased in solution (20% wt. in water with a molecular weight of 100,000 to 200,000) and used as stock. The PSS was purchased in powder form (molecular weight ~70,000) and a stock solution was prepared by dissolving 543 mg PSS in 10 mL Millipore water (Resistance = 18.2 $M\Omega/cm^2$) in an ultrasonic bath. The PEs tend to form long, stretched out, ultrathin layers to minimise electrostatic forces affecting them. Sometimes it is not particularly desirable to have such thin layers, and NaCl can be added to the solutions to increase the thickness of the polymer layers. The Na^+ and Cl^- ions screen the polymer charge when they dissociate in the solution and this allows for the PEs to curl and fold thus forming thicker layers.[199]

The PE solutions for the LbL procedure were prepared as follows:

- **PDDA**: 170 µL PDDA + 0.2 mL NaCl (3 M) + 5.8 mL Millipore water
- **PSS**: 560 µL PSS (Stock) + 0.2 mL NaCl (3 M) + 5.3 Millipore water

The above mentioned PE solutions give bilayer (PDDA/PSS) thicknesses of ~ 3 nm.

3.1.2 Description of the Layer-by-Layer Process

As mentioned above the LbL process involves the deposition of alternating layers by immersion in solutions of oppositely charged species.

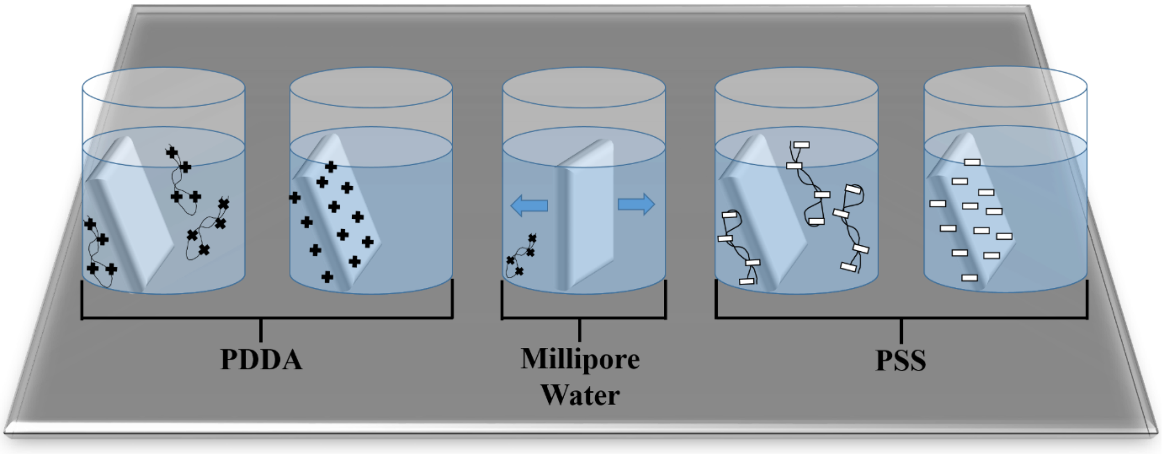

Figure 3.1: Schematic diagram of the LbL process showing the initial immersion of the substrate and absorption of the PE, followed by the rinsing and removal of excess PE, and the immersion and absorption of the second PE.

For the preparation of a LbL structure, the ITO/glass substrate is first immersed in a solution containing positively charged PDDA. The substrate is kept immersed in solution for 10 minutes to allow for complete coverage of the substrate with the positive PE, giving a net positive charge. The substrate is then removed from the PE solution and rinsed in Millipore water for 1 min to remove any loosely bound excess PE. The substrate is then immersed in the solution containing negatively charged PSS. Similarly, the substrate is kept immersed in the solution for 10 minutes to form the bilayer (PDDA/PSS). The substrate is then removed from the PE solution and rinsed in Millipore water to remove the excess and loosely bound PSS. These steps are repeated multiple times to achieve the desired number of layers. A schematic diagram of this process is given in Figure 3.1.

The samples studied in Chapter 4 required close proximity between the QDs and the Ag nanohelices to allow for effective coupling, and as such, two PE bilayers and a final layer of PDDA (resulting total thickness of the PE layers is ~ 7.5 nm) were deposited before the addition of the QDs, on both the Ag nanohelices and the reference ITO substrate. The TGA stabilized QDs have a negative charge and hence the outermost PE layer was positively charged PDDA to allow for the QDs to adhere to the PE due to electrostatic attraction. A schematic diagram of the LbL structure, including dimensions, on the Ag/ITO substrates is given in Figure 3.2.

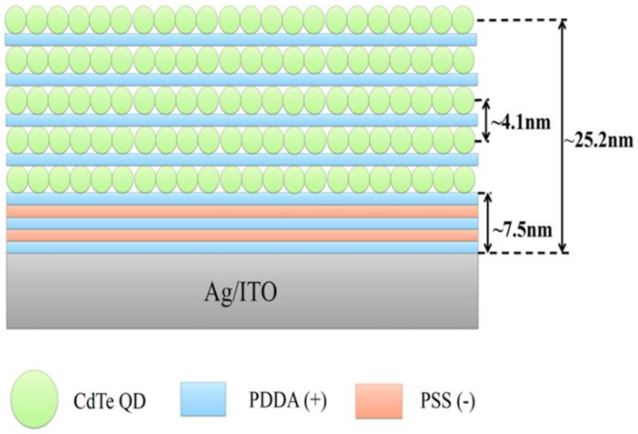

Figure 3.2: (a) Schematic diagram of the LbL samples on the Ag nanohelices/ ITO substrate surface.

3.1.3 Ag NP Decorated Graphene Oxide: Materials and Methods

The samples described in this section were used to investigate the influence of Ag NPs, graphene oxide (GO), and Ag NP decorated GO (AgGO) on the fluorescence and surface enhanced Raman scattering (SERS) properties of three organic dyes; R6G, RhB, and SR101.

Expandable graphite flakes, purchased from Asbury Graphite Mills, US, with an average flake size > 500 μm were used as starting material for the synthesis of GO. Chemicals used for GO synthesis included potassium permanganate ($KMnO_4$), sulphuric acid (H_2SO_4 97%), hydrochloric acid (HCl 37%) and hydrogen peroxide (H_2O_2 30%). Chemicals used for the AgGO synthesis were Poly-(N-vinyl-2-pyrrolidone) (PVP) (molecular weight = 40,000) and silver nitrate ($AgNO_3$) (molecular weight = 169.87). The fluorescent dyes used in the experiments were R6G, RhB and SR101. Unless otherwise stated all chemicals and dyes were purchased from Sigma Aldrich. The dyes were purchased in powder form and dissolved in Millipore water to achieve the desired concentration.

3.1.4 Synthesis of GO and AgGO

Large GO sheets were prepared by modified Hummers'[196] method using expandable flake graphite with a typical size of 500 - 600 μm as the raw material. In a typical procedure, graphite flakes were heated in a 100 W microwave for 15 s to produce expanded graphite (EG) (volume expansion ratio 70:1) as the precursor for GO synthesis. Then 4 g of EG and 500 ml of H_2SO_4 were mixed and stirred in a three neck flask for 2 hours. Next, 20 g of $KMnO_4$ was slowly added to the mixture. After 24 hours of stirring at room temperature, the mixture was transferred into an ice bath and 500 mL of deionized water and 100 mL of H_2O_2 were added dropwise into the mixture under controlled temperature ($T < 60$ °C) resulting in a colour change from dark green to golden yellow. Having stirred for another 30 minutes, the resulting oxidized EG particles were washed and centrifuged with HCl solution (9:1 vol water: HCl) three times, then centrifuged again and washed with deionized water. Repeated centrifugation and washing steps with deionized water were carried out until a solution of pH ≥ 5 was achieved. During the washing process, oxidized EG particles were exfoliated to GO sheets resulting in a highly viscous solution with concentrations above 4.5 mg/mL.

The obtained solution of GO in water was then further sonicated for 1 hour and a stock solution of 1.6 mg/mL was prepared for use as the precursor for the synthesis of the AgGO composite. The AgGO composite was prepared according to the method described by Zhang *et al.*[156] With this synthesis, 1.88 g PVP was dissolved in 8 mL of stock GO solution. The solution was then heated to 60 °C under constant stirring. Once the GO solution had reached 60 °C, 3 mL of 188 mM $AgNO_3$ in water was added and stirred for a further 5 minutes. The stirring was then stopped and the reaction was allowed to proceed for 24 hours. Four AgGO samples, labelled Sample A, B, C, and D, were prepared with different levels of Ag NP coverage on the GO flakes by altering the GO concentration in the reaction solution. Transmission electron microscope (TEM) images of the four AgGO samples with varying degrees of Ag NP coverage on the GO flakes can be seen in Figure 3.3. To obtain complete Ag NP coverage of the GO flakes the concentration of GO in the reaction solution was reduced to 0.01 mg/mL. The coverage of Ag NPs on the GO could not be increased beyond this point as the GO flakes were completely covered with dense clusters of Ag NPs. The product of the reaction was then centrifuged at 9000 RPM/5705 g using a Labnet Spectrafuge 7M (6.3 cm centrifuge radius and a 12 x 1.5 mL rotor) for 20 minutes and washed with Millipore water. This step was repeated 5 times to remove all of the excess and unbound Ag NPs. The resulting AgGO was then re-dispersed in 5 mL Millipore water and sonicated in an ultrasonic bath with a frequency of 35 kHz for 30 minutes. The microscopy based characterisation of the GO and AgGO samples are further discussed in Chapter 5.

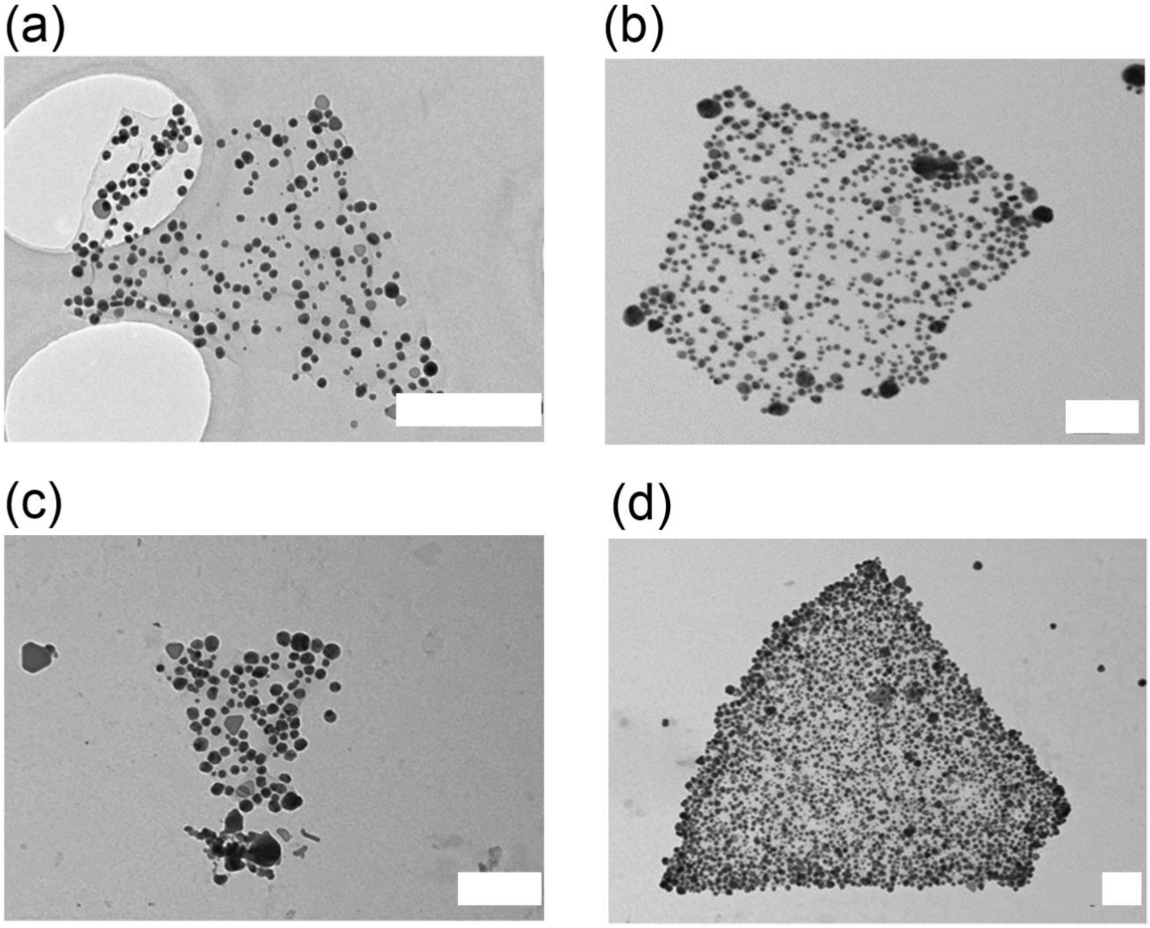

Figure 3.3: TEM images of AgGO samples with increasing Ag NP coverage. (a) Sample A (0.8 mg/mL GO), (b) Sample B (0.2 mg/mL GO), (c) Sample C (0.02 mg/mL GO), and (d) Sample D (0.01 mg/mL GO). The scale bar in each image is 200 nm.

3.1.5 Spin-coating of QD/PMMA Layers: Materials and Methods

The samples described in this section were used to investigate the nonradiative energy transfer (NRET) from QDs to 2D materials, such as, InGaN/GaN quantum wells (QWs) in Chapter 6, and MoS_2 in Chapters 7 and 8. The QDs used for these studies were alloyed CdSeS/ZnS core-shell semiconductor nanocrystals. The QDs have peak emission wavelengths of 450 nm, 530 nm and 630 nm. The QDs were purchased from Sigma Aldrich and were supplied in toluene at a concentration of 1 mg/mL and these solutions were used as stock. Unlike ‘traditional’ QDs, the optical properties of these alloyed QDs are tuned through the elemental composition of the nanocrystal[200] and not by the physical dimensions. This tuning of the QD optical properties through the composition of the nanocrystal is beneficial for spectral dependence studies as the QDs with emission wavelengths of 450 nm, 530 nm, and 630 nm, all have the same diameter (6.0 ± 0.8) nm and this removes any ambiguity regarding the centre-to-centre separation between the QD (donor) and acceptor species. Poly(methyl methacrylate) (PMMA) with a molecular weight of 996,000 was purchased in powder form from Sigma Aldrich. The PMMA solution for the spin-coating of QD/PMMA layers was prepared to a concentration of 0.1% wt in toluene.

The samples used in the first section of Chapter 6, for the study of the distance dependence of NRET from 450 nm QDs to InGaN/GaN QWs with GaN barrier thicknesses of 3 nm, 5nm, and 7 nm, consisted of QDs and colloidal Ag NPs dispersed in a solution of 0.1% wt. PMMA in toluene. To ensure even dispersion of the QDs and the Ag NPs in the PMMA solution, the blend was then sonicated for ~ 20 s. The resultant mixture was subsequently spincast at a speed of 5000 RPM onto the InGaN/GaN QWs of different GaN barrier thicknesses and the GaN reference substrates. Spin-coating of the QDs in the 0.1% PMMA results in an ultrathin layer with a thickness of (6 ± 2) nm, as confirmed by atomic force microscopy (AFM) (See Figure 3.4). A schematic diagram of the colloidal Ag NP samples is also given in Figure 3.4c.

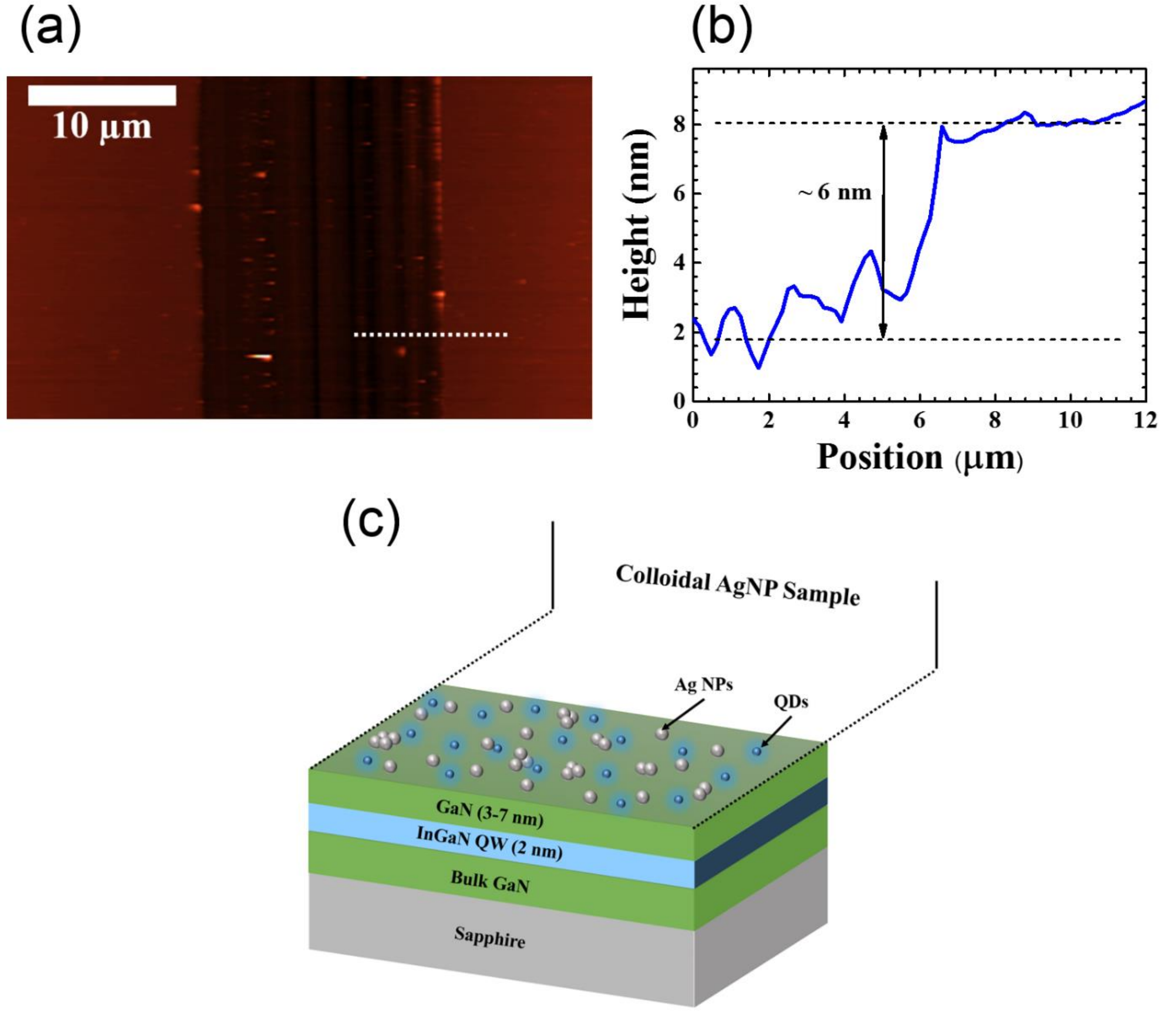

Figure 3.4: (a) AFM image of a single trench cut into the QD/PMMA layer on a GaN substrate. (b) Height profile of the QD/PMMA layer corresponding to the dotted white line in the AFM image in a. (c) Schematic diagram of the colloidal QD and Ag NP sample on the QWs with different GaN barrier thicknesses.

The second section in Chapter 6 focusses on the plasmon mediated NRET from 450 nm QDs to an InGaN/GaN QW with a GaN barrier thickness of 3 nm. In this section, lithographically defined arrays of Ag NPs are used as the plasmonic element as opposed to the colloidal Ag NPs used in the distance dependence study in the first section of Chapter 6. The arrays of Ag NPs were fabricated on the InGaN/GaN QW and the GaN reference substrate using electron beam lithography (EBL). The arrays of Ag NPs in the form of nanoboxes and nanodiscs were fabricated by patterning a PMMA resist using EBL. The focussed electron beam draws the pattern of the arrays in the PMMA resist, causing the long chained PMMA molecules to be broken up into short chain molecules. The short chain molecules are then removed in the developer solution leaving the exposed regions void of any polymer. The developer solution consists of methyl-isobutyl ketone (MIBK) and isopropyl alcohol (IPA) in a ratio of 1:3 (MIBK:IPA). The Ti/Ag (5 nm/ 35 nm) metals were deposited using electron beam evaporation. The PMMA is then removed in acetone using a standard lift-off process, leaving behind only the plasmonic structures that have adhered to the substrate. A schematic diagram of the arrays, including dimensions, is given in Figure 3.5a with SEM images of the nanobox and nanodisc arrays given in Figure 3.5b and Figure 3.5 c, respectively.

The samples used to study the NRET and photocurrent enhancements in QD-sensitized MoS_2 devices in Chapter 7 consisted of alloyed CdSeS/ZnS QDs with a peak emission wavelength of 630 nm in an ultrathin PMMA layer on a variety of MoS_2 electrical devices. The QD/PMMA blend was prepared by dispersing 12.5 µL of the stock QDs in 500 µL of 0.1% wt. PMMA in toluene and the solution was placed in an ultrasonic bath for ~ 20 s to ensure the even dispersion of the QDs in the PMMA solution. The MoS_2 islands giving large area coverage were grown on Si/SiO_2 substrates using CVD techniques[198] by our collaborators in the Duesberg group, TCD. The electrical devices were fabricated by patterning a PMMA resist using EBL. The Ti/Au (5 nm/ 45 nm) contact pads and electrodes were deposited using electron beam evaporation. The contact pads have dimensions of 80 µm x 80 µm and each device has a 5 µm channel length between the electrodes. The QD/PMMA solution was subsequently spincast onto the Si/SiO_2 substrates containing the MoS_2 devices.

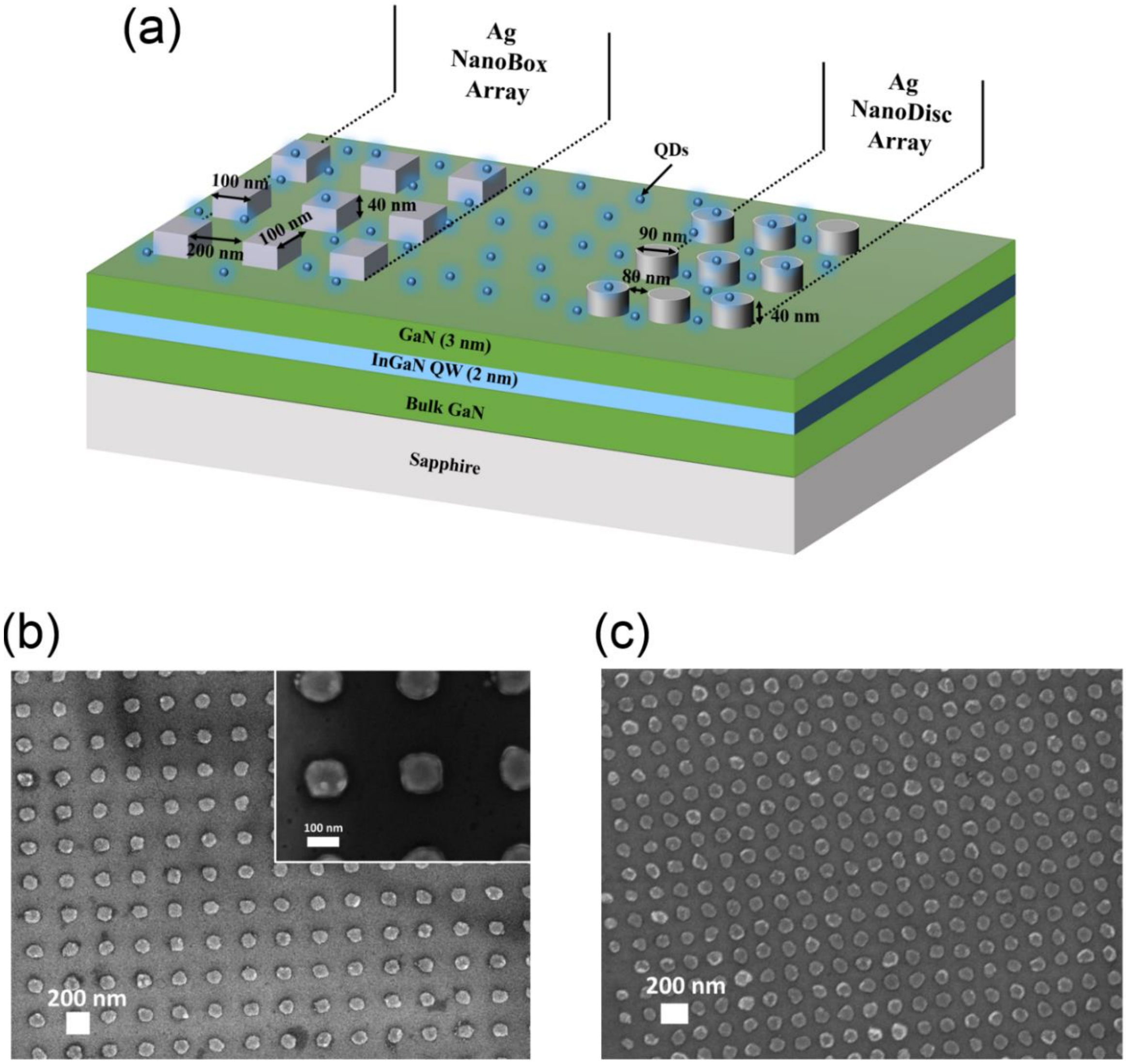

Figure 3.5: (a) Schematic diagram of EBL defined nanobox and nanodisc arrays. The diagram does not include the 5 nm Ti adhesion layer underneath the 35 nm Ag structures. (b) SEM image of the nanobox array. Inset: Zoom-in image of the nanoboxes to illustrate the box like shape of the structure. (c) SEM image of the nanodisc array.

The samples used in Chapter 8 to investigate the spectral dependence of NRET and photocurrent enhancements in hybrid QD-MoS_2 devices consisted of ultrathin sensitizing layers of alloyed CdSeS/ZnS QDs with peak emission wavelengths of 450 nm, 530 nm, and 630 nm on triangular monolayer MoS_2 electrical devices. Similar to the samples used in

Chapter 7, 12.5 µL of the QD (450 nm, 530 nm, and 630 nm) stock solutions were dispersed in 500 µL of 0.1% wt. PMMA and sonicated for ~ 20 s to ensure the even dispersion of the QDs in the PMMA solution. The triangular MoS_2 monolayers were grown using CVD techniques by our collaborators in the Duesberg group, TCD. The electrical devices were fabricated in an identical manner to those mentioned in the paragraph above for use in Chapter 7. The QD/PMMA solutions were then spincast onto the Si/SiO_2 substrates containing the triangular monolayer MoS_2 devices. The thickness of the QD/PMMA layers were verified using AFM (See Figure 3.6). The layer thicknesses as verified by AFM were (7 ± 3) nm, (9 ± 2) nm, and (8 ± 2) nm for the 450 nm, 530 nm, and 630 nm QD/PMMA layers, respectively. Schematic diagrams of the 630 nm QD-sensitized MoS_2 devices and the QD-sensitized triangular monolayer MoS_2 devices can be seen in Figure 3.6g and Figure 3.6h, respectively.

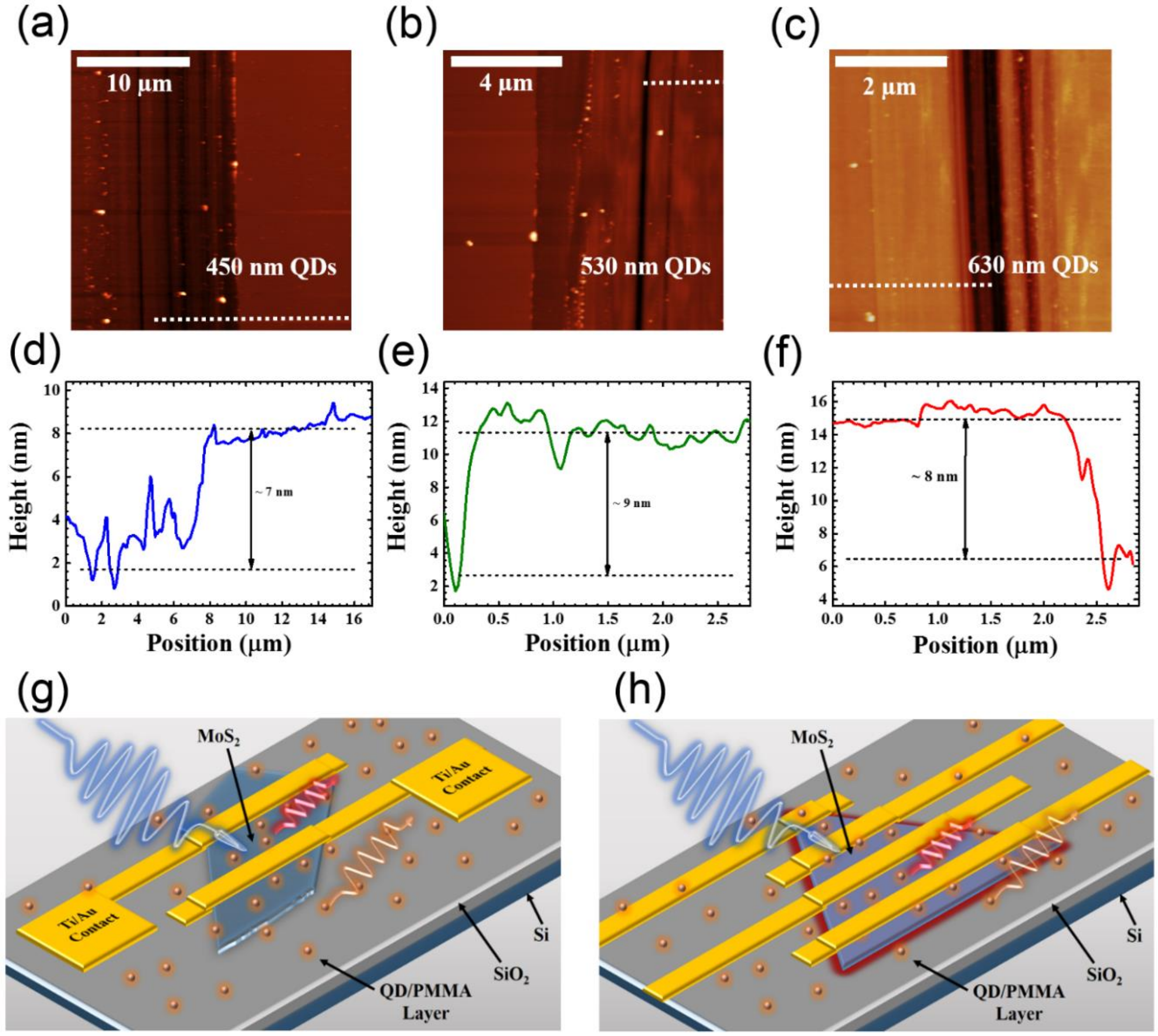

Figure 3.6: (a-c) AFM images of the trenches cut into the (a) 450 nm QD/PMMA layer, (b) 530 nm QD/PMMA layer, and (c) 630 nm QD/PMMA layer. (d-f) Height profiles corresponding to the white dotted lines in a-c, respectively. (g) Schematic diagram of the 630 nm QD sensitized MoS_2 devices. (h) Schematic diagram of the QD sensitized triangular monolayer MoS_2 devices.

3.2 Sample Characterisation

3.2.1 Transmission, Reflection and Extinction Measurements over Micron-Scale Areas

The array of Ag nanohelices studied in Chapter 4 was characterised by means of circularly polarised transmission and reflection measurements. Given the small size of the array of Ag nanohelices (~ 100 µm x 100 µm), a custom built setup had to be constructed to accurately measure the optical properties from the array itself. Standard, commercial UV-Vis spectrometers could not be used as the optical spot size is generally a few millimetres in diameter at the focus. Similarly, the CVD grown MoS_2 triangles studied in Chapter 8 have typical edge lengths of between 10 µm and 20 µm and as such commercial UV-Vis spectrometers are incapable of accurately measuring the optical properties of individual flakes. A schematic diagram of the custom built transmission apparatus is shown in Figure. 3.7.

The custom built setup shown in Figure 3.7 works on the principle of magnification. The setup magnifies the region of interest and forms an image of the sampling area on the face of a fibre optic cable which is fed directly to a spectrometer. The setup was carefully constructed to ensure that transmission and reflection measurements are easily performed without any modifications to the fixed components in the system. Flip mounted beam splitters and mirrors are used to redirect the optical path to perform reflection measurements. Flip mounted optical components are shown with dashed lines in Figure 3.7. There is also a collimated space in the system that allows for the addition of polarising optics such as linear polarisers and quarter wave plates for the circular dichroism (CD) measurements.

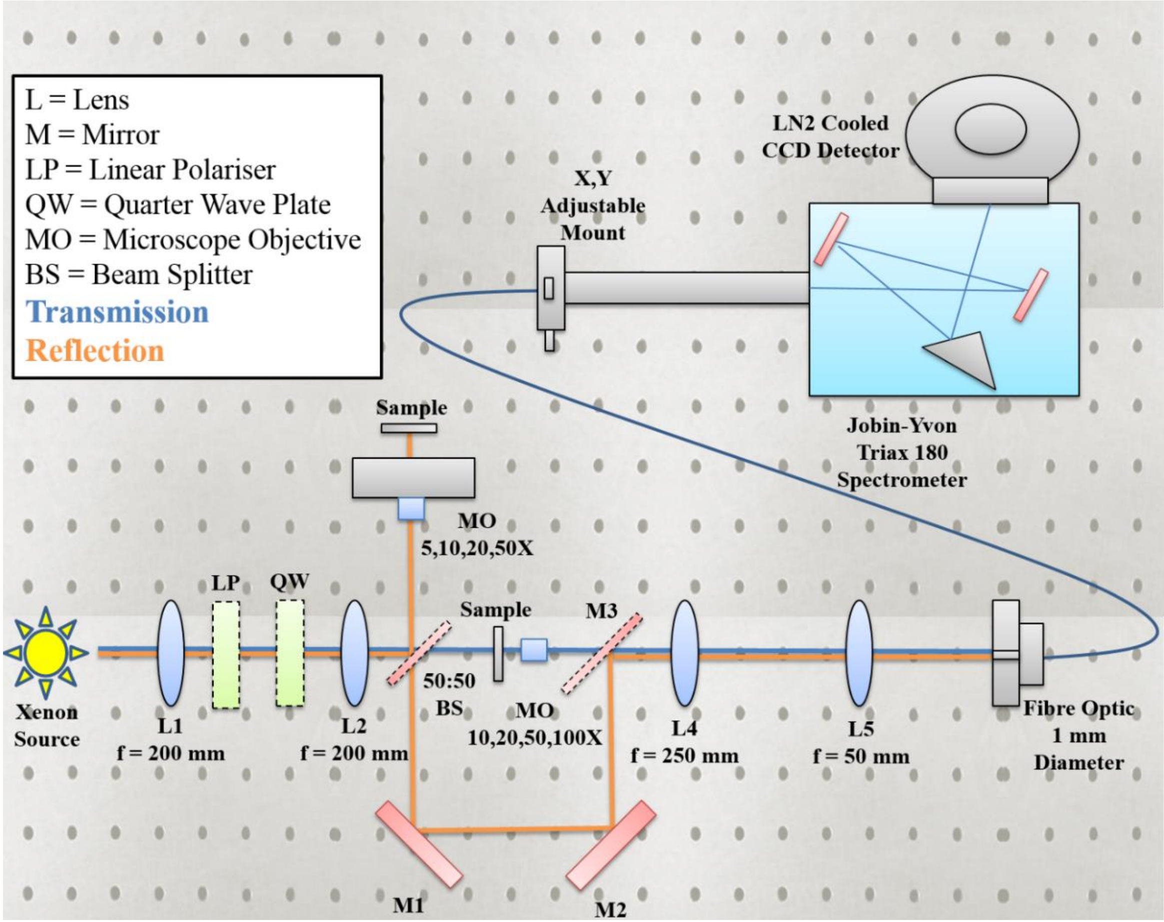

Figure 3.7: Schematic diagram of the custom built transmission apparatus.

The accuracy of the custom built system was confirmed by comparing the transmission spectrum of a Ti/Au film on a quartz substrate obtained in a commercial UV-Vis spectrometer and the custom built setup, as seen in Figure 3.8a. The system was also used to measure the extinction of triangular monolayers of MoS_2 with edge lengths of ~ 20 µm on quartz substrates (See Figure 3.8b). The ability to incorporate polarising optics into the collimated space in the setup allowed for the measurement of chiral signatures in the chiral Ag nanohelices by measuring the transmission and reflection from the arrays using both left- and right-circularly polarised (LCP and RCP, respectively) light. The transmission and reflection spectra of the Ag nanohelices under LCP and RCP illumination can be seen in Figure 3.8c and Figure 3.8d, respectively.

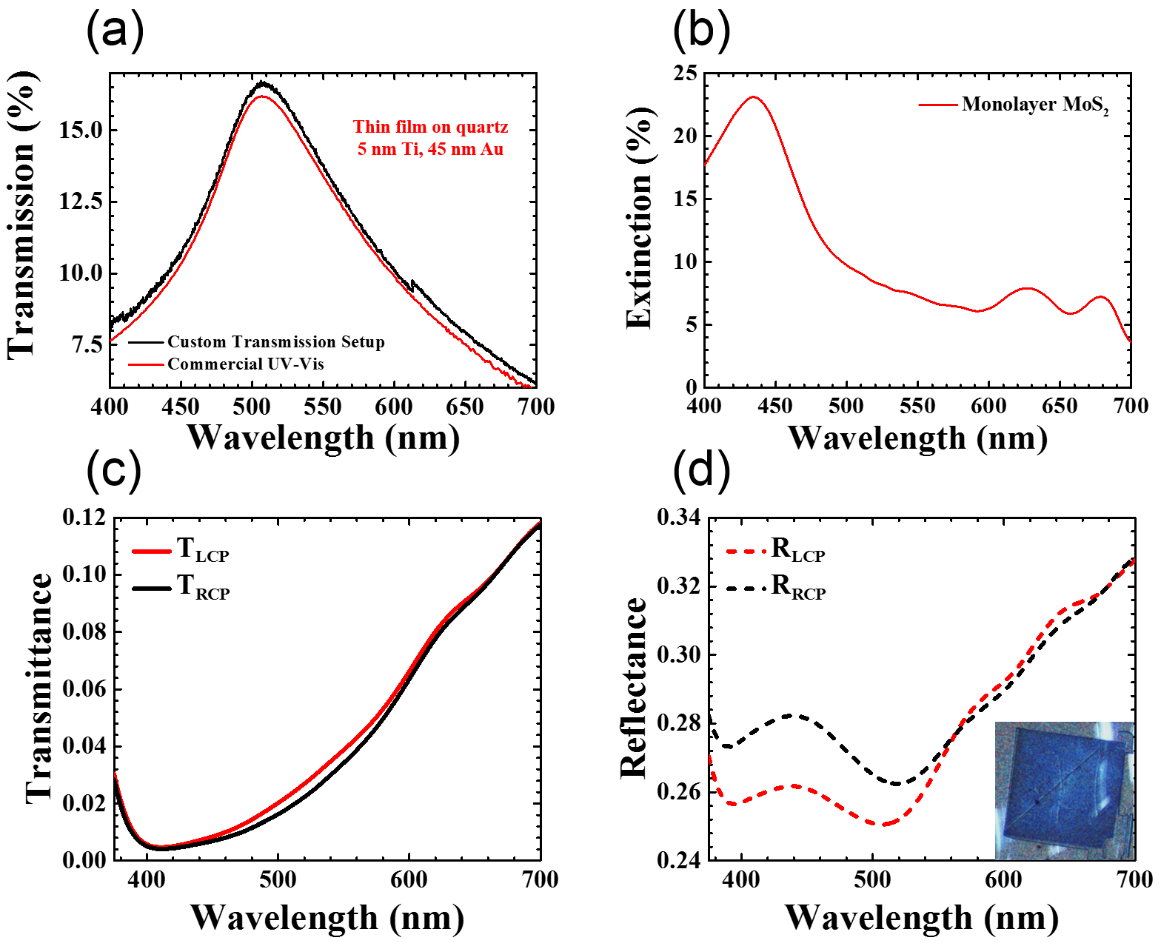

Figure 3.8: (a) Transmission spectra of a Ti/Au film measured using a commercial UV-Vis spectrometer (red) and using the custom built transmission setup (black). (b) Extinction spectrum of a triangular monolayer of MoS_2 (~ 20 µm edge length) measured using the custom built transmission setup. (c) Transmission spectra of 100 µm x 100 µm array of Ag nanohelices under LCP and RCP excitation. (d) Reflection spectra of the same array of Ag nanohelices in panel c under LCP and RCP excitation. Inset shows an optical image of the array of Ag nanohelices.

3.2.2 Angle- and Polarisation-Resolved Photoluminescence

To investigate the antenna properties of the arrays of Ag nanohelices, the far-field emission behaviour of the QDs coupled to the Ag nanohelices was examined. As previously mentioned, the general characteristics of antenna are the ability to convert localised energy (near-field) to propagating energy (far-field) and vice-versa. Within this conversion of energy, antennas also possess the ability to preferentially direct and influence the polarisation of the propagating energy. A custom built setup was constructed to measure the far-field emission pattern of the QDs coupled to the arrays of Ag nanohelices. The need for the custom built setup arises from the fact that the arrays are ~100 µm x 100 µm in dimension, therefore the laser excitation spot size should be smaller than the array and also that the collection optics would need to collect the emission from a spot size smaller than the complete array.

The custom built system utilises two motor controlled stages and can be used for scattering measurements, reflection measurements and a variety of angle-resolved measurements. A schematic diagram of the custom built setup is shown in Figure 3.9. The schematic diagram of the angle-resolved system shows elements labelled in black, orange and blue text. The components labelled in black text remain in the setup for each type of measurement. The orange and blue texts represent elements that are only in the setup for angle-resolved and polarisation-resolved measurements, respectively. For the angle-resolved measurements the emission intensity is measured using a Silicon avalanche photodiode connected to a lock-in amplifier. In the case of the polarisation-resolved measurements, the emission spectrum was measured using a fibre optic cable coupled to a spectrometer.

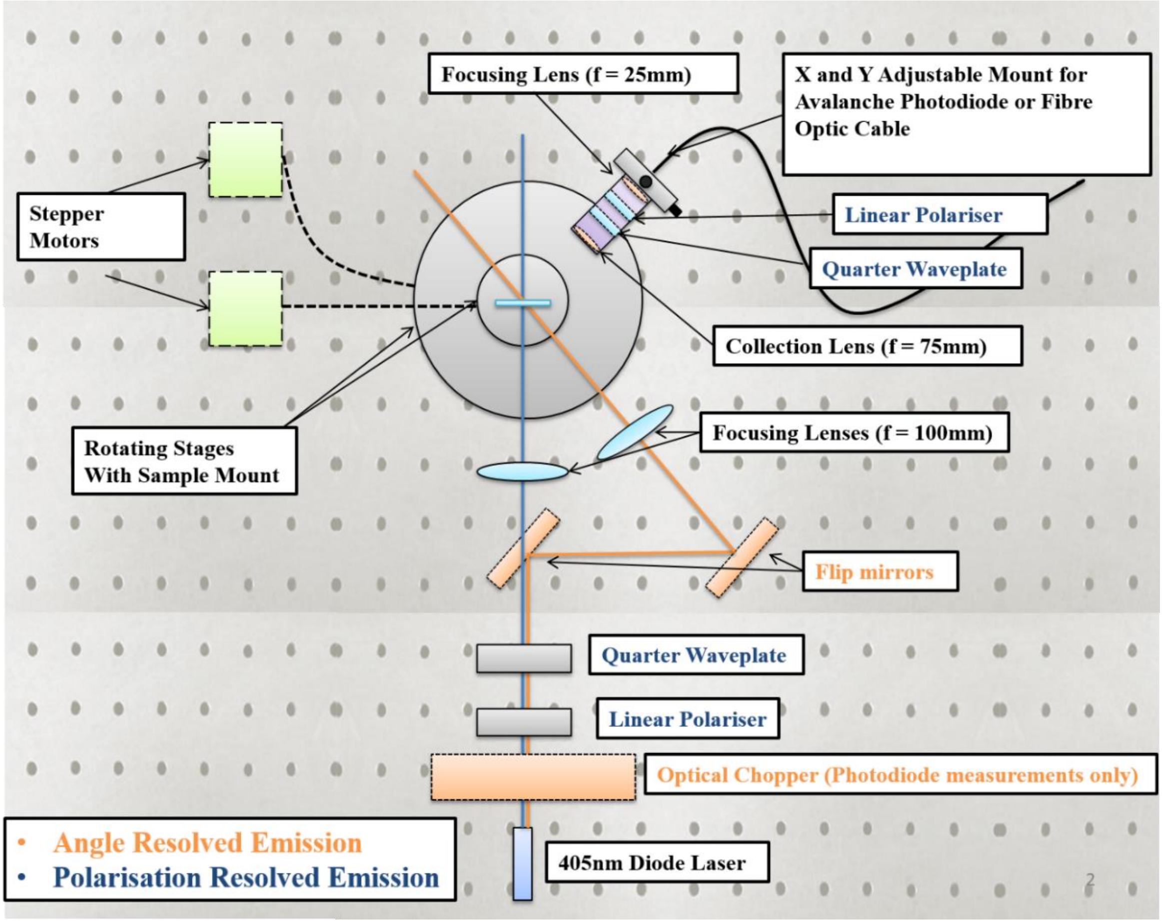

Figure 3.9: Schematic diagram of the custom built two stage rotation setup

The angle-resolved measurements are completely controlled using a LabVIEW program which operates both stages and the lock-in amplifier. The LabVIEW program records the photodetector voltage at each step and returns the corresponding voltage and step number in a text file after the measurement. The step number can be converted to angle (each step of the motor corresponds to 0.01º) and the polar emission plot can be generated. The excitation source for the angle-resolved emission measurements was a continuous wave 405 nm laser diode with an output power of 2.5 mW. The laser excitation was linearly polarised for the angle-resolved emission measurements, and the collection optics were configured to collect the absolute emission. The excitation optics were arranged so that the laser excitation of the sample was at an angle of -22.5º. This was done to ensure that the emission could be measured perpendicular to the array of Ag nanohelices ($\theta = 0°$) to observe any preferential directionality of the emission in the normal direction. An optical chopper was used in combination with the photodiode to ensure that all measured emission intensity was that from the QDs coupled to the Ag nanohelices. To dispel the influence of the excitation source from the measured intensity, the collection optics utilised a 450 nm long pass filter to block all wavelengths below 450 nm from being detected. Figure 3.10a shows the emission pattern from QDs on a planar ITO substrate and reveals that the emission pattern follows that of a Lambertian, $cos(\theta)$, dependence.

The polarisation-resolved emission measurements were performed using the same setup as the angle-resolved emission measurements (See Figure 3.9). For these measurements, the excitation angle was normal to the array plane in order to fully couple the circularly polarised excitation with the chiral structures. The detector was moved to an angle of 25º off normal and remained static so that the spectral dominance of the excitation was removed from the measured emission spectra. A linear polariser and quarter wave-plate were used in combination to form LCP and RCP light at the excitation end, whilst a quarter wave-plate and linear polariser were incorporated into the collection optics to resolve the polarised emission components. Polarisation-resolved emission measurements were carried out under a variety of conditions. Both circular polarisations and linearly polarised excitation conditions were used. Emission was collected for both circular polarisations, and also unpolarised conditions. For each excitation condition, unpolarised and circular polarised emission was measured. The polarisation-resolved PL spectra of the QDs coupled to the ‘right handed’ Ag nanohelices under LCP excitation in Figure 3.10b reveals that there is a larger intensity of RCP emission as compared with LCP.

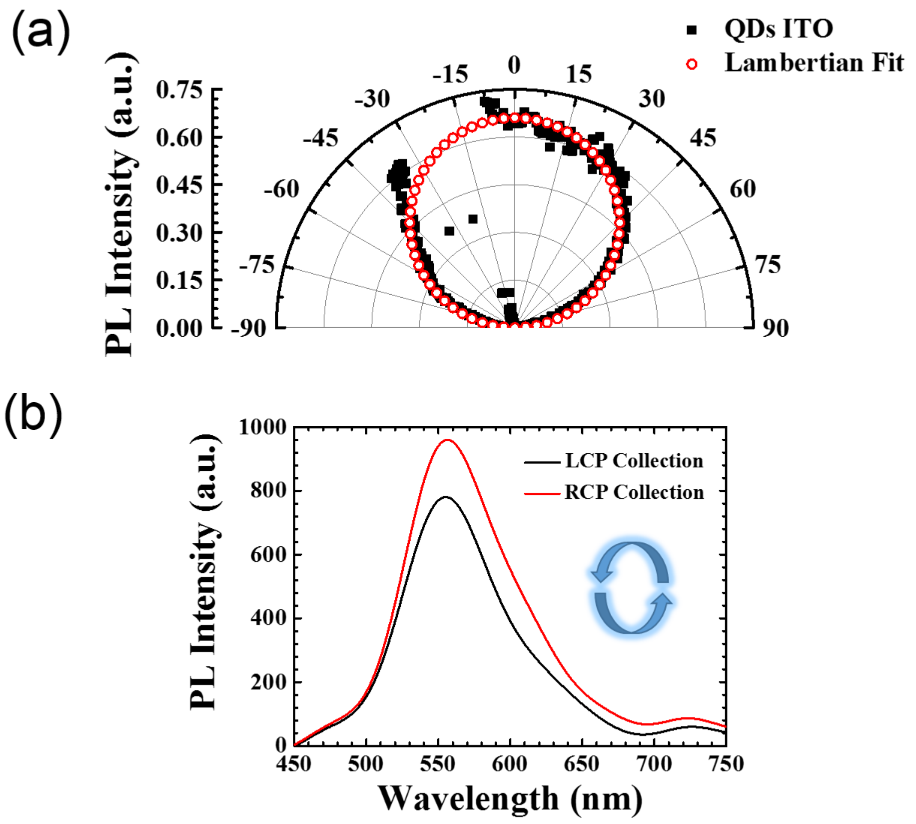

Figure 3.10: (a) Angle-resolved emission pattern of QDs on an ITO substrate. (b) Polarisation-resolved PL spectra of QDs on the Ag nanohelices under LCP excitation.

3.2.3 Absorption

The absorption spectrum of the colloidal QDs provides information regarding the concentration and the diameter of the QDs. The absorption measurements of the QDs in solution and in layers were performed using a Cary 50 UV-Vis spectrophotometer. The measurements were performed with a resolution of 1 nm over the spectral region from 300 nm to 800 nm. The absorption of light in a given material is characterised by the Beer-Lambert law, given by

$$A = \varepsilon(\lambda) \cdot C \cdot l \tag{3.1}$$

where $\varepsilon(\lambda)$ is the extinction coefficient of the material, C is the concentration and l is the length of the light path through the material (in cm). In solution, a standard cuvette for UV-Vis measurements has a path length of 1 cm and if the extinction coefficient, $\varepsilon(\lambda)$, is known, then the concentration, C, can be determined by measuring the absorption of the sample. The absorption and normalized PL spectra of the CdTe QDs in water is shown in Figure 3.11.

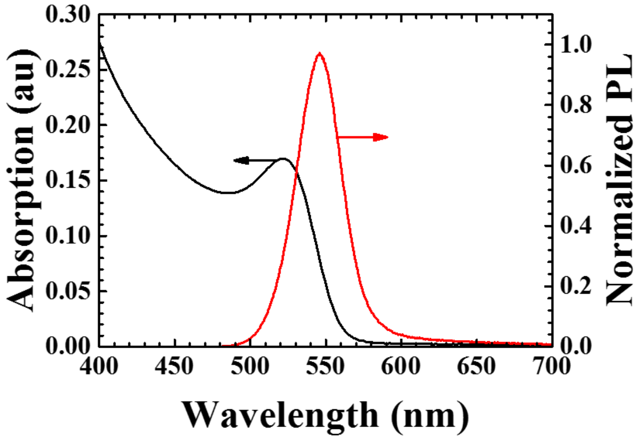

Figure 3.11: Absorption and normalized PL spectra of CdTe QDs in water.

The diameter (in nm) of the colloidal CdTe QDs, d_{QD}, can be calculated using the peak wavelength of the first absorption peak, λ_1, from the empirical sizing curve, given by[183,201]

$$d_{QD} = (9.1827 \times 10^{-7})\lambda_1^3 - (1.7147 \times 10^{-3})\lambda_1^2 + 1.0064\lambda_1 - 194.84\ nm \qquad (3.2)$$

Similarly, the extinction coefficient (in M^{-1} cm^{-1}) of the CdTe QD, ε_{QD}, can be determined from the diameter of the QDs, d_{QD}, by[201]

$$\varepsilon_{QD} = 10043(d_{QD})^{2.12} \qquad (3.3)$$

The diameter of the CdTe QDs shown in Figure 3.11 was found to be (2.6 ± 0.2) nm using Equation 3.2. The absorption spectrum reveals a peak absorption value of 0.171 ± 0.002 at the first absorption peak, λ_1, of (522 ± 2) nm. The extinction coefficient, ε_{QD}, of the CdTe QDs was calculated using Equation 3.3 and gives a value of (7.61 ± 0.03) x10^4 M^{-1} cm^{-1} at the first absorption peak, λ_1. Knowing the path length (l = 1 cm) and the extinction coefficient, ε_{QD}, of the QD solution allows for the calculation of the solution concentration, C, using Equation 3.1. The concentration, C, of the CdTe solution given in Figure 3.11 was found to be (3.24 ± 0.03) M.

The deposition of the QDs on the ITO and Ag nanohelix samples was monitored using the Cary 50 UV-Vis spectrophotometer, however, when the QDs are densely packed on a substrate they can no longer be considered as non-interacting single elements (as they would be in a colloidal solution with a diameter of 2.6 nm). This consideration of scattering is more important in the case of the Ag samples as the Ag nanohelices are anisotropic in geometry and have dimensions which are sufficiently large enough to scatter the incoming light. With this in mind, the extinction is considered, where the extinction is the sum of the absorption and scattering.[102]

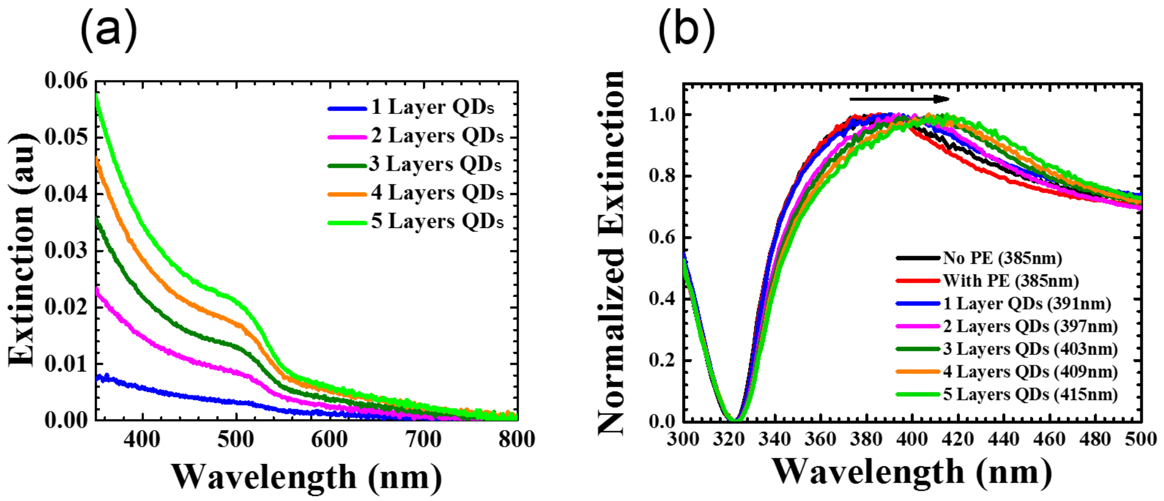

Figure 3.12: (a) Extinction spectra of CdTe QD layers on an ITO substrate. (b) Extinction spectra of CdTe QD layers on Ag nanohelix sample.

The extinction spectra of the QD layers on the ITO reference substrate can be seen in Figure 3.12a. It is clear from the increase in the extinction spectrum following the addition of each layer that the QD layers have been successfully deposited on the ITO substrate.

Similarly, the deposition of the QD monolayers can also be probed through the influence of the QD layers on the optical properties of the Ag nanohelix array and the surrounding Ag film. The normalized extinction spectra of the QDs on the Ag nanohelix sample are shown in Figure 3.12b. A clear redshift (~ 6 nm) in the peak extinction wavelength for the Ag sample is observed following the deposition of each QD layer. The peak extinction wavelength of the Ag sample corresponds to the localised surface plasmon resonance (LSPR). The redshift of the peak LSPR wavelength in the extinction spectrum indicates the deposition of each QD layer through a change in the refractive index surrounding the plasmonic structure.

3.2.4 Extinction, Absorption and Scattering

The spectral characteristics of the AgGO composites studied in Chapter 5 were investigated using a combination of UV-Vis techniques to elucidate the roles of absorption and scattering in the overall extinction spectrum. The extinction spectrum of the AgGO composite revealed a significantly broader spectrum as compared to the Ag NPs from the reaction solution, these Ag NPs are identical to the Ag NPs adhered to the GO in the AgGO composite. This led to the use of a UV-Vis spectrometer with an integrating sphere to extract the absorption and scattering spectra from the extinction spectrum. Extinction, scattering and absorption measurements were performed using a Perkin-Elmer Lambda 650 S UV-Vis spectrometer equipped with a 150 mm integrating sphere. To distinguish between contributions from absorption and scattering to the extinction spectrum, the AgGO dispersions were measured in the integrating sphere using a custom-built sample holder to place the cuvette in the centre of the integrating sphere. It should be noted that the cuvettes need to be transparent on all sides for these measurements. The absorption spectrum is obtained from the measurement inside the sphere. While the extinction spectrum is obtained from a measurement outside the sphere. This allows the scattering spectrum to be calculated as extinction-absorption.

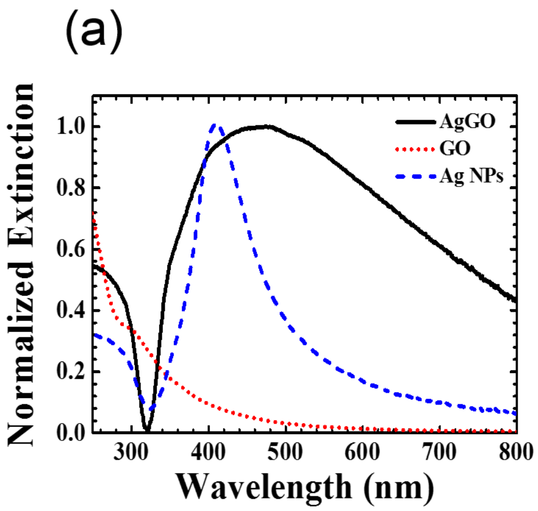

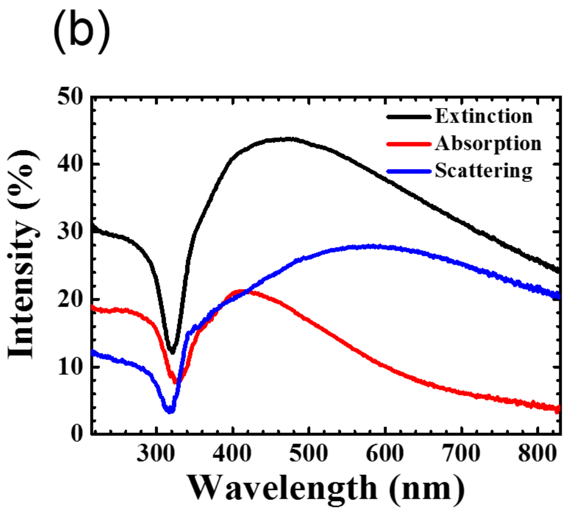

Figure 3.13: (a) Normalized extinction spectra of AgGO (black line), GO (red dot) and Ag NPs (blue dash). (b) Extinction (black), absorption (red) and scattering (blue) spectra of AgGO.

The normalized extinction spectra of the AgGO sample and its individual components; GO and Ag NPs, can be seen in Figure 3.13a. The Ag NPs were removed from the AgGO reaction solution and therefore they are identical to those in the AgGO composite. The Ag NPs show a much sharper LSPR than that of the AgGO composite. The extinction, absorption and scattering spectra of the AgGO composite are presented in Figure 3.13b. Here it is clear that the scattering from the AgGO composite has a much larger influence in the overall extinction spectrum, particularly at longer wavelengths. This increase in the scattering component is due to both the polydisperse nature of the Ag NPs and the increased interaction between the neighbouring Ag NPs in the 2D AgGO composite.[202]

3.2.5 Photoluminescence and Quantum Yield

In order to calculate the quantum yield of a fluorescent sample, both the absorption and PL spectra are required. The PL spectra of QD and organic dye solutions were measured using a Perkin Elmer LS 55 fluorescence spectrometer for the quantum yield calculations. The fluorescence spectrometer utilises a pulsed Xenon lamp as a source which allows for a wide range of excitation wavelengths. The PL spectra of the QDs and the organic dyes were recorded at an excitation wavelength of 400 nm (except for the QDs with an emission wavelength of 450 nm), as the samples studied have a measurable absorbance at this wavelength. The PL spectra were generally recorded over a range from 420 – 700 nm with a spectral resolution of 0.5 nm. The QDs with a peak emission wavelength of 450 nm were excited at a wavelength of 350 nm and the PL spectra was recorded over the range of 380 – 680 nm. Saturation of the detector was avoided *via* the inclusion of a neutral density filter (1% transmission) during the measurements, given the high quantum yield of the samples in solution.

The quantum yield of a fluorescent sample is determined by comparison with a reference standard with a well-known quantum yield. For samples that emit in the spectral range of 400 – 500 nm, Quinine Sulphate was used as the reference standard, having a quantum yield of 58%. For samples emitting in the spectral range of 500 – 650 nm, R6G was used as the reference standard, having a quantum yield of 95%. The absorption and PL spectra of Quinine Sulphate, R6G, CdSeS/ZnS QDs and CdTe QDs are shown in Figure 3.14. The quantum yield of a fluorescent sample is determined by the ratio of the number of photons emitted to the number of photons absorbed. Any differences in the number of photons absorbed between the samples, $A_{Sample}(\lambda_{Ex})$, and the reference, $A_{Ref}(\lambda)_{Ex}$, are accounted for by the ratio of the absorption of the sample and the absorption of the reference at the excitation wavelength.

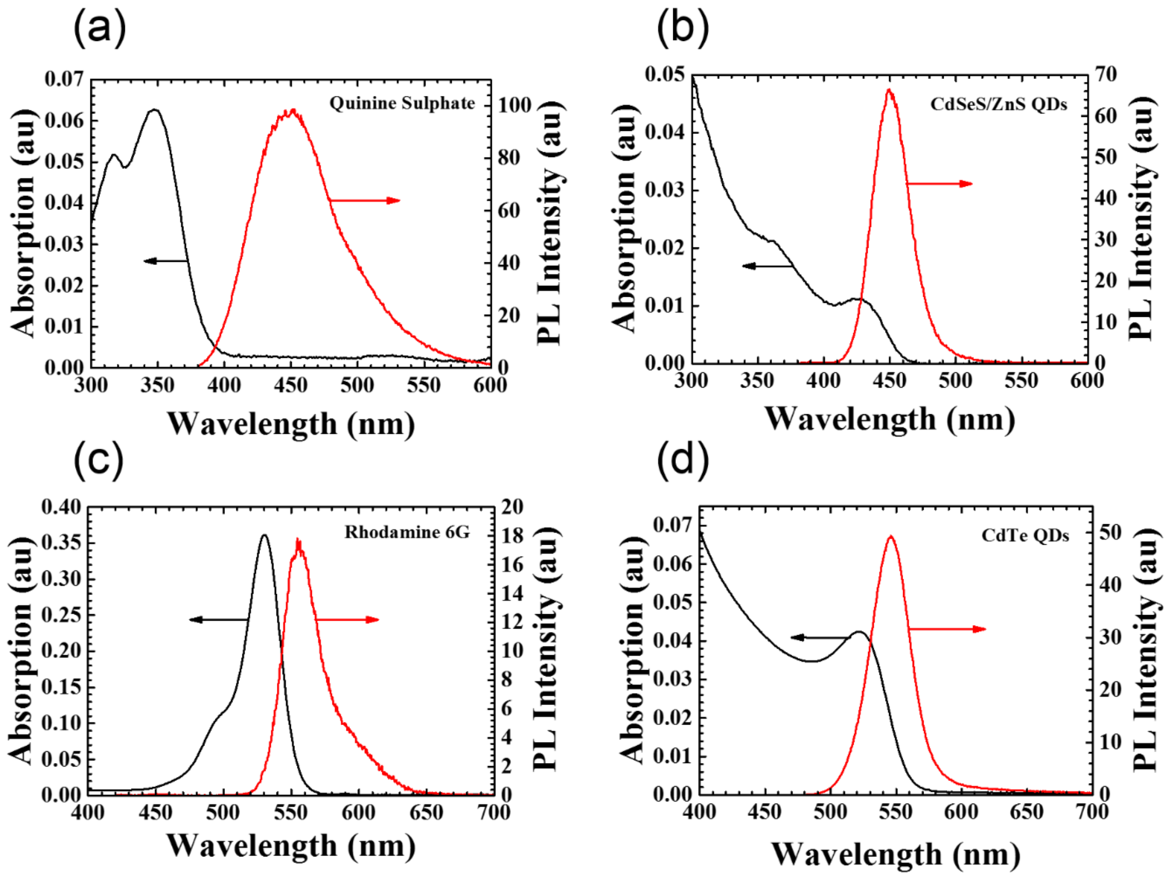

Figure 3.14: Absorption (left axis) and PL spectra (right axis) of (a) Quinine Sulphate, (b) CdSeS/ZnS QDs, (c) R6G, and (d) CdTe QDs.

The PL spectra of the sample, $I_{Sample}(\lambda)$, and the reference, $I_{Ref}(\lambda)$, are integrated to determine the number of photons emitted. For sample comparison with Quinine Sulphate, the PL spectra were integrated form 380 – 650 nm, and for samples comparing with R6G, the PL spectra were integrated from 500 - 700 nm. The PL spectra of the reference and the sample were measured using the same excitation wavelength to ensure that there is no difference in the excitation intensity for both measurements. For certain cases, the host solvent for the sample and the reference may be different, and as such, the refractive index for both the sample, n_{Sample}, and the reference, n_{Ref}, must be considered in the calculation. The equation for the quantum yield of a sample in solution, Q_{Sample}, is given by[82]

$$Q_{Sample} = \frac{A_{Ref}(\lambda_{Ex})}{A_{Sample}(\lambda_{Ex})} \cdot \frac{\int I_{Sample}(\lambda)d\lambda}{\int I_{Ref}(\lambda)\, d\lambda} \cdot \left(\frac{n_{Sample}}{n_{Ref}}\right)^2 \cdot Q_{Ref} \tag{3.4}$$

The ratio $A_{Ref}(\lambda_{Ex})/\int I_{Ref}(\lambda)d\lambda$ was obtained by measuring the reference PL spectrum as a function of concentration and plotting the integrated PL versus the absorption value at the excitation wavelength. The slope of this plot, m_{Ref}, gives the ratio. To avoid the inner filtering effects such as the attenuation of the incident and emitted light in this measurements[82], and similarly to avoid self-quenching of the reference samples[203,204], the concentrations used were quite low (optical density ≤ 0.01). The QD sample concentrations were also quite dilute in order to avoid reabsorption of the emitted photons.[205]

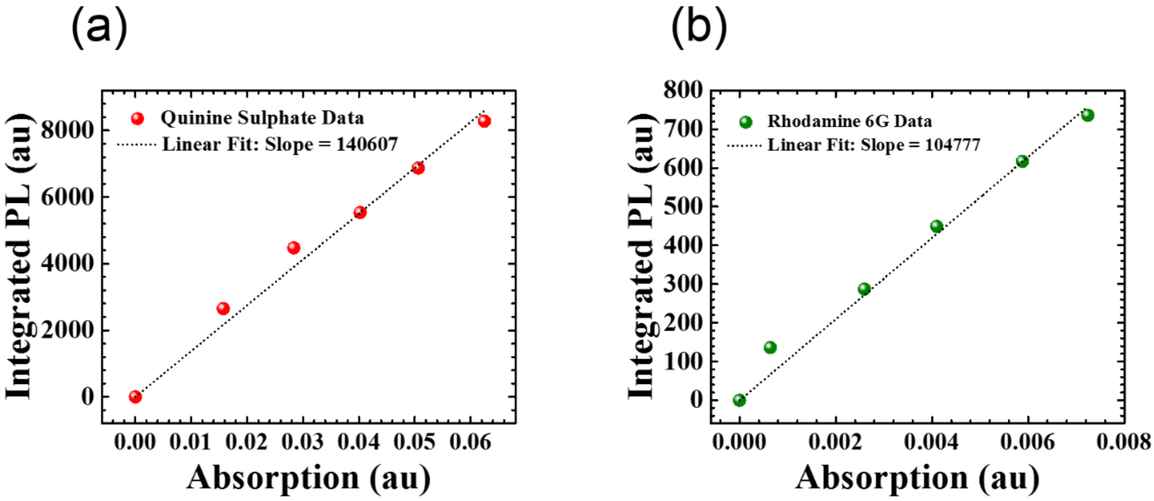

Figure 3.15: Integrated PL versus absorption for (a) Quinine Sulphate and (b) R6G. Black dotted lines in each plot are linear fits.

The slopes obtained from the integrated PL versus absorption curves which are shown in Figure 3.15 can then be placed into Equation 3.4, this gives

$$Q_{Sample} = \frac{\int I_{Sample}(\lambda)d\lambda}{A_{Sample}(\lambda_{Ex})} \cdot \frac{1}{m_{Ref}} \cdot \left(\frac{n_{Sample}}{n_{Ref}}\right)^2 \cdot Q_{Ref} \tag{3.5}$$

For Quinine Sulphate, m_{Ref} = 140607 and n_{Ref} = 1.42 as the host solvent was H_2SO_4 (0.1 M). The CdSeS/ZnS QDs were dispersed in PMMA and therefore, n_{Sample} = 1.49. Inputting these values in to Equation 3.5 in combination with the values obtained from the QD spectra in Figure 3.13b gives

$$Q_{Sample} = \frac{2402}{0.0223} \cdot \frac{1}{140607} \cdot \left(\frac{1.49}{1.42}\right)^2 \cdot 0.58 = 0.49 \; or \; 49\% \tag{3.6}$$

The measured quantum yield of (49 ± 7)% for the CdSeS/ZnS QDs is in agreement with the manufacturers stated value of 50%.

For R6G, m_{Ref} = 104777 and n_{Ref} = 1.329 as the host solvent was methanol. The CdTe QDs were dispersed in water and therefore, n_{Sample} = 1.333. Inputting these values and the values obtained from the absorption and PL spectra in Figure 3.14d into Equation 3.5 gives

$$Q_{Sample} = \frac{2376}{0.068} \cdot \frac{1}{104777} \cdot \left(\frac{1.333}{1.329}\right)^2 \cdot 0.95 = 0.32 \; or \; 32\% \tag{3.7}$$

PL measurements were also performed on a variety of different systems including the custom built setup described in Section 3.2.2 for the angle- and polarisation-resolved measurements and also using Andor Shamrock sr-303i spectrometer with an Andor Newton 970EMCCD. This spectrometer is coupled to an output port of the fluorescence lifetime imaging microscope (FLIM) used to measure time resolved PL decays. The excitation wavelength used for the majority of PL measurements presented in this thesis was 405 nm. In Chapter 7, the PL spectra that accompany the PL maps were measured at an excitation wavelength of 532 nm.

3.2.6 Time-Resolved Photoluminescence

Time-resolved PL (TRPL) decays were measured using a Picoquant Microtime FLIM system. The excitation in this system is provided by a diode laser with 90 ps pulses at a repetition rate of 10 MHz at an excitation wavelength of 405 nm. The signals are collected using a 40x microscope objective (NA = 0.65) and recorded using a single-photon avalanche diode. The system utilises time correlated single photon counting (TCSPC) to generate the PL decay curves. The PL decays were measured over square areas of varying size (depending on the sample under investigation) with an integration time of 4 ms per pixel.

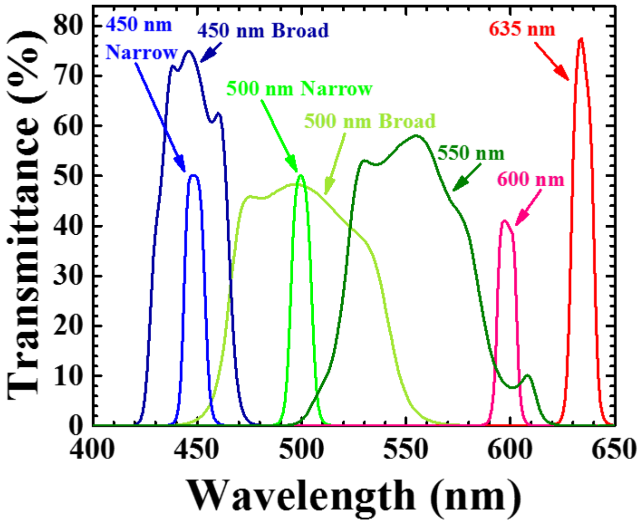

Figure 3.16: Transmittance spectra for band-pass filters used for TRPL measurements.

The PL decays of the QDs and dyes studied in this thesis were spectrally resolved using a variety of band-pass filters. The band-pass filter used are shown in Figure 3.16. The band-pass filter used to measure the CdTe QDs in Chapter 4 was the 550 nm Broad (FWHM = 75 ± 5 nm), however, other band-pass filters were used to measure the PL lifetime on the blue and red side of the PL spectrum, these are shown in Chapter 4. The band-pass filters used in Chapter 5 to measure the PL decays of the organic dyes were the 550 nm broad (FWHM = 75 ± 5 nm) for R6G and RhB, and the 600 nm (FWHM = 10 ± 2 nm) for the SR101. The filters used in Chapter 6 were the 450 narrow (FWHM = 10 ± 2 nm) for the QDs and the 500 narrow (FWHM = 10 ± 2 nm) for the QWs. The filter used in Chapter 7 was the 635 nm (FWHM = 10 ± 2 nm) to separate the QD emission from the MoS_2 emission. The band-pass filters used in Chapter 8 were the 450 nm broad (FWHM = 40 ± 5 nm) for the 450 nm QDs, the 500 nm broad (FWHM = 75 ± 5 nm) for the 530 nm QDs, and the 635 nm (FWHM = 10 ± 2 nm) for the 630 nm QDs.

The PL intensity decays were fitted with a bi-exponential fitting curve, given by

$$I(t) = I_1 e^{-\frac{t}{\tau_1}} + I_2 e^{-\frac{t}{\tau_2}} \tag{3.8}$$

where I_1 and I_2 are the intensity amplitudes having lifetimes of τ_1 and τ_2, respectively. The average lifetime was then calculated in terms of an intensity weighted average lifetime, τ_{Avg}, given by

$$\tau_{Avg} = \frac{I_1\tau_1^2 + I_2\tau_2^2}{I_1\tau_1 + I_2\tau_2} \tag{3.9}$$

Similarly, since the decay rate, $k = 1/\tau$, one easily obtains the average decay rate, $k_{Avg} = 1/\tau_{Avg}$. An example of a PL decay curve for the alloyed CdSeS/ZnS QDs with a peak emission wavelength of 630 nm and the bi-exponential fit are shown in Figure 3.17.

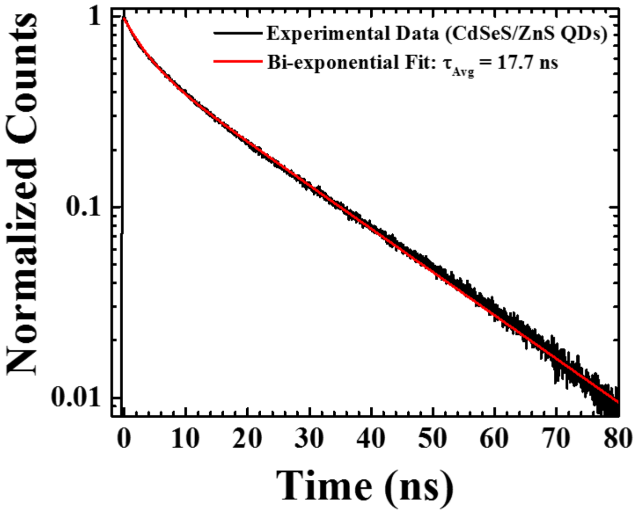

Figure 3.17: TRPL decay of CdSeS/ZnS QDs (black line) and a bi-exponential fit to the data giving an average lifetime, τ_{Avg} = 17.7 ns.

3.2.7 Raman and Surface Enhanced Raman Spectroscopy

The surface enhanced Raman scattering (SERS) measurements presented in Chapter 5 were performed using a Horiba Jobin Yvon LabRAM HR800 Spectrometer in air under ambient conditions. The Raman emission was collected by a 100x objective lens (N.A. = 0.8, spot size ~1 µm) and dispersed by 600 gr/mm. Prior to the acquisition of the samples, the spectral position was calibrated to the 521 cm^{-1} peak of Si/SiO$_2$. The samples used for the Raman study were prepared from a stock dye solution of 10^{-3} M and dilute AgGO solution in a 1:1 ratio. The mixture was left to settle for several hours and subsequently sonicated for 1 minute to disperse the AgGO flakes in the solution. 10 µL of the mixture was dropcast onto a glass cover slide and left to air dry in a fume hood. This technique ensures sufficient adsorption of dye molecules onto the substrate. Based on the absorption bands of the fluorescent organic dyes, the 532 nm excitation wavelength was chosen in order to excite fluorescence and provide resonance Raman scattering conditions. An example of the SERS spectra of R6G on the GO, AgGO and Ag NPs is shown in Figure 3.18a.

The CVD-grown MoS_2 studied in Chapters 7 and 8 was characterized by Raman spectroscopy. These measurements were performed using a WITec Alpha 300R tool with a 532 nm excitation laser operating at a power of ~250 µW with a 100x objective (N.A. = 0.95). Raman maps were obtained by acquiring 4 spectra per µm in x and y directions. An example Raman map plotting the separation between the characteristic *A* and *E* Raman modes in the MoS_2 Raman spectrum can be seen in Figure 3.18b with the corresponding average spectrum extracted from inside the dash yellow box shown in Figure 3.18c.

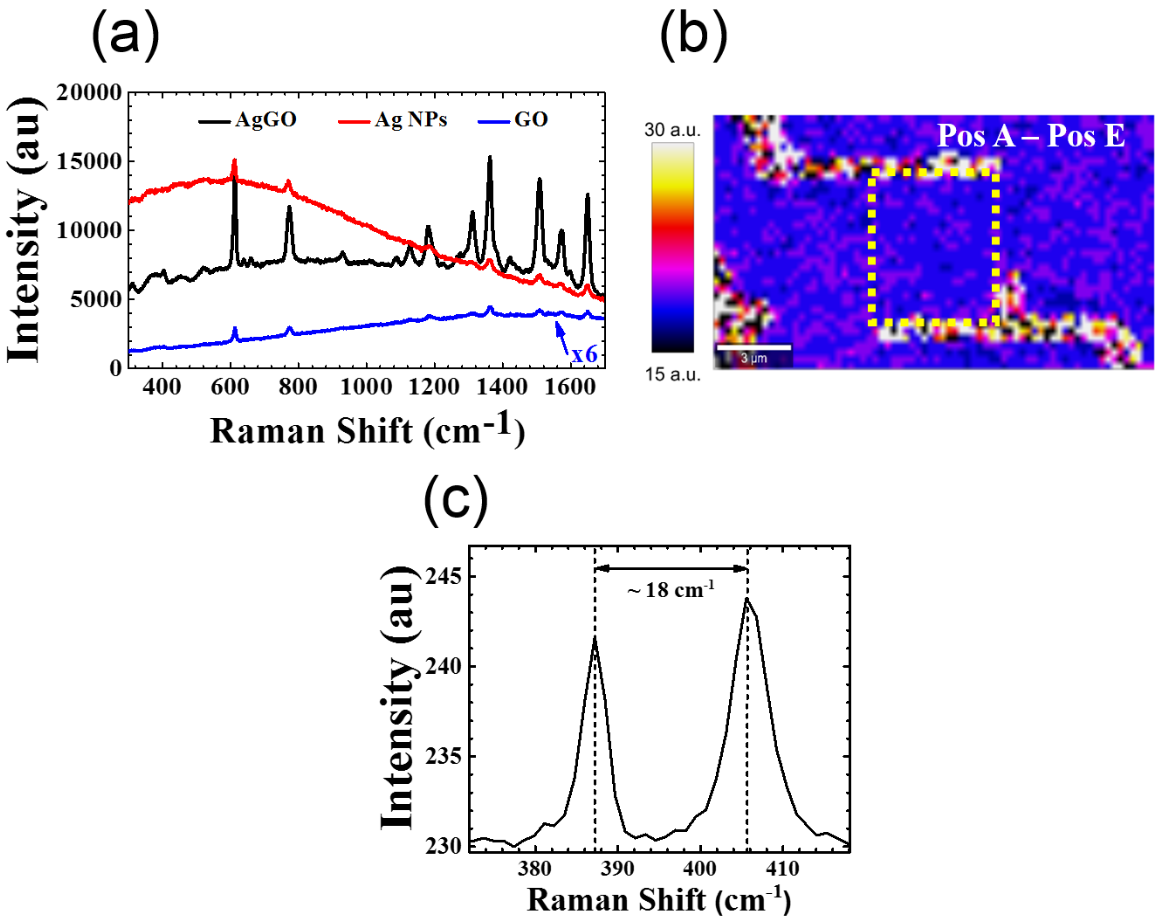

Figure 3.18: (a) SERS spectra of R6G on the AgGO (black line), Ag NPs (red line), and on the GO (blue line). (b) Raman map of monolayer MoS_2 device, plotting the separation between the characteristic *A* and *E* modes. (c) Average Raman spectrum extracted from inside the dash yellow box region in the Raman map in (b).

3.2.8 Photocurrent Measurements

Photocurrent measurements were performed on MoS_2 and QD sensitized MoS_2 devices in Chapters 7 and 8. The excitation laser used for the photocurrent measurements was a variable power Toptica iBeam smart laser diode with a 405 nm excitation wavelength. The wavelength of 405 nm was chosen as the corresponding PL and TRPL measurements were performed using a 405 nm excitation wavelength. The active regions of the devices were excited through a 10x (NA = 0.25) with an excitation spot diameter of ~3 μm. The electrical measurements were carried out using a Keithley 2400 source meter to provide a bias and measure the current through the devices. A white light source and a camera were used to image the sample to allow for successful contact between the contact probes and pads and also to ensure that the laser spot is tightly focussed on the active region between the electrodes. A LabVIEW program was written to control the Keithley 2400 source meter. This program allows for the measurement of looping I-V curves. The I-V curves were performed for -1 V to +1V in a four step process. Initially, the measurement sweeps from 0 V to +1 V in the first step, then from +1 V to 0 V in the second step, from 0 V to -1 V in the third step, and from -1 V to 0 V in the fourth and final step. The LabVIEW program then outputs the voltage and current values in a text file. An example I-V curve of the MoS_2 device with and without the QD sensitizing layer is given in Figure 3.19a. A schematic diagram of the setup can be seen in Figure 3.19b.

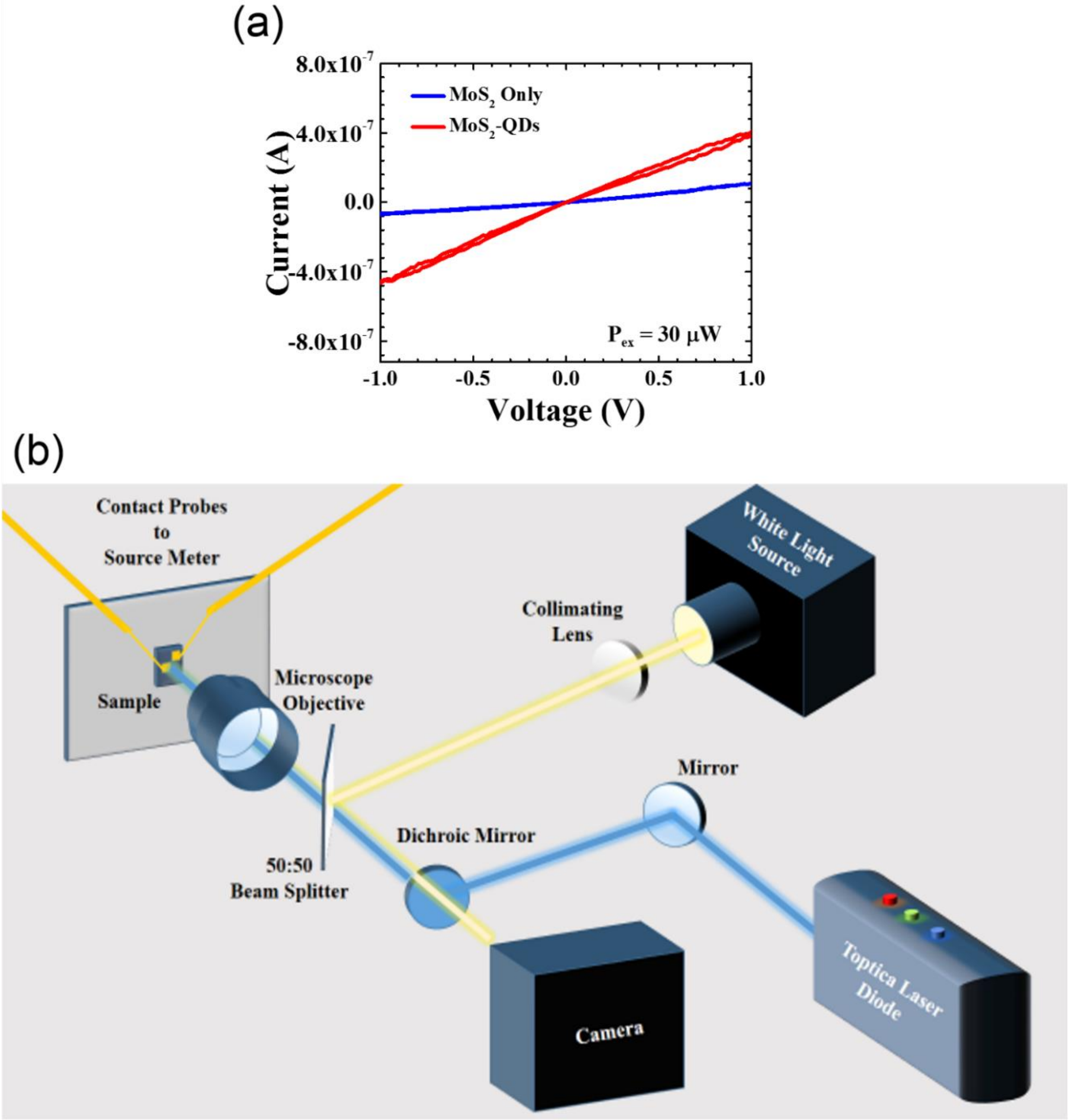

Figure 3.19: (a) I-V curve of MoS_2 device before (blue line) and after (red line) adding the QD sensitizing layer. (b) Schematic diagram of the photocurrent setup.

3.3 Summary

In summary, this chapter has provided all the relevant information regarding the controlled placement and separation of QD layers on the Ag nanohelices, using the LbL deposition technique. This enables the coupling between the QDs and the Ag nanohelices studied in Chapter 4. A detailed description of the synthesis of GO and the AgGO composite is also provided. The influence of the GO and AgGO composites on the emission and SERS properties of organic dyes is studied in detail in Chapter 5. The sample preparation and spin-coating procedure for the deposition of QDs and Ag NPs dispersed in PMMA layers is discussed in detail. These spin-coating techniques allow for the formation of the hybrid samples studied in Chapters 6, 7, and 8. The EBL fabrication of the ordered arrays of Ag NPs, studied in Chapter 6 (section 6.5), and the electrical contacts and electrodes, on the MoS_2 devices studied in Chapters 7 and 8, are also discussed. Detailed information about the custom built set-ups is also provided. Furthermore, the characterisation and data analysis techniques required to extract the relevant physical quantities are presented.

Chapter 4

Chiral Plasmonics

Chapter Summary

The work in this chapter will focus on light-matter coupling between semiconductor nanocrystal CdTe core-only quantum dots (QDs) and chiral plasmonic nano-antenna arrays. The chiral plasmonic Ag antennas have a helical form and were grown in arrays using a glancing angle vapour deposition (GLAD) technique. In terms of dimensions, each chiral Ag helical antenna has a diameter of 80 nm, pitch of 90 nm and a height of 220 nm. The centre-to-centre spacing between each individual antenna in the array is 150 nm and the total array consists of 670 x 670 individual units giving a total array size of ~100 µm x 100 µm. The chiral Ag helices were optically characterized by means of circularly polarised transmission and reflection spectroscopy, and consequently circular dichroism (CD) spectroscopy. Due to the small size of these arrays, standard commercial spectroscopic equipment could not be used as they are not capable of accurately measuring the optical properties over such small dimensions, given that commercial UV-Vis or CD spectrometers generally have a beam diameter of 1-3 mm at the focus. To overcome this obstacle, a custom setup was constructed and is shown in Chapter 3 (section 3.2.1). The QDs were characterised using absorption and photoluminescence (PL) measurements. The coupled QD-Ag helix structure was realised by depositing densely packed monolayers of QDs onto the Ag-helix array using the layer-by-layer (LbL) technique described in Chapter 3 (section 3.1.2). The interaction between the QDs and the Ag helices was investigated using steady state spectral PL, time-resolved PL (TRPL), and angle- and polarisation-resolved PL measurements.

4.1 Introduction

Plasmonic nanoparticles (NPs) have long been considered as antennas for optical frequencies given the ability to confine and enhance the local electric field.[9,99,100] More specifically, plasmonic structures capable of supporting the propagation of surface plasmon polaritons (SPPs) convert propagating electromagnetic radiation into localised energy (SPPs) and vice-versa.[206–208] The resulting novelty of having antennas composed of plasmonic nanostructures is the concentration, control and directed electromagnetic radiation at optical frequencies.[120,121,125] However, there are several limitations in terms of the implementation of optical antennas, most significantly, the nanometre scale design and structural requirements.[125] The characteristic dimensions of antennas are less than or very close to the operating wavelength,[120,125] thus in terms of optical antennas, this requires the fabrication of structures with dimensions of ~100 nm, and efficient antennas would require three dimensional structure. Ideally, the precise and reproducible fabrication of three dimensional nanoscale structures would allow for the fundamental study of optical antennas which would have significant benefits for optical communications and optoelectronic technologies.

The GLAD technique, which is a relatively new technique, allows for the growth of three dimensional anisotropic structures at the nanoscale, thus paving the way for the growth of helical structures with dimensions suitable for optical antenna technologies.[122,131,132,141] The GLAD technique has been reported to fabricate helical antenna at the nanoscale allowing for the growth of novel chiral structures having dimensions of the order of tens of nanometres.[122,131,132,141] Chirality in plasmonic structures is a growing field and has become a hot topic in recent years.[26,27,130,209–211] Similar to the dimensional requirements of optical antennas, chiral responses at optical frequencies have a strict reliance on sub 100 nm structural dimensions.[27,209] The bottom-up growth of anisotropic metallic structures using the GLAD technique allows for the growth of plasmonic nanostructures that meet the stringent dimensional requirements to obtain chiral responses at optical frequencies.[27,122,131,132,209,212]

The system studied in this chapter involves the coupling of QDs to chiral plasmonic helical antennas in arrays. The near-field interaction/coupling between the QDs and the helical antennas is investigated using TRPL measurements. Similarly, the influence of the near-field coupling between the QDs and antennas on the far-field emission properties of the QDs is investigated using angle- and polarisation-resolved PL measurements.

4.2 Characterisation of Ag nanohelices

Following the growth of the Ag nanohelix array, optical characterization was performed using circularly polarised transmission and reflection measurements using the custom-built system described in Chapter 3 (section 3.2.1). The circularly polarised measurements revealed the chiral nature of the Ag nanohelices through differences in the tramsmission and reflection of both left- and right-circular polarisations (LCP and RCP, respectively). The transmittance and reflectance spectra of the ‘right handed’ Ag nanohelices for both circular polarisations are shown in Figure 4.1a and 4.1b, respectively. The transmittance spectra in Figure 4.1a show that the ‘right handed’ Ag nanohelices have a higher transmittance of LCP light than RCP light, most notably in the range from ~450 nm to 650 nm. Consequently, the reflectance spectra in Figure 4.1b show a higher reflectance of RCP light than LCP light, a difference of 2% in the 400 nm – 500 nm region. It is worth pointing out that the ‘right handed’ Ag nanohelices absorb and reflect more light of polarisation in the same handedness as the helical structure. This effect is due to the structural chirality of the material, whereas a similar effect would not be observed for chiral molecules as their chirality is of a molecular nature. Chiral molecules exhibit a circular dichroism (CD) through a preferential absorption of either LCP or RCP light due to chiral absorption bands and this would have no influence on the reflection of LCP and RCP light. The peaks in the reflectance spectra at ~450 nm correspond to the structural colouring resulting from the scattering of incident light from the plasmonic Ag nanohelices,[213,214] as can be seen in the optical image of the Ag nanohelix array in the inset in Figure 4.1b.

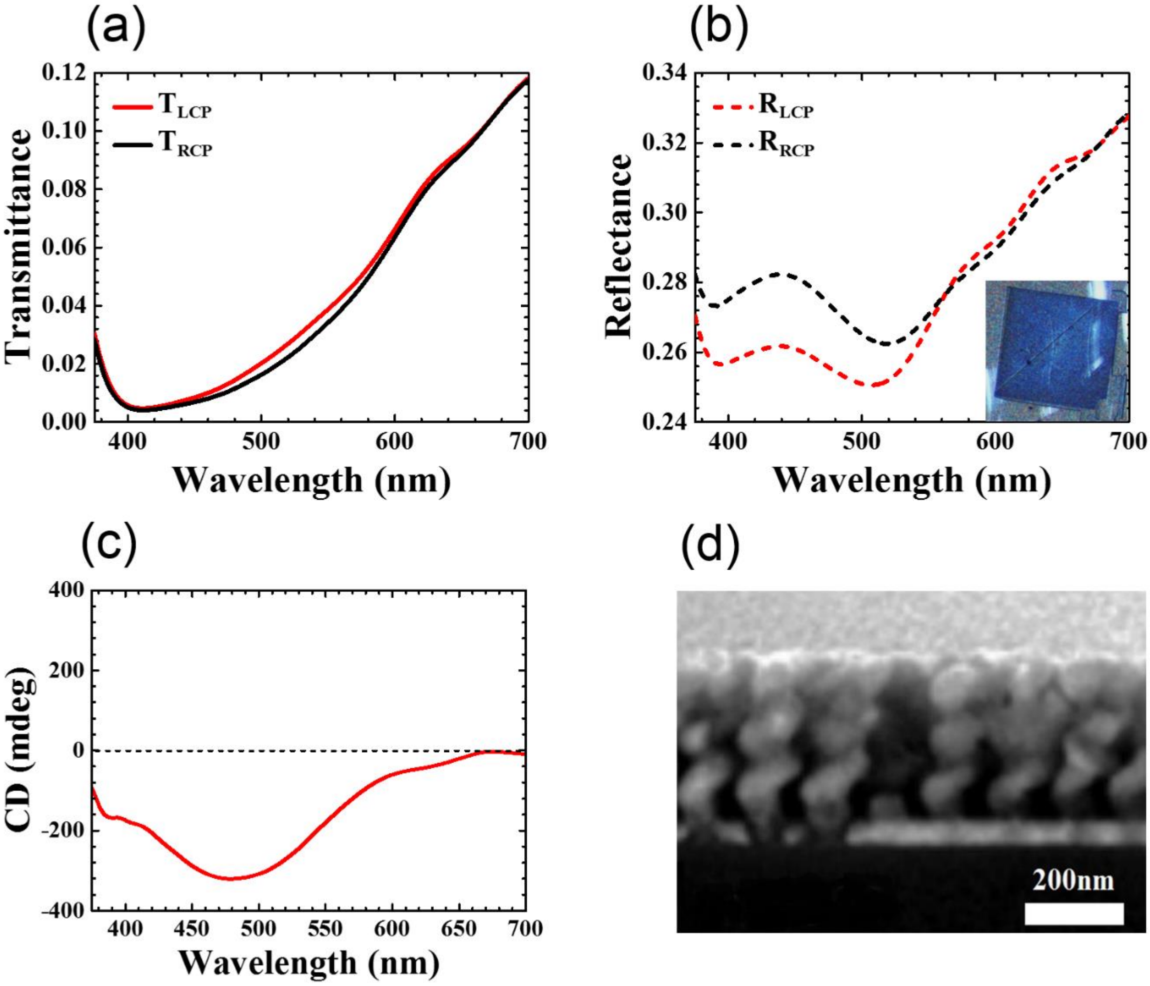

Figure 4.1: (a) LCP (red line) and RCP (black line) transmittance spectra for the right handed Ag nanohelix array. (b) LCP (red dash) and RCP (black dash) reflectance spectra for the right handed Ag nanohelix array. Inset: Optical image of Ag nanohelix array. (c) CD spectrum of the right handed Ag nanohelix array. (d) SEM image of the Ag nanohelix array.

The most common form of characterization for chiral molecules or structures is CD spectroscopy. CD is measured as the difference between the extinction of LCP and RCP light through a chiral material. Therefore, given that structurally chiral molecules absorb and reflect more light polarised in the same 'handedness' as the structure a 'left handed' chiral structure will exhibit a positive CD spectrum and a 'right handed' chiral structure would exhibit a negative CD spectrum.[130] However, structurally chiral particles that have been dispersed in solution show a bisignate response in the CD spectrum due to the random orientation of the particles in solution, resulting in a peak-dip (positive-negative CD) signature for 'left handed' structures and a dip-peak (negative-positive CD) signature for right handed molecules.[130,135] The extinction spectrum for both circular polarisations can be extracted from the transmission data. The CD spectrum is calculated from the extinction data as

$$CD = \epsilon_{LCP} - \epsilon_{RCP} \tag{4.1}$$

where ϵ_{LCP} and ϵ_{RCP} are the extinction spectra for LCP and RCP light, respectively. The CD spectrum of the 'right handed' Ag nanohelix array is given in Figure 4.1c. The CD spectrum clearly demonstrates a strong circular dichroism with a peak value of ~-320 mdeg at 480 nm, verifying the 'right handed' nature of the structures. Scanning electron microscopy (SEM) was also performed to confirm the 'handedness' of the structures. The SEM image in Figure 4.1d clearly shows the 'right handed' structure of the Ag nanohelices.

4.3 QD Coupled System

4.3.1 Sample Preparation

The QDs chosen for the study were negatively charged thiolglycolic acid (TGA) stabilised CdTe core-only QDs with a diameter of 2.6 nm in the aqueous phase. The QDs display maximum emission at a peak wavelength of 545 nm in solution, located close to the maximum CD peak of the Ag nanohelices. The normalised extinction and PL spectra for these CdTe QDs can be seen in Figure 4.2. The CdTe core-only QDs were deposited on the Ag nanohelices using the LbL technique described in Chapter 3 (section 3.1.2). The LbL technique works on the basis of electrostatic attraction whereby alternating layers of oppositely charged polyelectrolytes allows the formation of multi-layered structures. The charged ligand attached to the QDs is advantageous for the simple and versatile LBL technique. The polyelectrolytes (PE) used for the formation of (PE) bilayers were positively charged PDDA and negatively charged PSS.

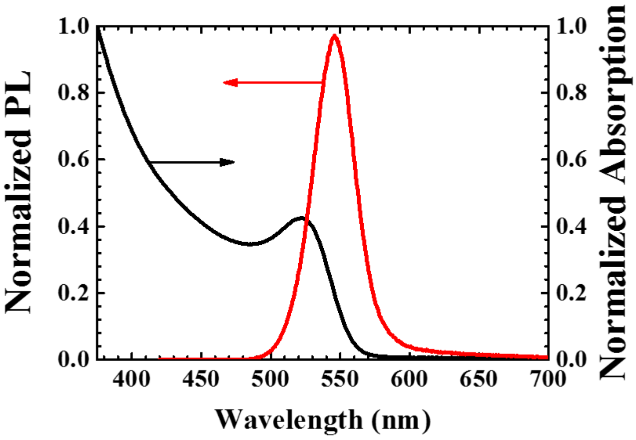

Figure 4.2: Normalized absorption and PL spectra of CdTe QDs in water.

The Ag nanohelix sample was immersed in PDDA initially for 20 minutes and each subsequent PE solution for 10 minutes. The samples were rinsed in Millipore water between each immersion to remove any excess or loosely bound PE to prevent cross-contamination and to ensure the formation of monolayers. Two bilayers of PDDA/PSS and a final layer of PDDA were deposited onto the Ag helix sample before depositing the QDs. The sample was immersed in the QD solution for 30 mins for each QD layer deposition. Each PE bilayer has an average thickness of 3 nm and therefore the separation between the Ag nanohelix surface and the surface of the initial layer of QDs is ~7.5 nm.[215] A schematic diagram of the structure, including dimensions, is given in Figure 4.3a. To improve the emission intensity from the QDs, 5 layers of QDs were added in total, each layer of QDs is separated by a PDDA layer. The final distance between the Ag nanohelix structures and the centre of the outermost layer of QDs was ~25 nm.

4.3.2 Optical Characterisation

The QD extinction and PL spectra were monitored after the addition of each subsequent layer on both the ITO (reference substrate) and the Ag nanohelices. The extinction spectrum of the QD-Ag sample was measured using a commercial UV-Vis spectrometer. To avoid the excitation and subsequent fluorescence from the QDs it was necessary to use scanning monochromatic excitation from a commercial UV-Vis spectrometer to measure the extinction as opposed to broadband excitation from a Xenon source in the custom built apparatus. Since the UV-Vis spectrometer was used to measure the extinction of the Ag helix sample, the array and the surrounding Ag film were subjected to the measurement conditions. Accurate spectra from the array itself were not obtained, however, the effect of the addition of QDs to the Ag sample is clearly evident as can be seen in Figure 4.3b.

The addition of each QD monolayer to the Ag nanohelix sample results in a red shift of ~6 nm in the peak extinction wavelength of the Ag sample. The red shift in the peak extinction wavelength indicates the influence of the QD deposition on the plasmon resonance of the Ag structures, resulting from a change in the refractive index surrounding the plasmonic material. The peak extinction wavelength of the bare Ag sample is 385 nm and had shifted by 30 nm to 415 nm after the deposition of the fifth and final layer of QDs. Multiple layers of QDs were deposited to achieve sufficiently strong PL intensity in order to measure the angular emission pattern from the QDs and also to resolve the QD emission into individual circularly polarised components.

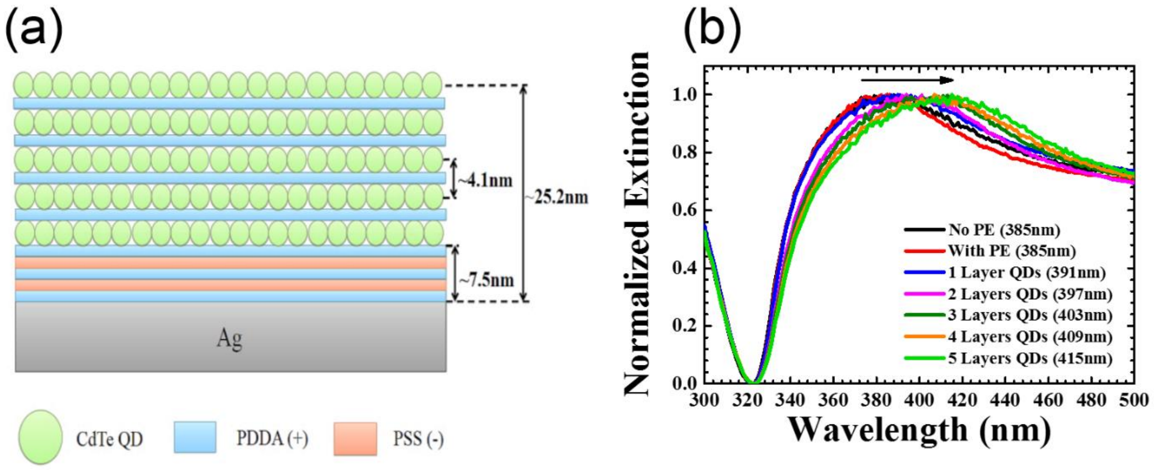

Figure 4.3: (a) Schematic diagram of the QD monolayers and the PE buffer layers on the surface on the Ag nanohelix structures. (b) Normalized extinction of the QD-Ag sample as the number of QD monolayers increases.

Following the addition of the fifth layer of QDs the PL intensity was sufficiently high for spectral measurements to proceed. The PL spectra of the QDs in solution, on the ITO reference substrate, and on the Ag nanohelices are shown in Figure 4.4a. It should be noted that the PL spectrum of the QDs in solution has been scaled to sit with the QDs on the ITO substrate, while the spectra of the QDs on the ITO substrate and the Ag nanohelices are absolute values. It is clear from Figure 4.4a that the PL intensity from the QDs coupled to the Ag helices is less than a quarter of that of the QDs on the bare ITO substrate. This reduction in intensity is due to quenching of the QDs to the metal. The full-width at half-maximum (FWHM) for each PL spectrum is shown in the legend. The QDs in solution exhibit a FWHM of (34.4 ± 0.1) nm, and in this case the individual QDs are considered to be equally spaced and non-interacting. The monolayers of QDs on the bare ITO substrate have a FWHM of (41.3 ± 0.4) nm which is slightly larger than that of those in solution. This is indicative of the interaction between neighbouring QDs in the densely packed monolayers.[216] The QDs coupled to the Ag helices show a much larger and asymmetric broadening of the emission with a FWHM of (57.1 ± 0.7) nm and small levels of emission at longer wavelengths.

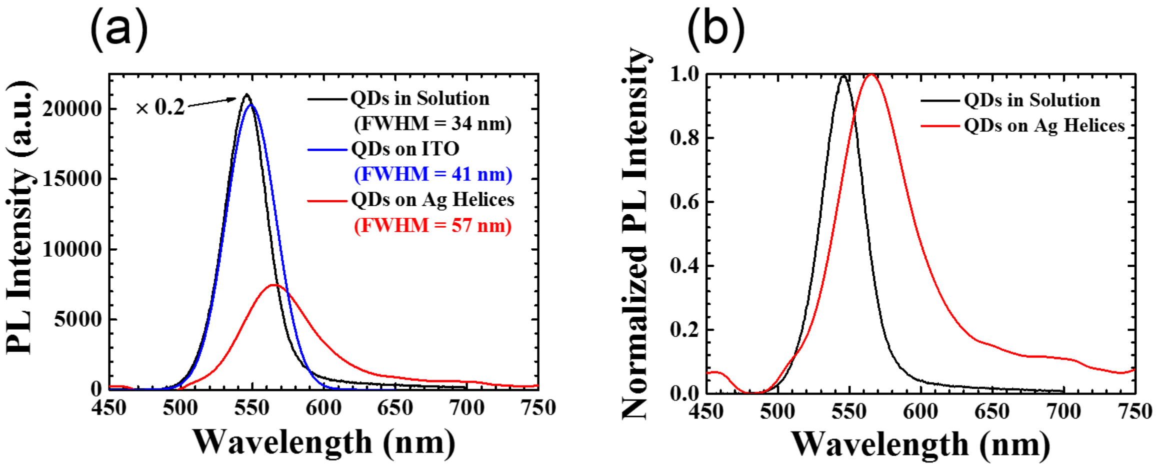

Figure 4.4: (a) PL spectra of QDs in solution (black), QDs on ITO substrate (blue) and QDs on the Ag nanohelix array (red). (b) Normalized PL spectra of the QDs in solution (black) and QDs on the Ag nanohelix array (red).

The normalized PL spectra for the QDs in solution and the QDs on the Ag nanohelix array are shown in Figure. 4.4b. The magnitude and asymmetry of the broadening of the PL spectrum from the QDs on the Ag nanohelix array can be seen much more clearly here. This large asymmetric broadening on the low energy side of the photon distribution is characteristic of intra-energy transfer between the QDs.[216] The smaller QDs in the distribution transfer their energy through nonradiative pathways to the larger QDs and these larger QDs subsequently radiate this energy. Since such broadening is not seen for the QDs on the bare ITO substrate it is most likely that the large asymmetry in the broadening is due to the plasmonic nature of the Ag nanohelices, and as such, the origin of the asymmetric broadening can be attributed to surface plasmon enhanced intra-energy transfer from the small QDs to the larger QDs in the monolayers.[88,216]

4.3.3 Time-Resolved Photoluminescence

Time-resolved PL (TRPL) measurements were performed to quantify the strength of the interaction between the QDs and the Ag nanohelices. The normalized PL decays for the QDs on the ITO substrate and the QDs on the Ag nanohelices and their respective lifetimes can be seen in Figure 4.5. The PL decays were fitted using a bi-exponential decay curve, given by Equation 3.8 in Chapter 3 to obtain the lifetime of the decays. The strength of the interaction was expressed in terms of an efficiency, η, given by

$$\eta = 1 - \frac{\tau_{QD-Ag}}{\tau_{QD}} \tag{4.2}$$

where τ_{QD} and τ_{QD-Ag} are the lifetimes of the QDs on the ITO substrate and the QDs on the Ag nanohelices, respectively. The efficiency, η, of the interaction was found to be (82 ± 2)% for the QDs on the Ag nanohelices after the addition of the fifth and final layer of QDs, indicating significant coupling between the emitters and the antennas.

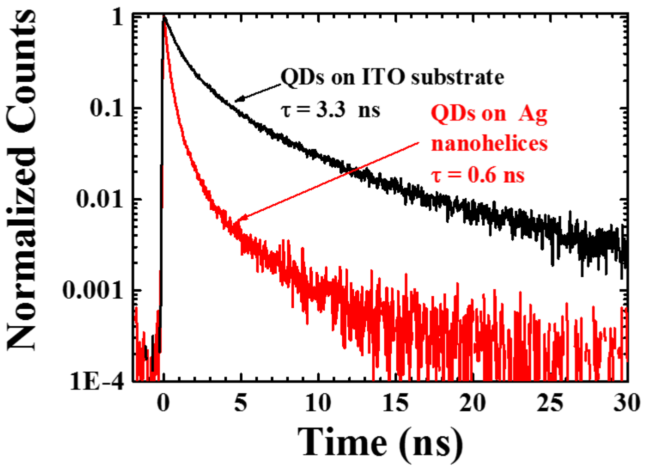

Figure 4.5: Normalized PL decays for the QDs on the ITO substrate (black line) and the QDs on the Ag nanohelices (red line).

The interaction between the QDs and the Ag nanohelices was further investigated in terms of the effect of the Ag nanohelices on the intra-energy transfer between the QDs in the monolayers. This intra-energy transfer can be investigated by probing the lifetimes recorded at the short (τ_{Blue}) and long (τ_{Red}) wavelength sides of the PL spectrum using spectral bandwidth filters. Previous concentration dependent studies performed in this group have shown that one signature of intra-energy transfer is a short blue lifetime and longer red lifetime. So to compare the variation in QD lifetime on the Ag nanohelices and on the ITO substrate, we define the parameter, $1 - \tau_{Blue}/\tau_{Red}$ as the lifetime difference between the blue and the red side.[88] Investigation and comparison between the lifetimes of the small QDs at short wavelengths and the large QDs at long wavelengths can provide insight into the interaction between the small and large QDs and also between the QDs and the Ag nanohelices.

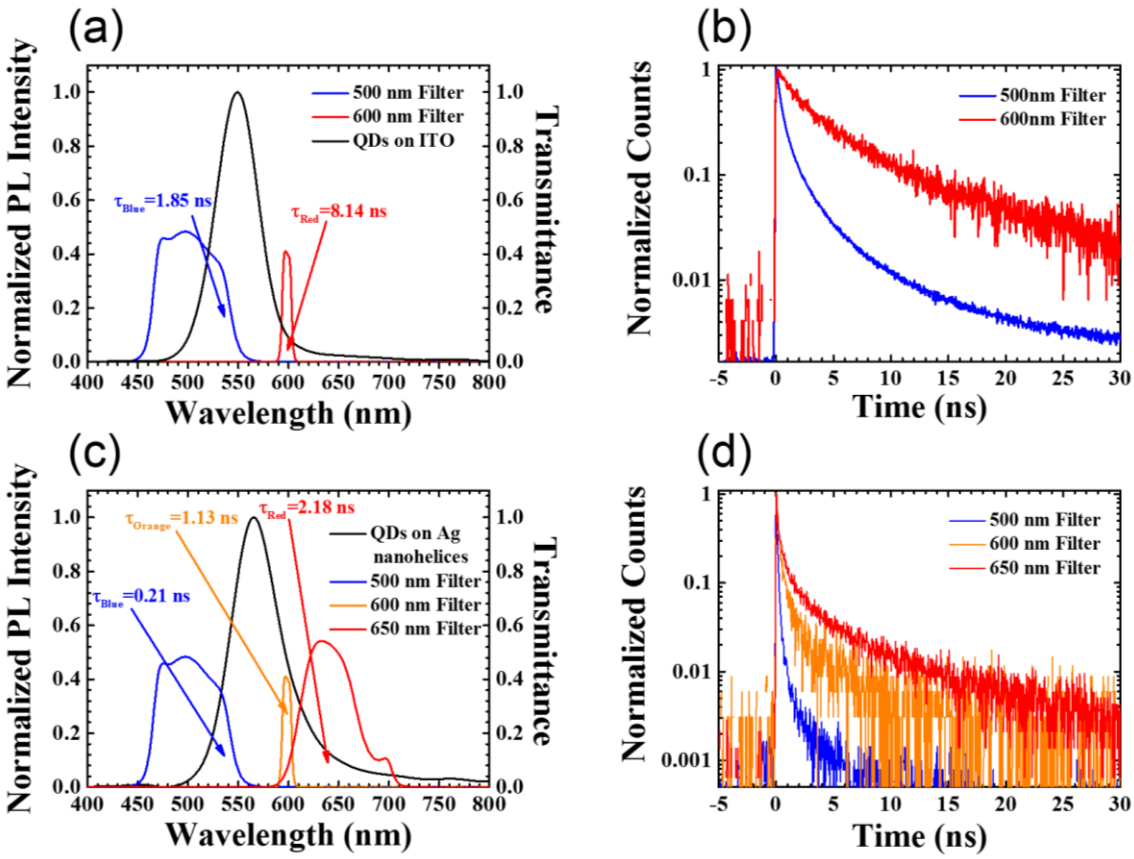

Figure 4.6: Filter transmittance and normalized PL spectra of QDs on ITO and QDs on the Ag nanohelices, in (a) and (c), respectively. (b) Normalized PL decays of QDs on the ITO substrate measured using the 500 nm and 600 nm filters shown in (a). (d) Normalized PL decays of the QDs on the Ag nanohelices measured using the 500 nm, 600nm and 650 nm filters shown in (c).

The PL spectrum for the QDs on the bare ITO substrate (black) is shown in Figure 4.6a along with the filter transmittances on the blue and red sides of the emission spectra. The filter transmittance spectra indicate the area of the spectrum from which the lifetime measurements are recorded. The average lifetime values of τ_{Blue} = (1.85 ± 0.1) ns and τ_{Red} = (8.14 ± 0.1) ns demonstrate the intra-energy transfer between the small and large QDs in the monolayers. The PL decay plots for the QDs at both sides of the emission spectrum are shown in Figure 4.6b and a clear difference in the PL lifetime can be seen from the decay curves. Taking the decrease in lifetime, $1 - \tau_{Blue}/\tau_{Red}$, gives a lifetime increase of (77 ± 2)% on the red side of the spectrum indicating FRET-like energy transfer from the small to large QDs.

PL lifetimes were also measured at the blue, intermediate and red side of the emission spectrum for the QDs coupled to the Ag nanohelices. Since there is a large shift and broadening on the red side of the emission spectrum when the QDs are coupled to the Ag nanohelices, lifetime measurements were recorded at 3 locations across the spectrum. The normalised PL spectrum for the QDs on the chiral Ag nanohelices (black) is shown in Figure 4.6c along with the filter transmittances at the blue, τ_{Blue}= (0.21 ± 0.1) ns (500 nm filter) and red, τ_{Red}= (2.18 ± 0.1) ns (650 nm filter) side of the spectrum with an intermediate position, τ_{Orange} = (1.13 ± 0.1) ns (600 nm filter). Taking the lifetime difference for the QDs on the Ag nanohelices we get a lifetime increase of (90 ± 1)% on the red side, $1 - \tau_{Blue}/\tau_{Red}$, of the emission spectrum and (80 ± 1)% at the intermediate position, $1 - \tau_{Blue}/\tau_{Orange}$. Figure 4.6d shows the PL decay plots recorded for each filter position. A significantly large difference between the lifetime on the blue and red sides ($\Delta\tau = \tau_{Red} - \tau_{Blue} = 1.97\ ns$) of the emission is clearly observed. This large difference in the PL decay is most likely due to the presence of the metal structures and the plasmonic nature of the structure which enhances the energy transfer rate between the small and large QDs in the monolayers.[50–53] This enhanced energy transfer process occurs as the NRET process is accelerated in the presence of a plasmonic structure due to the plasmon assisted amplification of the electric fields in the coupled nano-system.[42]

4.4 Angle- and Polarisation-Resolved Photoluminescence

The antenna properties of the arrays of Ag nanohelices were investigated by examining the far-field emission behaviour of the QDs in the coupled system. As mentioned above, the general characteristics of antenna are their ability to convert localised energy (near-field) to propagating energy (far-field) and vice-versa. Within this conversion of energy, antennas also possess the ability to preferentially direct and influence the polarisation of the propagating energy. The custom built setup described in Chapter 3 (section 3.2.2) was used to measure the far-field emission pattern of the QDs coupled to the Ag nanohelices. Given that the arrays are ~100 µm x 100 µm in dimension, it was necessary to ensure that the laser excitation spot size was smaller than the array and also that the collection optics collected the emission from a spot size smaller than the complete array.

4.4.1 Angle-Resolved Photoluminescence

To clarify that any directionality observed in the emission pattern from the QDs coupled to the Ag nanohelices was in fact due to the antenna properties of the nanohelices, the emission profile from the QDs on the bare ITO substrate was measured for comparison. The far-field emission pattern from the QDs on the bare ITO substrate (black squares) and that of an ideal Lambertian (red circles) are shown in Figure 4.7. It is clear from the plot that the multiple monolayers of QDs on a planar substrate have an emission pattern that follows a Lambertian, $\cos(\theta)$, dependence. The fit between the ideal Lambertian and the measured emission pattern are in almost perfect agreement, thus verifying the Lambertian nature of the far-field emission. One should also note the void in the far field emission pattern from ~ -7.5º and -37.5º. This results from the excitation of the sample. Despite the inclusion of the 450 nm long pass filter to block the laser excitation (405 nm) used for the measurement, alignment between the detector and the excitation beam gave a large auto-fluorescence on the surface of the filter and this caused the photodetector counts to rise significantly. To avoid this artefact in the measurement, the excitation beam was blocked when it began to impinge on the filter and the block was removed when the detector had passed by the region in which the beam was passing through.

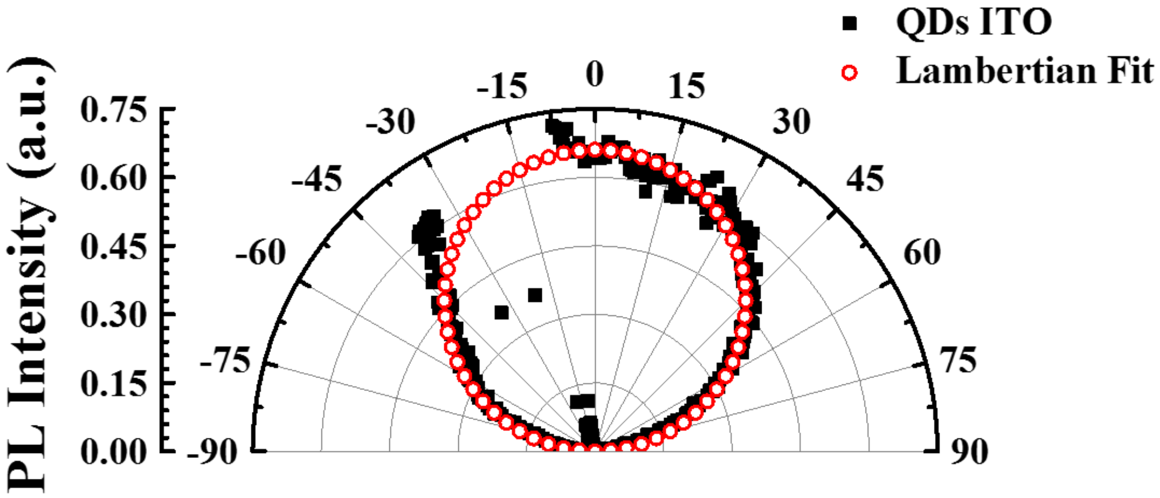

Figure 4.7: Polar plot of the far field emission pattern of QDs on the ITO substrate.

The far-field emission pattern from the QDs coupled to the array of Ag helices (blue triangles) can be seen in Figure 4.8, along with the ideal Lambertian fit (red dash) and the ordinary end-fire fit (purple squares). It is clear that the emission pattern from the QDs coupled to the Ag nanohelices does not follow that of the Lambertian, $\cos(\theta)$, but indeed has a greater directionality. The emission pattern from the QDs coupled to the Ag nanohelices more-so follows that of an array of equally spaced antenna elements, known as an ordinary end-fire emission pattern. The end-fire description used to fit the data is taken from traditional antenna theory. This end-fire mode describes the radiation pattern from an evenly spaced array of individual elements, considered as dipoles or radiation points. This agrees with the Ag nanohelix antenna itself as the helix is also considered as an evenly spaced array of dipoles, with each half-turn of the helix behaving as a dipole or radiation point, where the QD emission is scattered into the far-field.[120,123] The normalized end-fire pattern, $F(\theta)$, is given by[120]

$$F(\theta) = \frac{\left[sin\left(\frac{N\pi}{4}\right)(cos(\theta) - 1)\right]}{\left[sin\left(\frac{\pi}{4}\right)(cos(\theta) - 1)\right]} cos(\theta) \tag{4.3}$$

where N is the number of point dipoles contributing to the radiation into the far-field. A value of $N = 7$ gives the best fit to the experimental data. This can be understood by the number of scattering points on the Ag nanohelices and the ground plane. The Ag nanohelices have ~3 full turns as can be seen in the SEM image in Figure 4.1d. Each half turn can be considered as a dipole[123] or scattering point, this gives $N = 6$, there is also the interaction between the bottom turn on the helix and the ground plane, resulting in $N = 7$.

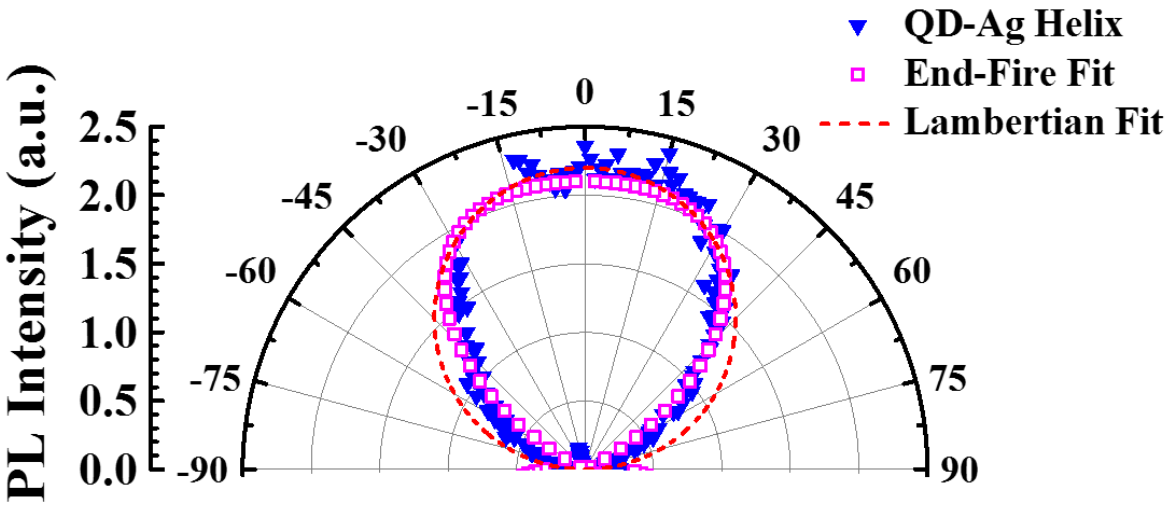

Figure 4.8: Polar plot of the far-field emission pattern of the QDs coupled to the array of Ag nanohelices (blue triangles), ideal Lambertian fit (red dash) and ordinary end-fire fit (purple squares).

The emission pattern from the QDs coupled to the Ag nanohelices demonstrates that 62% of the emitted power lies in the 30° cone normal to the array plane, whilst on the ITO reference substrate only 50% of the emitted power lies within the 30º cone normal to the substrate plane, as calculated from the fit for each pattern. This clear difference in the far-field emission patterns verifies that antenna properties of the Ag nanohelices have been imparted to the emission of the QDs.

4.4.2 Polarisation-Resolved Photoluminescence

Polarisation-resolved emission measurements were also performed to further investigate the antenna properties of the coupled system. The polarisation-resolved measurements were carried out under a variety of conditions. Both circular polarisations and linearly polarised excitation conditions were used. For each excitation condition, unpolarised and circular polarised emission was measured.

The polarisation-resolved emission components of the QDs coupled to the Ag nanohelices measured under LCP excitation are given in Figure 4.9a. It is clear from the plot that more RCP emission is measured. This demonstrates that the emission from the QDs coupled to the Ag nanohelices is polarised in accordance with the ‘handedness’ of the helices. This result agrees with that expected from antenna theory.[120] This is a significant result as it demonstrates that nanoscale helices can be used to modify the emission properties of emitters based upon the antenna properties possessed by the antenna-like structure itself. Figure 4.9b shows the difference between the emission components for both circular polarisations. A common quantification for circularly polarised emission is the degree or percentage of circularly polarised emission, ρ_C, given by

$$\rho_C = \frac{I_{LCP} - I_{RCP}}{I_{LCP} + I_{RCP}} \tag{4.4}$$

where I_{LCP} and I_{RCP} are the emission intensities of both LCP and RCP emission components, respectively. The percentage of circularly polarised emission, ρ_C, under LCP excitation is (10.0 ± 3.0)% at the emission peak wavelength of 560 nm and (17.7 ± 3.0)% at 600 nm. The increase in the amount of circularly polarised emission at 600 nm is attributed to scattering from the antenna-like structure.

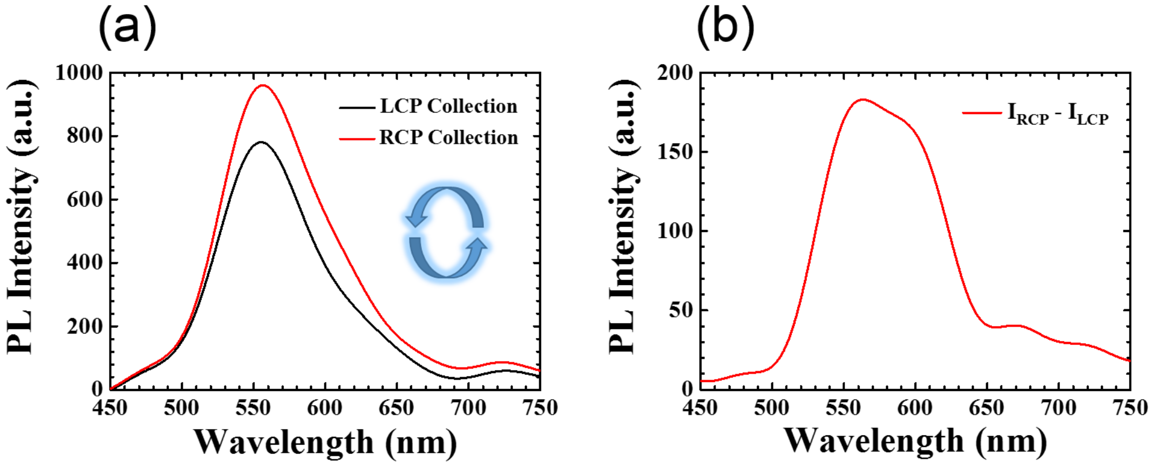

Figure 4.9: (a) LCP and RCP emission components measured under LCP excitation. (b) Difference between emission components corresponding to higher RCP emission.

The polarisation resolved emission components under RCP excitation can be seen in Figure 4.10a. A clear difference between the RCP and LCP emission components is observed, but the difference in the polarised components is not as significant here as in the case of LCP excitation. This is most likely due to the fact that the helices are right handed and therefore have a preference to absorb and reflect incident RCP light. A noticeable difference in the polarised components of the emission can be clearly seen at the peak emission wavelength, 560 nm and once again at 600 nm. This difference in circularly polarised emission can be more clearly observed in Figure 4.10b, where it becomes abundantly clear that the circularly polarised emission is much stronger at 600 nm. The percentage of circularly polarised emission for RCP excitation is (3.3 ± 3.0)% at 560 nm and (12.6 ± 3.0)% at 600 nm. Similar to the previous case under LCP excitation, a much higher degree of circular polarised emission is achieved at 600 nm which is not the peak emission wavelength.

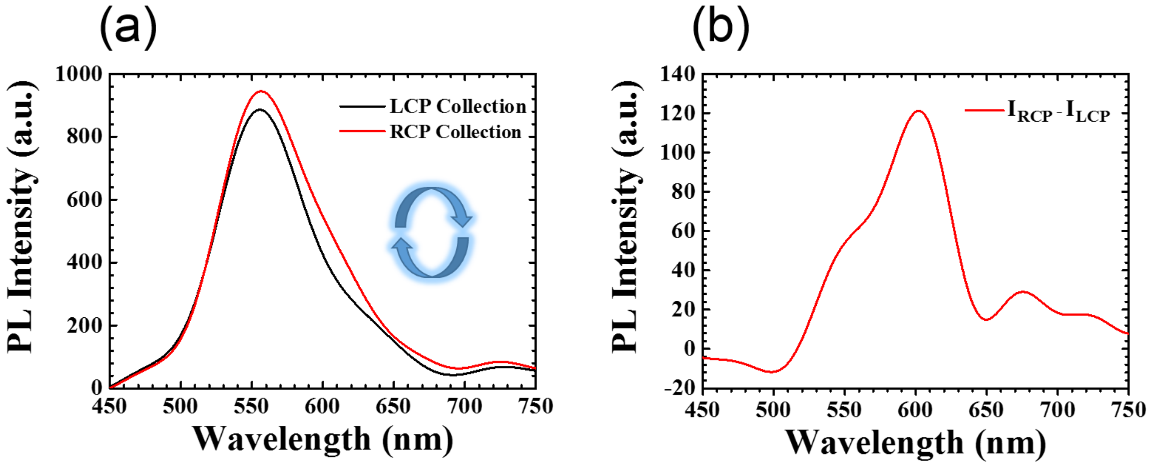

Figure 4.10: (a) LCP and RCP emission components measured under RCP excitation. (b) Difference between emission components corresponding to excess RCP emission.

Figure 4.11a shows a plot of the polarisation resolved components of the QD emission under excitation with the linearly polarised laser source. Clear differences in emission intensities are again observed, with greater emission intensity from the QDs with right circular polarisation. Similar to the previous polarisation resolved measurements one can see that there is a greater magnitude of circularly polarised emission on the red side of the emission spectrum. The higher polarised emission is shown in Figure 4.11b. This plot shows that the largest difference in the polarised emission is obtained at 600 nm, the same position that is seen in all previous plots. The percentage of circularly polarised emission obtained under linearly polarised excitation was (2.5 ± 3.0)% at the peak emission wavelength, 560 nm, and (9.0 ± 3.0)% at 600 nm. It should be noted that multiple linearly polarised measurements were performed every 15° from 0° to 180° with each measurement giving close to identical results. This indicates that the angle of the linearly polarised excitation has no influence on the emission properties of the QDs coupled to the Ag nanohelices.

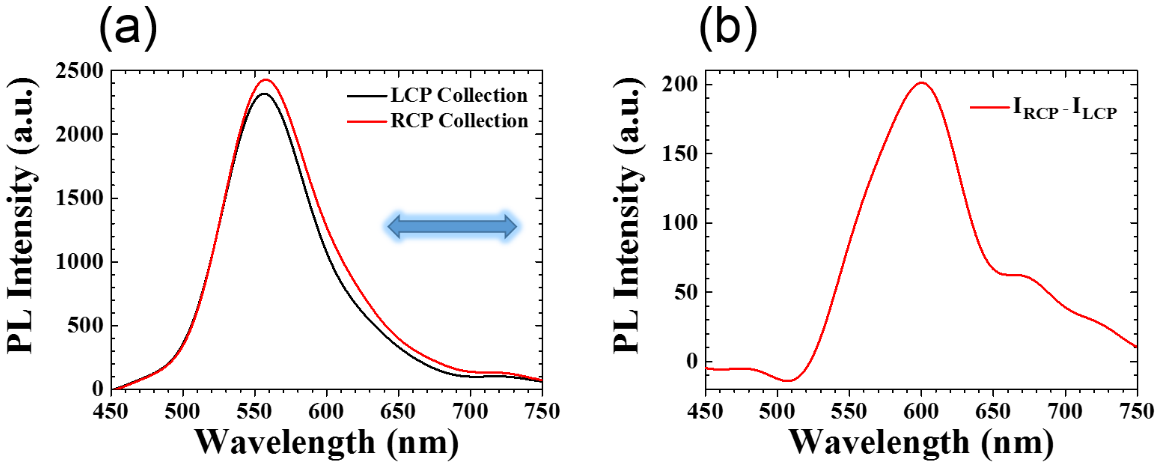

Figure 4.11: (a) LCP and RCP emission components measured under linearly polarised excitation. (b) Difference between emission components corresponding to excess RCP emission.

The absolute (unpolarised) emission from the QDs coupled to the Ag helices under LCP and RCP excitation can be seen in Figure 4.12. When the QDs are excited with circularly polarised light it appears that the total emission is equal for excitation with both circular polarisations. This indicates that in all cases the total emission from the QDs is equal but depending on the polarised character of the excitation a different amount of circularly polarised emission is achieved. The difference in the total emission components under excitation from both circular polarised components is negligible and amounts to (0.007 ± 3.0)% at the peak emission wavelength and (0.02 ± 3.0)% at 600 nm.

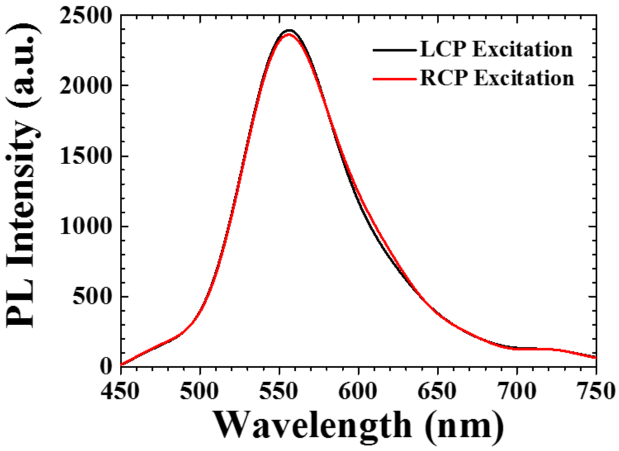

Figure 4.12 Unpolarised (absolute) emission components measured under LCP and RCP excitation.

4.5 Conclusion

The work in this chapter has demonstrated the effective coupling between core-only semiconductor nanocrystal CdTe QDs (emitters) and Ag nanohelices (antennas) and the resultant influence of the antenna properties from the Ag nanohelices on the far field emission properties of the QDs. The Ag nanohelices were characterised using circularly polarised transmission and reflection measurements and the chiral nature of the structures was revealed from the CD spectrum and SEM imaging. Multiple densely packed monolayers of QDs were deposited on the Ag nanohelices using the LbL deposition technique to achieve measureable PL intensities, given the significantly strong quenching of the QD PL to the metal structures. The extinction of the QD-Ag hybrid structure was measured following the deposition of each QD monolayer to monitor the formation of the coupled structure, illustrated by a 6 nm red shift in the peak extinction wavelength after the deposition of each QD monolayer. A large red shift and asymmetric broadening of the QD PL spectrum was observed after coupling to the Ag nanohelices, indicating that the system behaved as a coupled entity. The TRPL measurements further verified the interaction between the QDs and the Ag nanohelices. The PL lifetime measurements showed strong interaction between the QDs and the Ag nanohelices and the interaction was quantified in terms of the coupling efficiency, demonstrating a coupling efficiency of (82 ± 2)%.

PL lifetime measurements recorded on the blue and red side of the QD PL spectrum also indicated the presence of intra-energy transfer on the ITO substrate surface plasmon mediated intra-energy transfer with a lifetime increase of (77 ± 2)%. Similar measurements of the QD PL lifetimes when coupled to the Ag nanohelices demonstrated a lifetime increase of (90 ± 1)%, consistent with surface plasmon mediated intra-energy transfer in the coupled system.

The QDs coupled to the arrays of Ag nanohelices demonstrated a directional emission pattern fitting that of an ordinary end-fire pattern, as opposed to the Lambertian emission pattern of the QDs on the planar ITO substrate. Preferentially circularly polarised emission in the same handedness as the chiral structure was achieved under excitation with each circular polarisation and linearly polarised excitation. The degree of the circularly polarised emission was largest under LCP excitation (circular polarisation opposite to the handedness of the structure) with a value of (17.7 ± 3)% at a wavelength of 600nm. The peak emission wavelength of the QDs when coupled to the Ag nanohelices was 560 nm, however, the largest circularly polarised emission intensities were observed at 600 nm, which we attribute to scattering from the antenna like structures. Measurements of the absolute emission of the QDs under both circularly polarised excitations showed no difference in the emission intensity, revealing that there is no difference in the total amount of photons emitted but the differences arise in the number of photons that are circularly polarised. The number of circularly polarised photons was found to be dependent on the excitation condition, with the greatest advantage found for LCP excitation.

This chapter has provided clear evidence of the strong interaction between the QDs and the Ag nanohelices and the ability to impart the chiral properties of a structure to the emission properties of an emitter through coupling in the near-field. Ultimately, it would be desirable to achieve an emission pattern that has maximum directionality in a fairly narrow profile and total circular polarisation. In order to achieve such high levels of directionality fine tuning of the spatial parameters of each individual helix and also the parameters of the array are of paramount importance. Tuning the parameters of the helix can lead to a highly directional emission pattern within a single lobe, but the spacing between each antenna element in the array is extremely important in order to minimise the number of side lobes in the overall emission pattern. This tuning can also lead to the realisation of 100% circular polarisation within the main emission lobe.

Chapter 5

Influence of AgGO Composites on the Fluorescence Properties of Organic Dyes

Chapter Summary

This chapter will focus on the interaction between organic dye molecules and Ag nanoparticles, graphene oxide (GO) and a composite material of Ag nanoparticle (NP) decorated GO. This work investigates the impact of the AgGO composite, and its individual constituents, on the fluorescence properties and the Raman scattering signals of three organic dyes: Rhodamine 6G (R6G), Rhodamine B (RhB) and Sulforhodamine 101 (SR101). There are a number of processes associated with the AgGO composite: enhanced Raman scattering signals due to Ag NPs and/or GO, quenched or enhanced fluorescence due to the properties of the localised surface plasmon resonance (LSPR), and fluorescence quenching by the GO flakes. By studying the emission and Raman spectroscopy it is possible to isolate and examine the contributions of the various processes to the enhanced surface enhanced Raman scattering (SERS) signal for each of the dyes studied.

5.1 Introduction

Graphene and GO are strong quenchers of fluorescence[64,66,217,218] and along with other 2D materials are often referred to as 'exciton sinks'.[68] The ability to strongly quench fluorescence makes GO a promising species for use as an acceptor in a donor-acceptor pair. Graphene and GO have been shown to be efficient acceptors of excitation energy from nearby emitters due to highly efficient nonradiative energy transfer (NRET) through dipole-dipole coupling.[64,219] The inclusion of graphene and GO as an excitation energy acceptor *via*

NRET is a promising avenue for future optoelectronic applications, with a view towards light harvesting and photodetection devices.[220,221] The measurable signatures of the NRET process in these donor-acceptor pair systems are a reduction in the donor lifetime, quenching of the donor fluorescence and, enhancement of the acceptor fluorescence (if the acceptor is an emitting species). Ag NPs supporting LSPRs can also quench fluorescence *via* Joule heating or scattered radiation. The presence of Ag NPs can also lead to a reduction in the lifetime of nearby emitters, through a number of processes associated with plasmonic NPs, such as an enhanced excitation rate, enhanced radiative decay rate, and NRET from the donors to the Ag NPs. Such processes are extensively reported in the literature.[37–39,52]

Similarly, surface enhanced Raman scattering (SERS) can take advantage of the LSPR associated with Ag NPs. The large localised electromagnetic fields generated close to the surface of the Ag NPs can lead to significant enhancements of the SERS signal.[35,145,147–149,222] However, there is a downside to the use of Ag NPs for SERS of fluorescent molecules as the metal NPs can also give rise to metal/surface enhanced fluorescence.[49,223,224] This enhancement of the fluorescence is detrimental to SERS measurements, as the resulting fluorescence masks the Raman scattering peaks.

Combining the quenching properties of the GO with the large electromagnetic field enhancements of the Ag NPs provides an opportunity to overcome this enhancement of fluorescence associated with the Ag NPs. A one-pot chemical synthesis was used to form a composite material of Ag NPS decorated on GO (AgGO). Multiple samples were prepared to find the optimum Ag NP concentration and coverage on the GO in order to achieve large SERS enhancements and significant quenching efficiencies. Careful combination of both the Ag NPs and the GO allows for a large enhancement of the Raman scattering peaks and a reduction of the background fluorescence, which yields clearly identifiable Raman spectra with a reduced fluorescence background.

This chapter presents complimentary studies regarding the impact of each of the individual constituents in the composite material on the emission and Raman spectra of the three dyes. Steady state and time-resolved photoluminescence (PL) measurements were used to characterise the emission properties of the dyes. While the emission from the dye molecules is quenched more efficiently by the GO flakes, time-resolved PL (TRPL) measurements reveal that the dye molecules are more strongly coupled to the AgGO composite. The dye emission intensity is found to be higher on the AgGO composite compared to the GO flakes, with enhancement of the Raman scattering intensities also observed. The improvement in the SERS intensity is quantified using a signal-to-noise ratio (SNR). The SERS signal detection limits for each of the dyes are revealed using a concentration dependent study. For each of the dyes studied, the AgGO shows improved performance over each of the individual constituents in the composite and strong correlation is found between the SERS and TRPL data.

5.2. Initial Characterisation

5.2.1. Fabrication Characterisation

The GO flakes were prepared using a modified Hummers'[196] technique and the AgGO composites were prepared using a one-pot chemical synthesis as described in Chapter 3 (section 3.1.4). Multiple samples of the AgGO composite were prepared with varying Ag:GO ratios to identify the optimal level of Ag NP coverage on the GO flakes that provides the largest Raman signals from the dyes. Optimised packing density should yield a larger number of 'hot-spots'. Transmission electron microscope (TEM) images of the four samples prepared with differing levels of Ag NP coverage can be seen in Figure 5.1. The TEM images were recorded using a JOEL 2100 TEM operated at 200 kV. The initial concentration of Ag in the reaction solution was 5.53 mg/mL and this concentration was kept constant for all samples prepared. Sample A (0.8 mg/mL GO) has a Ag:GO weight ratio of ~7. Sample B (0.2 mg/mL GO) has a Ag:GO weight ratio of ~28. Sample C (0.02 mg/mL GO) has a Ag:GO weight ratio of ~277. Sample D (0.01 mg/mL GO) has a Ag:GO weight ratio of ~553. The TEM images (Figure 5.1) revealed that Sample D had the largest degree of Ag NP coverage. Preliminary SERS measurements with R6G were carried out using the composites of each Ag NP density. It was found that the largest enhancements were observed using the sample with the highest Ag NP density (Sample D). This is in line with expectations as the higher Ag NP density should produce a higher density of hotspots. Therefore, Sample D (0.01 mg/mL GO) was chosen for a more detailed study of the three dyes. The first aim of this work was to identify and select the AgGO sample that gave the largest Raman signals from the dyes. Subsequently, once the optimal substrate was identified, the main focus of the work was to investigate the influence of a single substrate on three different dyes.

It can be observed from the TEM images in Figure 5.1 that there is a range of Ag NP diameters and morphologies on the GO flakes. This is attributed to the excess amount of Ag present in the reaction solution in combination with the lengthy reaction time. Particle sizing was performed on each of the samples using ImageJ to gain a distribution of the Ag NPs size. The particle sizing was performed by taking multiple TEM images of each sample and measuring the diameter of over 300 Ag NPs from each sample to determine the mean diameter. The histograms of the Ag NP diameter for each of the AgGO samples are shown in Figure 5.2. The average diameters of the Ag NPs were found to be (19 ± 1) nm, (25 ± 13) nm, (31 ± 18) nm and (40 ± 16) nm for Samples A, B, C and D, respectively. These results from the particle sizing indicate that the average Ag NP diameter increased with increasing Ag:GO ratio.

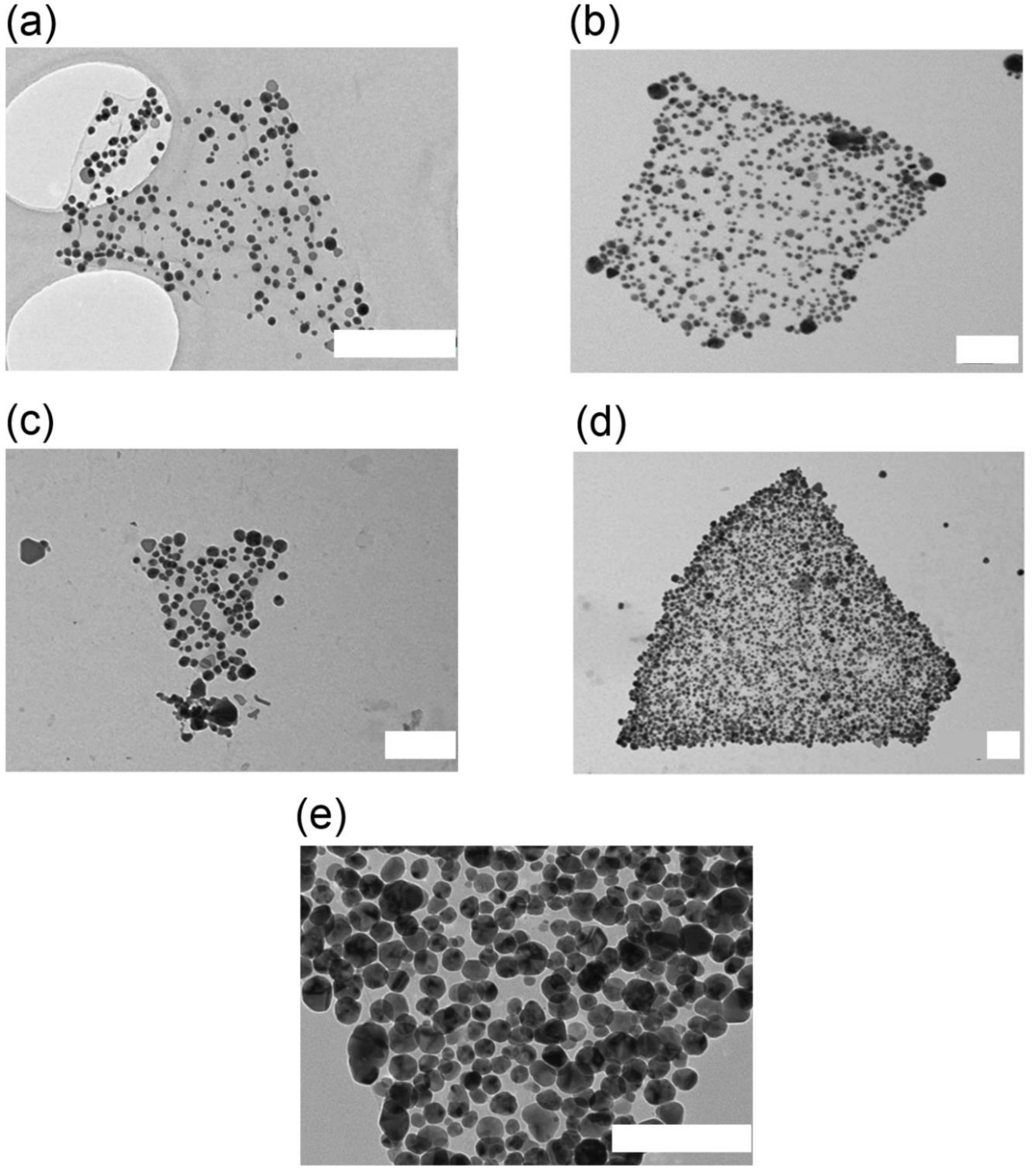

Figure 5.1: TEM images of AgGO composites with increasing Ag NP coverage. (a) Sample A (0.8 mg/mL GO), (b) Sample B (0.2 mg/mL GO), (c) Sample C (0.02 mg/mL GO), and (d) Sample D (0.01 mg/mL GO). (e) Close up image of Sample D. The scale bar in each image is 200 nm.

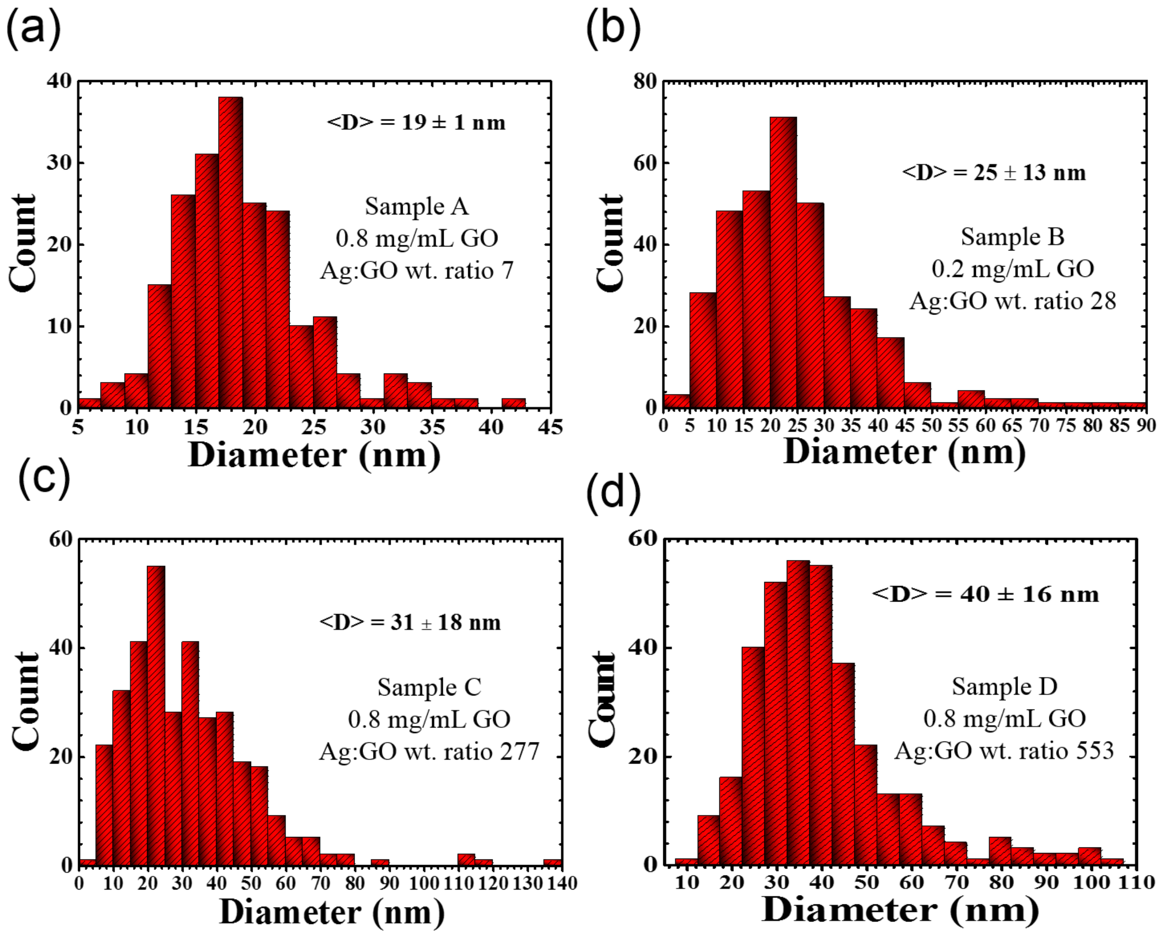

Figure 5.2: Histograms of Ag NP diameters. (a) Sample A (0.8 mg/mL GO), (b) Sample B (0.2 mg/mL GO), (c) Sample C (0.02 mg/mL GO), and (d) Sample D (0.01 mg/mL GO).

SEM images were recorded to obtain a better visual of the surface morphology of the AgGO composite (Sample D). The SEM images were recorded using a Carl Zeiss Ultra SEM. 10 μL of the AgGO dispersion was dropcast onto a Si/SiO$_2$ wafer with a 300 nm oxide layer and allowed to dry in a fume hood prior to imaging. The high density coverage of Ag NPs on the GO flakes can be clearly seen in the images in Figure 5.3. It is evident from Figure 5.3, panels c and d, that all GO flakes are completely covered in Ag NPs and that there are no unbound Ag NPs remaining on the substrate.

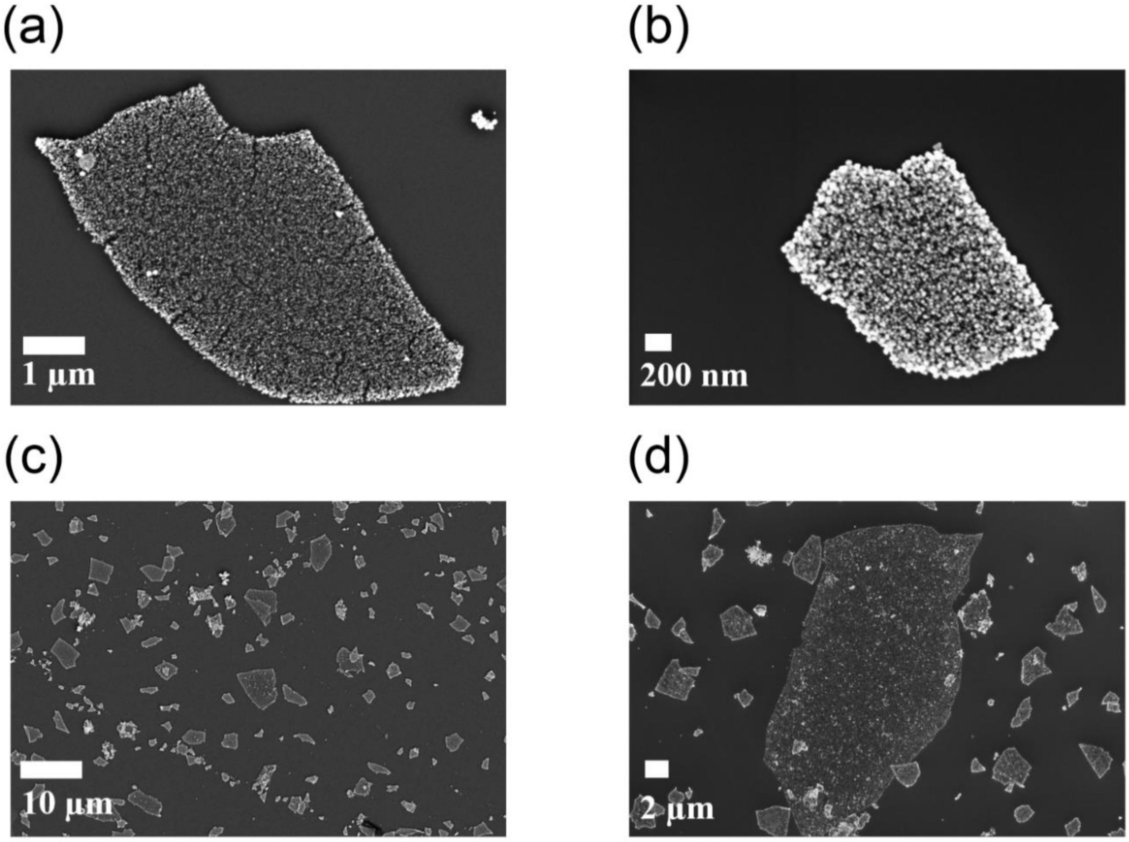

Figure 5.3: SEM images of AgGO Sample D.

To ensure that the GO flakes were coated on both sides by the Ag NPs AFM measurements were performed using a VeecoNanoscope-IIIa (Digital Instruments) system equipped with an E-head (13 μm scanner) in tapping mode. A 10 μL drop of the dispersion was deposited on a pre-heated (180 °C) Si/SiO_2 wafer with an oxide layer of 300 nm. After deposition, the wafer was rinsed with ~ 5 mL of Millipore water. AFM measurements were performed on both the GO flakes and the AgGO composite. AFM images of the GO flakes and the AgGO composite can be seen in Figure 5.4. The average thickness obtained for the monolayer GO was ~ 1.2 nm, which is in agreement with the literature values.[225] The AFM measurements of the AgGO composite gave thicknesses in the range of 50 – 100 nm, indicating that the Ag NPs are adhered to both sides of the GO flakes.

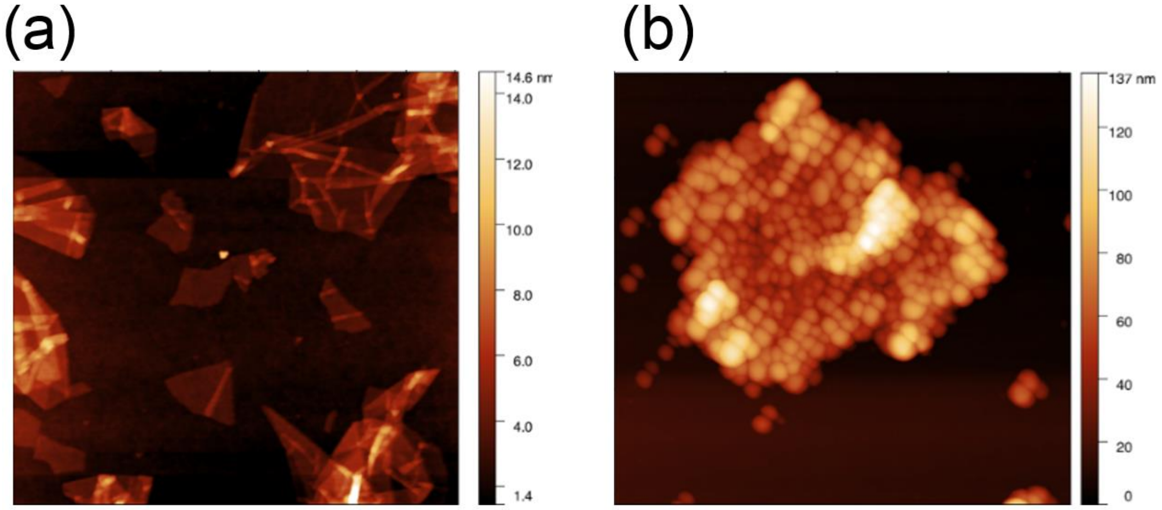

Figure 5.4: (a) AFM images of GO flakes and (b) AgGO Sample D.

5.2.2. Optical Characterisation

The spectral characteristics of the AgGO composites were examined using UV-Vis spectroscopy. The extinction spectra of Ag NPs (unbound NPs from Sample D), GO and the AgGO Sample D in aqueous solutions are shown in Figure 5.5. Figure 5.5a shows the typical extinction spectra associated with the LSPR of the Ag NPs (blue dash) with a peak extinction wavelength of ~ 405 nm. There is substantial broadening of the AgGO extinction spectra and a large red-shift of the peak extinction wavelength (~ 30 nm) as compared with the Ag NPs. The extinction spectra of each of the AgGO samples can be seen in Figure 5.5b. There is an increase in the peak wavelength and broadening of the extinction spectrum as the Ag:GO ratio is increased. To ensure that the red-shift of the peak wavelength and the broadening of the extinction spectra were not completely dominated by the Ag NP diameter, extinction spectra for each of the average diameters from the AgGO Samples were calculated using a Mie theory model[226] in combination with experimentally measured data.[227] The calculated extinction spectra are shown in Figure 5.5c. It is clear from Figure 5.5c that the red-shift in the peak wavelength and the broadening of the spectra with increasing Ag NP diameter are minute compared to those observed experimentally. The red-shift in the peak wavelength and the broadening of the measured extinction spectrum are attributed to the increasing diameter and polydisperse distribution of the Ag NPs as the Ag:GO ratio is increased, in combination with the increased interaction between the Ag NPs due to the dense packing on the GO flakes. The result of this interaction is a more prominent role of scattering at longer wavelengths.[202]

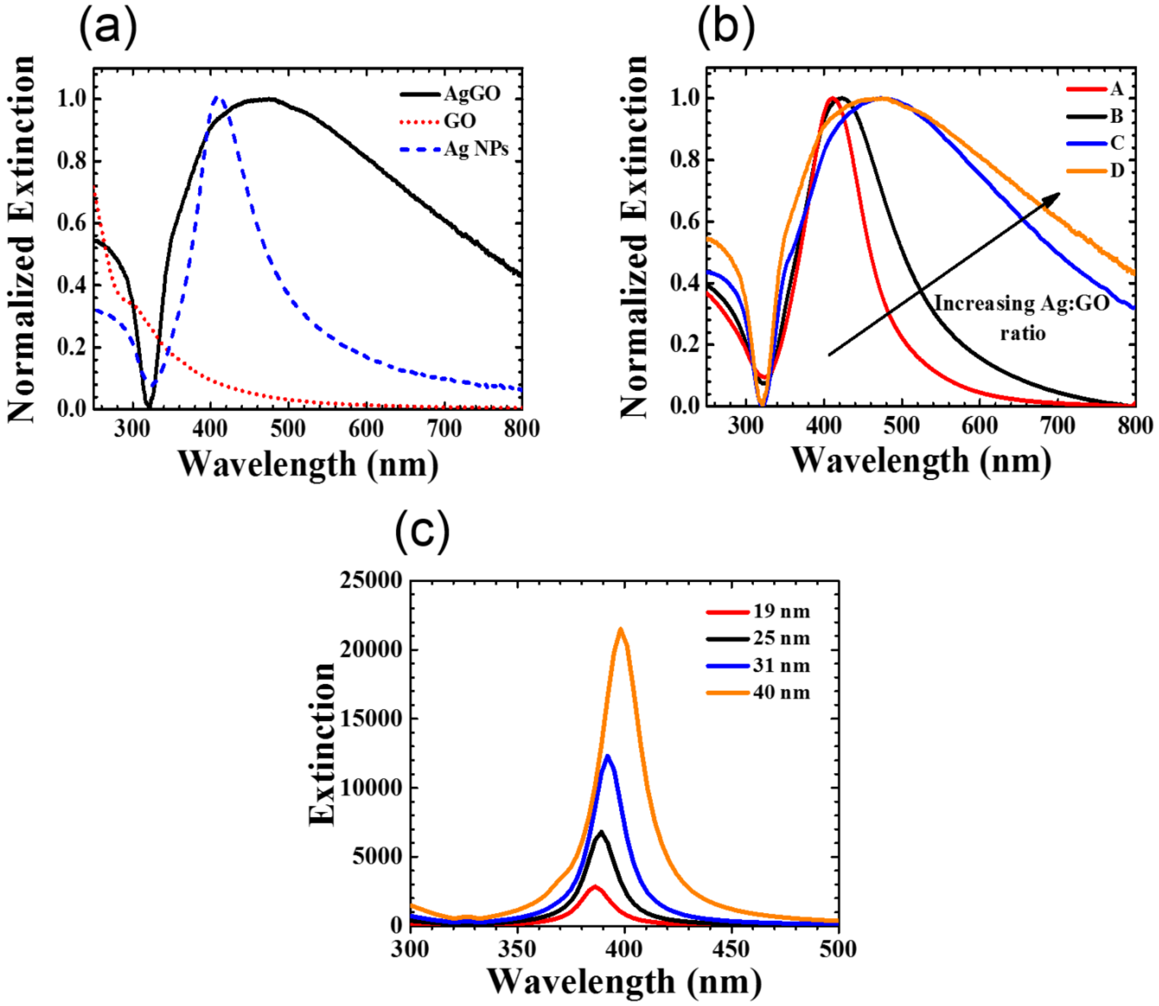

Figure 5.5: (a) Extinction spectra of GO (red dot), Ag NPs (blue dash) and AgGO (black solid). (b) Extinction spectra of Sample A (red), Sample B (black), Sample C (blue) and Sample D (orange). (c) Calculated extinction spectra of Ag NPs with diameters of 19 nm (red), 25 nm (black), 31 nm (blue) and 40 nm (orange), in comparison with the average Ag NP diameters in AgGO Samples A, B, C and D, respectively.

UV-Vis measurements were then performed with an integrating sphere to separate the extinction spectrum into absorption and scattering components. Separating the extinction spectrum into its absorption and scattering components offers insight into the more dominant contributions in the overall extinction spectrum. The extinction cross section, σ_{Ext}, is given by[102]

$$\sigma_{Ext} = \sigma_{Abs} + \sigma_{Sca} \tag{5.1}$$

where σ_{Abs} and σ_{Sca} are the absorption and scattering cross sections, respectively. As a result of this relationship the extinction, absorption and scattering spectra can be related in the same manner. Two measurements were performed to isolate the components. The extinction spectrum is acquired by performing a measurement outside the integrating sphere, while the absorption spectrum is acquired by performing a measurement inside the integrating sphere. This allows the scattering spectrum to be calculated as extinction minus absorption. The extinction, absorption, and scattering spectra of AgGO Sample D are shown in Figure 5.6.

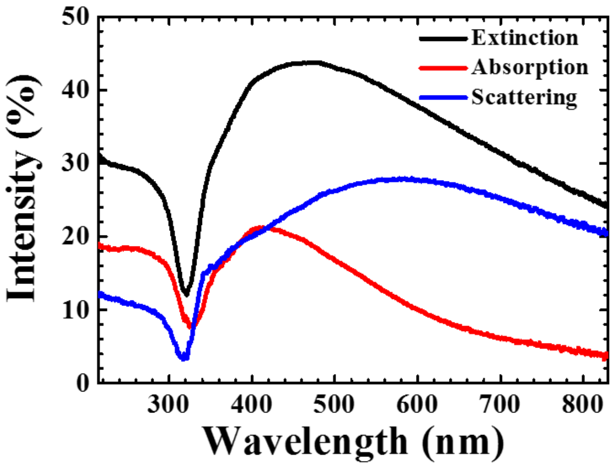

Figure 5.6: Extcinction (black), absorption (red) and scattering (blue) spectra of AgGO Sample D.

The spectra presented in Figure 5.6. show that the scattering contribution is much larger than the absorption component in the overall extinction, particularily at longer wavelengths. The broadened extinction spectra from the AgGO composite is beneficial for the Raman study of the dyes as the Raman excitation wavelength, 532 nm, overlaps the LSPR extinction spectrum, therefore local field enhancement is expected at this wavelength which is beneficial for SERS.

As mentioned previously, the dyes chosen for this study were Rhodamine 6G (R6G), Rhodamine B (RhB) and Sulforhodamine 101 (SR101). These dyes have emission wavelengths spanning 550 to 700 nm. Each dye can be optically excited using 532 nm excitation, and as such, the dyes should fluoresce during excitation in the Raman measurements. The extinction spectra for each of the dyes in aqueous solution (10^{-5} M) are shown in Figure 5.7a. The vertical dashed line in Figure 5.7a indicates the Raman excitation wavelength, 532 nm, and it can be seen that there is clear overlap between the laser excitation and each of the dye's optical absorption bands.

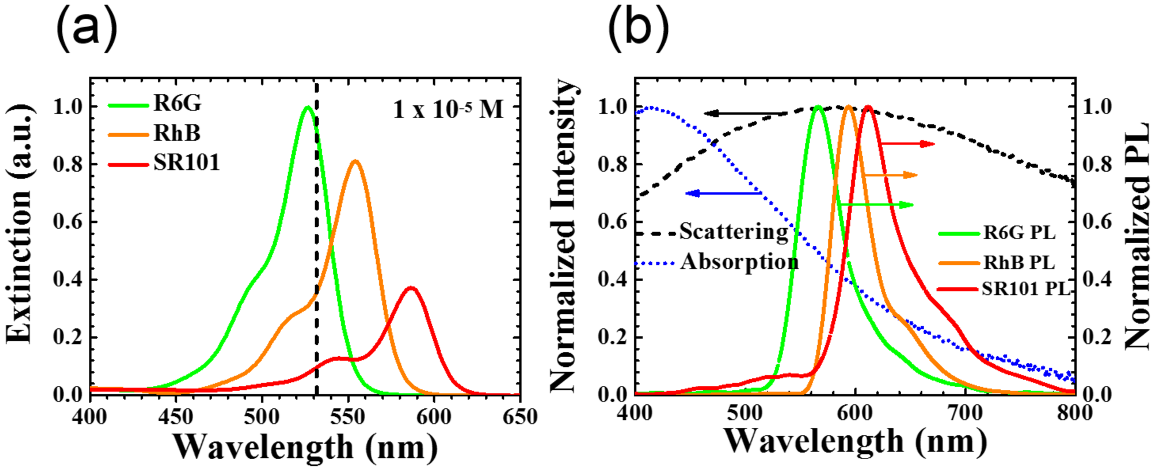

Figure 5.7: (a) Extinction spectra of R6G (green), RhB (orange) and SR101 (red) at 10^{-5} M concentration in solution. The dashed vertical line indicates the Raman excitation wavelength, 532 nm. (b) Normalised scattering (black dash) and absorption (blue dot) of AgGO Sample D and normalized PL of R6G (green), RhB (orange) and SR101 (red).

The normalised PL spectra for each dye are shown in Figure 5.7b along with the normalized extinction and scattering spectra from AgGO Sample D. There is greater overlap between the PL spectra and the AgGO scattering spectrum as compared to the absorption spectrum. In addition the peak PL wavelengths are all located close to the maximum of the AgGO scattering spectrum which can lead to metal/surface enhanced fluorescence.[49,223,224] This enhanced fluorescence can prove detrimental for SERS studies as the resulting fluorescence can mask the characteristic Raman peaks and, consequently, dramatically reduce the detection sensitivity.

5.3. Influence of AgGO composite on dye photoluminescence and surface enhanced Raman scattering

5.3.1. Time-Resolved and Steady State Photoluminescence

The interaction between the dyes and the AgGO/GO substrates was investigated using time-resolved photoluminescence (TRPL) and steady state photoluminescence (PL) measurements. The samples used for the TRPL and PL measurements were prepared as follows: 50 μL of dye solution (1 x 10^{-6} M) was added to 25 μL Millipore water and 50 μL of AgGO/GO, giving a dye concentration of 4 x 10^{-7} M. For the dye only measurements 50 μL of dye solution (1 x10^{-6} M) was dispersed in 75 μL Millipore water. The solutions were sonicated for ~ 60 s and spincast onto a hydrophilic quartz substrate at 2000 RPM for 180 s. The TRPL and PL measurements were performed using a PicoQuant Microtime200 time-resolved confocal microscope system using pulsed laser excitation (~ 90 ps) at a wavelength of 405 nm with a repetition rate of 10 MHz and an integration time of 4 ms per pixel. The samples were excited through a 40x microscope objective (NA = 0.65, spot size = ~430 nm) and the emission was collected through the same objective. The TRPL and PL measurements were performed over 5 µm x 5 µm areas. Both the TRPL and PL measurements for each dye and dye-substrate (AgGO/GO) combination were recorded from the same area to ensure correlation between the measurements. The TRPL measurements were performed first using relatively low excitation powers of 0.11 µW, 0.21 µW and 0.42 µW for R6G, RhB and SR101, respectively, taking account of the spectral mismatch between the excitation wavelength and the absorption bands of the individual dyes and ensuring that the dyes were not photo-bleached by high excitation intensities. The PL measurements were then subsequently performed at excitation powers of 4.2 µW, 6.3 µW and 8.4 µW for R6G, RhB and SR101, respectively. In the case of SR101, the electron multiplication setting of the spectrometer was doubled to compensate for the low dye absorption at the excitation wavelength and the low quantum yield.

As mentioned previously, the quenching of fluorescent molecules by GO has been extensively documented,[64,217] however, the interaction between fluorescent molecules and AgGO composite substrates is less studied. In this section steady state and TRPL measurements are implemented to elucidate the role of the individual components in the composite on the overall quenching of the organic dyes. The fluorescence decays of R6G, RhB and SR101 can be seen in Figure 5.8 a, Figure 5.8c, and Figure 5.8e, respectively. From the decays of the dyes alone (blue), on GO (red) and on AgGO (black) substrates, it is important to note that the dye only decay curves exhibit a single exponential decay. This decay was fitted using a single exponential decay curve, given by

$$I(t) = I_1 e^{-\frac{t}{\tau_1}} \tag{5.2}$$

where I_1 is the intensity amplitude of the single decay having a lifetime of τ_1. It is apparent from the decays in Figure 5.8 that the decay of the dyes on the GO and AgGO substrates now display bi-exponential decay curves.

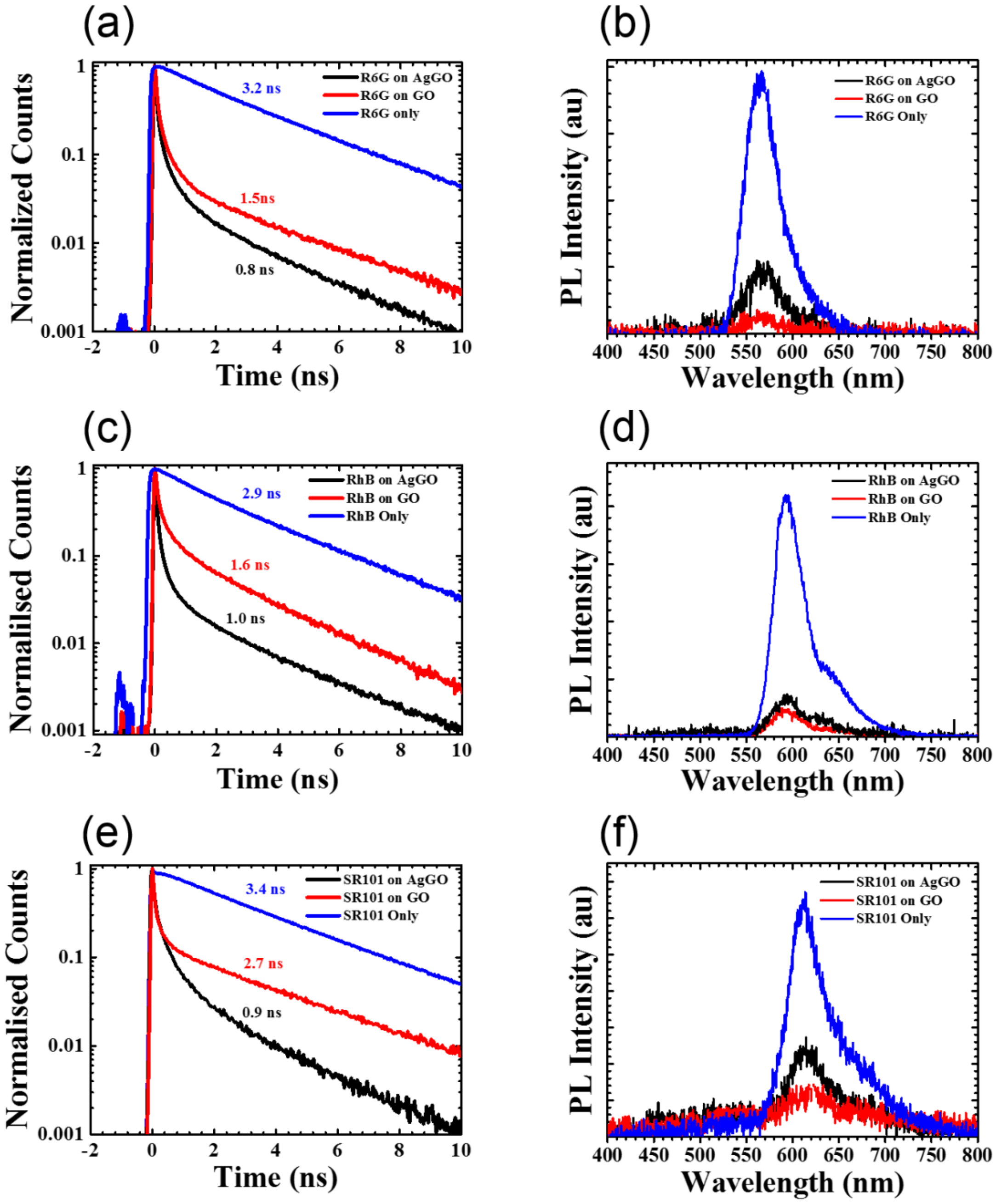

Figure 5.8: (a, c, e) Fluorescence decay curves for (a) R6G only (blue), on GO (red) and on AgGO (black). The extracted fluorescence lifetime is given for each decay. (c) RhB only (blue), on GO (red) and on AgGO (black). (e) SR101 only (blue), on GO (red) and on AgGO (black). (b, d, f) PL spectra for (b) R6G only (blue), on GO (red) and on AgGO (black). (d) RhB only (blue), on GO (red) and on AgGO (black). (f) SR101 only (blue), on GO (red) and on AgGO (black). The dye concentration in each spectrum is 4 x 10^{-7} M.

This extra exponent in the decay is due the introduction of an additional decay pathway when the dye is coupled to the GO/AgGO substrate. The decays of the dyes on the GO and AgGO substrates were fitted using a bi-exponential decay curve, given by

$$I(t) = I_1 e^{-\frac{t}{\tau_1}} + I_2 e^{-\frac{t}{\tau_2}} \tag{5.3}$$

where I_1 and I_2 are the intensity amplitudes for both decays having lifetimes of τ_1 and τ_2, respectively. A single representative lifetime is then extracted from the bi-exponential decay through the use of an intensity weighted average lifetime, τ_{Avg}, given by

$$\tau_{Avg} = \frac{I_1 \tau_1^2 + I_2 \tau_2^2}{I_1 \tau_1 + I_2 \tau_2} \tag{5.4}$$

All dye lifetime values on the GO and AgGO substrates mentioned herein are those of the average lifetime, τ_{Avg}. For each of the dyes, the TRPL curves show a decrease in the lifetime when adsorbed onto the GO as compared with the dye only, with a further reduction in the lifetime when adsorbed onto the AgGO. The further reduction of each dye's fluorescence lifetime when adsorbed onto the AgGO is attributed to processes associated with the Ag NPs. These processes include an enhanced excitation rate due to the large electromagnetic fields generated close to the surface of the Ag NPs, enhanced radiative rate, and non-radiative energy transfer from the dyes to the Ag NPs which can lead to emission quenching due to Joule heating or the scattering of radiation from the Ag NPs.[37–39,52] The fluorescence lifetime values obtained from the decays give a direct measure of the quenching efficiency in the case of the dye-GO and a measure of the interaction strength between the dye and the AgGO. This interaction between the dye and the AgGO can be quantified in terms of a coupling efficiency. These efficiencies, η, are given by

$$\eta = 1 - \frac{\tau_{DS}}{\tau_D} \tag{5.5}$$

where τ_D is the lifetime of the dye alone and τ_{DS} is the lifetime of the dye when adsorbed onto the GO or AgGO substrate. The efficiencies for each dye on the GO and AgGO substrates are presented in Table 5.1. The quantum yield for each of the dyes in aqueous solution are also presented in Table 5.1.

Table 5.1: Dye quantum yields, and efficiencies when adsorbed onto GO and AgGO.

Dye	Quantum Yield (%)	Efficiency (%)	
		GO	AgGO
R6G	95 ± 14	53 ± 7	75 ± 10
RhB	43 ± 6	45 ± 8	66 ± 7
SR101	19 ± 3	21 ± 2	74 ± 8

The data presented in Table 5.1 indicates a stronger interaction between each of the dyes and the AgGO composite when compared with the GO itself. Similar efficiency values of ~75% for R6G and SR101 on the AgGO composite are observed with a slightly lower value of 66% for RhB. This indicates a weaker interaction between RhB and the AgGO composite than for R6G and SR101. The quenching efficiency of SR101 on the GO is also lower than that of R6G and RhB. However, given that the quenching of the dyes in the presence of GO is due to NRET, it should be noted that this interaction is strongly dependent on the donor (dye) quantum yield and the spectral overlap between the donor (dye) emission spectrum and the acceptor (GO) absorption spectrum, both of which are lower for SR101. There is a significant recovery of the SR101 efficiency when adsorbed onto the AgGO. This is attributed to the enhanced excitation and radiative rates in the presence of the Ag NPs and, consequently, NRET to the Ag NPs, as mentioned earlier.

The steady state PL spectra of the dyes alone (blue), dyes on the GO (red) and AgGO (black) substrates are shown in Figure 5.8b, Figure 5.8d, and Figure 5.8f. The results from the steady state PL measurements show that the emission intensity is most strongly quenched when the dyes are adsorbed on GO. However, a slight increase in the emission intensity is observed when the dyes are adsorbed on the AgGO substrate compared to the GO substrate. This increase in the emission intensity can be attributed to metal enhanced fluorescence or an increased adsorption of the dye on the AgGO substrate.[160]

To measure the percentage of dye adsorbed onto the AgGO composite, adsorption capacity measurements were performed. The dye solutions were prepared to a concentration of 4 x 10^{-7} M, to replicate the conditions in the TRPL and PL measurements. To prepare the dye + AgGO solutions, 50 µL of stock AgGO solution was added to 2 mL of 4 x 10^{-7} M dye solution. The solution was mixed and sonicated for 20 seconds, then allowed to incubate for 3 hours at room temperature. The solutions were then centrifuged at 9000 RPM/ 5705 g for 20 minutes to precipitate the AgGO and consequently the dye adsorbed on the AgGO from the solution. Absorption measurements were then performed on the supernatant. To prepare the dye only reference samples, 50 µL of Millipore water was added to 2 mL of 4 x 10^{-7} M dye solution. The percentages of each dye adsorbed on the AgGO composite are shown in Figure 5.9.

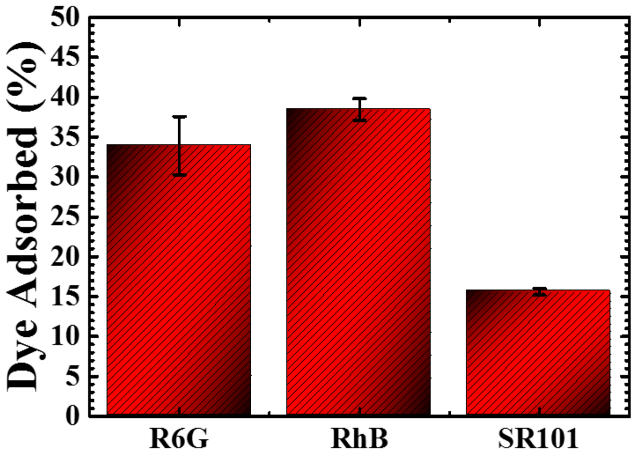

Figure 5.9: Percentage dye adsorbed on the AgGO composite.

The histogram in Figure 5.9 represents the adsorption capacity of the AgGO composite for each of the dyes. Similar levels of adsorption are observed for R6G and RhB while there are approximately half the number of SR101 molecules adsorbed onto the AgGO composite as compared to R6G and RhB. Taking this into account it should be noted that the lifetime values extracted from the TRPL measurements are concentration independent at the concentrations used in these experiments[228] and are not affected by the difference in adsorption capacity.

5.3.2. Surface Enhanced Raman Scattering

The advantages of the AgGO composite as a surface enhanced Raman scattering (SERS) substrate were assessed under excitation with a 532 nm laser, which also excites fluorescence from each of the dyes studied. The dyes were specifically chosen so that they would fluoresce under standard excitation conditions in the Raman system. This is commonly referred to as resonance Raman spectroscopy. This resonant excitation can enhance the Raman scattering signal by several orders of magnitude,[229] however, it can be masked by the fluorescence background arising as a result of the resonant excitation. The aim of the work is to assess the influence of the modified emission properties of the dyes in the presence of the AgGO composite on the SERS detection. As mentioned earlier, the dyes have emission wavelengths spanning the visible spectrum from 550 to 700 nm. To probe how the individual components of the AgGO composite influence the Raman scattering signals, Raman measurements were performed on GO flakes and Ag NPs. The Ag NPs used for the Raman measurements are unbound NPs from the AgGO Sample D reaction solution. This ensures that the Ag NPs are identical to those that are adsorbed onto the GO flakes. The Ag NPs were also found to form clusters upon drying, thus replicating the dense aggregation of

NPs found on the GO flakes in the AgGO composite and contributing to larger densities of ‘hot-spots’.

The Raman scattering spectra for each dye at a concentration of 10^{-4} M of can be seen in Figure 5.10. The Raman spectra presented in Figure 5.10, panels a, c, and e, are single measurements. This data has not been background subtracted to qualitatively demonstrate the influence of the AgGO composite (black), and its individual components; Ag NPs (red) and GO (blue) on the Raman scattering spectra of the dyes.

The Raman spectra for each dye on the Ag NPs show large overall signal intensity, however, this large signal intensity is the result of background fluorescence from the dye which dominates the spectra. While the signal intensity is large, it is difficult to resolve the characteristic Raman peaks. In the case of the dyes on the monolayer GO, the fluorescence background is significantly reduced due to the quenching of the dyes by the GO, consistent with the large quenching efficiencies observed in the TRPL measurements. However, Raman peak intensities are also low and very difficult to resolve for each of the dyes. In contrast, the dyes on the AgGO show large and clearly identifiable Raman peaks in combination with a moderate fluorescence background. The fluorescence background is significantly reduced and flatter compared with the Ag NP sample spectra. The Raman spectrum for each dye on the AgGO shows the most intense peaks compared to the GO and Ag NPs spectra. The reduction in the fluorescence background and the enhancement in the magnitude of the Raman peaks on the AgGO are attributed to contributions from of the GO and the Ag NPs, respectively. It can be noted that the background intensity is higher for the AgGO than the GO, which is consistent with the increase in PL discussed earlier. The Raman peaks are clearly more visible on the AgGO composite regardless of the higher fluorescence. These initial results qualitatively demonstrate the benefit of combining the quenching properties of the GO and the electromagnetic field enhancements from the Ag NPs to achieve low fluorescence intensities and enhanced Raman peaks.

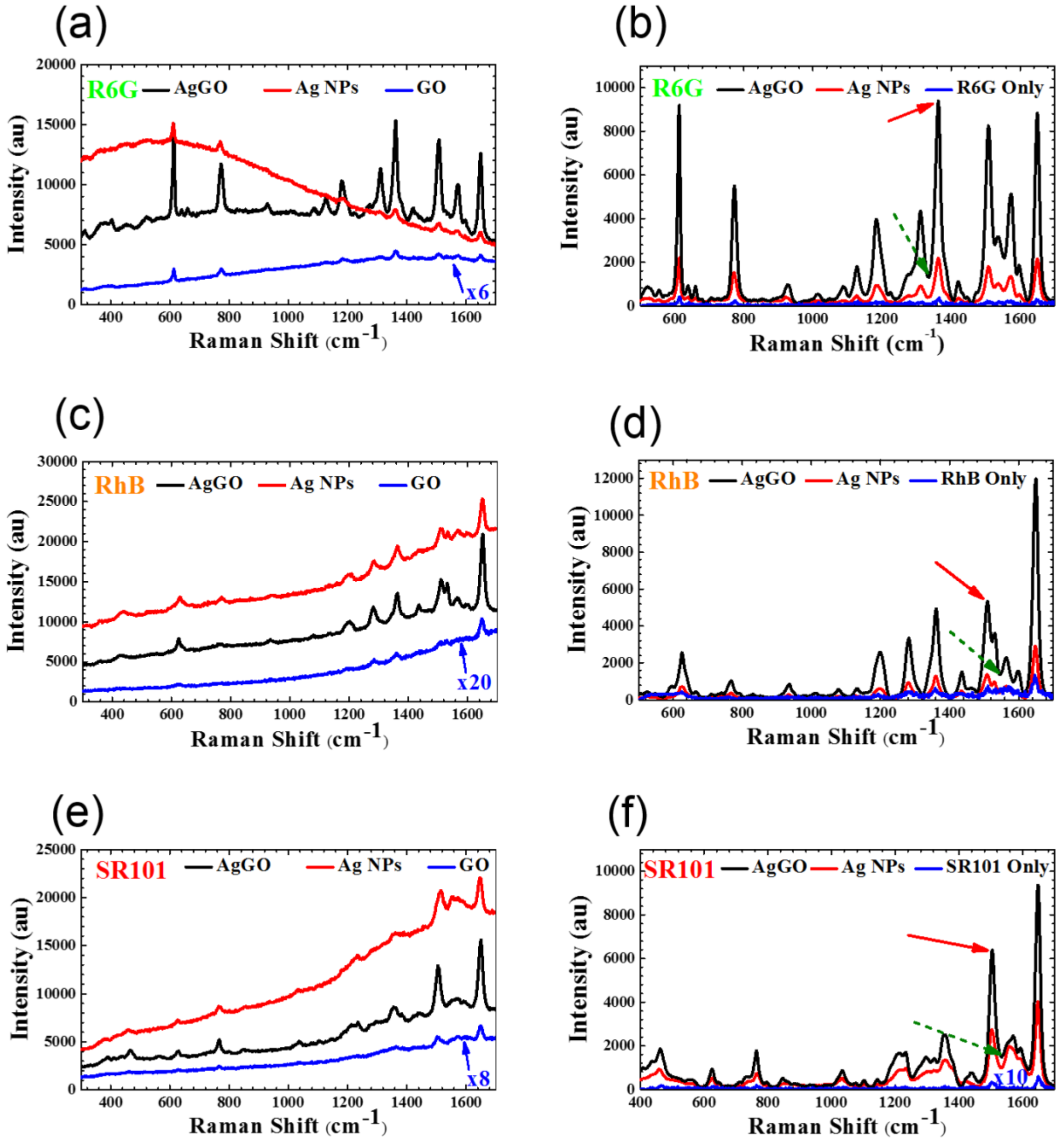

Figure 5.10: (a, c, e) Single Raman spectra of (a) R6G on AgGO (black), on Ag NPs (red) and on GO (blue). (c) RhB on AgGO (black), on Ag NPs (red) and on GO (blue). (e) SR101 on AgGO (black), on Ag NPs (red) and on GO (blue). The dye concentration in (a, c, e) is 10^{-4} M. (b, d, f) Average Raman scattering spectra at a concentration of 10^{-4} M for (b) R6G, (d) RhB and (f) SR101. In each panel the spectrum for the dye alone is shown in blue, dye on the AgGO composite is shown in black and dye on the Ag NPs is shown in red. The Raman spectra of dye only have a concentration of 10^{-3} M. The red solid [green dash] arrows in (d-f) indicate the peak [noise] positions chosen to calculate the SNR values.

In the following subsections, the improvement in the Raman spectra for each of the dyes due to the AgGO composite will be quantified in terms of three parameters; signal-to-noise (*SNR*) ratio, detection limit, and apparent enhancement factor (*AEF*).

5.3.3 Signal-to-Noise Ratio

Given that the Raman peak intensities on the GO were minute in comparison to the AgGO and the Ag NPs, it is more relevant to consider the performance of the AgGO over the Ag NPs. The impact of each component on the Raman spectra was quantified using a signal-to-noise ratio (*SNR*). The *SNR* is a measure of the detection sensitivity, essentially quantifying the visibility of the Raman peaks over the background signal/noise. The *SNR* is given by

$$SNR = \frac{S - N}{\sqrt{N}} \tag{5.6}$$

where S is the signal intensity and N is the noise intensity. The background was fitted and subtracted from each raw spectrum prior to the calculation of the *SNR*. Equation 5.6 shows large variations at low noise levels, and as such, the spectral peak and noise positions were chosen carefully to minimise uncertainty. Figure 5.10b, Figure 5.10d, and Figure 5.10f show the average background subtracted Raman spectra from over 50 measurements at a dye concentration of 10^{-4} M on Ag NPs (red) and AgGO (black). It is important to note that there were no changes in any of the peak positions on the different substrates.

For the *SNR* calculations, the spectral peak [noise] positions chosen for R6G, RhB and SR101 were 1362 cm^{-1}, 1511 cm^{-1} and 1508 cm^{-1} [1334 cm^{-1}, 1545 cm^{-1} and 1532 cm^{-1}], respectively. These peak [noise] positions are indicated in Figure 5.10b, Figure 5.10d, and Figure 5.10 by red [dash green] arrows. The results from the calculations show that the average *SNR* values are higher on the AgGO than on the Ag NPs alone. The distribution of the average *SNR* values for each of the dyes on the AgGO and Ag NPs are shown in Figure

5.11. The larger values on the AgGO are attributed to the fluorescence quenching of the dye due to the presence of the GO flakes and to larger enhancement of the Raman signal arising from the higher packing density of the Ag NPs on the GO flake, leading to a greater number of ‘hot-spots’. The greatest improvement in the average *SNR* value is seen for R6G. This is in agreement with the qualitative spectra shown in Figure 5.10. R6G has the highest quantum yield of the three dyes, it fluoresces more strongly than the other dyes and it has the largest spectral overlap with the excitation laser at 532 nm, and as such, it is expected that the influence of fluorescence quenching would yield the largest improvement for this dye.

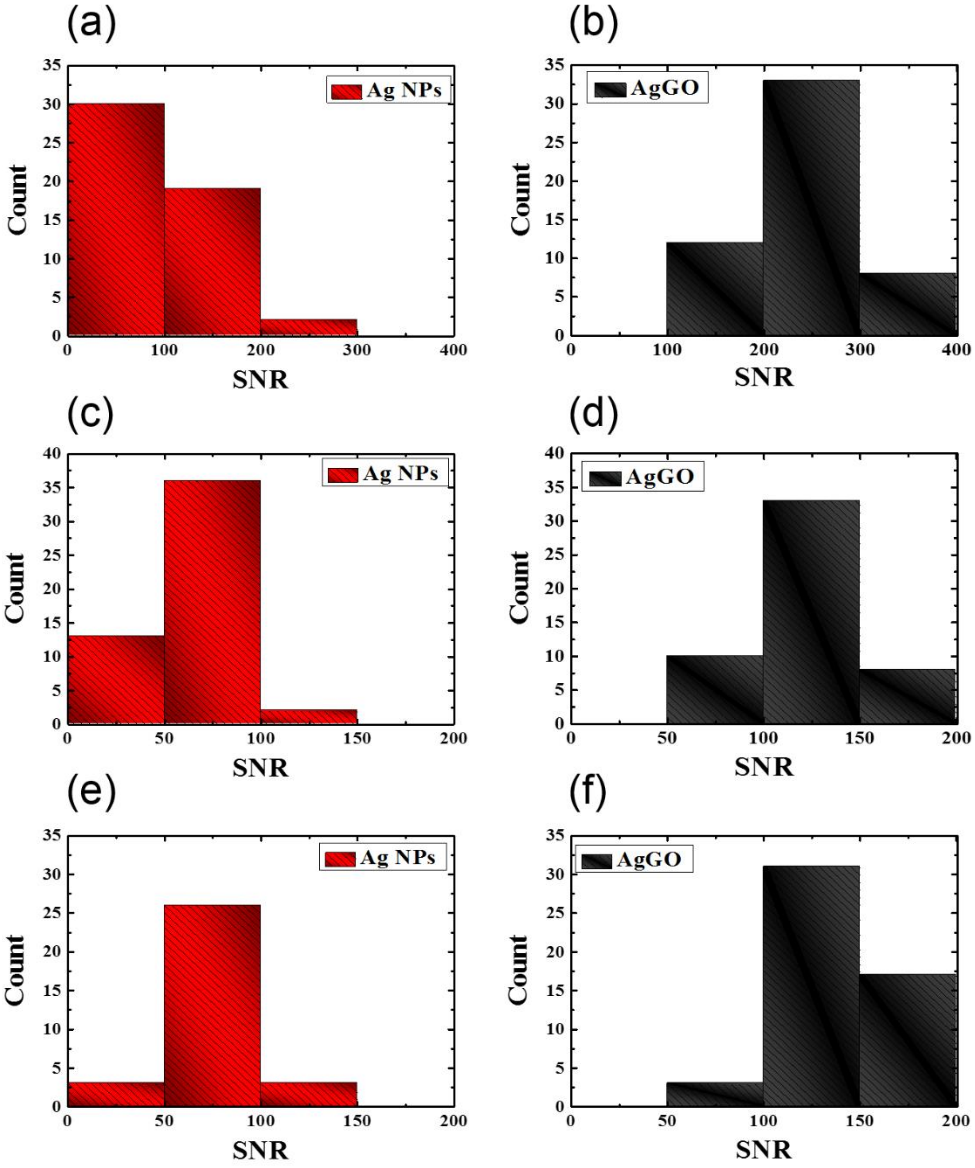

Figure 5.11: SNR distribution calculated from Raman spectra on Ag NPs (left) and AgGO (right) for (a, b) R6G, (c, d) RhB, and (e, f) SR101.

5.3.4 Detection Limit

Another important characteristic in terms of SERS substrates is that of the detection limit; the lowest concentration of analyte that can be detected on the chosen substrate. To identify the detection limit of the AgGO composite for each dye, a concentration dependent study was carried out. The results of the concentration dependent study are shown in Figure 5.12. The spectra at concentrations of 10^{-3}, 10^{-5} and 10^{-6} M were averaged over 30 spectra while 51 spectra were averaged at a concentration of 10^{-4} M. At dye concentrations of 10^{-7} M and lower, single spectra taken at ‘hot-spots’ showing the largest peak intensities are presented. This is due to the fact that, at the lower concentrations between 10^{-7} and 10^{-9} M, the broad D and G Raman peaks from the GO begin to dominate the spectrum in the 1300-1700 cm^{-1} range. Using the AgGO composite, detection limits of 10^{-9}, 10^{-8} and 10^{-8} M were achieved for R6G, RhB and SR101, respectively. These detection limits compare well with recent reports using metal-graphene composites in the literature. One of the most commonly used SERS analytes is R6G and the detection limit of 10^{-9} M reported here is similar to that reported by Kavitha *et al.* [230] and lower than some reports using similar substrates.[159,160] RhB is a less studied SERS analyte, however, the detection limit of 10^{-8} M observed here is within the range of 10^{-7} M reported by Sil *et al.* using a variety of treated graphene based materials[231] and 10^{-9} M reported by Fu *et al.* using an rGO-Ag dendrite composite.[232] The measurements reported here are the first using SR101 as an analyte on an AgGO composite. The Raman spectra presented in Figure 5.12 display all of the characteristic peaks from each dye above the detection limit while the quality of the measured spectra above the detection limit further demonstrates the benefits of the AgGO substrate for SERS detection of fluorescent analytes. For each of the dyes, the Raman scattering peak intensity is found to increase as the analyte concentration is increased from the detection limit to a concentration of 10^{-4} M. The Raman scattering peak intensities subsequently decrease at the higher concentration of 10^{-3} M corresponding to the *SNR* values as a function of dye concentration in Figure 5.13. At the highest studied concentration of 10^{-3} M, the dye molecules are densely packed on the substrate and as a result the overall signal intensity is reduced due to self-absorption.[203,204]

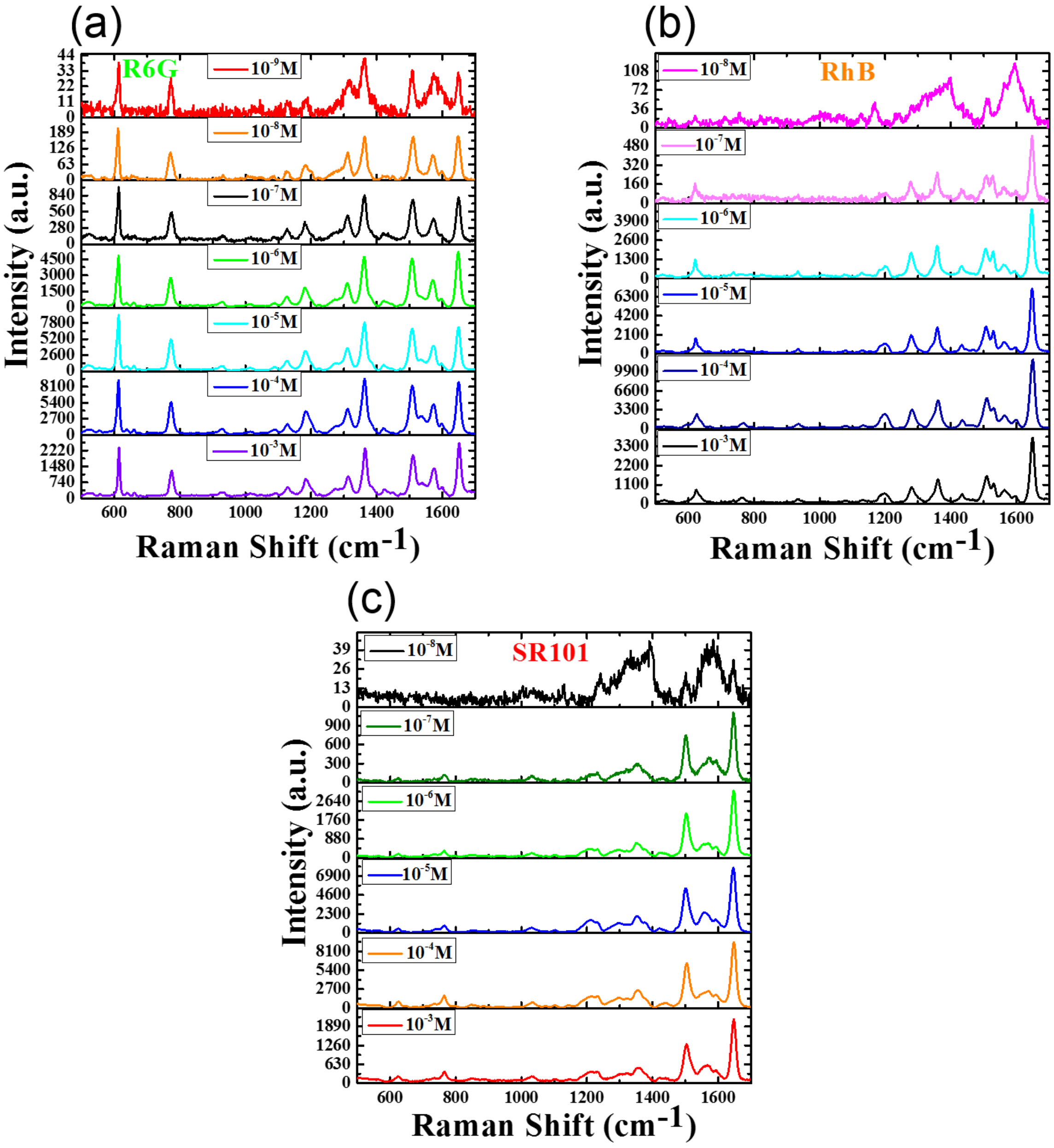

Figure 5.12: Concentration dependent Raman spectra of (a) R6G, (b) RhB and (c) SR101.

The *SNR* values presented in Figure 5.13 were calculated from the spectra given in Figure 5.12 using the same peak [noise] positions indicated by in red [green dash] arrows in Figure 5.10. As mentioned earlier, the sensitivity of the AgGO composite at a given concentration of analyte is quantified by the *SNR* value. This value is implemented here to assess the effectiveness of using the AgGO composite as a SERS substrate for fluorescent dye analytes. It is clear from Figure 5.13 that R6G performs the best on the AgGO substrate with *SNR* values approximately twice as large as the other two dyes. This increased performance of R6G is attributed to a number of factors; (i) the high quantum yield (95 ± 14)%, (ii) the resonant excitation of the dye at the Raman excitation wavelength, 532 nm, as the laser overlaps spectrally with the maximum of the electronic absorption band, and (iii) the large quenching efficiency by AgGO substrate (75 ± 10)%. SR101 demonstrates larger *SNR* values than RhB on the AgGO substrate which is consistent with the efficiency values extracted from the TRPL data. The TRPL data presented earlier had revealed that SR101 had a weak interaction with the GO flake. However, the presence of the Ag NPs in the AgGO composite lead to a stronger interaction with the SR101, indicating that the SR101 is coupled more strongly to the Ag NPs in the composite. Also taking the results of the adsorption capacity measurements into account whereby there are half as many SR101 molecules adsorbed to the AgGO than R6G and RhB, this further indicates improved performance from the SR101. RhB shows the lowest *SNR* values across all concentrations which is representative of the lowest coupling efficiency with the AgGO composite as revealed from the TRPL measurements.

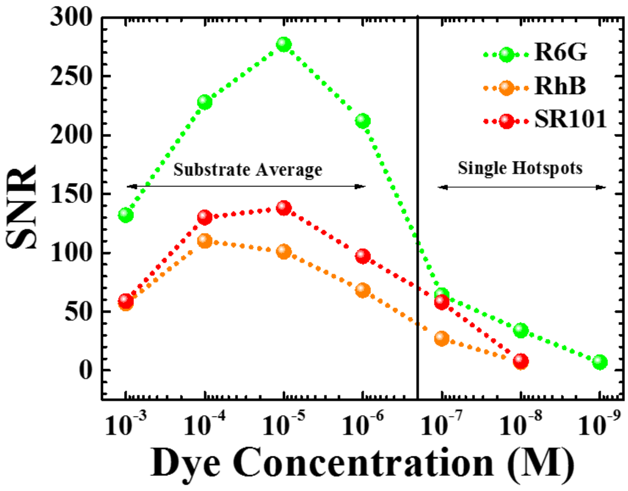

Figure 5.13: SNR values as a function of concentration.

5.3.5 Apparent Enhancement Factor

A commonly used figure of merit for SERS studies is that of an ‘enhancement factor’. However, there is no standardised method for calculating the ‘enhancement factor’, and as such, the further analysis of the impact of the AgGO substrate on the Raman scattering signal detection for a given concentration of solution lead to the definition of an apparent enhancement factor, (*AEF*), given by

$$AEF = \left(\frac{I_{SERS}}{I_{Glass}}\right) \cdot \left(\frac{C_{Glass}}{C_{SERS}}\right) \tag{5.7}$$

where I_{SERS} is the intensity of the dye Raman scattering peak on the AgGO substrate, C_{SERS} is the dye concentration of the solution used to prepare the dye-AgGO sample, I_{Glass} is the intensity of the dye Raman scattering peak measured from a dried sample prepared from dye solution with $C_{Glass} = 10^{-3}\ M$ drop cast onto a glass substrate. The calculation of the *AEF* was performed using averaged spectra, as presented in Figure 5.12. Averaged spectra were used to calculate the *AEF* due to the fact that single measurements may be performed at a ‘hot-spot’ but each of these ‘hot-spots’ does not necessarily produce the same Raman scattering enhancement and, therefore, any data obtained using these ‘hot-spots’ would not be representative of the substrate as a whole. The Raman scattering spectra were recorded over more than 30 measurements to gain an average Raman spectrum for each dye in the concentration range of 10^{-3}-10^{-6} M. The average Raman scattering peak intensities, I_{SERS}, used for the *AEF* calculation were taken from averaged spectra at the lowest dye concentration (in solution) of 10^{-6} M. The peak and noise values used for the *AEF* calculation were the same as those used for the *SNR* calculations. The *AEF* values calculated for R6G, RhB and SR101 at a solution concentration of 10^{-6} M were 1 x 10^4, 2 x 10^3 and 6 x 10^4, respectively. It should be remembered that these *AEF* values are representative of an average and not a single ‘hot-spot’ enhancement. The largest *AEF* value is found for SR101, this large enhancement of the dye signal on the AgGO substrate is attributed primarily to the presence of the Ag NPs in combination with the weak Raman scattering signal from the dye alone sample, I_{Glass}.

5.4 Correlation between Fluorescence and Raman Results

As mentioned earlier in this chapter, it is the combination of the fluorescence quenching properties of GO and the enhanced electromagnetic fields associated with the LSPR of the Ag NPs that reduce the fluorescence background and lead to the enhanced Raman scattering signals. The experimental studies in this chapter have demonstrated clearly the viability of the AgGO composite as a SERS substrate for fluorescent analytes. Comparing the Raman and TRPL data gives insight regarding the influence of each of these mechanisms for each of the dyes studied. The efficiency values obtained from the TRPL data for the dyes on the AgGO composite presented in Table 5.1 show a similar trend to the *SNR* values in Figure 5.13, particularly at the same dye concentration (10^{-7} M). The efficiency calculated from the TRPL data can be considered as a measure of the interaction strength between the dyes and the substrate as was discussed earlier. The efficiency and *SNR* values are largest for R6G, followed by SR101 and lowest values are found for RhB. The *AEF* values are found to be highest for SR101 and again lowest for RhB. This difference is even more pronounced when one takes consideration of the lower adsorption ability of the AgGO composite for SR101.

The efficiency data presented in Table 5.1 shows that R6G was strongly quenched by the GO directly with an efficiency of (53 ± 7)% with a further increase in the efficiency of ~ 22% in the presence of the AgGO composite, bringing the efficiency value to (75 ±10)%. The weakest direct quenching by the GO was found for SR101 with a value of (21 ± 2)%, which is to be expected given the lower quantum yield of SR101. However, the introduction of the Ag NPs in the AgGO composite caused the efficiency to increase by ~ 53% for SR101, resulting in an overall efficiency of (74 ± 8)% for the SR101 dye on the AgGO composite.

This is an indication that the quenching of emission is a much stronger factor for the SERS *SNR* and *AEF* for R6G than SR101. These findings also indicate that the SR101 is more strongly coupled to the Ag NPs than the GO which would be expected to yield the largest enhancements of the Raman signal, as seen in the *AEF*. In terms of RhB, the direct emission quenching by the GO is ~8% lower than for R6G, and while the relative increase of efficiency on the AgGO composite is similar to that of R6G, the overall efficiency is lowest for RhB compared with R6G and SR101, which mirrors the lowest *SNR* and *AEF* values from the Raman results for this dye.

5.5. Conclusion

This chapter has examined the impact of AgGO composite substrates on the fluorescence and Raman signals of fluorescent dye molecules with emission wavelengths spanning from 550 to 700 nm. Steady-state and time-resolved PL measurements reveal the impact of the addition of Ag NPs onto GO monolayer flakes, forming the AgGO composite on the dye emission. The stronger interaction between the dyes and the AgGO composite as compared to the GO flakes is indicated through a further reduction of the dye fluorescence lifetime on the AgGO composite. An important factor in the determination of the suitability of a substrate for SERS of fluorescent molecules is the interplay between fluorescence and SERS. The fluorescence quenching properties of the monolayer GO flakes are confirmed using steady-state PL measurements while a small increase in the fluorescence intensity is observed after the adsorption of the Ag NPs onto the GO flakes (AgGO). For each of the dyes, the fluorescence background in the Raman spectra was significantly reduced due to the dominance of the fluorescence quenching by the GO flakes in the AgGO composite. The impact of the AgGO composite on the Raman spectra for each of the dyes was quantified by the signal-to-noise ratio (*SNR*), obtained over many measurements to represent a substrate average and not a single ‘hot-spot’ measurement. For each of the dyes, large increases in the *SNR* are observed on the AgGO compared to Ag NPs. The high sensitivity of the AgGO substrate is revealed through ‘hot-spot’ measurements with detection limits of 10^{-9} M, 10^{-8} M, and 10^{-8} M for R6G, RhB and SR101, respectively. Analysis of the *SNR* data reveals that R6G benefits most from the composite substrate with similar improvements observed for RhB and SR101, despite the lower adsorption of SR101 dye on the AgGO composite. This correlates with the time-resolved PL data where the largest reductions in the fluorescence lifetimes on the AgGO composite are observed for both R6G and SR101. The fluorescence quenching by the GO is a more significant contribution in the SERS for R6G and RhB on the AgGO composite while the Ag NPs in the composite benefit SR101 more due to the direct enhancement of the Raman scattering signals.

Chapter 6

Nonradiative Energy Transfer from Semiconductor Quantum Dots to Quantum Wells

Chapter Summary

This chapter and the following two chapters will focus on the nonradiative energy transfer (NRET) from alloyed semiconductor nanocrystal quantum dots (QDs) to two-dimensional (2D) semiconducting materials with a view towards light harvesting and photodetection applications. This chapter in particular focuses on the NRET from QDs to three different InGaN/GaN quantum wells (QWs) having barrier thicknesses of 3 nm, 5 nm and 7 nm. The QWs were grown using a metal-organic vapour phase epitaxy (MOVPE) technique. It should be noted that the InGaN active region of each QW consists of the same thickness and composition and thus the only variation between each of the QWs is the barrier thickness. The NRET from the QDs to the QWs is studied in the hybrid system alone and also in the presence of colloidal and lithographically defined arrays of Ag nanoparticles (NPs). The defined arrays of Ag NPs were patterned using electron beam lithography (EBL).

6.1 Introduction

QDs have been considered as an ideal candidate for light harvesting systems due to their broadband absorption, high extinction coefficient and increased photostability in comparison with fluorescent organic dyes.[80,233,234] QDs also demonstrate significant versatility through the tunability of the absorption and emission properties from the UV to the IR *via* variation of the elemental composition and size of the nanocrystals.[200,235] However, a substantial drawback in terms of the use of QDs for electrical applications is their poor electrical properties.[60] The poor electrical performance of solution processed QDs is what leads to the use of QDs as optical absorbers or sensitizers in hybrid systems where an alternative semiconducting material is used as the extraction point for the electrical current. QWs on the other hand have good electrical properties[236] which deems them ideal candidates for the electrical component in this hybrid system, allowing for the efficient extraction of the generated photocurrent. Ag NPs were chosen for use in this hybrid system for multiple reasons. Firstly, Ag NPs can support a localised surface plasmon resonance (LSPR) which, when in the presence of optically absorbing media, can increase the effective absorption cross-section, and enhance the radiative and NRET rates.[37–39,237] Depending on the location of the Ag NPs in a layered system (i.e. at the surface of the layer) the Ag NPs can also behave as sub-wavelength scattering elements, where it has been proposed that they may be used to trap propagating light into thin layers.[238,239]

There have been previous reports demonstrating the use of NRET in light harvesting devices.[172,240,241] Similarly, the use of QWs in light harvesting devices has also been proposed.[170,172,242] It is with this in mind that the use of a coupled donor-acceptor system was implemented to investigate the viability of the hybrid structure for use as a light harvesting device. In the system studied in this chapter the donor and acceptor in this hybrid structure are the QDs and QWs, respectively. The use of QDs as donors in donor-acceptor pair systems is well documented. QDs have been proven as efficient donors to noble metals,[52] fluorescent organic dyes,[233,243] QDs,[53,88,244,245] and two-dimensional (2D) materials including semiconductor nanoplatelets,[246] graphene,[64,66] and transition metal dichalcogenides (TMDs) such as MoS_2.[65–67,247] The Ag NPs were incorporated in the hybrid system to increase the absorption of incident light by the QDs and to help overcome the short range distance dependence of NRET as discussed in Chapter 2. The presence of metal NPs in a donor-acceptor system has been proven to enhance the Förster radius of the donor-acceptor interaction.[40,53]

The first system discussed in this chapter involves QDs and colloidal Ag NPs dispersed in an ultrathin PMMA layer on top of the 3 nm, 5 nm and 7 nm barrier QWs. These colloidal samples were studied to investigate the distance dependence of the direct and plasmon enhanced NRET from the QDs to the QWs. The NRET was characterised through the donor (QD) lifetime on the 3 nm, 5 nm and 7 nm barrier QWs in the presence and absence of the Ag NPs. The second system studied looks at ordered Ag NP arrays and the impact of the array geometry on NRET from the QDs to the QW.

6.2. Initial Characterisation of the Colloidal Ag NP system

6.2.1. Absorption and Spectral Photoluminescence

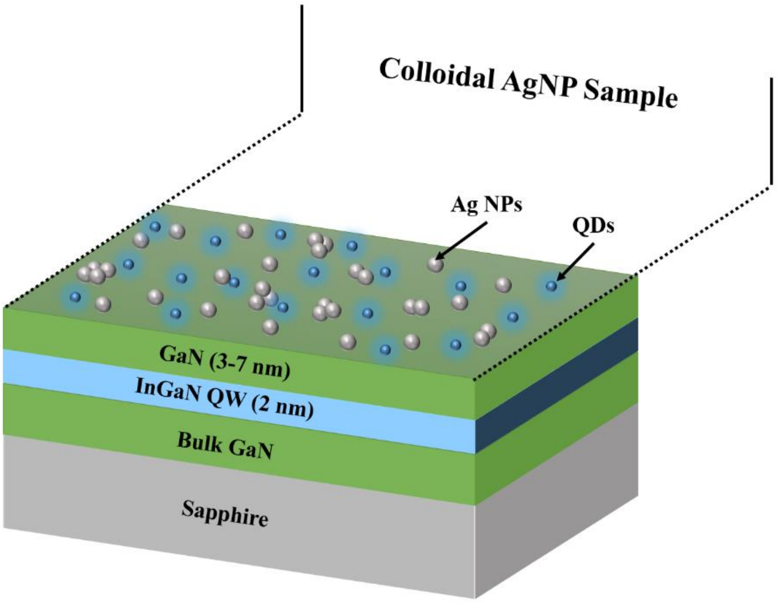

Figure 6.1: Schematic illustration of colloidal QD-Ag NPs on the InGaN/GaN QWs.

A schematic diagram of the colloidal QD-Ag NPs sample is presented in Figure 6.1. The QDs have a peak emission wavelength of 450 nm and a diameter of (6.0 ± 0.8) nm. The Ag

NPs also have a diameter of (6.0 ± 0.5) nm in solution. The QDs were purchased in solution at a concentration of 1 mg/mL in toluene from Sigma-Aldrich. This solution was used as stock. The Ag NPs were purchased in powder form from Plasmachem. The Ag NPs were then dispersed in toluene at a concentration of 2.5 mg/mL and this solution was used as stock. Aliquots of both QD and Ag NP solutions were then dispersed in 0.1% wt. PMMA in toluene and subsequently spincast onto the InGaN QWs with GaN barrier thicknesses of 3 nm, 5 nm and 7 nm. The colloidal QD-Ag NP dispersions in 0.1% wt. PMMA were made up to a total volume of 100 µL. These solutions consisted of 20 µL QDs, 40 µL Ag NPs and 40 µL 0.1% wt. PMMA. Reference samples were prepared by replacing the volume of the solution occupied by QDs, Ag NPs or both the QDs and Ag NPs, with toluene to give the same PMMA concentration in solution prior to spincasting the layer. Spincasting of the mixed QDs-PMMA solutions gave a layer thickness of ~ 6 nm; verified by atomic force microscopy (AFM) as shown in Figure 6.2.

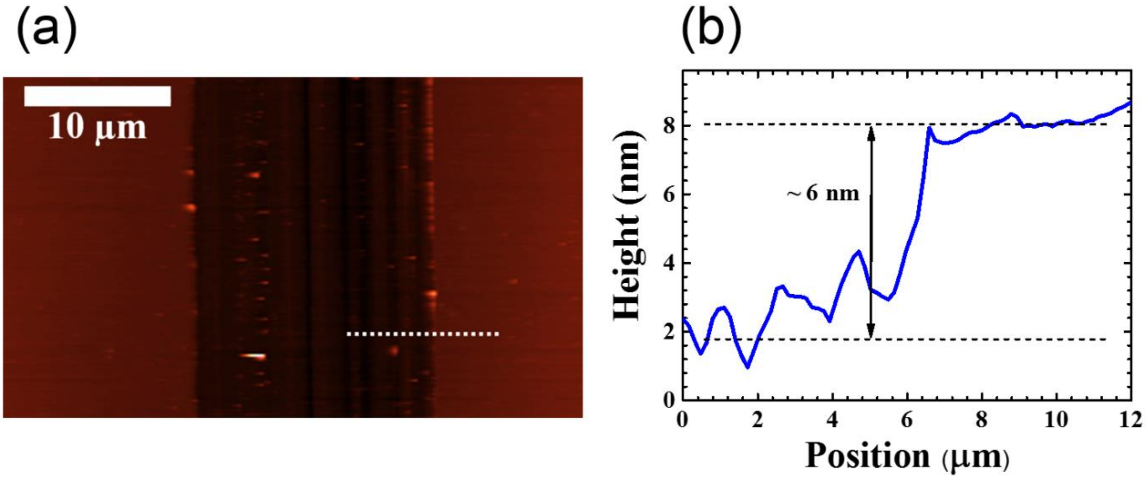

Figure 6.2: (a) AFM image of trench cut in the QDs-PMMA layer. (b) Corresponding height profile of the trench in the QDs-PMMA layer, indicated by the dash white line in (a).

The Ag NPs, in PMMA solution and in layers, were optically characterized by means of UV-Vis absorption spectroscopy. The extinction spectra of the Ag NPs in 0.1% wt. PMMA solution and in a layer on a quartz substrate are presented in Figure 6.3. The extinction spectrum of the Ag NPs in PMMA solution (red line) shows a peak extinction wavelength at ~ 460 nm corresponding to the LSPR of the Ag NPs. The extinction spectrum of the Ag NPs in the ultrathin PMMA layer shows a dampened and broadened LSPR compared with the Ag NPs in PMMA solution, indicating that the Ag NPs have aggregated during or after the spincasting of the layer.

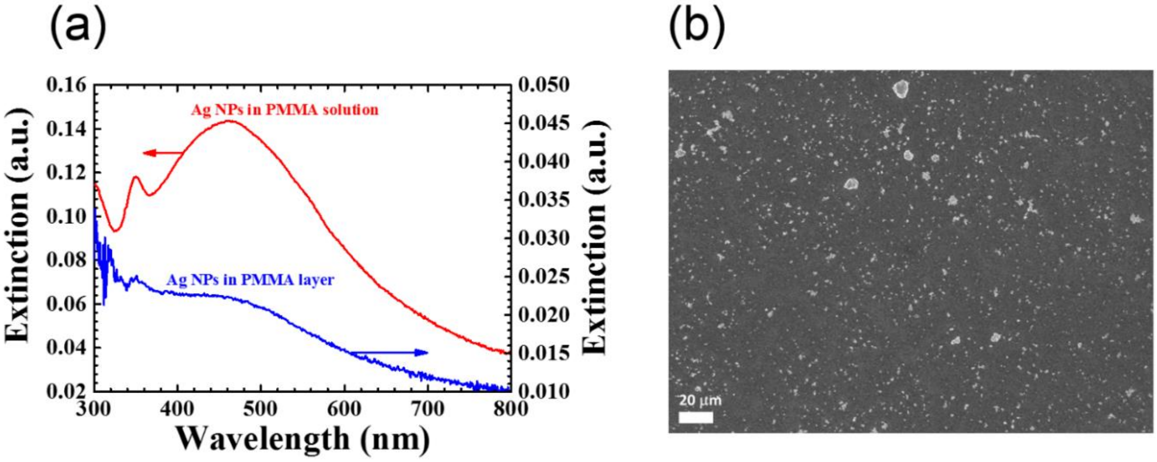

Figure 6.3: (a) Extinction spectra of Ag NPs in 0.1% wt. PMMA solution (red line) and in a layer on a quartz substrate (blue line). (b) SEM image of Ag NPs in 0.1% wt. PMMA film on a Si/SiO$_2$ substrate.

The aggregation of the Ag NPs was investigated using scanning electron microscopy (SEM). An SEM image of the Ag NPs in a PMMA layer on a Si/SiO$_2$ substrate is shown in Figure 6.3. It is clear from the SEM image that there is significant aggregation of the Ag NPs in the PMMA with aggregate sizes as large as 10 µm, confirming that the dampening and broadening of the Ag NP LSPR in the extinction spectrum is due to the aggregation of the NPs.

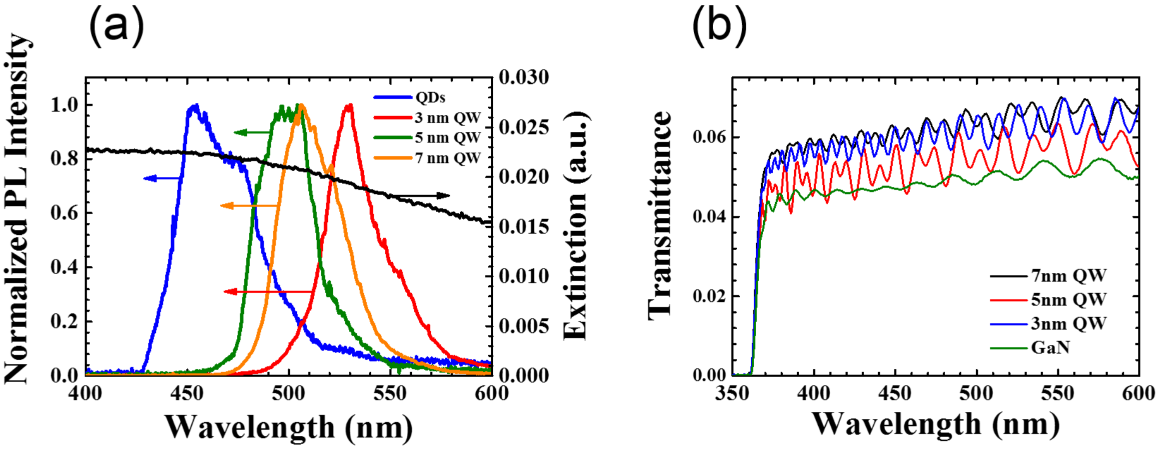

Figure 6.4: (a) Normalized PL spectra of the QDs (blue line), 3 nm QW (red line), 5 nm QW (olive line) and 7 nm QW (orange line) on the left axis. The extinction spectra of the Ag NPs in the PMMA layer is given on the right axis (black line). (b) Transmittance spectra of each QW and GaN sample.

The normalized PL spectra of the QDs and each of the QWs are shown in Figure 6.4a. The extinction spectrum of the Ag NPs in a PMMA layer is also shown to demonstrate the overlap between the QD emission and the LSPR of the Ag NPs. The QDs have a peak emission wavelength of 450 nm which overlaps well with the peak of the Ag NPs LSPR at ~ 460 nm. The 3 nm, 5 nm, and 7 nm barrier QWs have peak emission wavelengths of 530 nm, 500 nm, and 510 nm, respectively. The transmittance measurements of each of the different barrier thickness QWs in Figure 6.4b indicates that there is no significant change in the absorption and, subsequently, no variation in the spectral overlap between the QDs and each of the QWs.

6.2.2. QD and QW Power Dependences

In order to identify the optimal excitation power range for the study, the dependences of the QD and QW PL lifetimes and PL intensities on the optical excitation power were investigated. The QD PL lifetime and integrated PL intensity as a function of optical excitation power are shown in Figure 6.5a and Figure 6.5b, respectively. The QD PL lifetime and integrated PL intensity shows a close to linear increase with increasing excitation power (Figure 6.5b). At higher excitation powers the QD PL lifetime and integrated PL intensity begin to decrease due to photobleaching of the QDs. The linear region of the power dependence curve corresponds to powers at which single exciton generation occurs in each QD. The dashed black line in Figure 6.5a and 6.5b indicates the power at which all further PL lifetime measurements were performed.

The power dependences of the PL lifetime and the integrated PL intensity for the 3 nm, 5 nm, and 7 nm barrier QWs were also measured. However, in terms of the QWs one can consider the carrier density, n, corresponding to a given optical excitation power, P_{Ex}. The carrier density, n, is given by [248]

$$n = \frac{P_{Ex}}{E_{Ph} \cdot S \cdot \gamma \cdot d_{InGaN}} \cdot e^{-\alpha_{GaN} d_{GaN}} \cdot [1 - e^{-\alpha_{InGaN} d_{InGaN}}] \cdot [1 - R] \tag{6.1}$$

where E_{Ph} is the photon energy, S is the laser spot size, γ is the repitition rate of the excitation, d_{InGaN} and d_{GaN} are the thicknesses of the active region and the barrier in the QW, respectively, α_{InGaN} and α_{GaN} are the absorption coefficients for the active region and the barrier in the QW, respectively, and R is the reflectance of the pump laser at 405 nm. In our measurement setup, we utilize a 405 nm laser which gives a photon energy of $E_{Ph} = 3.1\ eV$, allowing for excitation of the InGaN active region without exciting the GaN barrier (~ 3.4 eV) and therefore $\alpha_{GaN} = 0$. $\alpha_{InGaN} = 10^4 cm^{-1}$,[249,250] $d_{InGaN} = 2\ nm$, $d_{GaN} = 3\ nm, 5\ nm,$ and $7\ nm$ for each of the QWs, $\gamma = 10\ MHz$, $S = 430\ nm$ and $R = 0.15$.[249]

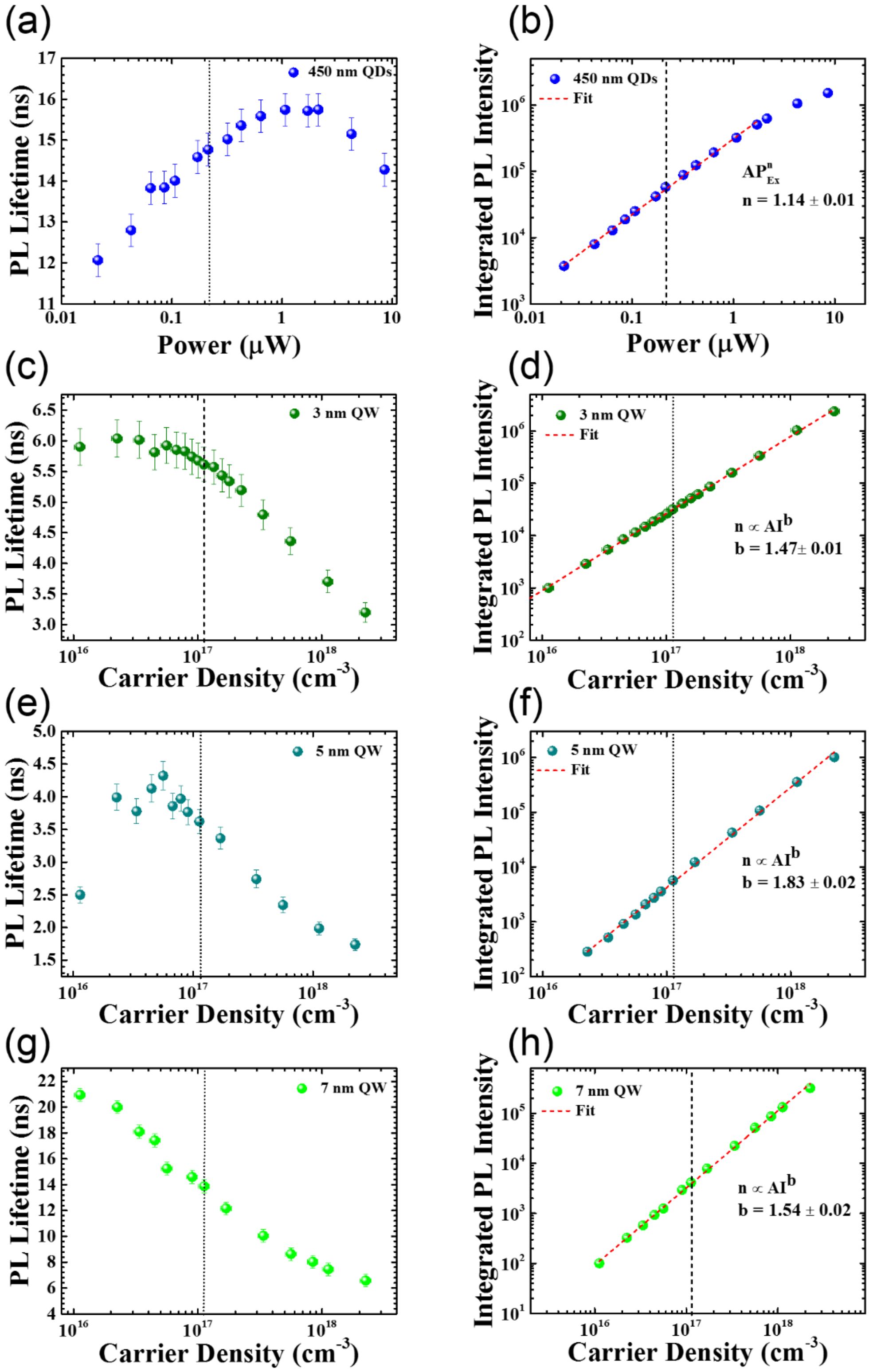

Figure 6.5: (a, c, e, g) QD PL lifetimes as a function of excitation power (a) and QW PL lifetimes as a function of carrier density (c, e, g). (b, d, f, h) Integrated PL intensity as a function of excitation power for the QDs (b) and as a function of carrier density for the QWs (d, f, h).

The dependence of the QW PL lifetime on the excitation power is influenced by many different decay dynamics, including the population of free carriers, heavy and light free excitons, and bound excitons, in combination with complex carrier formation.[251,252] However, if we consider the QW PL lifetimes of the 3 nm and 5 nm barrier QWs as a function of carrier density in Figure 6.5c and Figure 6.5e, there is an slight increase in the PL lifetime at low carrier densities. Increases in the PL lifetime can be attributed to defect filling due to the capture of charge carriers at defect sites.[248] Eventually the PL lifetime reaches a maximum before steadily decreasing. This decrease in the PL lifetime as the carrier density increases indicates that all defect states have been filled and the dominating mechanism for the recombination of charge carriers is that of radiative recombination.[253] However, in the case of the 7 nm barrier QW (Figure 6.5g), the lifetime is constantly decreasing indicating a lower number of defect states as they are filled with a lower number of excited carriers as compared with the 3 nm and 5 nm barrier QW. This indicates that the defects states are instantly filled at the lowest carrier density and the PL lifetime decreases as the carrier density increases. The dotted black line in the plots indicates the excitation power at which all further PL lifetime measurements were recorded. This is on the decreasing side of the curve where radiative recombination is the dominant recombination process for the charge carriers.

Similar to the characterization of the QDs, the integrated PL intensity was investigated as a function of carrier density for the 3 nm, 5 nm, and 7 nm barrier QWs and are shown in Figure 6.5d, Figure 6.5f, and Figure 6.5h, respectively. The integrated PL intensity data is fitted with a power law where $n \propto I^b$. From the fits, $b = 1.47 \pm 0.01, 1.83 \pm 0.02,$ and 1.54 ± 0.02 for the 3 nm, 5 nm, and 7 nm barrier QWs were extracted, respectively. These values indicate that the radiative recombination processes in the QWs can involve free carriers and excitons.[254,255]

6.3. Nonradiative Energy Transfer with Colloidal Ag NPs

In this section, NRET and its distance dependence from QDs to QWs of different barrier thicknesses is investigated. Ag NPs are introduced into the hybrid system as a plasmonic mediator for the NRET process. Four QD configurations are considered for each of the QWs in order to accurately quantify the magnitude of the NRET efficiency given that the trademark characteristic of NRET is the reduction of the donor (QD) lifetime. The reference for the direct interaction between the QDs and the QWs (QD-QW) consists of QDs in a PMMA layer on GaN (QDs Only), while the reference for the Ag NP plasmon mediated interaction between the QDs and QWs (QD-Ag NPs-QW) consists of QDs and Ag NPs in a PMMA layer on GaN (QD-Ag NPs). A schematic representation of the four samples can be seen in Figure 6.6.

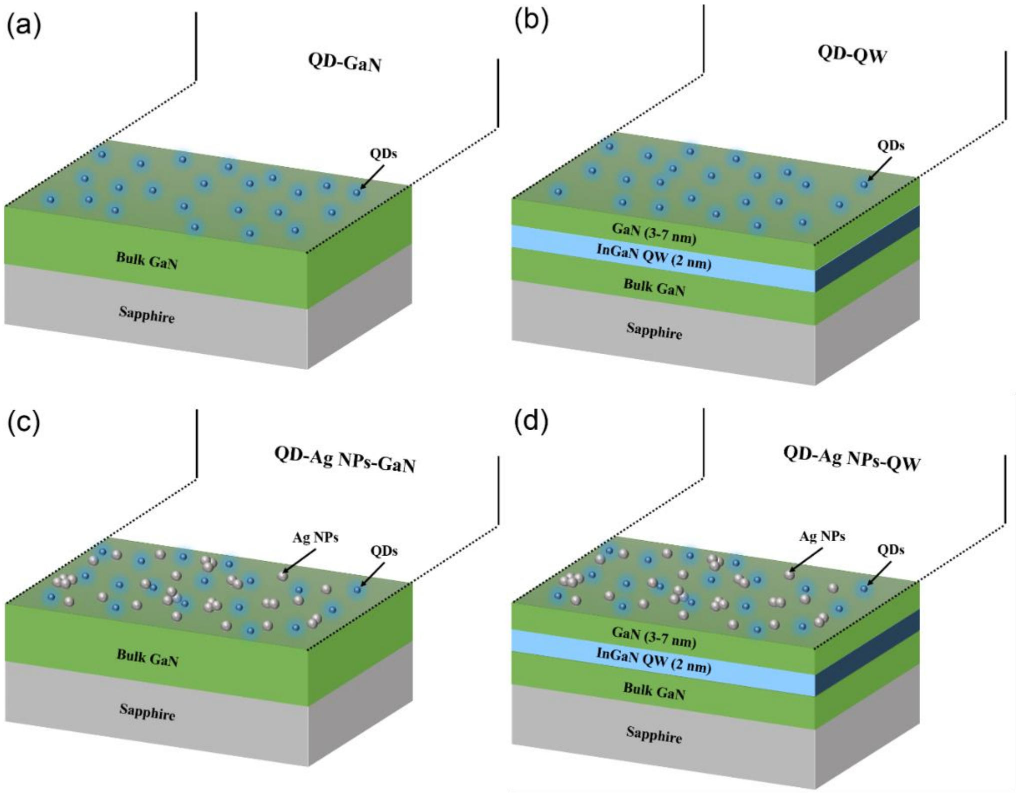

Figure 6.6: Schematic diagrams of the four colloidal samples, (a) QD-GaN, (b) QD-QW, (c) QD-Ag NPs-GaN, and (d) QD-Ag NPs-QW.

The normalized PL decays for the QDs on the 3 nm, 5 nm, and 7 nm barrier QWs are presented in Figure 6.7a, Figure 6.7c, and Figure 6.7e, respectively, with the corresponding PL lifetimes given in Figure 6.7b, Figure 6.7d and Figure 6.7f, respectively. It is instantly apparent from the PL decays that the largest reductions of the QD PL lifetimes occur on the 3 nm barrier QW (Figure 6.7a), which is expected as this QW provides the smallest centre-to-centre separation, d, between the QDs and QW. In a multi-component hybrid structure such as this it is important to first consider the direct interaction between the QD and the QWs. This direct interaction between the QD and the QW is evident by the separation between the black (QD Only) and the green (QD-QW) curves [and the PL lifetimes] in Figure 6.7a[b], Figure 6.7c[d], and Figure 6.7e[f]. The NRET efficiency for the direct QD-QW interaction, η_{QD-QW}, is quantified using the measured PL lifetimes as follows

$$\eta_{QD-QW} = 1 - \frac{\tau_{QD-QW}}{\tau_{QD}} \tag{6.2}$$

where τ_{QD} and τ_{QD-QW} are the PL lifetimes of the QDs in a PMMA layer on GaN (QDs Only) and the QDs in a PMMA layer on the QWs (QD-QW), respectively. Given that this system is that of a planar system, Equation 2.16 in Chapter 2 (section 2.2.1) shows that the NRET efficiency in a planar system has the form

$$\eta_{NRET} = \frac{1}{1 + kd^4} \tag{6.3}$$

where k is a constant and d is the centre-to-centre separation. It can be seen from Equation 2.16 that $k = 2/c_{Acc}\pi R_0^6$, where c_{acc} is the acceptor concentration and R_0 is the Förster radius. The NRET efficiencies for the QDs on each of the QWs were calculated using Equation 6.2 and are plotted as a function of centre-to-centre separation, d, in Figure 6.8. A linear plot of the NRET efficiency is given in Figure 6.8a where the dash red line is a fit to Equation 6.3 with $k = 2.9 \times 10^{-3} nm^{-4}$ which gives an R_0 for the direct NRET from the QDs to the QW of 4.3 nm. The logarithmic plot of the NRET efficiency in Figure 6.8b is fitted using a power law (Ad^n) with $n = -4$ and shows the d^{-4} dependence. A free fit to the data (black dotted line) gives $n = -3.8 \pm 0.09$, which is close to the ideal fit of $n = -4$ (red dash line). This is the first experimental validation showing that the distance dependence of direct NRET from QDs to QWs follows a d^{-4} dependence, in agreement with theoretical prediction.[83]

When considering NRET in the hybrid QD-Ag NPs-QW system, the interaction between the QDs and the Ag NPs must first be considered. There is a reduction of the QD lifetime in the presence of the Ag NPs on each reference sample for each of the barrier thickness QWs, as can be seen from the PL decays and PL lifetimes in Figure 6.7. This is to be expected given the spectral overlap between the QD emission spectrum and the Ag NPs extinction spectrum (Figure 6.4). There is a stronger interaction between the QDs and the Ag NPs than the QDs and the 5 nm and 7 nm barrier thickness QWs, while the interaction between the QDs and the 3 nm barrier QW is of similar magnitude to the QD-Ag NPs interaction. The efficiency of the interaction between the QDs and the Ag NPs is quantified in terms of a quenching efficiency, η_{Quench}, given by

$$\eta_{Quench} = 1 - \frac{\tau_{QD-Ag\ NPs}}{\tau_{QD}} \tag{6.4}$$

where τ_{QD} and $\tau_{QD-Ag\ NPs}$ are the PL lifetimes of the QDs in a PMMA layer on GaN (QDs only) and the QDs in a PMMA layer with Ag NPs on GaN (QD-Ag NPs). For each of the QD-Ag NPs reference samples the quenching efficiencies, η_{Quench}, were ~ 17%.

With the interaction between the QDs and the Ag NPs accounted for, the interaction in the complete QD-Ag NPs-QW structure can be quantified. While there is a reduction of the QD PL lifetime in the presence of the QW and also in the presence of the Ag NPs, there is a further reduction of the QD PL lifetime in the presence of both the Ag NPs and the QW, as can be seen in Figure 6.7. The plasmon mediated NRET efficiency can be calculated as follows

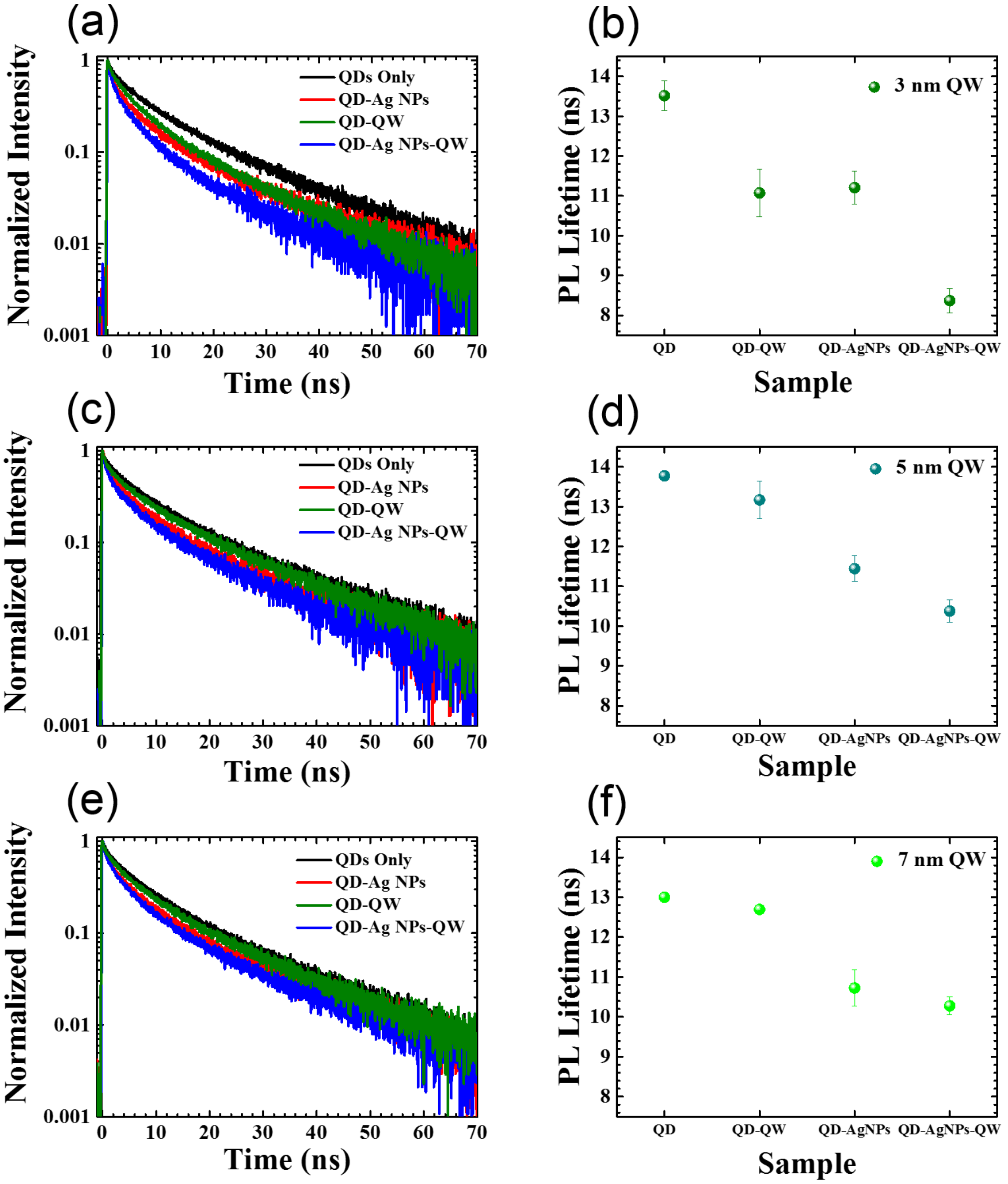

Figure 6.7: (a, c, e) Normalized PL decays of QDs Only in a PMMA layer on GaN (black line), QDs and Ag NPs in PMMA layer on GaN (red line), QDs in PMMA layer on QWs (green line) with barrier thicknesses of 3 nm, 5 nm and 7 nm in a, c and e, respectively, and QDs and Ag NPs in PMMA layer on QWs (blue line) with barrier thicknesses of 3 nm, 5 nm and 7 nm in a, c and e, respectively. (b, d, f) QD PL lifetimes extracted from bi-exponential fits of the corresponding decays in a, c and e, respectively.

$$\eta_{Plasmon} = 1 - \frac{\tau_{QD-Ag\ NPs-QW}}{\tau_{QD-Ag\ NPs}} \tag{6.5}$$

where $\tau_{QD-Ag\ NPs}$and $\tau_{QD-Ag\ NPs-QW}$ are the PL lifetimes of the QDs in a PMMA layer with Ag NPS on GaN (QD-Ag NPs) and the QDs in a PMMA layer with Ag NPs on the QW (QD-Ag NPs-QW), respectively.

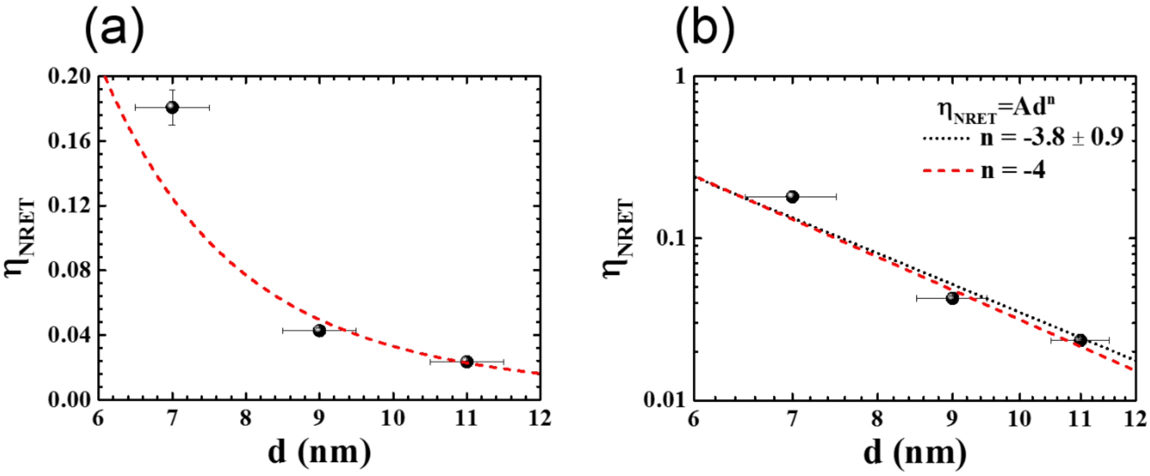

Figure 6.8: (a) NRET efficiency, η_{NRET}, as a function of centre-to-centre distance, d, between the QDs and the QW. The dashed red line is a fit to Equation 6.3. (b) Logarithmic plot of the measured NRET efficiency, η_{NRET}, and fit to a power law revealing the d^{-4} distance dependence. The dotted black line is a free fit to the data while the red dash line is a power law fit with a fixed n value of -4 illustrating the agreement between the ideal case and the experimental data.

Similar to the direct QD-QW NRET efficiencies in Figure 6.8, the plasmon mediated NRET efficiencies in the QD-Ag NPs-QW structure are plotted as a function of centre-to-centre separation, d, on a linear scale in Figure 6.9a and logarithmic scale in Figure 6.9b. The dashed red line in the linear plot of the plasmon mediated NRET efficiency, $\eta_{Plasmon}$, in Figure 6.9a is a fit to Equation 6.3 with $k = 1.6 \times 10^{-3} nm^{-4}$, revealing a smaller k value than the direct QD-QW case, and gives a larger R_0 value of 5 nm. The free fit (dotted black line) to the power law in Figure 6.9b with $n = -3.9 \pm 0.2$ is very close to the ideal fit of $n = -4$ (dash red line), revealing that the plasmon mediated NRET also follows a d^{-4} dependence. It should also be noted that this is the first experimental demonstration of plasmon mediated NRET in QD-QW systems.

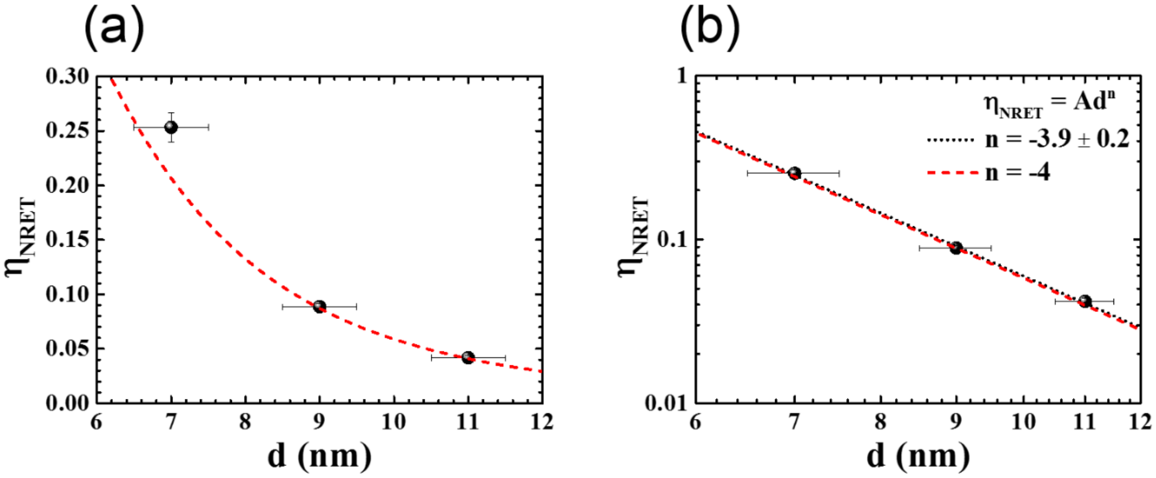

Figure 6.9: (a) Plasmon-mediated NRET efficiency, η_{NRET}, as a function of centre-to-centre distance, d, between the QDs and the QW. The dashed red line is a fit to Equation 6.3. (b) Logarithmic plot of the measured NRET efficiency, η_{NRET}, and fit to a power law revealing the d^{-4} distance dependence. The dotted black line is a free fit to the data, while the red dash line is a power law fit with a fixed n value of -4 illustrating the agreement between the ideal case and the experimental data.

The reduction of the k value in the case of the plasmon mediated NRET, where, $k = 2/c_{Acc}\pi R_0^6$, signifies an increased value of c_{Acc} or R_0 or both.[50,87] However, the same QW sample was used for all measurements presented here, for both the QD-QW and the QD-Ag NPs-QW studies. Therefore, the decrease in the value of k must correspond to an increase in the Förster radius, R_0, and not to an increase in the acceptor concentration, c_{Acc}. Given that the distance dependence of the NRET efficiency in the QD-Ag NPs-QW samples follows the same d^{-4} dependence as the QD-QW samples, combined with the increase of R_0 in the presence of the Ag NPs signifies that the coupled QD-Ag NPs can be considered as an enhanced donor dipole, in agreement with similar reports of plasmon mediated NRET in QD pairs.[43,53]

The presence of the Ag NPs in the hybrid system not only helps to increase the Förster radius, R_0, from 4.3 nm to 5 nm, but also increases the NRET efficiency from the QDs to each of the different barrier thickness QWs. For the 3 nm barrier QW the NRET efficiency is increased from (18.1 ± 1.1)% without the Ag NPs to (25.3 ± 1.3)% with the Ag NPs. Similarly, the NRET efficiency from the QDs to the 5 nm and 7 nm barrier QWs is increased from (4.3 ± 0.2)% to (8.9 ± 0.3)% and (2.3 ± 0.3)% to (4.2 ± 0.2)%, respectively, due to the presence of the Ag NPs. However, despite the presence of NRET in the hybrid structures there was no enhancement of the QW PL intensity. This may be due to the close proximity between the active region and the Ag NPs in the PMMA layer with the QDs which could lead to quenching of the QW emission by the Ag NPs. It should also be noted that there was large variation in the QW PL intensity (~ 15%) across the samples. This variation in the QW PL intensity makes it difficult to accurately quantify any enhancements, especially in the case of the direct QD-QW samples as the variation in the PL intensity is of the same magnitude as the NRET efficiency. While increasing the centre-to-centre distance between the QW and the Ag NPs (as for the 5 nm and 7 nm barrier QWs) reduces the quenching of the QW PL,[53] the NRET efficiency is much lower than the variation in the QW PL intensity (~ 15%) and as such hinders the observation of any enhancement of the QW PL.

6.4 Summary of Colloidal Ag NP System

The colloidal samples presented here in section 6.3 have demonstrated significant NRET efficiencies and strong interactions in QD donor and QW acceptor pairs following the fabrication of hybrid QD-QW and QD-Ag NPs-QW structures through simple and industrially scalable processing techniques. However, there is still significant room to improve the hybrid systems. The samples presented in section 6.3 utilize a mixed layer of QDs and Ag NPs which sit side by side in the PMMA layer. Some aggregation of the Ag NPs at the surface of the PMMA layer arises from issues regarding the compatibility of the Ag NPs surface ligands with the polymer. Ideally, it would be of significant benefit to isolate the Ag NPs which would avoid aggregation and simultaneously increase the magnitude of, and sharpen the LSPR, leading to a stronger interaction. To overcome issues regarding the uniformity of the QD and Ag NP deposition, other coating techniques could be considered, such as Langmuir-Blodgett techniques.[180,256] Similarly, wet-coating processes can be combined with chemical functionalization of the QW surface to produce ordered arrays of QDs and NPs.[257] However, this planar geometry of the QD-Ag NP layer, where the QDs and Ag NPs rest in the same plane, is not the optimal geometry for enhanced NRET. The optimal configuration incorporates a 180° separation between the donor, plasmonic NP and the acceptor.[42,43] In terms of an optoelectronic device, it would be of interest to investigate the role of NRET on the extraction of generated photocurrent in such a hybrid system. The reduction of the QD lifetime on the QW verifies the presence of NRET in the hybrid system despite the lack of an observable increase in the QW PL intensity. However, an increase in PL intensity is dependent on the increased recombination rate of charge carriers whereas the photocurrent is dependent on the separation and extraction of the charge carriers. These are two different processes and it is of interest to investigate whether or not the energy that has been transferred into the acceptor from the donor through NRET can be extracted electrically. This issue will be discussed in further detail in Chapter 7 and Chapter 8. These QWs, however, cannot be electrically contacted following the growth of the wafer and as such further investigation of the effect of NRET on the photocurrent would require purpose built QW devices, which is beyond the scope of this study.

6.5 Nonradiative Energy Transfer with Lithographically Defined Ag Nanoparticle Arrays

Two different lithographically defined arrays of Ag nanostructures, labelled nanobox and nanodisc, were chosen and fabricated using electron beam lithography (EBL) to investigate plasmon mediated NRET from the QDs to a QW. These nanobox and nanodisc arrays were chosen following the simulation of the array extinction, scattering and absorption spectra using Finite-Difference Time-Domain (FDTD) commercial software. The simulated extinction spectra of both arrays revealed good spectral overlap with the QD PL spectrum. The arrays were fabricated on the 3 nm QW and also on the GaN substrate to provide a reference for the QDs only and the QD-Ag NP Array. A schematic diagram of the arrays on the QW, including structural dimensions, is given in Figure 6.10.

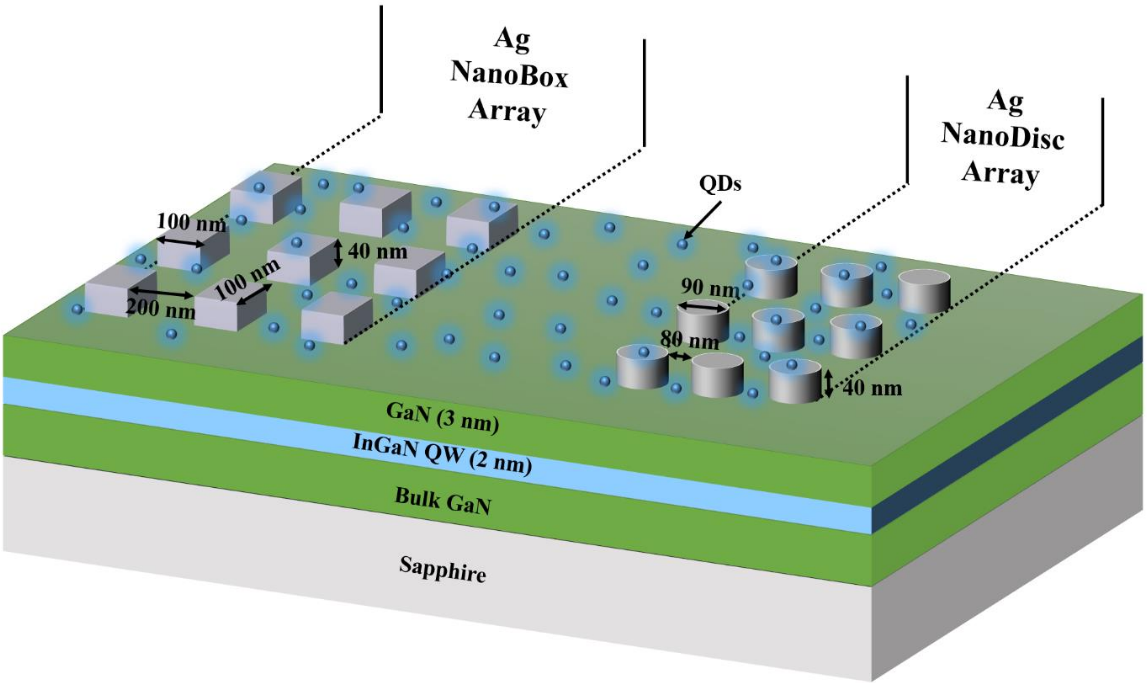

Figure 6.10: Schematic diagram of AgNP arrays on InGaN/GaN QW. The arrayed Ag nanostructures have a total height of 40 nm, consisting of a 5 nm Ti adhesion layer (not shown in the diagram) beneath the 35 nm Ag structure.

The nanobox and nanodisc arrays were fabricated by patterning a PMMA resist using EBL. The patterned resist was then developed by immersion in methyl-isobutyl ketone (MIBK) and IPA (1:3 MIBK:IPA). The Ti/Ag (5 nm/35 nm) metal was deposited using electron beam evaporation. The 5 nm Ti layer is incorporated as an adhesion layer and the 35 nm thick Ag nanobox/nanodisc nanostructures are the active plasmonic elements. The FDTD simulations of the structures have included the Ti adhesion layer and the effects of the layer have been accounted for. The resist was removed following the deposition of the metal using a standard lift-off process in acetone, leaving only the Ag nanobox/nanodisc arrays on the QW/GaN surface. Following the fabrication of the nanobox and nanodisc arrays on the 3 nm barrier QW and the GaN, SEM images were recorded to verify the successful fabrication of the arrays. The SEM images of the nanobox and nanodisc arrays can be seen in Figure 6.11a and 6.11b, respectively.

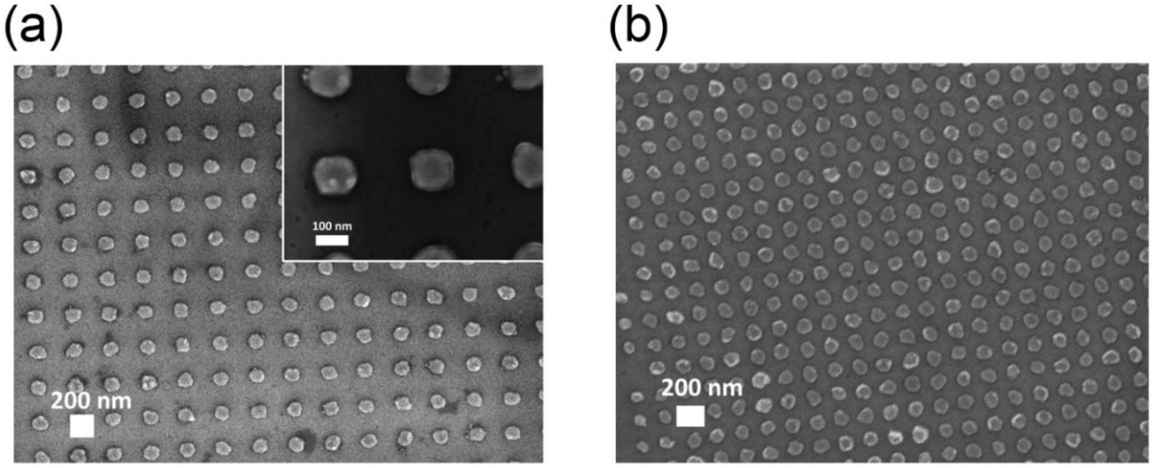

Figure 6.11: SEM images of (a) nanobox array, and (b) nanodisc array. Inset in (a) shows a zoomed in image of the nanobox array to illustrate the box-like shape of the nanostructures.

Both the nanobox and nanodisc arrays are comprised of 200 x 200 units, giving total areas of 60 µm x 60 µm and 34 µm x 34 µm, respectively (structural dimensions are given in Figure 6.10). The SEM images in Figure 6.11 show that the fabrication of structures with dimensions close to the limitations of EBL suffer from a lack of definition. However, in arrayed structures of plasmonic NPs, the plasmonic response depends not only on the individual response from each NP but also on the overall array geometry.

As mentioned above the dimensions of the nanobox and nanodisc arrays were chosen based on the simulated extinction, absorption and scattering spectra under plane-wave excitation conditions using FDTD commercial software. The simulations were performed in-house by Dr. Graham Murphy and Dr. Vasilios Karanikolas. The material parameters used for the simulations are as follows; the wavelength dependent dielectric permittivity, ε, of the Ti and the Ag are included in the simulation using the experimentally measured data [227], while the GaN and PMMA layers are modelled using constant dielectric permittivity of $\varepsilon_{GaN} = 5.35$[258] and $\varepsilon_{PMMA} = 2.2$,[259] respectively.

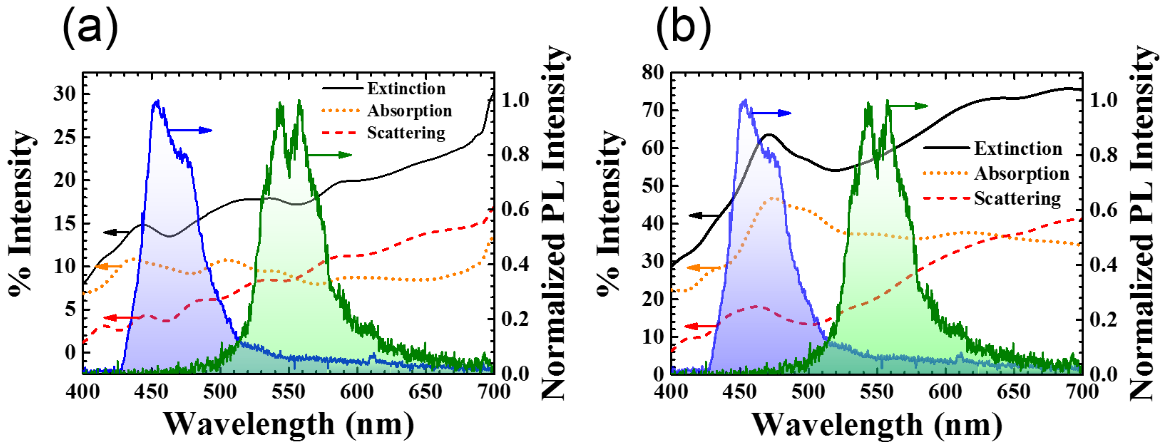

Figure 6.12: Normalized PL spectra of the QDs (blue line) and the 3 nm barrier QW (olive line). Extinction (black line), absorption (orange dot) and scattering spectra (red dash) of the nanobox array in (a) and the nanodisc array in (b).

The extinction, absorption and scattering spectra of the nanobox and nanodisc arrays are shown in Figure 6.12a and 6.12b, respectively. The QD and QW PL spectra are also shown in both panels to indicate the overlap between the QD and QW PL and the nanobox/nanodisc extinction spectra. Considering first the magnitude of the extinction for both NP arrays, the nanodisc array shows a much higher extinction value than the nanobox array at the QD peak emission wavelength (~450 nm), arising from the dense arrangement of the nanodiscs with a separation between elements of 80 nm as compared with a separation of 200 nm between each element in the nanobox array. This large extinction and, consequently, absorption at the peak QD emission wavelength results in strong quenching of the QD PL lifetime and intensity compared with the nanobox array.

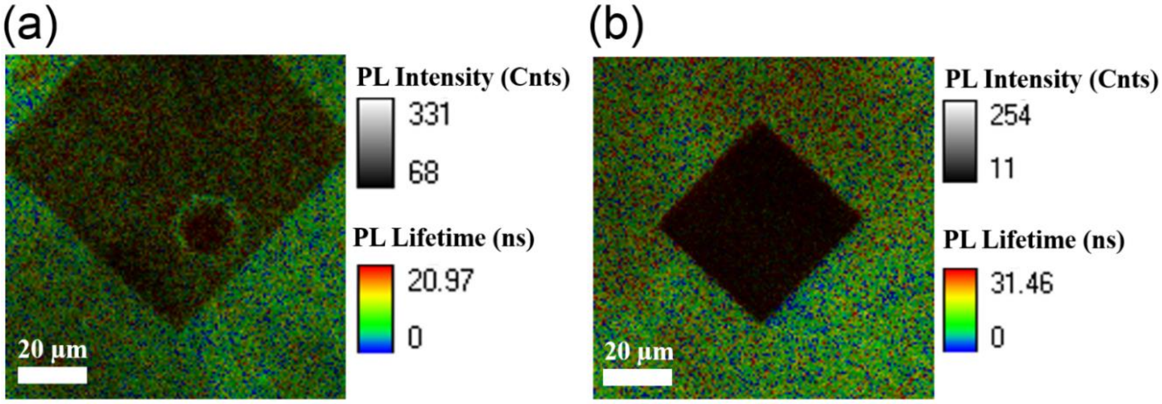

Figure 6.13: FLIM images of (a) nanobox array and (b) nanodisc array on the 3 nm barrier QW.

Similar to section 6.3 the interaction between the QDs and the QW was investigated using spectral and time-resolved PL (TRPL) measurements. The concentration of QDs used in this section has been reduced from $2.4 \times 10^{20} m^3$ with the colloidal Ag NPs to $6.0 \times 10^{19} m^3$ to ensure monolayer coverage and avoid clumping of the QDs around the plasmonic NPs during the spin coating process, given that the QD/PMMA layer thickness is smaller than the height of the Ag NPs. Following the deposition of the QDs in a PMMA layer on the QW, fluorescence lifetime imaging microscopy (FLIM) was used to record images of interaction between the QDs and each array over 80 µm x 80 µm areas. The FLIM images of the QDs on the nanobox and the nanodisc arrays (both on the QW) can be seen in Figure 6.13. It is instantly apparent that the QD PL intensity is substantially lower on the nanodisc array compared with the nanobox array, as expected. However, given that these arrays are also on the QW this is indicative of not only quenching of the QD PL to the arrays but also of NRET to the QW. To accurately characterize this system, PL and TRPL measurements were recorded over 20 µm x 20 µm areas in the centre of the arrays and 20 µm x 20 µm areas on the GaN/QW beside the arrays, giving reference positions of "on" and "off" the arrays. This gives four samples for each array; QDs on GaN (QDs Only), QDs on nanoboxes/nanodiscs on GaN (QD-NB/ND), QDs on QW (QD-QW), and QDs on nanoboxes/nanodiscs on QW (QD-NB/ND-QW).

The quenching of the QDs by the nanobox/nanodisc array is quantified from the PL lifetimes as

$$\eta_{Quench} = 1 - \frac{\tau_{QD-Array}}{\tau_{QD}} \tag{6.6}$$

where τ_{QD} and $\tau_{QD-Array}$ are the QD PL lifetime "off" the array on GaN and the QD PL lifetime "on" the nanobox/nanodisc array on GaN, respectively. Depending on the array being studied, the array term in Equation 6.6 will be replaced with NB (nanoboxes) or ND (nanodiscs). The direct NRET from the QD to the QW is given by Equation 6.2, similar to the colloidal samples in section 6.3. The plasmon mediated NRET from the QDs to the QW is given by

$$\eta_{Plasmon-Array} = 1 - \frac{\tau_{QD-Array-QW}}{\tau_{QD-Array}} \tag{6.7}$$

where $\tau_{QD-Array-QW}$ is the QD PL lifetime on the nanobox/nanodisc array on the QW.

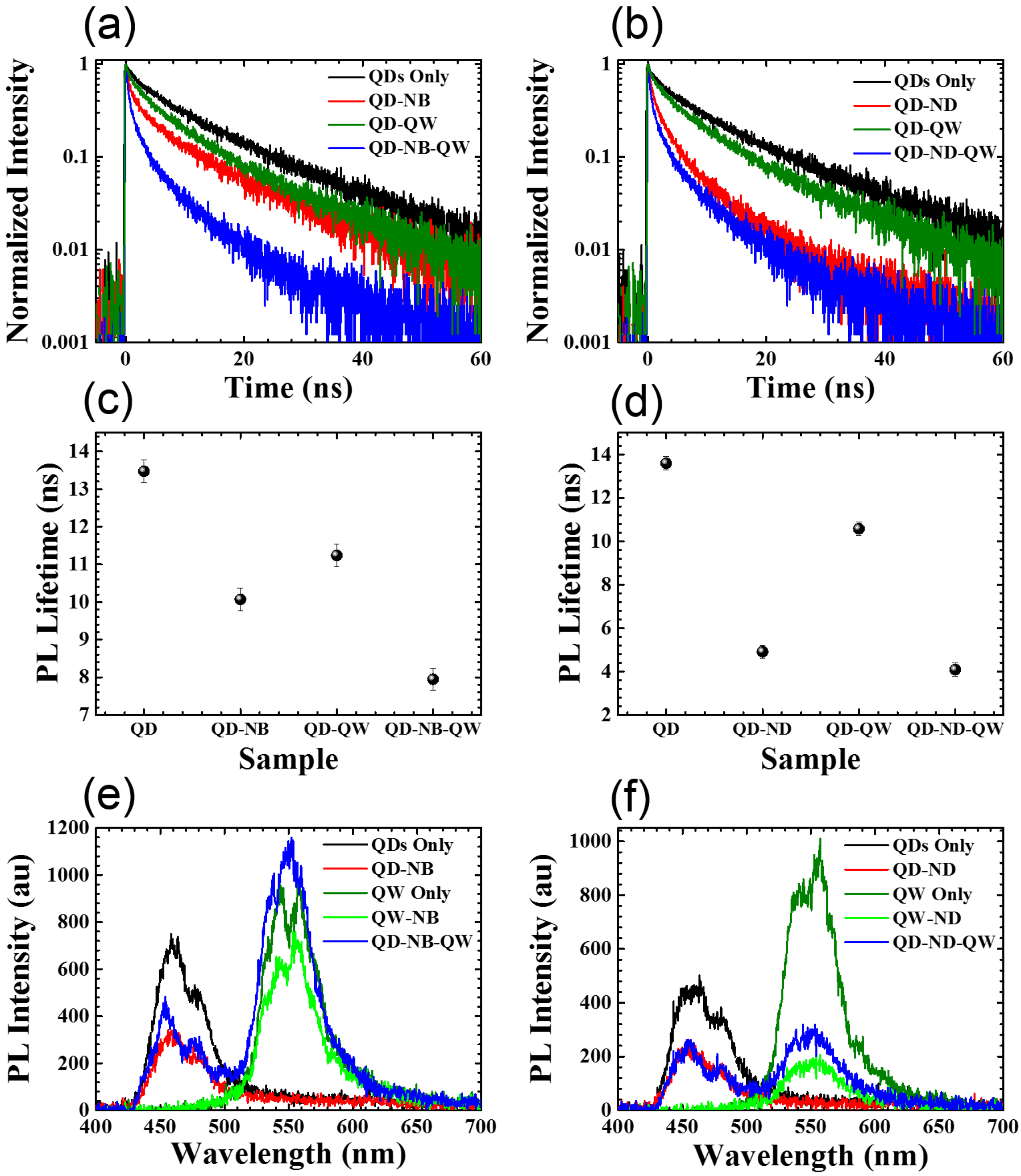

Figure 6.14: (a) [b] PL decays of QDs only on GaN (black line), QDs on the nanobox [nanodisc] array on GaN (red line), QDs on the QW (green line), and QDs on the nanobox [nanodisc] array on the QW (blue line). (c) [d] PL lifetimes extracted from bi-exponential fits to the PL decays in (a) [b]. (e) [f] PL spectra of QDs only (black line), QDs on the nanobox [nanodisc] array on GaN (red line), QW only (olive line), QW with nanobox [nanodisc] array (green line), and QDs on the nanobox [nanodisc] array on the QW (blue line).

The normalized QD PL decays for the nanobox and nanodisc samples are presented in Figure 6.14a and Figure 6.14b, respectively. There is a clear reduction of the QD PL decay lifetime, relative to the QD Only, for each of the sample combinations. Consider first the interaction between the QDs and the arrays, represented by a change from the black line (QDs Only) to the red line (QDs-NB/ND) in the PL decay plots. There is a much stronger interaction between the QDs and the nanodiscs compared with the nanoboxes, in agreement with the larger extinction (Figure 6.12) and the stronger quenching in the FLIM images (Figure 6.13). This strong interaction is further clarified in terms of the PL lifetimes in Figure 6.14c and 6.14d. It is also clear from the PL decays that there is a further reduction in the lifetimes on the arrays on the QW, indicating the presence of plasmon mediated NRET.

The measured PL lifetimes for each of the sample configurations, presented in Figure 6.14c and Figure 6.14d, were then used to quantify the NRET efficiency. The NRET efficiencies for the configurations with the nanobox arrays are as follows: using Equation 6.6, the NRET from the QDs to the nanobox array gives an efficiency, η_{Quench}, of (25 ± 1)%; using Equation 6.2 the direct NRET from the QDs to the QW has an efficiency, η_{QD-QW}, of (17 ± 1)%; and using Equation 6.7 the plasmon mediated NRET from the QDs to the QW has an efficiency, $\eta_{Plasmon-NB}$, of (21 ± 1)%. Similarly the same equations are used to calculate the efficiency of the NRET for the configurations with the nanodisc arrays, where the NRET from the QDs to the nanodisc array has an efficiency, η_{Quench}, of (64 ± 4)%, the direct NRET from the QDs to the QW has an efficiency, η_{QD-QW}, of (22 ± 1)%, and the plasmon mediated NRET from the QDs to the QW has an efficiency, $\eta_{Plasmon-ND}$, of (17 ± 2)%. A comparison of the NRET efficiencies measured on each array will be discussed in further detail below.

The PL spectra for the nanobox and nanodisc sample configurations are presented in Figure 6.14e and Figure 6.14f, respectively. There is a similar level of reduction in the intensity of the QD PL spectrum on both the nanobox and nanodisc arrays (red line) compared to the QDs Only spectrum (black line) in each case. The intensity of the QW Only PL spectrum (olive line), however, is much more strongly quenched by the nanodisc array in Figure 6.14e compared with the nanobox array in Figure 6.14f (green lines). This is due to the close proximity (80 nm) of the elements in the nanodisc array. Considering the PL spectrum of the hybrid QD-Array-QW (blue line) structure, there is an increase in the QW PL for both arrays compared with the QW-Array (green line). In the case of the nanoboxes (Figure 6.14e), the QD-NB-QW PL spectrum (blue line) has a slightly larger intensity compared with the QW Only spectrum (olive line), revealing a slight enhancement of the acceptor (QW) PL intensity due to the plasmon mediated NRET. However, in the case of the nanodiscs, while there is an enhancement of the QW PL intensity in the QD-ND-QW PL spectrum (blue line) compared with the QW-ND spectrum (green line), the PL intensity does not recover to the initial QW Only PL intensity (olive line). The larger quenching of the QW PL intensity on the nanodiscs compared with the nanoboxes is consistent with the simulated extinction data presented in Figure 6.12, where the magnitude of the extinction for the nanodisc arrays at the QW peak emission wavelength is ~3 times larger than that for the nanobox arrays.

The NRET efficiencies and NRET rates for the QD-QW, QW-Array and QD-Array-QW sample configurations as a function of array structure (nanobox/nanodisc) are presented in Figure 6.15a and Figure 6.15b, respectively. From the NRET efficiencies plotted in Figure 6.15a it is clear that the largest NRET efficiency for both the nanobox and nanodisc arrays, occurs between the QDs and the arrays. The NRET efficiency for the hybrid QD-NB-QW with the nanobox array is larger than the direct QD-QW NRET efficiency revealing the plasmon enhanced NRET with the nanobox structures. However, in the case of the nanodisc array, the NRET efficiency of the hybrid QD-ND-QW structure is less than the direct QD-QW NRET efficiency, thus revealing that the nanodisc array hinders the full potential of the NRET due to large extinction associated with the structures (Figure 6.12).

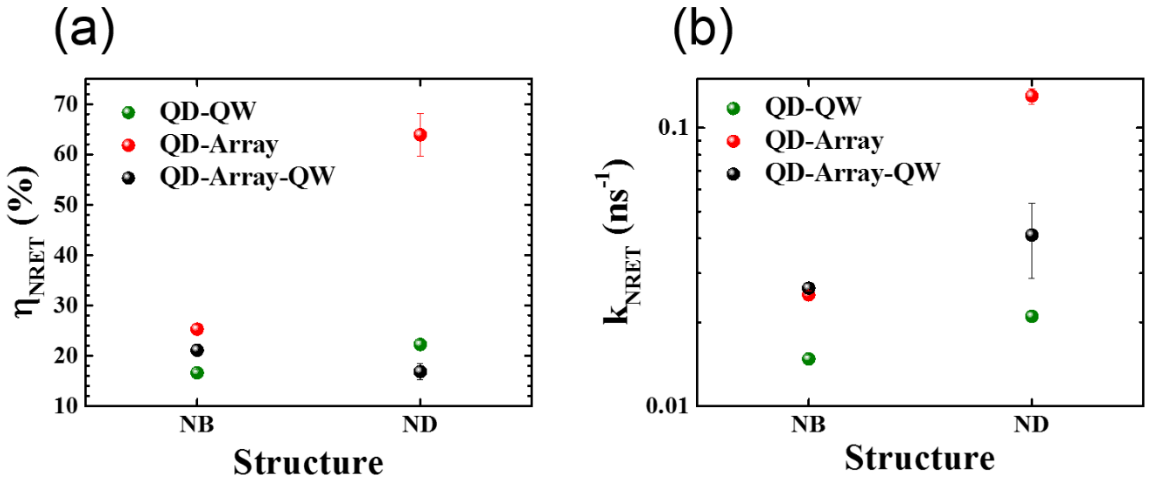

Figure 6.15: (a) NRET efficiencies as a function of structure for QD-QW (green circle), QD-MNP array (red Circle) and the hybrid QD-MNP Array-QW structure (black dot). NRET rates as a function of structure for QD-QW (green circle), QD-MNP array (red Circle) and the hybrid QD-MNP Array-QW structure (black dot).

Further insight can be gained by examining the NRET rates as a function of array structure, plotted in Figure 6.15b. The NRET rate from the QDs to the nanodisc array is fastest, corresponding to the highest efficiency in Figure 6.15a. This fast NRET rate from the QDs to the nanodisc array reveals that the low NRET efficiency in the plasmon mediated NRET (QD-ND-QW) is due to the inability of the plasmon mediated NRET rate to compete with the NRET rate to the array (QD-ND). The NRET rate from the QDs to the nanodisc array (QD-ND) is more than 3 times faster than the plasmon mediated NRET rate in the complete structure (QD-ND-QW). In terms of the nanobox array, the NRET rates for both the QD-NB and the QD-NB-QW are similar, allowing for competition between plasmon mediated NRET to the QW (QD-NB-QW) and quenching by the array (QD-NB), ultimately resulting in a larger NRET efficiency in the plasmon mediated configuration. However, further adjustments of the nanoparticle structure and the choice of metal combined with a better understanding of the balancing between the rate of NRET (quenching) to the metal and the plasmon mediated NRET rate could lead to significant improvements in the magnitude of the plasmon mediated NRET efficiency, and ultimately lead to a greater enhancement of the acceptor PL intensity.

Other studies have shown that the absorption and scattering profiles of metal NP arrays can be altered significantly by tailoring the size, shape and spacing between the individual plasmonic elements.[260] These modifications to the plasmonic arrays can lead to substantial variations in QD and QW emission. Optimization of the NP arrays could lead to an enhancement of the QW emission due to plasmon mediated NRET, relative to the direct enhancement of the QW emission due to the presence of the NRET from QDs alone. However, further modelling, simulation, fabrication and experimental verification of a large range of plasmonic structures could be undertaken to develop this approach to light harvesting devices. The lack of the acceptor PL enhancement observed in this study, despite the significant NRET efficiencies raised the question of whether energy that has been transferred into the acceptor material, while not observed optically in terms of an acceptor enhancement, can be extracted electrically. This is a very important question for future applications, which is pursued in the following chapters.

6.6 Conclusion

This chapter has demonstrated the NRET from alloyed CdSeS/ZnS semiconductor nanocrystal QDs to InGaN/GaN QWs with GaN barrier thicknesses of 3 nm, 5 nm, and 7 nm. The QWs with different barrier thicknesses allowed for a distance dependence study of the direct QD-QW NRET. The distance dependence of the NRET was found to follow a characteristic d^{-4} dependence of NRET from point dipoles (QDs) to a plane (QW), validating that the acceptor (QW) dimensionality determines the distance dependence.[83]

The work carried out in this chapter demonstrated the first case of plasmon mediated NRET from QDs to a QW, utilising both colloidal Ag NPs and lithographically defined arrays of Ag NPs. Colloidal Ag NPs were used to perform the distance dependence study of NRET, ultimately verifying the d^{-4} distance dependence of the plasmon mediated NRET from the QDs to the planar QW. This is the same distance dependence as explained by conventional Förster-type NRET theory from a point dipole donor to a 2D plane of acceptors, but with a larger interaction distance, indicating that the coupled QD-Ag NP is acting as an enhanced donor dipole.[43,53] Despite the presence of the NRET in the system, no enhancement of the acceptor (QW) PL was observed. Nonetheless, fine tuning of the plasmonic elements in the system in terms of the uniformity of the colloidal Ag NPs and the geometry of the NPs could lead to far greater NRET efficiencies and enhancement of the acceptor PL intensity.

In terms of lithographically defined arrays of Ag NPs, two structures were chosen, nanoboxes and nanodiscs. Significant differences were observed between both arrays indicating that further tuning of the plasmonic elements in the arrays could lead to substantial improvements in the NRET efficiency, and, similarly, the enhancement of the QW emission. There was a stronger interaction between the nanodisc array and both the QDs and QW compared to the nanobox array. However, the strong interaction between both the emitting species and the plasmonic array lead to significant quenching by the metal that ultimately limited the efficiency of the NRET process. The nanobox array, however, demonstrated a weaker interaction with both the QDs and the QW, but given that the quenching to the metal was less influential, this led to an overall enhancement of the QW emission and a larger plasmon mediated NRET efficiency compared to the nanodisc array. The variation in the interactions observed across just two arrays indicates that the scope for optimization and tunability of performance *via* the structure size, shape and spacing.

Chapter 7

Dependence of MoS_2 Film Quality for Photocurrent Enhancements in QD-Sensitized MoS_2 Devices

Chapter Summary

This Chapter will focus on NRET from alloyed semiconductor nanocrystal CdSeS/ZnS QDs with a peak emission wavelength of 630 nm to MoS_2 devices, and the photocurrent enhancements that arise. The MoS_2 devices consist of varying layer thickness and crystalline properties, including pristine monolayers, mixed monolayer/bilayer, polycrystalline bilayers and bulk-like thicknesses. The large-area MoS_2 films were grown on Si/SiO_2 substrates by chemical vapor deposition (CVD) by our collaborators in the Duesberg group, TCD. The hybrid QD-sensitized MoS_2 devices were realised by spin coating an ultrathin layer of QDs in PMMA on the chip containing the devices. NRET from the QDs to the MoS_2 devices was studied using time-resolved photoluminescence (TRPL) and quantified through the reduction in the QD (donor) lifetime in the presence of the MoS_2 (acceptor) devices. The photocurrent was measured from the MoS_2 devices before and after adding the QD sensitizing layer, as a function of excitation power.

The electrical devices were fabricated by patterning a PMMA resist using electron beam lithography (EBL). The Ti/Au (5 nm/ 45 nm) contact pads and electrodes were deposited using electron beam evaporation. The contact pads have dimensions of 80 µm x 80 µm and each device has a 5 µm channel length between the electrodes. All MoS_2 devices discussed in this chapter were grown on the same Si/SiO_2 chip in a single growth process, these devices were also patterned in a single EBL run.

7.1 Introduction

Over the past decade there has been a plethora of research involving 2D materials. In particular, the transition metal dichalcogenide (TMD) family of materials has been the subject of substantial investigation driven by their favorable optical and electrical properties.[61–63,261] A lot of this interest arises due to the fact that the layered materials' electronic bandgap transitions from an indirect bandgap at a few-layer thickness to a direct bandgap at monolayer thickness.[61,63] The presence of a direct optical bandgap in the TMD monolayers paves the way for promising applications for 2D materials in optoelectronic devices such as phototransistors[262–264] and photodetectors.[265] Early studies using these devices were most commonly composed of few-layer and monolayer MoS_2 flakes obtained from mechanical exfoliation techniques, a process that is not particularly scalable or reproducible. However, bottom-up approaches such as CVD are more desirable as these methods can achieve larger area coverage of monolayer and few-layer regions of the active material on the substrate in a single growth process.[198,266]

One substantial drawback with 2D materials is the low absorption of incident light, resulting from the atomic thickness of the active region. Low light absorption limits both the performance and efficiency of the device. A common and simple method used to increase the absorption of incoming light is to incorporate a sensitizing layer on top of the active region. There have been a few reports of dye sensitized[267] and QD sensitized[268,269] MoS_2 photodetectors in the literature. However, these demonstrations have focussed on devices that consist of mechanically exfoliated MoS_2, and the energy transfer mechanism from the sensitizing species was that of charge transfer. Although charge transfer is an efficient energy transfer process, charge transfer has a stringent distance dependence (< 3 nm) and will only occur if the donor and acceptor carrier wavefunctions overlap.[68,90]

In comparison to mechanical exfoliation techniques, CVD-grown films of MoS_2 provide large-area coverage of monolayer and mixed layer MoS_2 on the substrate. This provides a quicker, cheaper and more suitable method for industrial processing. Furthermore, the energy transfer mechanism implemented in this work is that of NRET. In contrast to charge transfer, while NRET also has a well-defined distance dependence the distances over which it can occur extend beyond the limits of charge transfer to ~10 nm.[82,85] One of the goals of this work was to utilize commercially scalable techniques such as CVD growth of the MoS_2 and spin coating of the QD sensitizing layer to demonstrate the viability of these devices for commercial applications.

It can also be noted that recent studies demonstrated highly efficient NRET from semiconductor QDs to mono- and few-layer MoS_2.[65–67,247] These demonstrations have shown that the NRET efficiency increases as the number of layers of MoS_2 decreases, in contrast to the trend observed for NRET to graphene.[66] The increase in the NRET efficiency as the number of MoS_2 layers decreases is attributed to the reduced dielectric screening of the QD electric field in monolayer MoS_2.[65,66]

The work in this Chapter addresses how the performance of the hybrid devices varies as the MoS_2 channels gradually change from pristine monolayers to more polycrystalline channels. The degree of crystallinity of the MoS_2 channels was identified using Raman and photoluminescence (PL) mapping and the MoS_2 layer thicknesses were determined using Raman spectroscopy. As will be seen later in this chapter, the largest photocurrent enhancements are observed for the pristine monolayer devices, after the addition of the QDs, and little to no enhancement for the polycrystalline and bulk-like thickness devices. This indicates that the NRET from the QDs has less impact on the extracted photocurrent of polycrystalline and bulk-like thickness samples.

7.2 Initial Characterization

7.2.1 Absorption and Spectral Photoluminescence

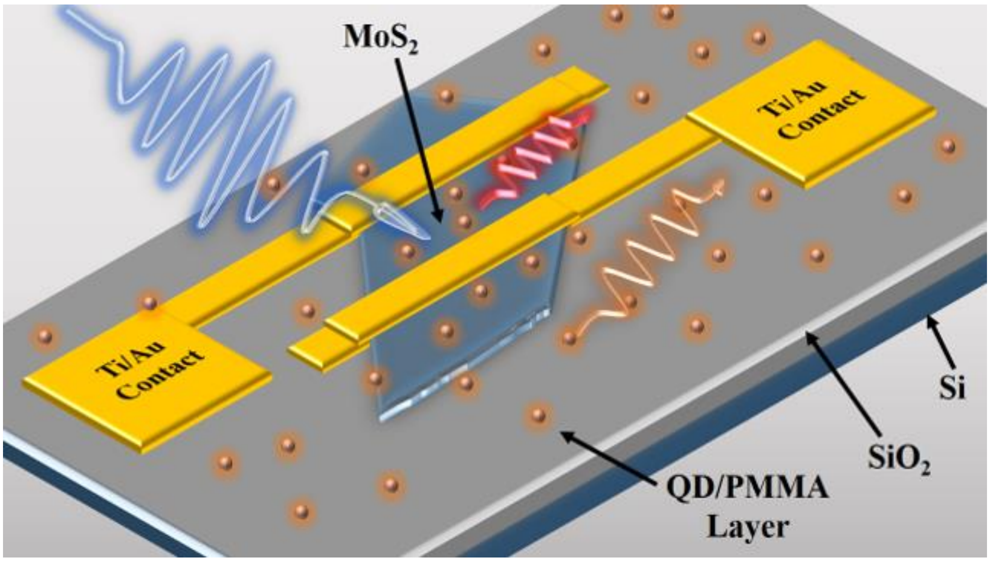

Figure 7.1: Schematic representation of the QD-sensitized MoS_2 device.

A schematic diagram of the hybrid QD-MoS_2 devices is presented in Figure 7.1. The alloyed CdSeS/ZnS QDs have a peak emission wavelength of 630 nm and a diameter of (6.0 ± 0.8) nm. The QDs were purchased in solution at a concentration of 1 mg/mL in toluene from Sigma-Aldrich, this solution was used as stock. The QD/PMMA dispersions were prepared by dispersing 12.5 μL of the QD stock solution in 500 μL of 0.1% wt. PMMA. The QD/PMMA solutions were then sonicated for ~20 s to ensure the even distribution of the QDs in the PMMA. The solution was spincast onto the chip containing the devices. The height of the QD/PMMA layer was found to be ~ (8 ± 2) nm, as verified by atomic force microscopy (AFM) measurements (See Figure 7.2). The layer thickness of ~8 nm verifies the presence of a monolayer of QDs on top of the devices.

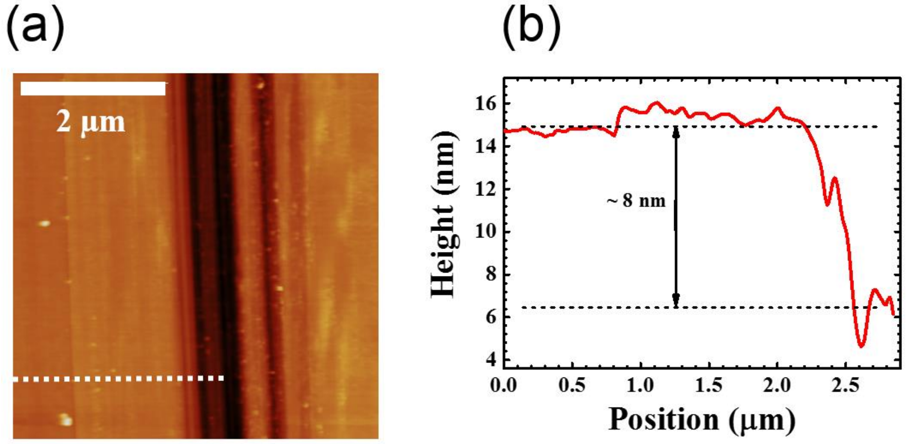

Figure 7.2: (a) AFM image of a single trench cut into the QD/PMMA layer. (b) Height profile corresponding to the white dash line in a.

The optical characteristics of monolayer MoS_2 and QDs in 0.1% wt. PMMA are shown in Figure 7.3. The CdSeS/ZnS QDs have a peak emission wavelength of 630 nm which overlaps well with the B exciton of the monolayer MoS_2 at ~630 nm. The monolayer MoS_2 has a peak emission wavelength of ~677 nm corresponding with the spectral position of the A exciton. The extinction spectrum of the monolayer MoS_2 was measured following the CVD of MoS_2 onto a quartz substrate, using a custom built transmission apparatus using a Xenon lamp and a 100x microscope objective as described in Chapter 3 (section 3.2.1).

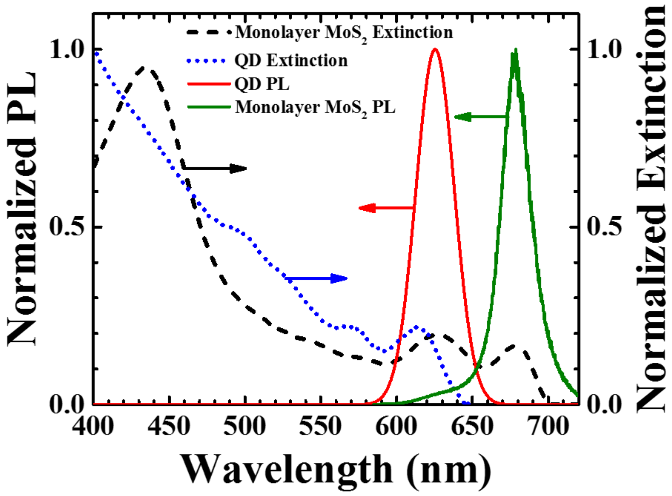

Figure 7.3: (a) Normalized extinction spectra of monolayer MoS_2 (black dash) and QDs in 0.1% wt. PMMA (blue dot) on the right axis, and normalized PL spectra of QDs in PMMA (red line) and monolayer MoS_2 (green line).

7.2.2 Raman Spectroscopy

The MoS_2 devices used in this study were characterised using Raman spectroscopy. A total of five devices were chosen for this study, labelled as D1-D5. These devices consist of pristine monolayer MoS_2 (D1), mixed monolayer and bilayer devices (D2 and D3), polycrystalline bilayer device (D4) and a bulk-like thickness device (D5). Devices, D2 and D3, both consist of a mix of monolayer and bilayer MoS_2, however, D2 has a greater abundance of monolayer material in the device channel while D3 has a greater abundance of bilayer material in the device channel. Optical images of the devices and the corresponding Raman maps can be seen in Figure 7.4. The Raman maps plot the separation between the characteristic in-plane, E, mode and the out-of-plane, A, mode. Raman spectroscopy is a proven technique for the identification of the layer thickness of MoS_2.[270,271] This is due to the change in the frequency of these characteristic modes as the MoS_2 layer number increases. The in-plane mode softens and red-shifts, while the out-of-plane mode stiffens and blue-shifts with increasing layers. This blue- and red-shifting of the out-of-plane and in-plane modes, respectively, as the MoS_2 layer number increases leads to an increasing separation between the A and E modes with increasing layer numbers.[270,271] The separation between the two Raman modes can then be used to identify the layer number of MoS_2 without the need for scanning probe microscopy techniques.

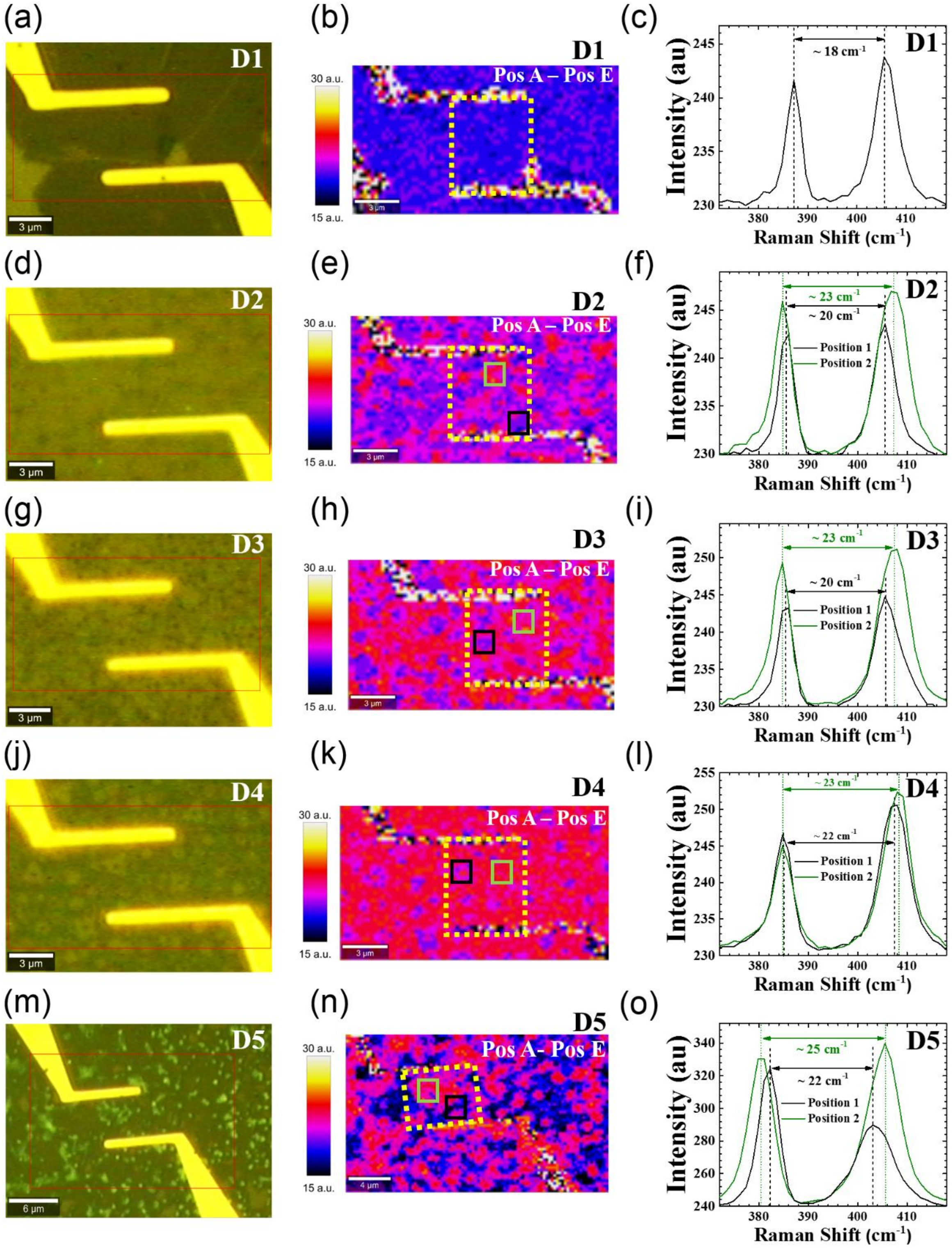

Figure 7.4: (a, d, g, j, m) Optical images of MoS_2 devices. (b, e, h, k, n) Corresponding Raman maps, plotting the separation between the characteristic *A* and *E* Raman modes. (c, f, i, l, o) Raman spectra extracted from the corresponding coloured squares in the Raman maps.

Optical images of the five devices (D1, D2, D3, D4 and D5) and the corresponding Raman maps are shown in Figure 7.4. The volume of bilayer MoS_2 is increasing across devices D1 to D4, moving from a purely pristine monolayer device, D1 (Figure 7.4a), to a polycrystalline bilayer device, D4 (Figure 7.4j). Devices D2 and D3 (Figure 7.4, panels d and g, respectively), are representative of intermediary phases between pristine monolayer and polycrystalline bilayer MoS_2. The red rectangle in each optical image indicates the region in which Raman and PL mapping were performed. It is clear from the optical images that the polycrystallinity of the devices is increasing from D1 to D4, with D1 showing a pristine and uniform channel area while D4 appears to have a multitude of nucleation points throughout the channel and a clear abundance of bilayer MoS_2. It is also worth noting that device, D3 (Figure 7.4g), has more bilayer regions in the channel than device, D2 (Figure 7.4d). It is also clear from the optical images that device D5 is several layers thick, resembling the appearance of bulk-like MoS_2 (Figure 7.4m).

Raman maps of the areas indicated by red boxes in the optical images are presented in Figure 7.4. These Raman maps plot the separation between the A and E peak positions in the MoS_2 Raman spectrum. Device D1 (Figure 7.4b) shows no variation in the peak position across the device, indicating the presence of a uniform and pristine layer. The corresponding Raman spectrum averaged over the region indicated by a dash yellow box (excluding the electrodes) in Figure 7.4b is given in Figure 7.4c, showing a separation between the A and E peaks of ~18 cm^{-1}, which is consistent with the presence of monolayer MoS_2.[270,271] The Raman maps of the mixed monolayer/bilayer devices in Figure 7.4, panels e and h, indicate the emergence of nucleation points of bilayer thicknesses through an increased separation between the A and E peaks.[270,271] The Raman spectra in Figure 7.4, panels f and i, are taken from the regions identified by black and green squares in Figure 7.4, panels e and h, respectively. The black and green line spectra are measured in the areas indicated by black and green squares, respectively. The regions indicated in black and green on both devices in

Figure 7.4, panels e and h, show a separation between the A and E peaks of ~20 cm^{-1} and ~23 cm^{-1}, respectively, indicating the presence of both monolayer and bilayer MoS_2.[270,271] The slight increase in the separation between the A and E peaks on the monolayer regions from 18 cm^{-1} on the purely monolayer device, D1 (Figure 7.4c), to a separation of 20 cm^{-1} on the devices containing a mixture of both monolayer and bilayer MoS_2, D2 and D3 (Figure 7.4, panels f and i), is attributed to signal mixing due to the small size of the grains on the devices. It should be noted that while both devices, D2 and D3, contain a mixture of monolayer and bilayer MoS_2, there is a larger proportion of bilayer MoS_2 in the channel of the device D3 (Figure 7.4h) as compared to device D2 (Figure 7.4e). The Raman map for device D4 (Figure 7.4k) again shows little variation in the separation between the A and E peaks. The corresponding Raman spectra (Figure 7.4l) reveal separations of ~22 cm^{-1} and ~23 cm^{-1} indicating that the majority of MoS_2 in the device channel is of bilayer thickness.[270,271] The channel in the bulk-like device (Figure 7.4n) consists mainly of bulk thicknesses with a separation between the A and E Raman peaks of ~25 cm^{-1}, with a small region of bilayer thickness, having a separation between the A and E Raman peaks of ~22 cm^{-1}.

7.3 Nonradiative Energy Transfer

7.3.1 Photoluminescence Mapping

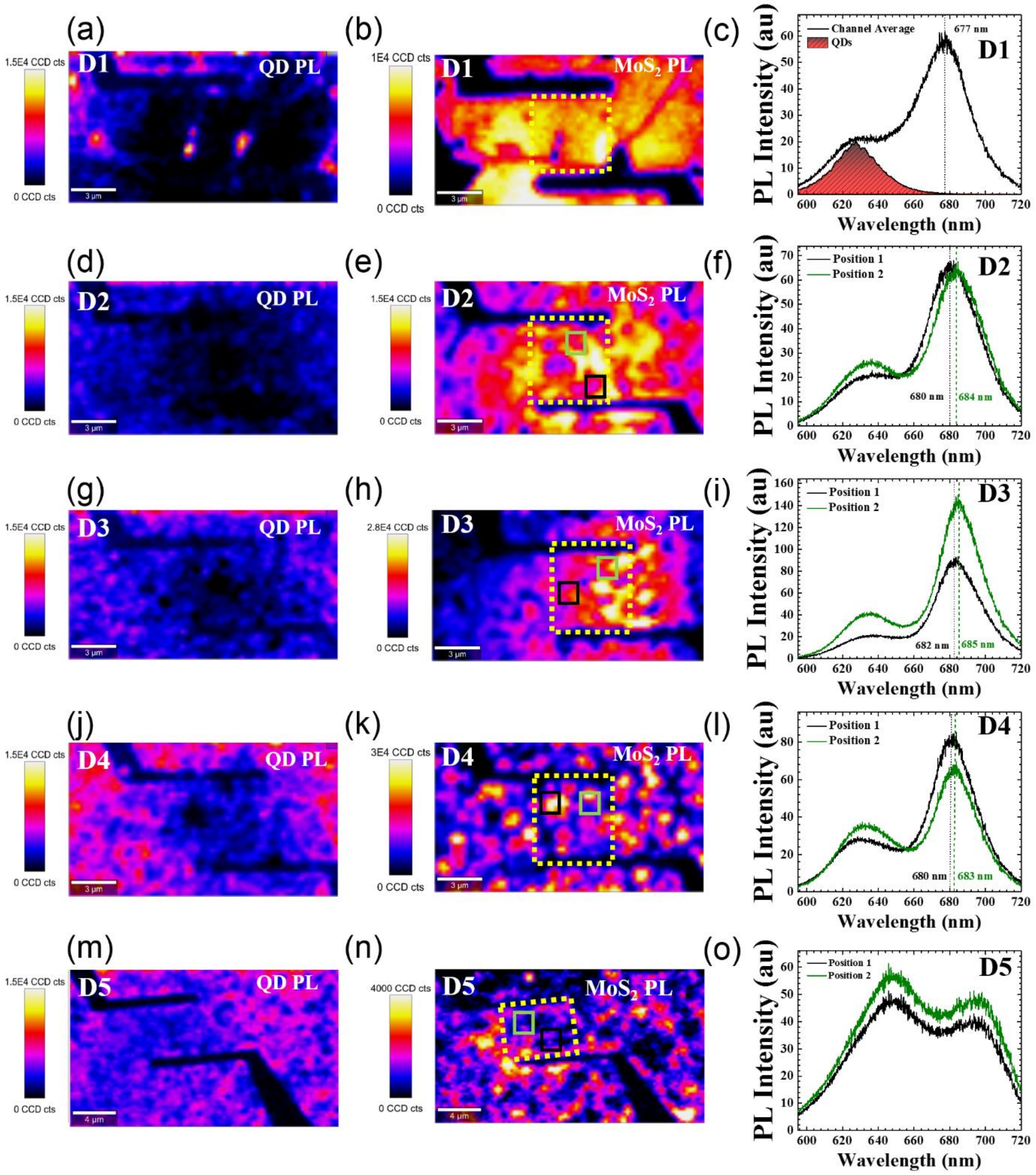

Figure 7.5: (a, d, g, j, m) PL maps centered on the QD peak emission wavelength. (b, e, h, k, n) PL maps centered on the MoS$_2$ peak emission wavelength. (c, f, i, l, o) PL spectra extracted from the regions indicated in blue and green squares in the PL maps.

The strong interaction between the QDs and the MoS_2 devices was verified optically using PL mapping after adding the QD sensitizing layer. The PL maps of each device and the corresponding PL spectra are shown in Figure 7.5. These PL maps help not only to identify the MoS_2 emission intensity and peak wavelength, but they can also reveal information regarding the interaction between the QDs and the MoS_2, such as quenching of the QD PL which is indicative of NRET. The QD PL maps for each device can be seen in Figure 7.5, panels a, d, g, j, m. The PL maps are centered on the QD peak emission wavelength (630 nm) to indicate the relative PL intensity on each of the devices. It is instantly apparent that the strongest quenching of the QD emission occurs on the monolayer device, D1 (Figure 7.5a). Quenching of the QD emission decreases moving from devices D2 to D4, as the devices become more polycrystalline with the nucleation of bilayer regions. Similarly, the QD PL shows a lower level of quenching in comparison to the thinner devices, D1-D4. This indicates that the NRET efficiency decreases as the MoS_2 layer number increases, which is consistent with optical studies in the literature,[65,66] resulting from the reduced dielectric screening of the donor electric field dipole in the monolayer material. From the QD PL maps for the devices D2 and D3 (Figure 7.5, panels d and m) the quenching of the QD PL is strongest in the monolayer regions that can be seen in the corresponding Raman maps (Figure 7.4, panels f and i), respectively, further confirming the decrease in NRET efficiency as the MoS_2 layer number increases. There is a much weaker quenching of the QD PL on the polycrystalline bilayer and bulk-like devices, D4 and D5, as can be seen from the PL map (Figure 7.5, panels g and j), which is expected due to increased dielectric screening of the QD electric field dipole in the bilayer material, in contrast to the monolayer material.[65,66]

PL maps of the devices, centered on the MoS_2 peak emission wavelength are presented in Figure 7.5, panels b, e, h, k, n. These PL maps clearly demonstrate that the regions of high PL intensity are decreasing as the devices transition from pristine monolayer (D1) to bulk-like thicknesses (D5). The MoS_2 PL intensity is fairly uniform across the monolayer device, D1 (Figure 7.5b), while the PL is quite non-uniform across devices D2 to D4 and the areas showing high PL intensity are reducing, Figure 7.5, panels e, h and k, respectively. While the Raman maps in Figure 7.4 indicate the regions of the device that differ in layer thickness, the corresponding MoS_2 PL maps do not show similar patterns in terms of the PL intensity. The PL maps reveal that for devices D2 and D3 (Figure 7.5, panels e and h) the PL intensity is larger in regions where there is variation of layer number as can be seen in the corresponding Raman maps (Figure 7.4, panels e and h) and not solely higher PL intensity from monolayer regions, which might have been expected. The corresponding PL spectra for each of the PL maps are shown in Figure 7.5, panels c, f, i, l, o. Similar to the Raman spectra in Figure 7.4c, the PL spectra in Figure 7.5c is an average over the device channel indicated by the yellow dash box in the Raman and PL maps. The pristine monolayer MoS_2 has a peak emission wavelength of ~677 nm which is expected for monolayer MoS_2 flakes.[63] The QD PL spectrum is also shown in Figure 7.5c to indicate the peak position relative to the MoS_2 B emission peak. The black and green lines in the PL spectra in Figure 7.5, panels c, f, i, l, o, were extracted from the same regions as the Raman spectra in Figure 7.4. The PL spectra in Figure 7.5 show both a redshift in the peak emission wavelength for MoS_2 and an increase in QD PL intensity at the bilayer and bulk-like thickness locations, as expected. However, both devices consisting of a mix of monolayer and bilayer MoS_2 show PL intensities for the bilayer region either equal to or greater than the PL intensity from the purely monolayer region. This increase in PL intensity can be attributed to increased scattering at defect sites introduced by the grain boundaries[272] at the edges of the nucleation sites where the 2nd layer of MoS_2 has formed. The PL spectra for the polycrystalline bilayer device, D4 (Figure 7.5l), shows a larger QD PL intensity as compared to the other devices and shows very little variation in the MoS_2 PL intensity across the whole device, once again verifying the decrease in the NRET efficiency. Similarly, the bulk-like device presented in Figure 7.5o shows higher QD PL intensities and lower MoS_2 PL intensities as compared with the devices of lower layer numbers (D1-D4), indicating a lower NRET efficiency from the QDs to the bulk-like MoS_2 and reduced emission intensity from the bulk-like material.

7.3.2 Time-Resolved Photoluminescence

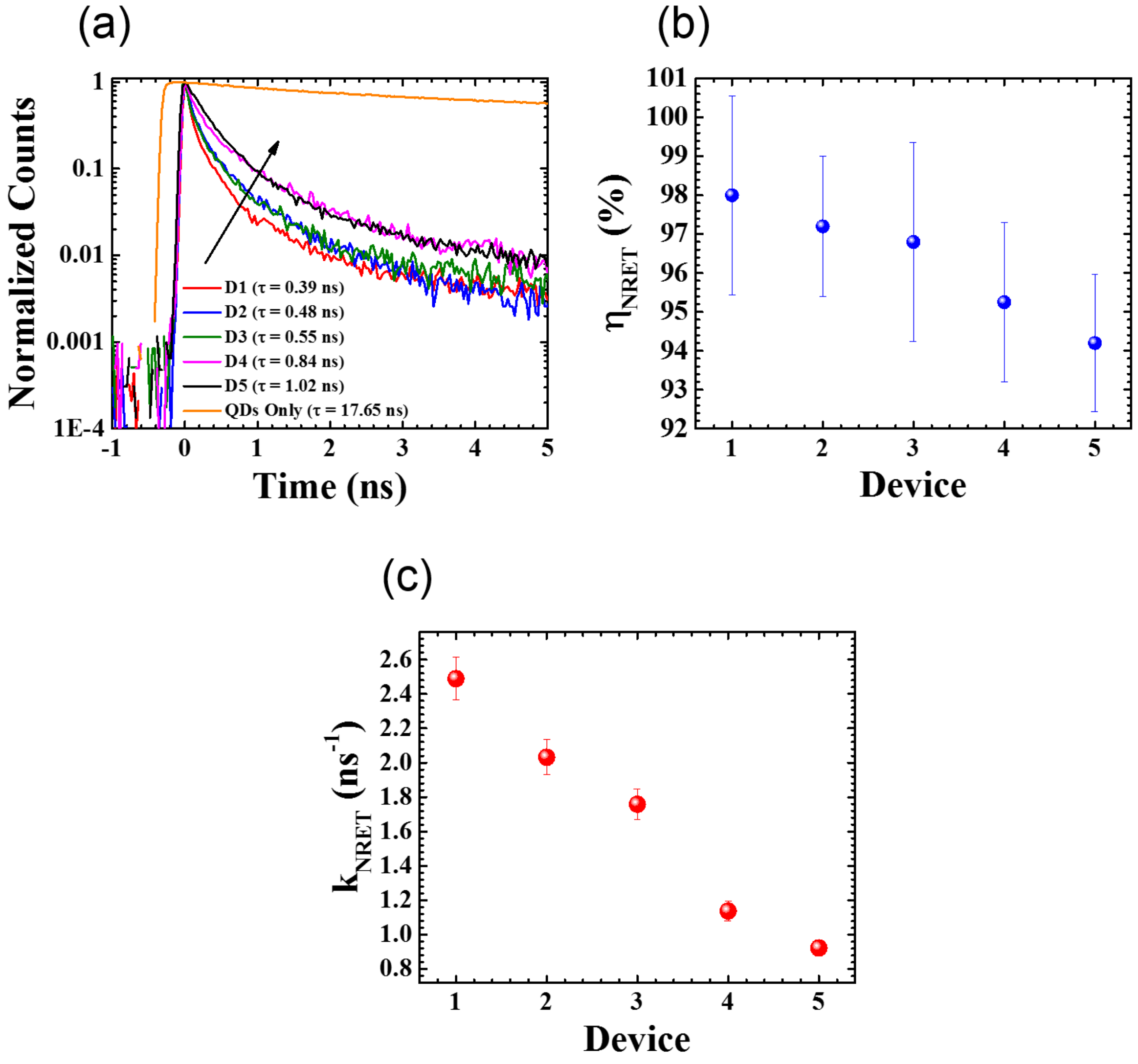

Figure 7.6: (a) PL decays of QDs alone and the QDs on each of the MoS_2 devices. (b) NRET efficiency as a function of device. (c) NRET rate for the QDs on each device.

TRPL measurements were performed to further investigate the interaction between the QDs and the MoS_2 devices. The PL decays of the QDs on each of the devices can be seen in Figure 7.6a. The substantial reduction in the QD PL lifetime on the MoS_2 devices indicates that the NRET process is highly efficient in this hybrid system, with NRET efficiencies, η_{NRET}, given by $\eta_{NRET} = 1 - (\tau_{QD-MoS_2}/\tau_{QD})$, of over 90% for each of the devices including the bulk-like thickness device, as can be seen in Figure 7.6b. The highest NRET efficiency is found for the pristine monolayer device, D1, with an NRET efficiency of (98 ± 3)%, while the TRPL measurements on the more polycrystalline devices, D2, D3 and D4, reveal NRET efficiencies of (97 ± 2)%, (97 ± 3)% and (95 ± 2)%, respectively. The NRET efficiency for the bulk-like thickness device, D5, is (94 ± 2)%.

The NRET rate, k_{NRET}, provides further information on the temporal scale over which the NRET process occurs, where $k_{NRET} = k_{QD-MoS_2} - k_{QD}$ with $k = 1/\tau$. A plot of the NRET rates for each device is presented in Figure 7.6c. There is a clear trend in the reduction of the NRET rate as the devices become more polycrystalline. The NRET rate between the QDs and the polycrystalline bilayer device, D4, is (1.1 ± 0.1) ns^{-1} which is less than half the NRET rate between the QDs and the monolayer device, D1, which has an NRET rate of (2.5 ± 0.1) ns^{-1}. Similarly, the NRET rate between the QDs and the bulk-like device, D5 has a value of (0.9 ± 0.1) ns^{-1}. This increase in the NRET rate as the devices reach monolayer thickness is due to the reduced dielectric screening of external electric fields in the MoS_2 as the layer number decreases.[65,66]

It is also worth pointing out that despite these ultrahigh NRET efficiencies and rates that there is no enhancement of the MoS_2 PL intensity due to the NRET. Ideally, the acceptor would display an increased PL intensity due to the NRET from the donor. This lack of a PL enhancement is attributed to nonradiative recombination of excitons at defect sites which arise from susceptibility of CVD-grown MoS_2 to growth induced defects. The PL spectra of the QDs only, QDs on monolayer MoS_2, and MoS_2 only is given in Figure 7.7. In a similar manner to that described above, the NRET efficiency can be calculated from the integrated PL spectrum of the QDs alone, $Int\ PL_{QDs}$, and the integrated PL spectrum of the QDs on the MoS_2, $Int\ PL_{QD-MoS_2}$, and is given by, $\eta_{NRET-PL} = 1 - (Int\ PL_{QD-MoS_2}/Int\ PL_{QD})$.

Calculating the NRET efficiency using the integrated PL spectra gives an NRET efficiency of (99 ± 5)%, which is in good agreement with the NRET efficiency of (98 ± 3)% as measured from the lifetimes. Nonetheless, observation of increased PL emission from the acceptor (MoS_2) resulting from NRET relies on the recombination of excitons. However, the electrical processes depend more on the separation of the photo-generated charge carriers under an applied bias. Therefore, it is of significant interest to investigate the electrical extraction of energy transferred from the donor to the acceptor by NRET.

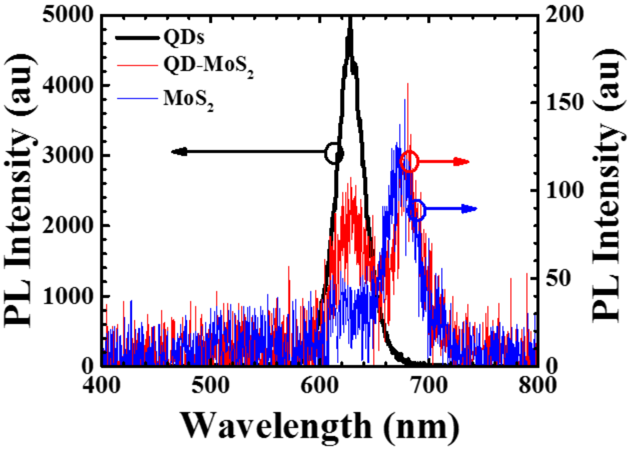

Figure 7.7: PL spectra of QDs only, QDs on MoS_2, and MoS_2 only.

7.4 Photocurrent Measurements

The current-voltage (I-V) characteristics for each device (before and after the addition of the QD sensitizing layer) were measured as a function of laser excitation power in the power range of ~1-100 µW between -1 and +1 V. All devices were measured under the same conditions and had a linear or close to linear I-V curve at all laser powers before and after the addition of the QD sensitizing layer. I-V curves for each device at a laser excitation power of 30 µW with (red) and without (blue) the QD sensitizing layer are shown in Figure 7.8, panels a, d, g, j, m. The largest enhancement in photocurrent is seen for the pristine monolayer device, D1 (Figure 7.8a). Similar enhancements are observed for devices D2 and D3, both containing portions of monolayer and bilayer MoS_2 (Figure 3, panels d and g).

There is little to no enhancement of the photocurrent for the polycrystalline bilayer or bulk-like thickness devices, D4 and D5, respectively, as can be seen in Figure 7.8, panels j and m.

Figure 7.8, panels b, e, h, k, n, show the generated photocurrent, I_{Ph}, as a function of laser excitation power for the four devices. All devices exhibit a similar dependence on the excitation power before and after the addition of the QD sensitizing layer, having either a linear or slightly sub/super-linear slope. Similar to the I-V curves (Figure 7.8, panels a, d, g, j, m) it is clear that the largest enhancement in the photocurrent is obtained from the purely monolayer device, D1 (Figure 7.8b), with comparable levels of photocurrent enhancement across the full excitation power range for the devices D2 and D3, containing regions of both monolayer and bilayer MoS_2 (Figure 7.8, panels e and h). It is worth pointing out that while the device, D3, containing more bilayer than monolayer regions (Figure 7.4g) should give higher levels of photocurrent due to a greater abundance of charge carriers, we observe lower levels of photocurrent compared to device, D2, which contains almost equal portions of monolayer and bilayer regions (Figure 7.4d). This is attributed to a larger number of grain boundaries in the channel leading to a larger density of scattering points (Figure 7.4g), and is also in agreement with the PL from the bilayer regions shown in Figure 7.5h. The photocurrent obtained from the polycrystalline bilayer device, D4 (Figure 7.8k), shows almost identical curves with and without the QD sensitizing layer indicating that the addition of the sensitizing layer has no effect on polycrystalline bilayer devices resulting from a combination of grain boundaries leading to electron scattering at defect points, and increased dielectric screening of the QD electric field dipole in the bilayer material.[65,66] Measurements performed on the bulk-like device also reveal that there is no enhancement of the photocurrent after adding the QD sensitizing layer (Figure 7.8n).

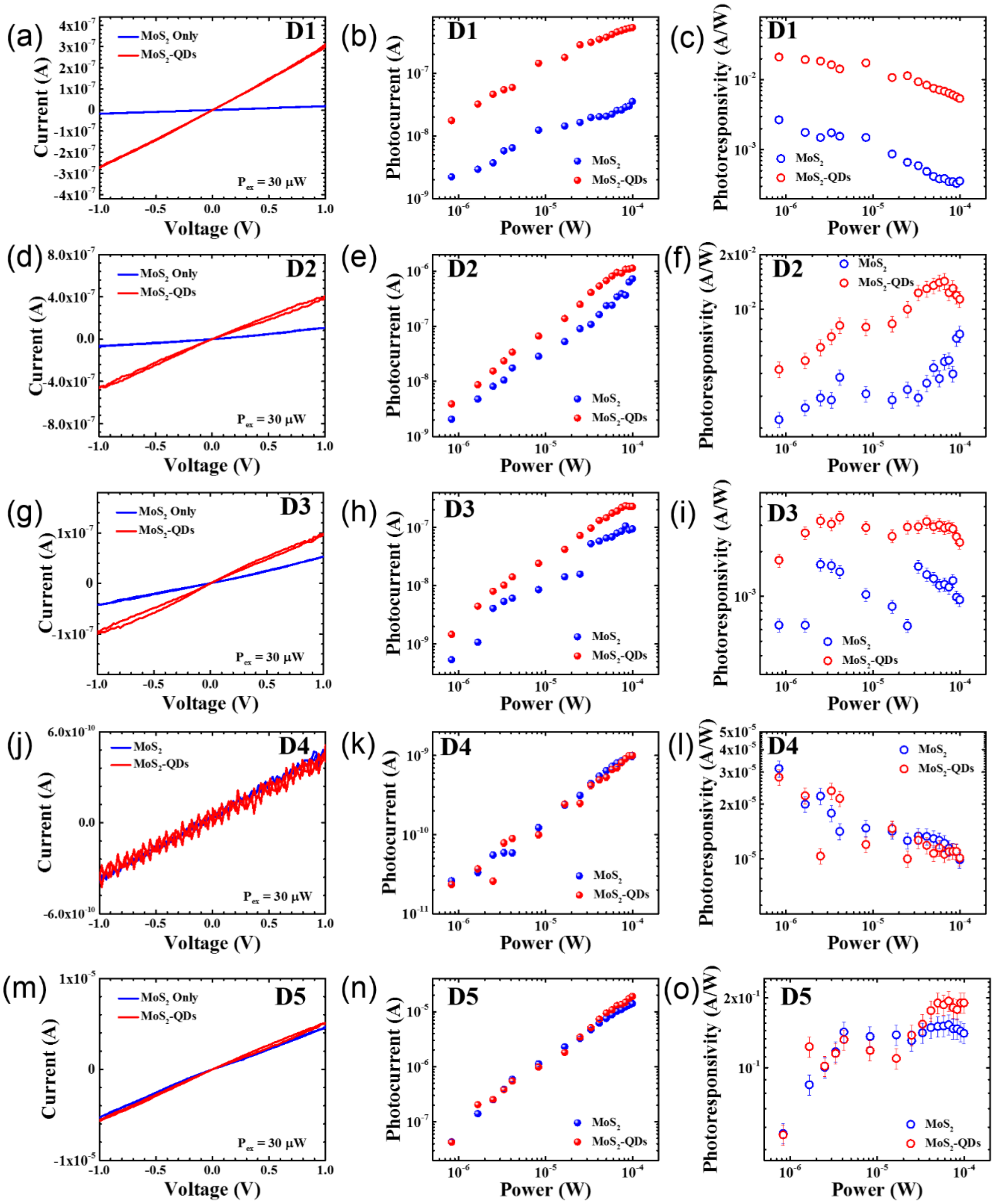

Figure 7.8: (a, d, g, j, m) I-V curves for the MoS$_2$ devices before (blue) and after (red) adding the QD sensitizing layer. (b, e, h, k, n) Photocurrent versus excitation power for the devices without (blue dots) and with QD sensitizing layer (red dots). (c, f, i, l, o) Photoresponsivity as a function of power for the devices before (blue circles) and after adding the QD sensitizing layer (red circles).

The photoresponsivity, R, gives a measure of the current output as a function of incident optical power. The photoresponsivity is given by $R = I_{Ph}/P_{ex}$, where P_{ex} is the excitation power. The photoresponsivity measured for each of the devices across the full excitation power range is given in Figure 7.8, panels c, f, i, l, o. The photoresponsivity of the pristine monolayer device, D1 (Figure 7.8c), shows a typically steady decrease in photoresponsivity as the optical excitation power increases which corresponds to a sub-linear dependence of photocurrent on the excitation power. The largest photoresponsivity for the monolayer device is achieved at the lowest excitation power of ~1 µW for both the MoS_2 device only ($R = 2.6 \times 10^{-3} A/W$) and with the QD sensitizing layer ($R = 2.1 \times 10^{-2} A/W$), giving > 8 fold enhancement in the photoresponsivity. The photoresponsivity curves for the mixed layer devices, D2, D3, and the bulk-like thickness device, D5 (Figure 7.8, panels f, i, o, respectively), however, display a different character as compared to the monolayer device, D1. These devices show a combination of increasing, constant and decreasing photoresponsivity regimes as the excitation power increases. The increasing and constant regimes correspond to super-linear and linear dependences of photocurrent on excitation power, respectively. Sub-linear dependence of photocurrent on excitation power in MoS_2 devices is commonly observed at large excitation intensity[265,273,274] while linear dependences are observed at lower excitation intensities.[262,264,265] However, a super-linear dependence of the photocurrent on excitation power is less documented and can be explained by multi-centre recombination models.[275] The presence of surface defects and edge states at grain boundaries, due to the granular nature of the channel in devices D2, D3, and D5, could give rise to a variety of recombination centers such as dangling bonds at the MoS_2 surface, and contribute to this super-linear behaviour.[275–279] Device D4 also shows a similar decrease in the photoresponsivity with increasing excitation power as D1 both with and without the QD sensitizing layer.

To calculate the average photocurrent enhancement for each of the devices, the photocurrent *vs.* excitation power curves were averaged across the full laser excitation power range. The enhancement was then calculated as I_{QD-MoS_2}/I_{MoS_2}. We find photocurrent enhancements as high as ~14 fold for the pristine monolayer device, D1, and photocurrent enhancements of ~2 fold for devices D2 and D3, and no enhancements for device D4 and D5 after adding the QD sensitizing layer as can be seen in Figure 7.9. This indicates that the QD sensitizing layer is most effective for monolayer devices, while the benefits of the QD sensitizing layer disappear as the MoS_2 regions in the device become polycrystalline.

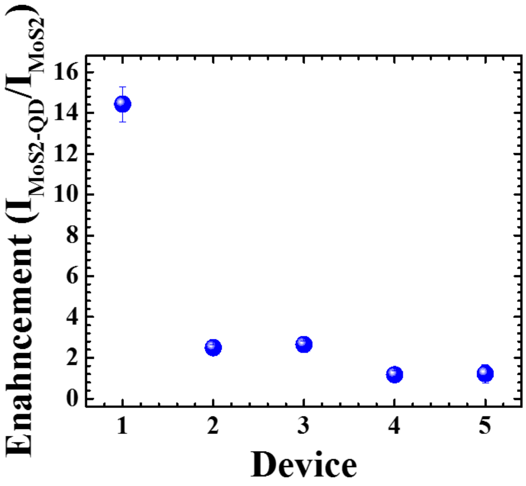

Figure 7.9: Photocurrent enhancement for each QD-sensitized MoS_2 device.

It is worth pointing out that there is a significant difference in the trends observed for the NRET efficiency (and rate) on each device in comparison with the photocurrent enhancements measured from each device. The difference in NRET across the devices cannot account for the larger difference in the photocurrent enhancement. The larger variation in the photocurrent enhancement can be explained by the increased number of grain boundaries arising from the formation of bilayer MoS_2 at nucleation points leading to greater scattering of electrons[280–282] and consequently reduced mobility. This lower enhancement resulting from poor carrier transport due to the scattering of electrons is consistent with the photocurrent and photoresponsivity values obtained from the devices as they become more polycrystalline in Figure 7.8, panels d, g, j, and e, h, k, respectively. Typically, as the proportion of bilayer MoS_2 increases an increase in photocurrent could be expected due to the larger number of charge carriers available.[61,273,283] However, the observed decrease in device performance is due to the increased number of grain boundaries and defect sites.

7.5 Conclusion

In summary the optoelectronic properties of hybrid QD-MoS_2 devices show a strong dependence on the properties of the MoS_2 layer, despite highly efficient NRET from semiconductor QDs in an ultrathin sensitizing layer to a variety of MoS_2 devices varying from pristine monolayer to polycrystalline devices composed of mixed layer thicknesses (monolayer and bilayer) and bulk-like thickness devices. While NRET efficiencies exceeding 90% have been demonstrated across all devices, measurements reveal a decrease in the NRET efficiency and rate as the ratio of bilayer to monolayer MoS_2 in the device channels increases. Despite the high NRET efficiency, spectral PL measurements reveal that there is little to no enhancement of the MoS_2 PL intensity after the addition of the QD-sensitizing layer, attributed to nonradiative recombination of excitons at defect sites. Optoelectronic measurements revealed that the energy transferred from the QDs to the MoS_2 through NRET pathways could be extracted electrically. Photocurrent enhancements as large as ~14 fold were found for the pristine monolayer MoS_2 device after adding the QD sensitizing layer, while devices consisting of a mixture of monolayer and bilayer MoS_2 gave ~2 fold enhancement. No enhancement was observed as the active region of the devices became more polycrystalline and predominantly bilayer and bulk-like thickness. The photocurrent measurements also revealed that the photocurrent decreased as the devices became more polycrystalline due to increased scattering of charge carriers, and lower photocurrent enhancements were observed. Importantly, it has been demonstrated that increased absorption of incident light in a 2D photodetection system can enhance the electrical output from the 2D material using NRET, with the greatest advantages obtained from monolayer MoS_2 devices. This hybrid system which combines large-area synthesis of MoS_2 films and a simple spin-coating process, both of which are industrially scalable and economically viable methods, suggests a potential route for hybrid 2D optoelectronic devices, most notably, photodetection and light harvesting applications.

Chapter 8

A Spectral Dependence Study of Nonradiative Energy Transfer and Photocurrent Enhancement in Hybrid Quantum Dot-MoS_2 Devices

Chapter Summary

This chapter will focus on the spectral dependence of nonradiative energy transfer (NRET) and enhanced photocurrent from three spectrally separated alloyed CdSeS/ZnS QDs, with peak emission wavelengths of 450 nm, 530 nm and 630 nm, spanning the visible spectrum, to monolayer MoS_2 devices. The triangular MoS_2 islands were grown by chemical vapor deposition (CVD) on Si/SiO_2 and these samples were grown by our collaborators in the Duesberg group, TCD. Similar to the previous chapter, the hybrid QD-sensitized MoS_2 devices were fabricated by spin coating an ultrathin layer of QDs in PMMA on the chips containing the devices. The NRET from the QDs to the MoS_2 devices was studied using time-resolved photoluminescence (TRPL). The photocurrent was measured from the MoS_2 devices as a function of excitation power, before and after adding the QD sensitizing layer, using the custom built setup described in Chapter 3 (section 3.2.8).

8.1 Introduction

As highlighted in the previous chapter, research aimed towards the application of semiconducting 2D materials in optoelectronic technologies has gained substantial momentum in recent years.[284,285] Initially, graphene was considered to be the superior candidate as the active 2D material in many devices, given graphene’s extremely high mobility[8] and fast photoresponse,[286] however, the lack of a direct optical bandgap in graphene limits its applicability in many optoelectronic devices. Transition metal dichalcogenides (TMDs) on the other hand, such as MoS_2, possess the striking ability to transition from an indirect bandgap at few-layer thicknesses to a direct optical bandgap material at monolayer thicknesses.[61–63] The presence of this direct optical bandgap at monolayer thicknesses gives these TMDs a significant advantage over graphene for many optoelectronic devices.

Considering devices for photodetection in the visible spectral range, many applications require broadband optical absorption. A further consideration is that given the monolayer thickness of these materials, there are significant limitations in terms of the absorption of incoming light which, consequently, affects the overall device performance and efficiency. A simple method to overcome this low absorption of incident light is to incorporate a sensitizing layer on top of the 2D material. Depending on the sensitizing species, most commonly organic dyes[267] or quantum dots (QDs),[268,269] the absorption of incident light in the hybrid system can be improved. However, several factors must be taken into account when selecting a sensitizing species including the sensitizer's quantum yield, photostability and the spectral location of the optical absorption band. Regarding the above factors, QDs present many advantages over organic dye molecules including high quantum yields, improved photostability, broadband optical absorption and the ability to tune the emission profiles using the size or chemical composition dependence of the QDs.[233,234,287] The broadband optical absorption associated with QDs is a significant benefit when considering light harvesting or photodetection devices operating across a larger optical bandwidth.

This chapter investigates the spectral dependence of NRET to monolayer MoS_2 devices using three alloyed CdSeS/ZnS QDs with peak emission wavelengths of 450, 530, and 630 nm, spanning the visible spectrum. These alloyed QDs are ideal for a spectral dependent study as spectral tuning is achieved by varying the chemical composition and not the size of the QD.[200,287] Having the alloyed QDs of the same diameter (6.0 ± 0.8) nm allows for similar photoluminescence (PL) quantum yields[287] across the three QD samples (50 ± 5)% for these

QDs in particular) and avoids any variation in the centre-to-centre distance influencing the measurements. The latter is a particularly important factor given the strong distance dependence of NRET.

Herein, the spectral dependence of NRET from three spectrally separated QDs to monolayer MoS_2 devices and the influence of the NRET on the generated photocurrent is investigated. Based on the results from the previous chapter, pristine monolayer MoS_2 was used. The uniformity and monolayer thickness of the MoS_2 was identified using Raman mapping and Raman spectroscopy, respectively. The efficiency of the NRET was investigated using TRPL measurements. The enhancement of the photocurrent extracted from the hybrid devices was investigated through photocurrent measurements on the devices before and after adding the QD-sensitizing layers, over a broad range of optical excitation powers. We observe enhancements of the photocurrent on each hybrid QD-MoS_2 device and find the largest photocurrent enhancements and the largest NRET efficiency for the 630 nm QD-MoS_2 device. Similar trends are found between the NRET efficiencies, photocurrent enhancements and the spectral overlap as a function of QD emission wavelength. To the best of our knowledge this is the first spectral dependence study of NRET from QDs to monolayer $MoS_{2,}$ and, similarly the first spectral dependence study of photocurrent enhancement in QD-MoS_2 hybrid devices. It is believed that the findings from this study provide significant insight for the optimization of future QD-sensitized hybrid devices for optoelectronic applications.

8.2 Initial Characterisation

8.2.1 Absorption and Photoluminescence

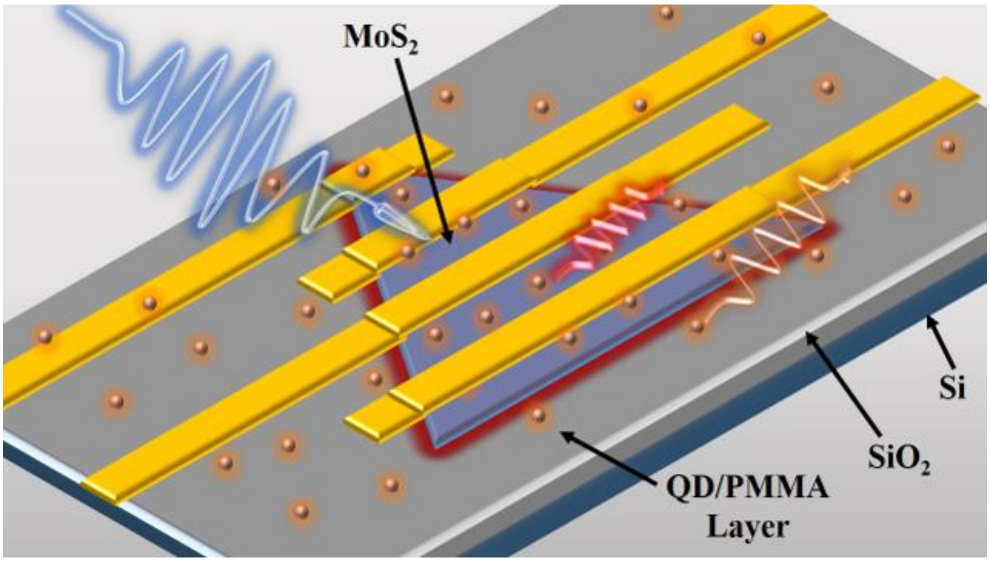

Figure 8.1: Schematic illustration of the QD-sensitized MoS_2 devices.

A schematic representation of the QD-sensitized MoS_2 devices is given in Figure 8.1. The alloyed CdSeS/ZnS QDs used for this spectral dependence study have peak emission wavelengths of 450 nm, 530 nm, and 630 nm and each of the alloyed QDs has a diameter of (6.0 ± 0.8) nm. The QDs were purchased in solution at a concentration of 1 mg/mL in toluene from Sigma-Aldrich and these solutions were used as stock. To make up the QD/PMMA dispersions, 12.5 μL of the QD stock solutions was dispersed in 500 μL of 0.1% wt. PMMA. The QD/PMMA solutions were then sonicated for ~20 s, ensuring the even distribution of the QDs in the PMMA. The solutions were then spincast onto the chips containing the devices. The height of the QD/PMMA layers were found to be ~ (7 ± 3) nm, ~ (9 ± 2) nm, and ~ (8 ± 2) nm, for the 450 nm, 530 nm, and 630 nm QDs, respectively, as verified by atomic force microscopy (AFM) measurements (Figure 8.2). Layer thicknesses between 7-9 nm ensures the presence of a monolayer of QDs on top of the devices.

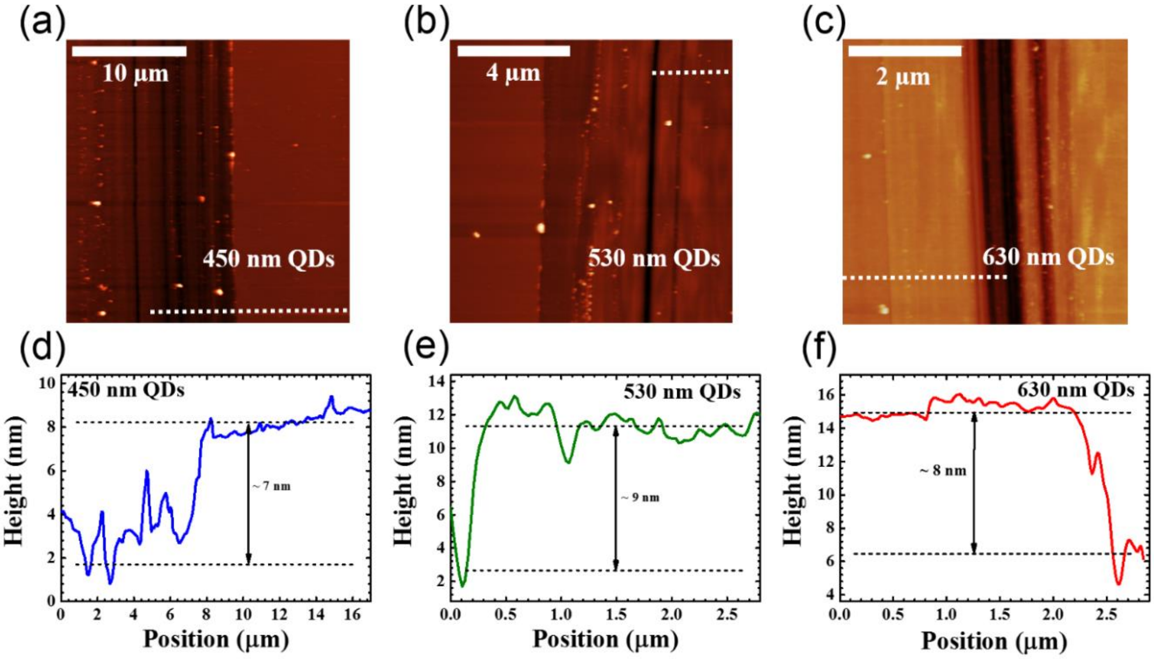

Figure 8.2: (a-c) AFM images of the QD/PMMA layers with single trenches cut into the films. (d-f) Height profiles of the QD/PMMA layers corresponding to the white dash lines in (a-c).

The extinction spectra for each of the QDs and the monolayer MoS_2 are shown in Figure 8.3 along with the normalized PL spectra of each of the QDs. Figure 8.3 also shows that the 630 nm QDs are on-resonance with the B exciton of the MoS_2 and the 450 nm QDs are slightly off-resonance with the C exciton. The 530 nm QDs were chosen as they do not overlap with any of the MoS_2 exciton absorption peaks and therefore provide an off-resonance reference. Recent studies of NRET from QDs to MoS_2 have primarily focused on QDs with emission wavelengths located close to the A and B excitons,[65–67,247] however, when considering a light harvesting or photodetector type device it is important to assess the variation in the efficiency of NRET across a larger spectral bandwidth. Herein, the MoS_2 devices sensitized with the 450 nm, 530 nm and 630 nm QDs will be labelled as D450, D530 and D630, respectively.

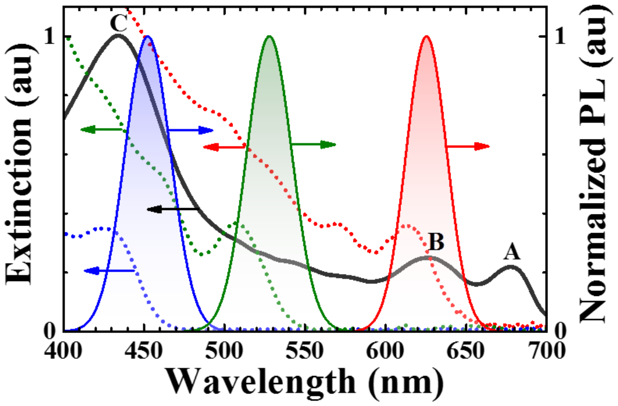

Figure 8.3: Normalized PL spectra of the 450 nm QDs (blue line), 530 nm QDs (green line), and 630 nm QDs (red line) on the right axis. The normalized extinction spectrum of monolayer MoS_2 (black line) and the scaled extinction spectra of the 450 nm QDs (blue dot), 530 nm (green dot), and the 630 nm QDs (red dot) on the left axis. The QD extinction spectra are scaled to have the first absorption peak at the same intensity, for presentation purposes.

8.2.2 Raman Spectroscopy

Optical images of each of the devices, D450, D530 and D630 are shown in Figure 8.4, panels a, b and c, respectively. Each of the MoS_2 islands chosen for use as devices in this study are of triangular form with edge lengths > 20 μm. The monolayer thickness of the devices was verified using Raman spectroscopy. Raman maps of devices D450, D530 and D630 are presented in Figure 8.4, panels d, e and f, respectively. These Raman maps plot the separation between the characteristic *A* and *E* Raman peaks of the MoS_2 Raman spectrum. Each of the Raman maps (Figure 8.4, panels d-f) show uniform regions in the device channels indicating that there is very little variation in the separation between the characteristic Raman peaks. Device D530, however has a large nucleation point in the central channel (not used for measurements) which can be clearly seen in the optical image

(Figure 8.4b) and the Raman map (Figure 8.4e). Raman spectra were extracted from each of the Raman maps (averaged over the device channel area indicated by the white dotted box in Figure 8.4, panels d-f) to identify the layer number of the MoS_2 islands.

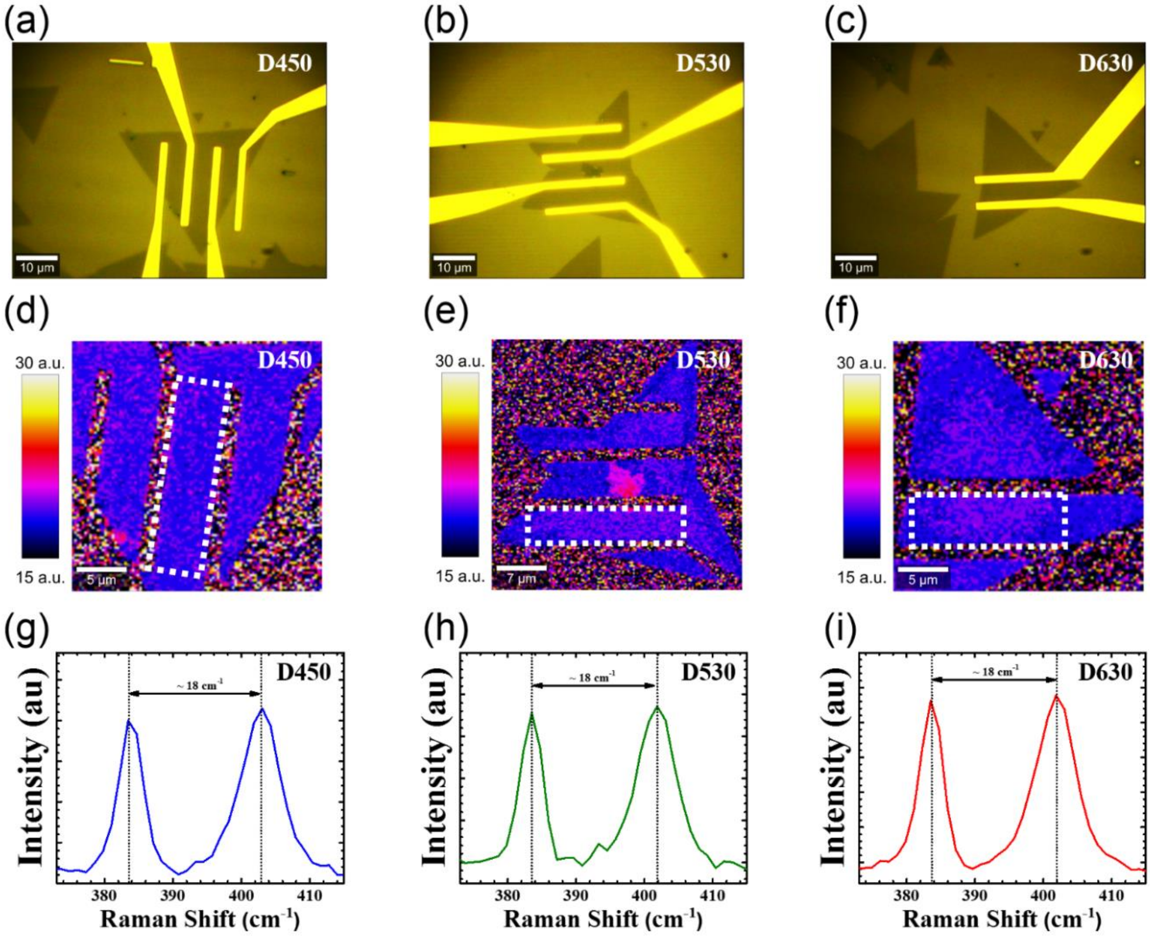

Figure 8.4: (a-c) Optical images of the devices. (d-f) Raman maps corresponding to the devices in (a-c) plotting the separation between the A and E peaks in the Raman spectrum. (g-i) Raman spectra extracted from the channel regions indicated in dash white boxes in the Raman maps (d-f).

The Raman spectra obtained from each of the device channels reveal separations of ~ 18 cm^{-1} between the A and E Raman peaks on each of the devices (Figure 8.4, panels g-i), verifying the monolayer thickness of the devices.[270,271] As mentioned above, previous reports in the literature regarding NRET from QDs to monolayer (and few-layer) MoS_2 have utilised QDs with emission wavelengths located close to the MoS_2 A and B excitons.[65–67,247]

However, a systematic spectral dependence has not been reported. The spectral dependence of NRET to monolayer MoS_2 across the visible spectrum is a critical consideration for broadband applications and optimal spectral location of sensitizing species for use in a hybrid QD-MoS_2 photodetection or light harvesting devices.

8.3 Nonradiative Energy Transfer

The strength of the interaction between the QDs (donor) and the MoS_2 (acceptor) devices was quantified using TRPL measurements. The PL decays were recorded over 3 µm x 3µm areas in the device channel (QD-MoS_2) and 3 µm x 3µm areas close to the device containing no MoS_2 (QDs alone). The excitation power used for the measurements was 0.2 µW. The PL decays presented in Figure 8.5 reveal the strong interaction between the QDs and the monolayer MoS_2 through the significant decrease in the QD PL decay on the MoS_2. The decrease in the QD (donor) lifetime is a characteristic signature of NRET. The QD lifetime is reduced from ~20 ns to ~1 ns on each of the devices (D450, D530 and D630) after the hybrid structure is formed. The efficiency of this interaction between the QDs and the monolayer MoS_2 was quantified by the NRET efficiency, given by $\eta_{NRET} = 1 - \left(\tau_{QD-MoS_2}/\tau_{QD}\right)$, where $\tau_{QD-MoS_2}$and τ_{QD} are the intensity weighted average lifetimes of the QDs on the monolayer MoS_2 and the lifetime of the QDs alone, respectively. The NRET efficiencies, measured on each of the devices were found to be (94 ± 5)% for the 450 nm QDs on device D450, (92 ± 5)% for the 530 nm QDs on device D530, and (96 ± 5)% for the 630 nm QDs on device D630.

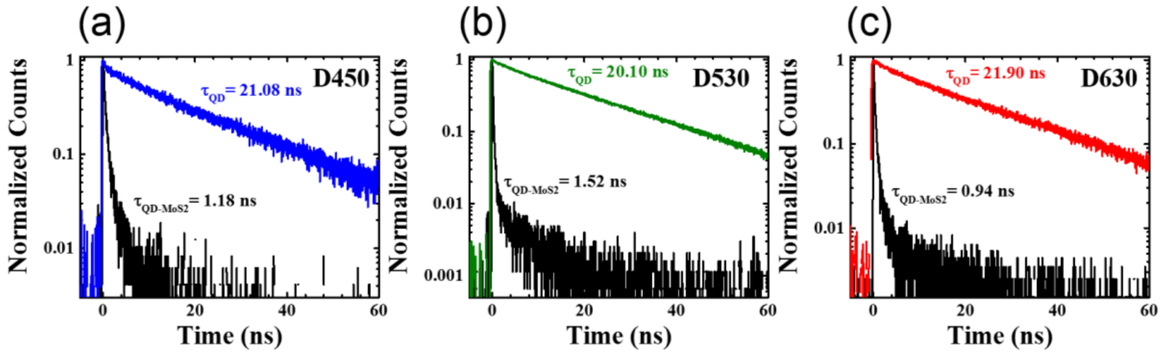

Figure 8.5: PL decays of (a) 450 nm QDs alone (blue) and on MoS_2 device, D450 (black), (b) 530 nm QDs alone (green) and on MoS_2 device, D530 (black), and (c) 630 nm QDs alone (red) and on MoS_2 device, D630 (black).

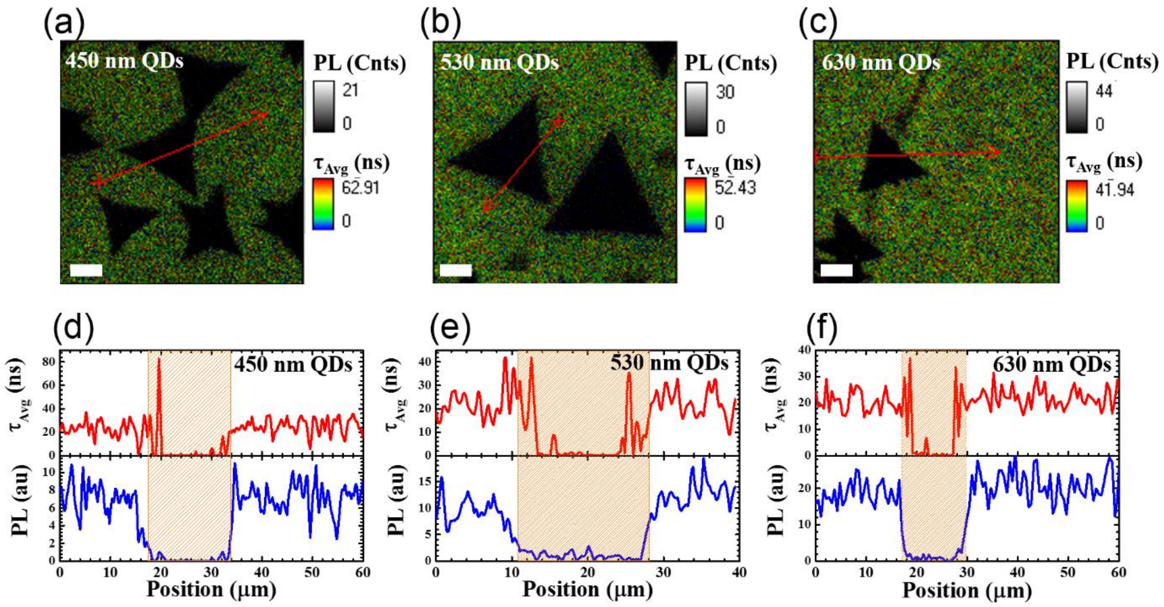

Figure 8.6: (a-c) Fluorescence lifetime images of QDs on MoS_2 monolayers. (d-f) Average lifetime, τ_{Avg}, and PL intensity profiles corresponding to the regions indicated by the red arrows in (a-c). Scale bars in (a-c) are 10 µm. The images were recorded over 80 µm x 80 µm areas.

To further illustrate the strength of the interaction, fluorescence lifetime images were recorded on monolayer MoS_2 triangles located close to the devices on each chip. The fluorescence lifetime images and cross-sectional profiles of the PL intensity and average lifetimes can be seen in Figure 8.6. These images were recorded on separate MoS_2 flakes as the Au contacts on the devices make it difficult to fully appreciate the magnitude of the quenching of the PL and lifetime due to the NRET from the QD to the monolayer MoS_2. Similar to the PL decays in Figure 8.5, the cross sectional profiles of the average lifetime in Figure 8.6d-f reveal a reduction in lifetime from ~ 20 ns to ~ 1 ns when the QDs are on the monolayer MoS_2. Similarly it can be seen that the PL intensity is also quenched to a near zero value as a result of the highly efficient NRET.

8.4 Photocurrent Measurements

Figure 8.7, panels a-c, show the photocurrent, I^{Ph}, measured from each device, with and without the QD sensitizing layers, as a function of optical excitation power at a voltage of +1 V, and the respective fits to the experimental data (dotted lines). It should be pointed out that an excitation wavelength of 405 nm was used for the TRPL measurements, photocurrent measurements, and the PL measurements used to calculate the spectral overlap. The black data points in Figure 8.7, panels a-c, show the photocurrent obtained from the MoS_2 devices before adding the QD sensitizing layers. The blue, green and red data points in Figure 8.7, panels a, b and c, are photocurrent values obtained after the addition of the 450 nm, 530 nm and 630 nm QD sensitizing layers, respectively. There is a clear enhancement of the generated photocurrent across the full excitation power range for each of the QD-MoS_2 hybrid devices (Figure 8.7, panels a-c). The curves maintain similar dependences of photocurrent on the excitation power after the addition of the QD sensitizing layers. The photocurrent measured from each device exhibits a sub-linear dependence at low excitation powers which transitions to a linear dependence at mid-range powers and finally transitions to a super-linear dependence at the higher powers. While linear and sub-linear dependences of photocurrent on the optical excitation power are widely documented in the literature,[262,264,265,273,274] super-linear dependences are less reported.[275] This super-linear dependence of photocurrent on the optical excitation power has been explained by multi-centre recombination models.[275] Given the monolayer thickness of the MoS_2, a variety of recombination centers can be present due to imperfections including surface defects, edge states at grain boundaries and dangling bonds at the MoS_2 surface, which could all contribute to the super-linear behavior.[275–279]

A polynomial curve was used to fit the photocurrent data measured from the devices before and after adding the QD sensitizing layers, given by

$$I^{Ph} = AP_{Ex}^{0.5} + BP_{Ex} + CP_{Ex}^{2} \qquad (8.1)$$

where A, B, and C are fitting coefficients. This polynomial fitting curve was chosen to fit the data in a similar manner to the traditional interpretation of the '*ABC*' recombination model,[288,289] given by $R = An + Bn^2 + Cn^3$, where R is the total recombination rate, and the three main carrier recombination mechanisms in semiconductors are given by; the An term, which is the Shockley-Read-Hall (SRH) nonradiative recombination rate, the Bn^2 term, which is the radiative recombination rate, and the Cn^3 term, which is the Auger nonradiative recombination rate. While the '*ABC*' model describes the recombination of electron-hole pairs, our photocurrent measurements involve the separation of electron-hole pairs, and as such, differences arise in the fitting parameters. The form of Equation 8.1 was chosen to resemble the form of the '*ABC*' model given the three regimes in the photocurrent dependence on excitation power as can be seen in Figure 8.7, panels a-c. The regimes correspond to a sub-linear, linear, and super-linear dependence of the photocurrent on the excitation power, and as such it was found that the experimental data gave the best fit to the power of 0.5, 1, and 2, for the sub-linear, linear, and super-linear regimes, respectively.

As can be seen from Figure 8.7, panels a-c, there is good agreement between the fits and the experimental data for each of the devices both with and without the QD sensitizing layers. The coefficients extracted from the fits using Equation 8.1 are presented in Figure

8.7, panels a-c. To quantify the average enhancement of photocurrent across the full excitation power range in the MoS_2 devices due to the inclusion of the QD sensitizing layers, the average photocurrent enhancement, $\langle E \rangle$, was considered. The average photocurrent enhancement, $\langle E \rangle$, is given by

$$\langle E \rangle = \frac{\langle I_{MoS_2-QD}^{Ph} \rangle}{\langle I_{MoS_2}^{Ph} \rangle} \tag{8.2}$$

where $\langle I_{MoS_2-QD}^{Ph} \rangle$ is the average photocurrent measured from the QD-sensitized devices and $\langle I_{MoS_2}^{Ph} \rangle$ is the average photocurrent measured from the same devices without the QD sensitizing layer. The average enhancements, $\langle E \rangle$, for each of the devices are 4.4 ± 0.8, 4.0 ± 1.5 and 6.8 ± 1.5 for the D450, D530 and D630, respectively. Similar to the NRET efficiencies measured from the QD lifetimes on each of the devices, we find the largest average enhancement on device, D630 and the lowest average enhancement on device D530.

As was mentioned above, the 450 nm QDs are close to resonance with the MoS_2 C exciton and the 630 nm QDs are on-resonance with the MoS_2 B exciton, while the 530 nm QDs provide an off-resonance reference (Figure 8.3). Given that the NRET rate depends strongly on the spectral overlap between the QD PL spectra and the MoS_2 absorption spectra, it will be shown in section 8.5 that the spectral dependence of the photocurrent displays the same trend as the spectral overlap function for each of the three QDs.

The photocurrent enhancement in the acceptor (MoS_2) due to the NRET from the donor (QDs), was quantified in terms of the acceptor enhancement, E_{Acc}. The acceptor enhancement, E_{Acc} is the percentage difference, and is given by

$$E_{Acc} = \frac{I_{MoS_2-QD}^{Ph} - I_{MoS_2}^{Ph}}{I_{MoS_2}^{Ph}} \tag{8.3}$$

where $I_{MoS_2-QD}^{Ph}$ and $I_{MoS_2}^{Ph}$ are the photocurrent values of the QD-MoS_2 (donor-acceptor) hybrids and the MoS_2 only (acceptor) devices, respectively. For each of the QD-MoS_2 hybrid devices in Figure 8.7, panels d-f, there is a step-like increase in the acceptor enhancement,

E_{Acc}, as the excitation power increases, while the enhancement appears to saturate and remain constant at higher excitation powers. In terms of the optimal excitation power range, the largest enhancements of the photocurrent are found at the higher excitation powers in the super-linear regime.

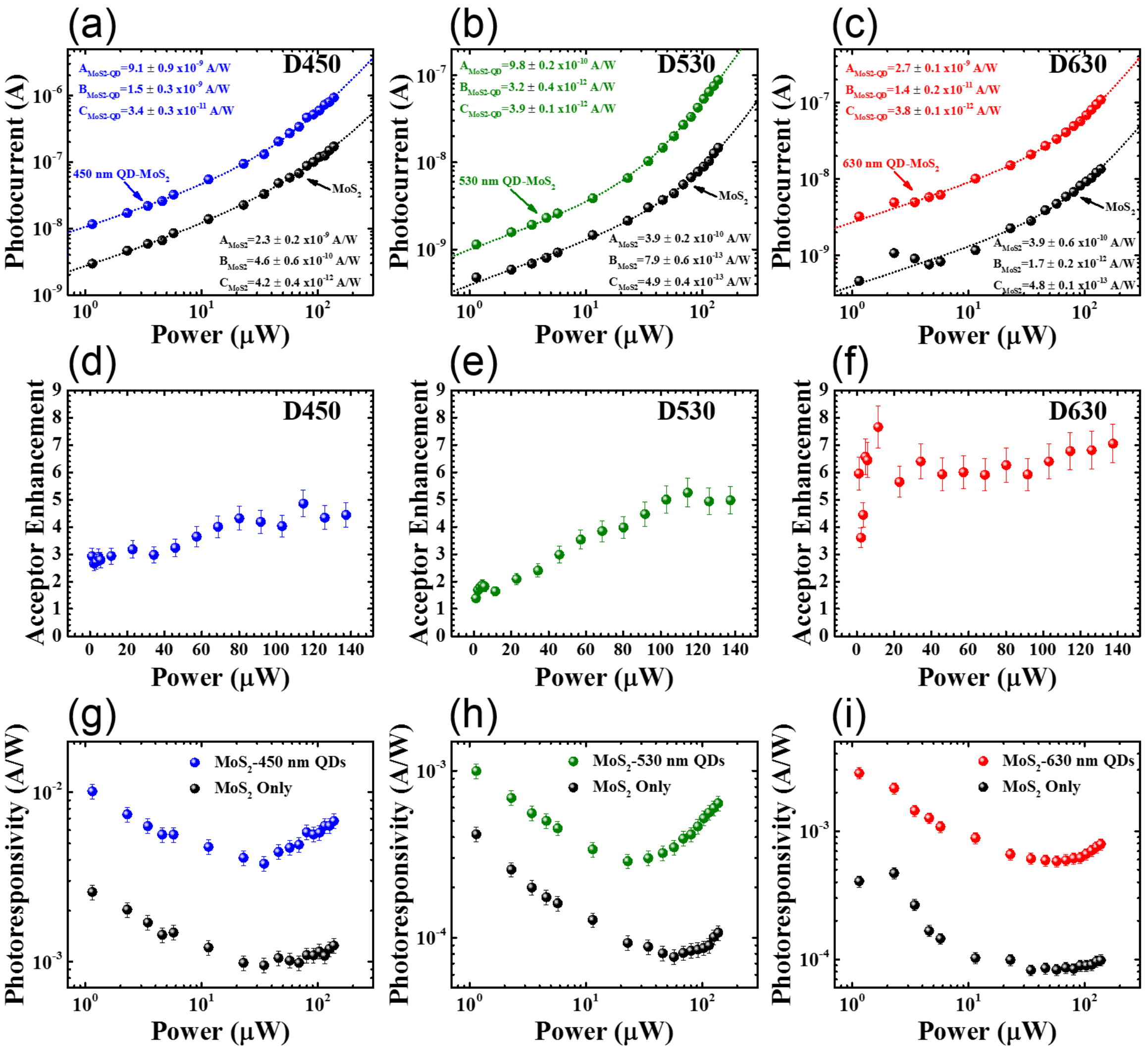

Figure 8.7: (a-c) Photocurrent measured from MoS_2 devices as a function of laser excitation power before (black circles) and after the addition of the QD sensitizing layers. Dotted lines in a-c are fits to the experimental data. (d-f) Acceptor enhancement of MoS_2 due to the presence of the QD sensitizing layers as a function of laser excitation power. (g-i) Photoresponsivity as a function of optical excitation power for each of the MoS_2 devices before (black circles) and after the addition of the QD sensitizing layers (450 nm QDs blue circles in g, 530 QDs green circles in h, 630 QDs red circles in (i)).

The 630 nm QD sensitizing layer gives the largest acceptor enhancement, of 7.0 ± 0.7 at the maximum excitation power of ~140 µW. Similarly, the 450 nm and 530 m QD sensitizing layers lead to acceptor enhancements of 4.4 ± 0.4 and 5.0 ± 0.5, respectively, at the maximum excitation power of ~140 µW. The fact that the 630 nm QDs give the largest enhancement of the MoS_2 photocurrent is beneficial also in terms of maximizing the absorption of white light as the 630 nm QDs absorb over a larger spectral region of the visible spectrum compared to the 530 nm and 450 nm QDs (Figure 8.3).

The photoresponsivity, R, is a good measure of a device's output current as a function of optical excitation power. The photoresponsivity, is given by $R = I^{Ph}/P_{ex}$, where P_{ex} is the optical excitation power. The photoresponsivity curves for the hybrid 450 nm, 530 nm and 630 nm QD-MoS_2 devices are presented in Figure 8.7, panels g, h and i, respectively. Each curve (with and without the QD sensitizing layer) shows a decreasing trend in the photoresponsivity as the excitation power increases at low powers (~1-10 µW). This decrease in the photoresponsivity corresponds to a sub-linear dependence of photocurrent on the optical excitation power. When the optical excitation power reaches tens of µWs (depending on the device), the photoresponsivity begins to level off and remains constant to a certain point. This constant photoresponsivity is the result of a linear dependence of the generated photocurrent, I^{Ph}, on the optical excitation power, P_{ex}. Moreover, with a further increase in the optical excitation power, the photoresponsivity begins to rise as the excitation power is increased. This rising behavior of the photoresponsivity results from a super-linear dependence of generated photocurrent on the optical excitation power. This behavior is observed for each of the devices presented in this study, both with and without the QD sensitizing layers.

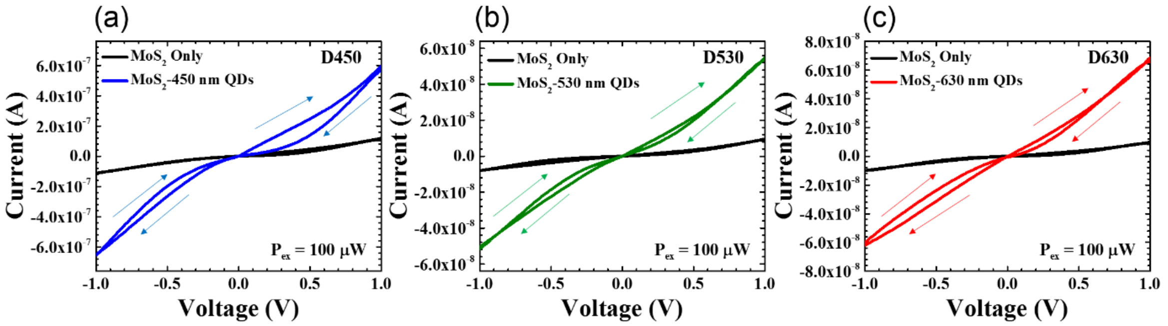

Figure 8.8: Looping I-V curves for each of the devices before adding the QDs (black) and after adding the (a) 450 nm QDs (blue), (b) 530 nm QDs (green), and (c) 630 nm QDs (red).

The measured current-voltage (I-V) characteristics of the MoS$_2$ and the hybrid QD-MoS$_2$ devices are presented in Figure 8.8. These I-V curves were measured at an excitation power of 100 μW. There is a clear enhancement in the photocurrent after the addition of the QD-sensitizing layers, however, there is some hysteresis in the curves as they sweep back from the maximum voltage. The sweep out from 0 V to +1 V (-1 V) has a close to linear form while the sweep back from the maximum voltage demonstrates a drop in current, as indicated by the arrows (Figure 8.8). This hysteresis in the curves is well documented and is attributed to charge trapping at surface defect states at the interface between the MoS$_2$ and the surrounding medium.[290] The hysteresis in the I-V curves, arising due to the surface trap states, further supports the hypothesis that it is the presence of these defects that contribute to the super-linear behaviour of the photocurrent.[275]

8.5 Comparison of Nonradiative Energy Transfer Efficiencies and Photocurrent Enhancements

As discussed earlier, the NRET rate and efficiency between donor-acceptor pairs is governed by the centre-to-centre separation and the spectral overlap, J, between the donor emission and the acceptor absorption spectra. Given that each of the QD samples used in this study have the same diameter (6.0 ± 0.8) nm, the centre-to-centre distance is the same for each hybrid device. It is therefore of interest to compare the trends of the average enhancement, $\langle E \rangle$, with the NRET efficiencies, η_{NRET}, and the spectral overlap, J, for each of the hybrid devices. The spectral overlap integral, J, is given by

$$J = \int_{0}^{\infty} I_{QD}(\lambda) \cdot \varepsilon_{MoS_2}(\lambda)\, \lambda^4 \, d\lambda \tag{8.4}$$

where $I_{QD}(\lambda)$ is the area normalised donor emission spectrum and $\varepsilon_{MoS_2}(\lambda)$ is the acceptor extinction coefficient. Given that the MoS_2 islands used in this study are single flakes on a solid substrate, an accurate extinction coefficient could not be obtained. However, in terms of the spectral overlap calculation, the extinction coefficient acts only as a scaling factor for the absorption spectrum. Similarly, the extinction coefficient, ε_{MoS_2}, is directly proportional to the absorption coefficient, α_{MoS_2}, a quantity that can be measured directly from our samples. Therefore, in order to obtain a purely qualitative comparison of trends, the measured extinction spectrum of the MoS_2 monolayer was converted to an absorption coefficient, α_{MoS_2}, and substituted for the extinction coefficient, ε_{MoS_2}, in Equation 8.4. This comparison is validated as the NRET efficiency can be expressed in terms of the acceptor enhancement and is given by[215]

$$\eta_{NRET} = \frac{Abs_{MoS_2}}{Abs_{QD}} \left(\frac{I^{Em}_{QD-MoS_2}}{I^{Em}_{MoS_2}} - 1 \right) \tag{8.5}$$

where Abs_{MoS_2}/Abs_{QD} is the acceptor:donor absorption ratio (constant) at the excitation wavelength, $I^{Em}_{QD-MoS_2}$ is the integrated emission intensity of the MoS2 in the presence of the QDs, $I^{Em}_{MoS_2}$ is the integrated emission intensity of the MoS2 in the absence of the QDs, and the $\left[(I^{Em}_{QD-MoS_2}/I^{Em}_{MoS_2}) - 1\right]$ term can be obtained from the average photocurrent enhancement with the inclusion of the -1 term, presented here as $\langle E\rangle = (\langle I^{Ph}_{MoS_2-QD}\rangle/\langle I^{Ph}_{MoS_2}\rangle) - 1$, which is consequently the average acceptor enhancement, E^{Avg}_{Acc}. Similarly, $J \propto \eta_{NRET}$. Therefore, it should be noted that the QD PL spectra used to calculate the spectral overlap were measured at low excitation powers, and the lifetime measurements used to calculate the NRET efficiency for each QD were carried out at low excitation powers. With this in mind, the A coefficients from Equation 8.1 were used to calculate the average photocurrent enhancements at low powers as $(A_{QD-MoS_2}/A_{MoS_2}) - 1$. This provide a more accurate description of the relationship between the photocurrent, spectral overlap, and the NRET efficiency.

A comparison of the spectral overlap, J, average photocurrent enhancements, $\langle E\rangle$, and NRET efficiency, η_{NRET}, as a function of QD emission wavelength are presented in Figure 8.9. There is good agreement between the trends of the average photocurrent, the spectral overlap, and the NRET efficiency, however, there is much better agreement between the average photocurrent enhancement at low powers, which indicates that the photocurrent enhancement in each of the hybrid devices, D450, D530 and D630 is driven by the NRET from the QDs to the MoS2. The noteworthy agreement between the trends in the average photocurrent enhancement at low powers, the NRET efficiency, and the spectral overlap, removes any ambiguity regarding the mechanism of the energy transfer, such as charge transfer, but most importantly reveals the dependence of the generated photocurrent on the NRET efficiency and similarly the spectral overlap.

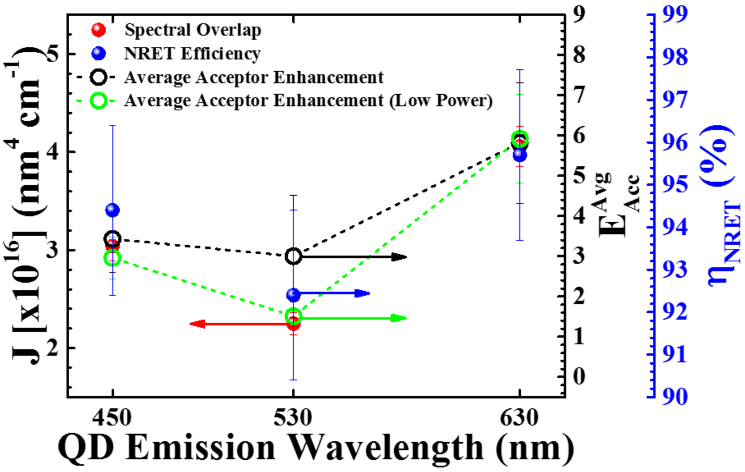

Figure 8.9: Plot of the spectral overlap, J (red dots), average photocurrent enhancement, E_{Avg} (black hollow circles), average photocurrent enhancement at low powers (green hollow circles, on black right axis) and NRET efficiency, η_{NRET} (blue dots and blue outer axis) as a function of the QD emission wavelength.

8.6 Conclusion

In summary, the work in this Chapter has demonstrated ultra-high efficiency NRET from three spectrally separated QDs to monolayer MoS_2, with emission wavelengths spanning the visible spectrum. Time-resolved photoluminescence measurements reveal NRET efficiencies exceeding 90% at each QD emission wavelength, with values of (94 ± 5)%, (92 ± 5)% and (96 ± 5)% for the 450 nm, 530 nm and 630 nm QDs, respectively. Photocurrent measurements were performed on the devices before and after adding the QD-sensitizing layers and each device displayed large enhancements of the average photocurrent due to the NRET from the QDs, with average enhancement values averaged across the full range of excitation powers, $\langle E \rangle$, of 4.4 ± 0.8, 4.0 ± 1.5 and 6.8 ± 1.5 for the D450, D530 and D630, respectively. Using low power fitting coefficients, we find average low power enhancements, of 2.9 ± 0.5, 1.51 ± 0.1 and 5.9 ± 1.1 for the devices D450, D530 and D630, respectively. The largest acceptor enhancements of the MoS_2 photocurrent were observed at the highest excitation power (~140 µW), with values of 4.4 ± 0.4, 5.0 ± 0.5 and 7.0 ± 0.7 for devices D450, D530 and D630, respectively. We observe the emergence of a super-linear dependence of photocurrent on the excitation power at high powers in each of the MoS_2 devices, with and without the QD-sensitizing layers, attributed to multi-centre recombination due to the presence of surface defects. This super-linear behavior at higher powers causes the photoresponsivity to recover and approach values close to those measured at lower excitation powers. Regarding the significance of the spectral position of the QDs, analysis and comparison of the NRET efficiencies, average low power photocurrent enhancements and the spectral overlap reveals a noteworthy agreement between each of the trends. The similarity between the trends indicates the enhancements of the photocurrent in the MoS_2 devices are due to the NRET from the QDs. We find the largest enhancements for the hybrid 630 nm QD device, which is beneficial also in terms of a solar harvesting system as the optical absorption of the 630 nm QDs has greater spectral coverage as compared to the 450 nm and 530 nm QDs, revealing that the optimal sensitizing species studied here is that of the 630 nm QDs.

Chapter 9

Conclusions and Outlook

9.1 Summary

This thesis has investigated a variety of coupled nano-systems. These systems include coupled QD-Ag nanohelices operating as optical antennas, hybrid Ag NP decorated GO composites for use as SERS substrates, QD-QW hybrid structures as a route towards light harvesting applications, and in particular the enhancement of these devices due to plasmon mediated NRET, a fundamental study of the dependence of the film quality of the active material for photocurrent enhancements in a coupled system of QDs and MoS_2, and a spectral dependence study of the NRET and photocurrent enhancements in QD-monolayer MoS_2 devices with a view towards photodetection and light harvesting applications. This summary indicates that the focus of this work involves the underlying physical concepts in these coupled nano-systems with a view towards the inclusion of these systems in a variety of device applications.

A common mechanism found throughout the thesis was that of NRET. The basics and fundamentals of NRET, and how this can be applied to systems containing QDs, particularly plane layers of QDs, were presented in Chapter 2. This chapter also includes all the relevant background for each of the physical concepts and material systems studied in this thesis and a summary of the most relevant and state-of-the-art advances in the literature. Chapter 3 introduced all the relevant information regarding the synthesis, fabrication and measurement techniques and gave detailed information about the custom built set-ups used to measure the samples throughout this thesis.

Chapter 4 focussed on the use of chiral Ag nanohelices as optical antennas. Circular dichroism spectroscopy revealed the chiral nature of the Ag nanohelices showing a strong negative circular dichroism in the visible spectrum. Time-resolved photoluminescence measurements revealed a strong interaction in the coupled system of QDs and the Ag nanohelices with an interaction efficiency of (82 ± 2)%. Analysis of the QD lifetimes on the blue (high energy) and red (low energy) side of the photoluminescence spectrum indicates the presence of plasmon enhanced intra-energy transfer between the densely packed QDs on the Ag nanohelices, with a lifetime increase of (90 ± 1)% on the red side of the spectrum. Angle-resolved photoluminescence measurements revealed the enhanced directionality of the QD far field emission pattern when the QDs were coupled to the Ag nanohelices as compared to the QDs on a planar reference substrate. Similarly, polarisation-resolved photoluminescence measurements found that the QD emission when coupled to the Ag nanohelices displayed ~17% circular polarisation in accordance with the handedness of the Ag nanohelices, further confirming the antenna behaviour in the coupled system as these properties are consistent with traditional helical antennas.[120] The near-field coupling, permitting the strong interaction between the QDs and the Ag nanohelices allows for the coupled system to behave as optical antennas.

The influence of Ag NP decorated graphene oxide (GO) composites on the fluorescence and SERS of three organic dyes; R6G, RhB, and SR101, was the investigated in Chapter 5. The impact on the dye emission due to the addition of Ag NPs on the GO monolayer flakes, forming the AgGO composite, was studied using photoluminescence and time-resolved photoluminescence measurements. Significant reductions in the dye lifetimes on the GO flakes were observed, however, further reduction of the dye lifetimes on the AgGO composite revealed the stronger interaction between the dyes and the composite. The interplay between fluorescence and SERS was further investigated with a view towards the suitability of the composite as a SERS substrate. Photoluminescence measurements confirmed the quenching of dye fluorescence on the GO flakes, however, a slight increase in the dye fluorescence intensity was observed following the addition of the Ag NPs to the GO flakes (AgGO composite). SERS measurements of each of the dyes on the AgGO substrate demonstrated a reduced fluorescence background due to the fluorescence quenching by the GO flakes in the composite. The impact of the AgGO composite on the Raman spectra for each of the dyes was quantified by the signal-to-noise ratio (*SNR*). Substantial increases in the *SNR* were found for each of the dyes on the AgGO composite as compared to the Ag NPs. The high detection sensitivity of the AgGO substrate is revealed through 'hot-spot' measurements with detection limits of 10^{-9} M, 10^{-8} M and 10^{-8} M for R6G, RhB and SR101, respectively. Analysis of the *SNR* data reveals that R6G benefits most from the composite substrate with similar improvements observed for RhB and SR101, despite the lower adsorption of SR101 dye on the AgGO composite. This agrees with the time-resolved photoluminescence data where the largest reductions in the fluorescence lifetimes on the AgGO composite are observed for both R6G and SR101. It was ultimately found that the fluorescence quenching by the GO is a more significant contribution in the SERS for R6G and RhB on the AgGO composite while the Ag NPs in the composite benefit SR101 more due to the direct enhancement of the Raman scattering signals.

In Chapter 6, the first demonstration of plasmon mediated NRET from QDs to a QW is demonstrated. Similarly, this Chapter demonstrates that the direct NRET from the QD to the QWs is well described by the d^{-4} distance dependence of conventional Förster-type NRET theory. This, in itself, is an important insight as it extends the conventional NRET formalism from its origins in molecular systems towards systems in the optoelectronics industry. It also verifies the generalised theory of Förster-type NRET, in that it is the dimensionality of the acceptor that governs the distance dependence of the NRET.[83] The plasmon mediated NRET also follows a d^{-4} distance dependence, with an enhanced characteristic distance (R_0). This indicates that the strongly coupled QD-plasmon acts as an enhanced donor dipole, as compared with the QD donor alone. Lithographically defined arrays of Ag NPs in the form of nanoboxes and nanodiscs were also introduced to investigate the plasmon mediated NRET between the QDs and the QW. A 21% increase in the NRET efficiency from the QD to the QW is found using the nanobox array, as compared to the direct QD-QW NRET efficiency. The nanobox array also gave rise to an enhancement of the QW emission above that of the QW alone. Varying the structural geometry of the plasmonic NPs allows for the interaction strength to be tuned. Quenching efficiencies of ~64% were measured on the nanodiscs array which can be reduced to ~25% on the nanobox array. The vast differences across both arrays indicate the possibility to tune the QW emission intensity through the careful consideration of the NP and array geometry.

The dependence of MoS_2 film quality for QD-sensitized MoS_2 devices was studied in Chapter 7. Raman mapping techniques were implemented to identify the MoS_2 layer thickness and the interaction between the QDs and the MoS_2 devices was investigated using photoluminescence mapping. Five MoS_2 devices were chosen for the study and consisted of varying layer thickness and quality. Time-resolved photoluminescence measurements were used to quantify the strength of the interaction between the QDs and the MoS_2 devices. The time-resolved photoluminescence measurements revealed NRET efficiencies of over 90% between the QDs and each of the MoS_2 devices. The largest NRET efficiency was found for the pristine MoS_2 monolayer device, with lower efficiencies for devices consisting of mixed monolayer/bilayer thickness, polycrystalline bilayers, and bulk-like thicknesses. Despite the high NRET efficiency, spectral photoluminescence measurements show no enhancement of the MoS_2 photoluminescence intensity due to the inclusion of the QD-sensitizing layer. The lack of photoluminescence enhancement in the MoS_2 is attributed to nonradiative recombination of excitons at defect sites. Photocurrent measurements revealed enhancements as large as ~14 fold for the pristine monolayer device due to the NRET from the QDs, with modest enhancements of ~2.5 fold for the devices consisting of mixed monolayer/bilayer thickness. There was no enhancement of the photocurrent in the polycrystalline bilayer and bulk-like thickness devices. The lack of photocurrent enhancement in these polycrystalline devices is due to the increased number of defect sites and grain boundaries at nucleation sites which increases the scattering of charge carriers and reduces the carrier mobility. Most notably, this chapter shows that the QD sensitizing layer leads to increased absorption of incident light in a 2D photodetection system and can enhance the current output from the MoS_2 devices using NRET, with the most significant advantages obtained from the pristine monolayer devices. In terms of applications, the coupled QD-MoS_2 system combines large-area synthesis of the MoS_2 films and a straight forward spin coating process, both of which are cost effective and industrially scalable methods, suggesting a potential route for hybrid 2D optoelectronic devices in light harvesting and photodetection technologies.

In Chapter 8, the first spectral dependence study of NRET and photocurrent enhancements in coupled QD-monolayer MoS_2 devices is presented. Three spectrally separated QDs with peak emission wavelengths of 450 nm, 530 nm, and 630 nm, were chosen as donors for this spectral dependence study. The 450 nm and 630 nm QDs behave as ‘on-resonance’ donors, as they overlap with the C and B excitons in the MoS_2 absorption spectrum, while the 530 nm QDs provided an ‘off-resonance’ reference. Time-resolved photoluminescence measurements reveal NRET efficiencies exceeding 90% at each QD emission wavelength, with values of (94 ± 5)%, (92 ± 5)% and (96 ± 5)% for the 450 nm, 530 nm and 630 nm QDs, respectively. The photocurrent measurements reveal large enhancements of the photocurrent on each of the devices, with average photocurrent enhancements of 4.4 ± 0.8, 4.0 ± 1.5, and 6.8 ± 1.5 for the devices sensitized with 450 nm (D450), 530 nm (D530), and 630 nm (D630) QDs, respectively. The greatest acceptor enhancements of the MoS_2 photocurrent were observed at the highest excitation power (~140 µW), with values of 4.4 ± 0.4, 5.0 ± 0.5 and 7.0 ± 0.7 for devices D450, D530 and D630, respectively. The emergence of a super-linear dependence of photocurrent on the excitation power at high powers in each of the MoS_2 devices is observed, with and without the QD-sensitizing layers. This super-linear behavior is attributed to multi-centre recombination due to the presence of surface defects. Similarly, the super-linear behavior which emerges at higher powers causes the photoresponsivity to recover and approach values close to those measured at lower excitation powers. The significance of the spectral position of the QDs is revealed following the analysis and comparison of the NRET efficiencies, spectral overlap, and the average photocurrent enhancements, which demonstrates a noteworthy agreement between each of the trends. Even better agreement between the trends is observed when considering the low excitation power photocurrent enhancements. This is due to the fact that the time-resolved photoluminescence measurements used to calculate the NRET efficiency are performed at low excitation powers and the photoluminescence spectra of the QDs used to calculate the spectral overlap were measured at low excitation powers. The similarity between the trends indicates that the enhancements of the photocurrent in the MoS_2 devices are due to the NRET from the QDs. The largest NRET efficiency and photocurrent enhancement is found for the MoS_2 device sensitized with the 630 nm QDs which is beneficial in terms of a solar harvesting application given that the optical absorption of the 630 nm QDs has greater spectral coverage as compared to the 450 nm and 530 nm QDs, revealing that the optimal sensitizing species studied here is that of the 630 nm QDs.

In conclusion, this thesis has demonstrated the importance and the relevance of understanding coupling between hybrid nanostructured systems for future compact devices with higher performance and lower power consumption in the areas of light harvesting, light emission, and sensing. Further comments on the possible future developments are provided in the following section.

9.2 Outlook

The work presented in this thesis gives insight towards the vast range of possibilities and applications that emerge from the coupling of nano-systems. The coupled QD-Ag nanohelices system only scratched the surface in terms of the manipulation of the coupled antenna system. Precise tailoring of the Ag nanohelix antenna parameters could allow for greater directionality in the emission profile and complete circular polarisation of the QD emission. Similarly, the ability to grow semiconductor nanohelices with a direct optical bandgap would eradicate the need to couple emitters to the structure and could give rise to a range of exotic, intrinsic properties in the antennas themselves, as the structural asymmetry would have a direct influence over the optical properties of the antenna.

The SERS study using the Ag NP decorated GO composite offers insight for future SERS studies and provides a guide for the choice of substrate for specific fluorescent dyes. The composite substrate studied in this thesis allows for Raman detection of high concentrations of fluorescent dyes (~10^{-3} -10^{-5} M) whereby under standard Raman or SERS protocol these dyes would fluoresce too strongly and the background fluorescence would mask the characteristic Raman peaks. This opens up a variety of potential applications for the detection of high concentrations of fluorescent dyes as DNA labels[291] in biological studies and as target analyte molecules in non-biological studies. However, some of the current challenges with these substrates and SERS in general is the surface variation of the substrate, meaning that not all dye molecules will experience the same enhancement due to the variation in ‘hot-spot’ locations, and also, not all ‘hot-spots’ will give the same enhancement. Similarly, another challenge with SERS is the quantification of the enhancement factor. At present, there is no standardised method for calculating the enhancement factor, and as a result, these enhancement factors vary quite significantly throughout the literature which makes it difficult to compare experimental results. Nonetheless, there are ongoing efforts to formulate a standardised method to calculate the enhancement factor[292] and given the ceaseless activity in this perpetually growing field it is simply a matter of time before a standardised method is introduced.

Revealing that the plasmon mediated NRET in the coupled QD-QW system follows a d^{-4} distance dependence is fundamentally interesting, although the enhancement of the characteristic interaction distance, R_0, is quite small, ~1.1 times that of the situation without the Ag NPs. Therefore, it would be shrewd to further pursue this work by optimizing the strength of the interaction. Other coating techniques could be employed to improve the uniformity of colloidal QD and Ag NP deposition on the QW surface including Langmuir–Blodgett techniques.[180,256] These, and other wet-coating processes, can be combined with chemical functionalization of the surface to produce ordered arrays.[257] Another method would be to fabricate the structure in a more ideal geometry, such as separating the QDs and Ag NPs into separate layers and placing the Ag NPs layer between the QD layer and the QW. This proves difficult however, given that both the QDs and Ag NPs are soluble in similar solvents and as such both layers would blend during separate spin coating processes. Moving to water soluble plasmonic NPs it is possible to utilise a water based polymer such as PVA as a host for the plasmonic NPs and to separate the QD/PMMA layer from QW, however, the successive deposition of water based polymers and solvent based polymers give rise to porous defects at the polymer interfaces[293] and could lead to considerable uncertainties regarding the separation distances. Regarding the lithographically defined arrays of Ag NPs, there is plenty of room from tuning. The two arrays presented in this thesis have already shown that vast differences in the interaction can be observed. This trade-off between the quenching of emission to the plasmonic NPs and NRET in the system demonstrates the tuning of the acceptor enhancement. The implementation of other geometries including triangles, rings, or split-rings[260] could lead to stronger interactions and larger enhancements in the coupled system. Alternatively, it would be interesting to reverse the system and investigate the NRET in a coupled system consisting of QW and 2D materials such as MoS_2. Utilising the QWs with different barrier thicknesses would allow for a distance dependence study between both 2D materials and it would be of significant interest to validate the generalized Förster-type NRET theory[83] in this particular materials system.

The work with the coupled QD-sensitized MoS_2 devices revealed the importance of the MoS_2 film quality and also that the photocurrent enhancements in monolayer MoS_2 devices are driven by the NRET in agreement with the spectral overlap. In terms of a light harvesting application it would be interesting to incorporate sensitizing layers of mixed QDs to further increase the absorption of incident light and allow for a cascaded NRET process[294] into the MoS_2. Similarly, this same cascaded system could be used to increase the absorption of solar energy by swapping out the MoS_2 for $MoSe_2$ which extends the absorption spectrum into the IR.[295]

References

(1) Mews, A. Nanomaterials Handbook. *Angew. Chemie Int. Ed.* **2007**, *46*, 2143–2143.

(2) Dingle, R.; Wiegmann, W.; Henry, C. H. Quantum States of Confined Carriers in Very Thin $Al_xGa_{1-x}As$-GaAs-$Al_xGa_{1-x}As$ Heterostructures. *Phys. Rev. Lett.* **1974**, *33*, 827–830.

(3) Broers, A. N.; Molzen, W. W.; Cuomo, J. J.; Wittels, N. D. Electron-Beam Fabrication of 80-Å Metal Structures. *Appl. Phys. Lett.* **1976**, *29*, 596–598.

(4) Ekimov, A. I.; Onushchenko, A. A. Quantum Size Effect in the Optical-Spectra of Semiconductor Micro-Crystals. *Soviet Physics Semiconductors-USSR*, 1982, *16*, 775–778.

(5) Rossetti, R.; Nakahara, S.; Brus, L. E. Quantum Size Effects in the Redox Potentials, Resonance Raman Spectra, and Electronic Spectra of CdS Crystallites in Aqueous Solution. *J. Chem. Phys.* **1983**, *79*, 1086–1088.

(6) Brus, L. E. Electron–electron and Electron- hole Interactions in Small Semiconductor Crystallites: The Size Dependence of the Lowest Excited Electronic State. *J. Chem. Phys.* **1984**, *80*, 4403–4409.

(7) Brus, L. E. Electronic Wave Functions in Semiconductor Clusters: Experiment and Theory. *J. Phys. Chem.* **1986**, *90*, 2555–2560.

(8) Novoselov, K. S.; Geim, A. K.; Morozov, S. V.; Jiang, D.; Zhang, Y.; Dubonos, S. V.; Grigorieva, I. V.; Firsov, A. A. Electric Field Effect in Atomically Thin Carbon Films. *Science (80).* **2004**, *306*, 666–669.

(9) Gaponenko, S. *Introduction to Nanophotonics*; Cambridege University Press, 2010.

(10) Ritchie, R. H. Plasma Losses by Fast Electrons in Thin Films. *Phys. Rev.* **1957**, *106*, 874–881.

(11) Otto, A. Excitation of Nonradiative Surface Plasma Waves in Silver by the Method of Frustrated Total Reflection. *Zeitschrift für Phys. A Hadron. Nucl.* **1968**, *216*, 398–

410.

(12) Kretschmann, E.; Raether, H. Radiative Decay of Non Radiative Surface Plasmons Excited by Light. *Zeitschrift für Naturforsch. A* **1968**, *23*, 2135–2136.

(13) Liu, N.; Tang, M. L.; Hentschel, M.; Giessen, H.; Alivisatos, A. P. Nanoantenna-Enhanced Gas Sensing in a Single Tailored Nanofocus. *Nat. Mater.* **2011**, *10*, 631–636.

(14) Lozano, G.; Louwers, D. J.; Rodríguez, S. R.; Murai, S.; Jansen, O. T.; Verschuuren, M. A.; Gómez Rivas, J. Plasmonics for Solid-State Lighting: Enhanced Excitation and Directional Emission of Highly Efficient Light Sources. *Light Sci. Appl.* **2013**, *2*, e66.

(15) Chen, W. T.; Yang, K. Y.; Wang, C. M.; Huang, Y. W.; Sun, G.; Chiang, I. Da; Liao, C. Y.; Hsu, W. L.; Lin, H. T.; Sun, S.; *et al.* High-Efficiency Broadband Meta-Hologram with Polarization-Controlled Dual Images. *Nano Lett.* **2014**, *14*, 225–230.

(16) Knight, M. W.; Sobhani, H.; Nordlander, P.; Halas, N. J. Photodetection with Active Optical Antennas. *Science* **2011**, *332*, 702–704.

(17) Kosako, T.; Kadoya, Y.; Hofmann, H. F. Directional Control of Light by a Nano-Optical Yagi–Uda Antenna. *Nat. Photonics* **2010**, *4*, 312–315.

(18) Lindfors, K.; Dregely, D.; Lippitz, M.; Engheta, N.; Totzeck, M.; Giessen, H. Imaging and Steering Unidirectional Emission from Nanoantenna Array Metasurfaces. *ACS Photonics* **2016**, *3*, 286–292.

(19) Mühlschlegel, P.; Eisler, H.-J.; Martin, O. J. F.; Hecht, B.; Pohl, D. W. Resonant Optical Antennas. *Science* **2005**, *308*, 1607–1609.

(20) Curto, A. G.; Volpe, G.; Taminiau, T. H.; Kreuzer, M. P.; Quidant, R.; van Hulst, N. F. Unidirectional Emission of a Quantum Dot Coupled to a Nanoantenna. *Science* **2010**, *329*, 930–933.

(21) Huang, K. C. Y.; Seo, M.-K.; Huo, Y.; Sarmiento, T.; Harris, J. S.; Brongersma, M.

L. Antenna Electrodes for Controlling Electroluminescence. *Nat. Commun.* **2012**, *3*, 1005.

(22) Eliel, E. L.; Wilen, S. H. *Stereochemistry of Organic Compounds*; John Wiley & Sons, 2008.

(23) Baase, W. A.; Johnson, W. C. Circular Dichroism and DNA Secondary Structure. *Nucleic Acids Res.* **1979**, *6*, 797–814.

(24) Govorov, A. O. Plasmon-Induced Circular Dichroism of a Chiral Molecule in the Vicinity of Metal Nanocrystals. Application to Various Geometries. *J. Phys. Chem. C* **2011**, *115*, 7914–7923.

(25) Fan, Z.; Govorov, A. O. Helical Metal Nanoparticle Assemblies with Defects : Plasmonic Chirality and Circular Dichroism Helical Metal Nanoparticle Assemblies with Defects : Plasmonic Chirality and Circular Dichroism. *J. Phys. Chem. C* **2011**, *115*, 13254–13261.

(26) Govorov, A. O.; Gun'ko, Y. K.; Slocik, J. M.; Gérard, V. a.; Fan, Z.; Naik, R. R. Chiral Nanoparticle Assemblies: Circular Dichroism, Plasmonic Interactions, and Exciton Effects. *J. Mater. Chem.* **2011**, *21*, 16806.

(27) Valev, V. K.; Baumberg, J. J.; Sibilia, C.; Verbiest, T. Chirality and Chiroptical Effects in Plasmonic Nanostructures: Fundamentals, Recent Progress, and Outlook. *Adv. Mater.* **2013**, *25*, 2517–2534.

(28) Cotrufo, M.; Osorio, C. I.; Koenderink, a F. Spin-Dependent Emission from Arrays of Planar Chiral Nanoantennas Due to Lattice and Localized Plasmon Resonances. *ACS Nano* **2016**, *10*, 3389–3397.

(29) Guo, K.; Du, M.; Osorio, C. I.; Koenderink, A. F. Broadband Light Scattering and Photoluminescence Enhancement from Plasmonic Vogel's Golden Spirals. *Laser Photonics Rev.* **2017**, *11*, 1–11.

(30) Mohtashami, A.; Osorio, C. I.; Koenderink, A. F. Angle-Resolved Polarimetry of

Antenna-Mediated Fluorescence. *Phys. Rev. Appl.* **2015**, *4,* 1–7.

(31) Curto, A. G.; Taminiau, T. H.; Volpe, G.; Kreuzer, M. P.; Quidant, R.; van Hulst, N. F. Multipolar Radiation of Quantum Emitters with Nanowire Optical Antennas. *Nat. Commun.* **2013**, *4,* 1750.

(32) Rose, A.; Hoang, T. B.; McGuire, F.; Mock, J. J.; Ciracì, C.; Smith, D. R.; Mikkelsen, M. H. Control of Radiative Processes Using Tunable Plasmonic Nanopatch Antennas. *Nano Lett.* **2014**, *14*, 4797–4802.

(33) Hoang, T. B.; Akselrod, G. M.; Argyropoulos, C.; Huang, J.; Smith, D. R.; Mikkelsen, M. H. Ultrafast Spontaneous Emission Source Using Plasmonic Nanoantennas. *Nat. Commun.* **2015**, *6*, 7788.

(34) Algar, W. R.; Kim, H.; Medintz, I. L.; Hildebrandt, N. Emerging Non-Traditional Förster Resonance Energy Transfer Configurations with Semiconductor Quantum Dots: Investigations and Applications. *Coord. Chem. Rev.* **2014**, *263–264*, 65–85.

(35) Jeanmaire, D. L.; Van Duyne, R. P. Surface Raman spectroelectrochemistryPart I. Heterocyclic, Aromatic, and Aliphatic Amines Adsorbed on the Anodized Silver Electrode. *J. Electroanal. Chem.* **1977**, *84*, 1–20.

(36) Chance, R. R.; Prock, A.; Silbey, R. Molecular Fluorescence and Energy Transfer near Interfaces. *Adv. Chem. Phys* **1978**, *37*, 65.

(37) Dulkeith, E.; Morteani, A. C.; Niedereichholz, T.; Klar, T. A.; Feldmann, J. Fluorescence Quenching of Dye Molecules near Gold Nanoparticles : Radiative and Nonradiative Effects. **2002**, 12–15.

(38) Anger, P.; Bharadwaj, P.; Novotny, L. Enhancement and Quenching of Single-Molecule Fluorescence. *Phys. Rev. Lett.* **2006**, *96*, 3–6.

(39) Kühn, S.; Håkanson, U.; Rogobete, L.; Sandoghdar, V. Enhancement of Single-Molecule Fluorescence Using a Gold Nanoparticle as an Optical Nanoantenna. *Phys. Rev. Lett.* **2006**, *97*, 1–4.

(40) Yun, C. S.; Javier, A.; Jennings, T.; Fisher, M.; Hira, S.; Peterson, S.; Hopkins, B.; Reich, N. O.; Strouse, G. F. Nanometal Surface Energy Transfer in Optical Rulers, Breaking the FRET Barrier. *J. Am. Chem. Soc.* **2005**, *127*, 3115–3119.

(41) Hua, X. M.; Gersten, J. I.; Nitzan, A. Theory of Energy Transfer between Molecules near Solid State Particles. *J. Chem. Phys.* **1985**, *83*, 3650–3659.

(42) Govorov, A. O.; Lee, J.; Kotov, N. A. Theory of Plasmon-Enhanced Förster Energy Transfer in Optically Excited Semiconductor and Metal Nanoparticles. *Phys. Rev. B* **2007**, *76*, 125308.

(43) Marocico, C. A.; Zhang, X.; Bradley, A. L. A Theoretical Investigation of the Influence of Gold Nanosphere Size on the Decay and Energy Transfer Rates and Efficiencies of Quantum Emitters. *J. Chem. Phys.* **2016**, *144*, 24108.

(44) Zhang, J.; Fu, Y.; Chowdhury, M. H.; Lakowicz, J. R. Enhanced Förster Resonance Energy Transfer on Single Metal Particle. 2. Dependence on Donor−Acceptor Separation Distance, Particle Size, and Distance from Metal Surface. *J. Phys. Chem. C* **2007**, *111*, 11784–11792.

(45) Faessler, V.; Hrelescu, C.; Lutich, A. A.; Osinkina, L.; Mayilo, S.; J??ckel, F.; Feldmann, J. Accelerating Fluorescence Resonance Energy Transfer with Plasmonic Nanoresonators. *Chem. Phys. Lett.* **2011**, *508*, 67–70.

(46) Zhao, X.; Wang, P.; Li, B. Surface Plasmon Enhanced Energy Transfer in Metal–semiconductor Hybrid Nanostructures. *Nanoscale* **2011**, *3*, 3056.

(47) Zhao, L.; Ming, T.; Shao, L.; Chen, H.; Wang, J. Plasmon-Controlled Förster Resonance Energy Transfer. *J. Phys. Chem. C* **2012**, *116*, 8287–8296.

(48) L-Viger, M.; Brouard, D.; Boudreau, D. Plasmon-Enhanced Resonance Energy Transfer from a Conjugated Polymer to Fluorescent Multi Layer Core-Shell Nanoparticles: A Photophysical Study. *J. Phys. Chem. C* **2011**, *115*, 2974–2981.

(49) Komarala, V. K.; Rakovich, Y. P.; Bradley, A. L.; Byrne, S. J.; Gun'ko, Y. K.;

Gaponik, N.; Eychmüller, A. Off-Resonance Surface Plasmon Enhanced Spontaneous Emission from CdTe Quantum Dots. *Appl. Phys. Lett.* **2006**, *89*, 2004–2007.

(50) Lunz, M.; Gerard, V. A.; Gun'ko, Y. K.; Lesnyak, V.; Gaponik, N.; Susha, A. S.; Rogach, A. L.; Bradley, A. L. Surface Plasmon Enhanced Energy Transfer between Donor and Acceptor CdTe Nanocrystal Quantum Dot Monolayers. *Nano Lett.* **2011**, *11*, 3341–3345.

(51) Lunz, M.; Zhang, X.; Gerard, V. A.; Gun'ko, Y. K.; Lesnyak, V.; Gaponik, N.; Susha, A. S.; Rogach, A. L.; Bradley, A. L. Effect of Metal Nanoparticle Concentration on Localized Surface Plasmon Mediated Förster Resonant Energy Transfer. *J. Phys. Chem. C* **2012**, *116*, 26529–26534.

(52) Zhang, X.; Marocico, C. A.; Lunz, M.; Gerard, V. A.; Gun'Ko, Y. K.; Lesnyak, V.; Gaponik, N.; Susha, A. S.; Rogach, A. L.; Bradley, A. L. Wavelength, Concentration, and Distance Dependence of Nonradiative Energy Transfer to a Plane of Gold Nanoparticles. *ACS Nano* **2012**, *6*, 9283–9290.

(53) Zhang, X.; Marocico, C. A.; Lunz, M.; Gerard, V. A.; Gun'ko, Y. K.; Lesnyak, V.; Gaponik, N.; Susha, A. S.; Rogach, A. L.; Bradley, A. L. Experimental and Theoretical Investigation of the Distance Dependence of Localized Surface Plasmon Coupled Förster Resonance Energy Transfer. *ACS Nano* **2014**, *8*, 1273–1283.

(54) Delalande, C.; Orgonasi, J.; Brum, J. A.; Bastard, G.; Voos, M.; Weimann, G.; Schlapp, W. Optical Studies of GaAs Quantum Well Based Field-Effect Transistor. *Appl. Phys. Lett.* **1987**, *51*, 1346–1348.

(55) Nakamura, S.; Senoh, M.; Iwasa, N.; Nagahama, S. chi. High-Power InGaN Single-Quantum-Well-Structure Blue and Violet Light-Emitting Diodes. *Appl. Phys. Lett.* **1995**, *67*, 1868–1870.

(56) Achermann, M.; Petruska, M. A.; Kos, S.; Smith, D. L.; Koleske, D. D.; Klimov, V.

I. Energy-Transfer Pumping of Semiconductor Nanocrystals Using an Epitaxial Quantum Well. *Nature* **2004**, *429*, 642–646.

(57) Achermann, M.; Petruska, M. a; Koleske, D. D.; Crawford, M. H.; Klimov, V. I. Nanocrystal-Based Light-Emitting Diodes Utilizing High-Efficiency Nonradiative Energy Transfer for Color Conversion. *Nano Lett.* **2006**, *6*, 1396–1400.

(58) Klimov, V. I.; Mikhailovsky, A. A.; Xu, S.; Malko, A.; Hollingsworth, J. A.; Leatherdale, C. A.; Eisler, H.; Bawendi, M. G. Optical Gain and Stimulated Emission in Nanocrystal Quantum Dots. *Science* **2000**, *290*, 314–317.

(59) Lu, S.; Madhukar, A. Nonradiative Resonant Excitation Transfer from Nanocrystal Quantum Dots to Adjacent Quantum Channels. *Nano Lett.* **2007**, *7*, 3443–3451.

(60) Lee, K.-H.; Han, C.-Y.; Kang, H.-D.; Ko, H.; Lee, C.; Lee, J.; Myoung, N.; Yim, S.-Y.; Yang, H. Highly Efficient, Color-Reproducible Full-Color Electroluminescent Devices Based on Red/Green/Blue Quantum Dot-Mixed Multilayer. *ACS Nano* **2015**, *9*, 10941–10949.

(61) Mak, K. F.; Lee, C.; Hone, J.; Shan, J.; Heinz, T. F. Atomically Thin MoS_2: A New Direct-Gap Semiconductor. *Phys. Rev. Lett.* **2010**, *105*, 136805.

(62) Eda, G.; Yamaguchi, H.; Voiry, D.; Fujita, T.; Chen, M.; Chhowalla, M. Photoluminescence from Chemically Exfoliated MoS_2. *Nano Lett.* **2011**, *11*, 5111–5116.

(63) Splendiani, A.; Sun, L.; Zhang, Y.; Li, T.; Kim, J.; Chim, C.-Y.; Galli, G.; Wang, F. Emerging Photoluminescence in Monolayer MoS_2. *Nano Lett.* **2010**, *10*, 1271–1275.

(64) Yeltik, A.; Kucukayan-Dogu, G.; Guzelturk, B.; Fardindoost, S.; Kelestemur, Y.; Demir, H. V. Evidence for Nonradiative Energy Transfer in Graphene-Oxide-Based Hybrid Structures. *J. Phys. Chem. C* **2013**, *117*, 25298–25304.

(65) Prins, F.; Goodman, A. J.; Tisdale, W. A. Reduced Dielectric Screening and Enhanced Energy Transfer in Single- and Few-Layer MoS_2. *Nano Lett.* **2014**, *14*,

6087–6091.

(66) Raja, A.; Montoya-Castillo, A.; Zultak, J.; Zhang, X.-X.; Ye, Z.; Roquelet, C.; Chenet, D. a; van der Zande, A. M.; Huang, P.; Jockusch, S.; *et al.* Energy Transfer from Quantum Dots to Graphene and MoS_2: The Role of Absorption and Screening in Two-Dimensional Materials. *Nano Lett.* **2016**.

(67) Sampat, S.; Guo, T.; Zhang, K.; Robinson, J. a.; Ghosh, Y.; Acharya, K. P.; Htoon, H.; Hollingsworth, J. a.; Gartstein, Y. N.; Malko, A. V. Exciton and Trion Energy Transfer from Giant Semiconductor Nanocrystals to MoS_2 Monolayers. *ACS Photonics* **2016**, *3*, 708–715.

(68) Guzelturk, B.; Demir, H. V. Near-Field Energy Transfer Using Nanoemitters For Optoelectronics. *Adv. Funct. Mater.* **2016**.

(69) Gaponenko, S. V. *Optical Properties of Semiconductor Nanocrystals*; Cambridge University Press: Cambridge, 1998.

(70) Hines, M. A.; Guyot-Sionnest, P. Synthesis and Characterization of Strongly Luminescing ZnS-Capped CdSe Nanocrystals. *J. Phys. Chem.* **1996**, *100*, 468–471.

(71) Gaponik, N.; Talapin, D. V; Rogach, A. L.; Hoppe, K.; Shevchenko, E. V; Kornowski, A.; Eychmüller, A.; Weller, H. Thiol-Capping of CdTe Nanocrystals: An Alternative to Organometallic Synthetic Routes. *J. Phys. Chem. B* **2002**, *106*, 7177–7185.

(72) Chan, W. C. .; Maxwell, D. J.; Gao, X.; Bailey, R. E.; Han, M.; Nie, S. Luminescent Quantum Dots for Multiplexed Biological Detection and Imaging. *Curr. Opin. Biotechnol.* **2002**, *13*, 40–46.

(73) Reiss, P.; Bleuse, J.; Pron, A. Highly Luminescent CdSe/ZnSe Core/Shell Nanocrystals of Low Size Dispersion. *Nano Lett.* **2002**, *2*, 781–784.

(74) Shirasaki, Y.; Supran, G. J.; Bawendi, M. G.; Bulović, V. Emergence of Colloidal Quantum-Dot Light-Emitting Technologies. *Nat. Photonics* **2012**, *7*, 13–23.

(75) Somers, R. C.; Bawendi, M. G.; Nocera, D. G. CdSe Nanocrystal Based Chem-/bio-Sensors. *Chem. Soc. Rev.* **2007**, *36*, 579.

(76) Wang, C.; Gao, X.; Su, X. In Vitro and in Vivo Imaging with Quantum Dots. *Anal. Bioanal. Chem.* **2010**, *397*, 1397–1415.

(77) Konstantatos, G.; Howard, I.; Fischer, A.; Hoogland, S.; Clifford, J.; Klem, E.; Levina, L.; Sargent, E. H. Ultrasensitive Solution-Cast Quantum Dot Photodetectors. *Nature* **2006**, *442*, 180–183.

(78) McDonald, S. A.; Konstantatos, G.; Zhang, S.; Cyr, P. W.; Klem, E. J. D.; Levina, L.; Sargent, E. H. Solution-Processed PbS Quantum Dot Infrared Photodetectors and Photovoltaics. *Nat. Mater.* **2005**, *4*, 138–142.

(79) Tu, C.-C.; Lin, L. Y. High Efficiency Photodetectors Fabricated by Electrostatic Layer-by-Layer Self-Assembly of CdTe Quantum Dots. *Appl. Phys. Lett.* **2008**, *93*, 163107.

(80) Kamat, P. V. Quantum Dot Solar Cells. Semiconductor Nanocrystals as Light Harvesters. *J. Phys. Chem. C* **2008**, *112*, 18737–18753.

(81) Rogach, A. L. *Semiconductor Nanocrystal Quantum Dots*; Rogach, A. L., Ed.; Springer Vienna: Vienna, 2008.

(82) Lakowicz, J. R. *Principles of Fluorescence Spectroscopy*; Lakowicz, J. R., Ed.; Springer US: Boston, MA, 2006.

(83) Hernández-Martínez, P. L.; Govorov, A. O.; Demir, H. V. Generalized Theory of Förster-Type Nonradiative Energy Transfer in Nanostructures with Mixed Dimensionality. *J. Phys. Chem. C* **2013**, *117*, 10203–10212.

(84) Förster, T. Zwischenmolekulare Energiewanderung Und Fluoreszenz. *Ann. Phys.* **1948**, *437*, 55–75.

(85) Medintz, I.; Hildebrandt, N. FRET – Förster Resonance Energy Transfer: From Theory to Applications. **2014**.

(86) Wolber, P. K.; Hudson, B. S. An Analytic Solution to the Förster Energy Transfer Problem in Two Dimensions. *Biophys. J.* **1979**, *28*, 197–210.

(87) Lunz, M.; Bradley, A. L.; Gerard, V. A.; Byrne, S. J.; Gun'ko, Y. K.; Lesnyak, V.; Gaponik, N. Concentration Dependence of Förster Resonant Energy Transfer between Donor and Acceptor Nanocrystal Quantum Dot Layers: Effect of Donor-Donor Interactions. *Phys. Rev. B* **2011**, *83*, 115423.

(88) Lunz, M.; Bradley, a. L.; Chen, W.-Y.; Gerard, V. a.; Byrne, S. J.; Gun'ko, Y. K.; Lesnyak, V.; Gaponik, N. Influence of Quantum Dot Concentration on Förster Resonant Energy Transfer in Monodispersed Nanocrystal Quantum Dot Monolayers. *Phys. Rev. B* **2010**, *81*, 205316.

(89) Scholes, G. D.; Andrews, D. L. Resonance Energy Transfer and Quantum Dots. *Phys. Rev. B* **2005**, *72*, 125331.

(90) Dexter, D. L. A Theory of Sensitized Luminescence in Solids. *J. Chem. Phys.* **1953**, *21*, 836–850.

(91) Marcus, R. A. On the Theory of Oxidation-Reduction Reactions Involving Electron Transfer. *J. Chem. Phys.* **1956**, *24*, 966–978.

(92) Marcus, R. A. Electrostatic Free Energy and Other Properties of States Having Nonequilibrium Polarization. *J. Chem. Phys.* **1956**, *24*, 979–989.

(93) Adams, D. M.; Brus, L.; Chidsey, C. E. D.; Creager, S.; Creutz, C.; Kagan, C. R.; Kamat, P. V.; Lieberman, M.; Lindsay, S.; Marcus, R. A.; *et al.* Charge Transfer on the Nanoscale: Current Status. *J. Phys. Chem. B* **2003**, *107*, 6668–6697.

(94) Andrews, D. L. A Unified Theory of Radiative and Radiationless Molecular Energy Transfer. *Chem. Phys.* **1989**, *135*, 195–201.

(95) Andrew, P.; Barnes, W. L. Energy Transfer Across a Metal Film Mediated by Surface Plasmon Polaritons. *Science (80-.).* **2004**, *306*, 1002–1005.

(96) Barbara, P. F.; Meyer, T. J.; Ratner, M. a. Contemporary Issues in Electron Transfer

Research. *J. Phys. Chem.* **1996**, *100*, 13148–13168.

(97) Goodfellow, K. M.; Chakraborty, C.; Sowers, K.; Waduge, P.; Wanunu, M.; Krauss, T.; Driscoll, K.; Vamivakas, a. N. Distance-Dependent Energy Transfer between CdSe/CdS Quantum Dots and a Two-Dimensional Semiconductor. *Appl. Phys. Lett.* **2016**, *108*, 21101.

(98) Murphy, G. P.; Gough, J. J.; Higgins, L. J.; Karanikolas, V. D.; Wilson, K. M.; Garcia Coindreau, J. A.; Zubialevich, V. Z.; Parbrook, P. J.; Bradley, A. L. Ag Colloids and Arrays for Plasmonic Non-Radiative Energy Transfer from Quantum Dots to a Quantum Well. *Nanotechnology* **2017**, *28*, 115401.

(99) Maier, S. a. *Plasmonics : Fundamentals and Applications*; Springer, 2004.

(100) Shalaev, V. M.; Kawata, S. *Nanophotonics with Surface Plasmons*; Elsevier, 2007.

(101) Willets, K. A.; Van Duyne, R. P. Localized Surface Plasmon Resonance Spectroscopy and Sensing. *Annu. Rev. Phys. Chem.* **2007**, *58*, 267–297.

(102) Bohren, C. F.; Huffman, D. R. *Absorption and Scattering of Light by Small Particles*; Wiley-Interscience, 1983.

(103) Ferry, V. E.; Sweatlock, L. A.; Pacifici, D.; Atwater, H. A. Plasmonic Nanostructure Design for Efficient Light Coupling into Solar Cells. *Nano Lett.* **2008**, *8*, 4391–4397.

(104) Gersten, J. I.; Nitzan, A. Accelerated Energy Transfer between Molecules near a Solid Particle. *Chem. Phys. Lett.* **1984**, *104*, 31–37.

(105) Lakowicz, J. R.; Kuśba, J.; Shen, Y.; Malicka, J.; D'Auria, S.; Gryczynski, Z.; Gryczynski, I. Effects of Metallic Silver Particles on Resonance Energy Transfer between Fluorophores Bound to DNA. *J. Fluoresc.* **2003**, *13*, 69–77.

(106) Zhang, J.; Fu, Y.; Lakowicz, J. R. Enhanced Förster Resonance Energy Transfer (FRET) on a Single Metal Particle. *J. Phys. Chem. C* **2007**, *111*, 50–56.

(107) De Torres, J.; Ferrand, P.; Colas Des Francs, G.; Wenger, J. Coupling Emitters and Silver Nanowires to Achieve Long-Range Plasmon-Mediated Fluorescence Energy

Transfer. *ACS Nano* **2016**, *10*, 3968–3976.

(108) Ghenuche, P.; Mivelle, M.; De Torres, J.; Moparthi, S. B.; Rigneault, H.; Van Hulst, N. F.; García-Parajó, M. F.; Wenger, J. Matching Nanoantenna Field Confinement to FRET Distances Enhances Förster Energy Transfer Rates. *Nano Lett.* **2015**, *15*, 6193–6201.

(109) Su, X.-R.; Zhang, W.; Zhou, L.; Peng, X.-N.; Pang, D.-W.; Liu, S.-D.; Zhou, Z.-K.; Wang, Q.-Q. Multipole-Plasmon-Enhanced Förster Energy Transfer between Semiconductor Quantum Dots via Dual-Resonance Nanoantenna Effects. *Appl. Phys. Lett.* **2010**, *96*, 43106.

(110) Wang, C. H.; Chen, C. W.; Chen, Y. T.; Wei, C. M.; Chen, Y. F.; Lai, C. W.; Ho, M. L.; Chou, P. T.; Hofmann, M. Surface Plasmon Enhanced Energy Transfer between Type I CdSe/ZnS and Type II CdSe/ZnTe Quantum Dots. *Appl. Phys. Lett.* **2010**, *96*, 94–97.

(111) West, R. G.; Sadeghi, S. M. Enhancement of Energy Transfer between Quantum Dots: The Impact of Metallic Nanoparticle Sizes. *J. Phys. Chem. C* **2012**, *116*, 20496–20503.

(112) Ozel, T.; Hernandez-Martinez, P. L.; Mutlugun, E.; Akin, O.; Nizamoglu, S.; Ozel, I. O.; Zhang, Q.; Xiong, Q.; Demir, H. V. Observation of Selective Plasmon-Exciton Coupling in Nonradiative Energy Transfer: Donor-Selective versus Acceptor-Selective Plexcitons. *Nano Lett.* **2013**, *13*, 3065–3072.

(113) Pons, T.; Medintz, I. L.; Sapsford, K. E.; Higashiya, S.; Grimes, A. F.; English, D. S.; Mattoussi, H. On the Quenching of Semiconductor Quantum Dot Photoluminescence by Proximal Gold Nanoparticles. *Nano Lett.* **2007**, *7*, 3157–3164.

(114) Wargnier, R.; Baranov, A. V.; Maslov, V. G.; Stsiapura, V.; Artemyev, M.; Pluot, M.; Sukhanova, A.; Nabiev, I. Energy Transfer in Aqueous Solutions of Oppositely Charged CdSe/ZnS Core/Shell Quantum Dots and in Quantum Dot−Nanogold

Assemblies. *Nano Lett.* **2004**, *4*, 451–457.

(115) Govorov, A. O.; Bryant, G. W.; Zhang, W.; Skeini, T.; Lee, J.; Kotov, N. A.; Slocik, J. M.; Naik, R. R. Exciton−Plasmon Interaction and Hybrid Excitons in Semiconductor−Metal Nanoparticle Assemblies. *Nano Lett.* **2006**, *6*, 984–994.

(116) Viste, P.; Plain, J.; Jaffiol, R.; Vial, A.; Adam, P. M.; Royer, P. Enhancement and Quenching Regimes in Metal−Semiconductor Hybrid Optical Nanosources. *ACS Nano* **2010**, *4*, 759–764.

(117) Ozel, T.; Nizamoglu, S.; Sefunc, M. A.; Samarskaya, O.; Ozel, I. O.; Mutlugun, E.; Lesnyak, V.; Gaponik, N.; Eychmuller, A.; Gaponenko, S. V.; *et al.* Anisotropic Emission from Multilayered Plasmon Resonator Nanocomposites of Isotropic Semiconductor Quantum Dots. *ACS Nano* **2011**, *5*, 1328–1334.

(118) Guzatov, D. V.; Vaschenko, S. V.; Stankevich, V. V.; Lunevich, A. Y.; Glukhov, Y. F.; Gaponenko, S. V. Plasmonic Enhancement of Molecular Fluorescence near Silver Nanoparticles: Theory, Modeling, and Experiment. *J. Phys. Chem. C* **2012**, *116*, 10723–10733.

(119) IEEE Transactions on Antennas and Propagation, Vols. AP-17, No. 3, May 1969; AP-22, No. 1, January 1974; and AP-31, No. 6, Part II, November 1983.

(120) Balanis. *Antenna Theory: Analysis and Design*; Wiley, 2005.

(121) Schuller, J. a; Barnard, E. S.; Cai, W.; Jun, Y. C.; White, J. S.; Brongersma, M. L. Plasmonics for Extreme Light Concentration and Manipulation. *Nat. Mater.* **2010**, *9*, 193–204.

(122) Caridad, J. M.; McCloskey, D.; Donegan, J. F.; Krstić, V. Controllable Growth of Metallic Nano-Helices at Room Temperature Conditions. *Appl. Phys. Lett.* **2014**, *105*, 233114.

(123) Caridad, J. M.; McCloskey, D.; Rossella, F.; Bellani, V.; Donegan, J. F.; Krstić, V. Effective Wavelength Scaling of and Damping in Plasmonic Helical Antennae. *ACS*

Photonics **2015**, 150513092537001.

(124) Bharadwaj, P.; Deutsch, B.; Novotny, L. Optical Antennas. *Adv. Opt. Photonics* **2009**, *1*, 438.

(125) Novotny, L.; van Hulst, N. Antennas for Light. *Nat. Photonics* **2011**, *5*, 83–90.

(126) Gersen, H.; García-Parajó, M. F.; Novotny, L.; Veerman, J. a.; Kuipers, L.; Van Hulst, N. F. Influencing the Angular Emission of a Single Molecule. *Phys. Rev. Lett.* **2000**, *85*, 5312–5315.

(127) Taminiau, T. H.; Stefani, F. D.; van Hulst, N. F. Enhanced Directional Excitation and Emission of Single Emitters by a Nano-Optical Yagi-Uda Antenna. *Opt. Express* **2008**, *16*, 10858–6.

(128) Rakovich, A.; Albella, P.; Maier, S. A. Plasmonic Control of Radiative Properties of Semiconductor Quantum Dots Coupled to Plasmonic Ring Cavities. **2015**, 2648–2658.

(129) Kern, J.; Kullock, R.; Prangsma, J.; Emmerling, M.; Kamp, M.; Hecht, B. Electrically Driven Optical Antennas. *Nat. Photonics* **2015**, *9*, 582–586.

(130) Mark, A. G.; Gibbs, J. G.; Lee, T.-C.; Fischer, P. Hybrid Nanocolloids with Programmed Three-Dimensional Shape and Material Composition. *Nat. Mater.* **2013**, *12*, 802–807.

(131) Larsen, G. K.; He, Y.; Wang, J.; Zhao, Y. Scalable Fabrication of Composite Ti/Ag Plasmonic Helices: Controlling Morphology and Optical Activity by Tailoring Material Properties. *Adv. Opt. Mater.* **2014**, *2*, 245–249.

(132) Gibbs, J. G.; Mark, A. G.; Lee, T.; Eslami, S.; Schamel, D.; Fischer, P. Nanohelices by Shadow Growth. *Nanoscale* **2014**, *6*, 9457–9466.

(133) Melnikau, D.; Savateeva, D.; Gun’ko, Y. K.; Rakovich, Y. P. Strong Enhancement of Circular Dichroism in a Hybrid Material Consisting of J-Aggregates and Silver Nanoparticles. *J. Phys. Chem. C* **2013**, *117*, 13708–13712.

(134) Abdulrahman, N. a; Fan, Z.; Tonooka, T.; Kelly, S. M.; Gadegaard, N.; Hendry, E.; Govorov, A. O.; Kadodwala, M. Induced Chirality through Electromagnetic Coupling between Chiral Molecular Layers and Plasmonic Nanostructures. *Nano Lett.* **2012**, *12*, 977–983.

(135) Kuzyk, A.; Schreiber, R.; Fan, Z.; Pardatscher, G.; Roller, E.-M.; Högele, A.; Simmel, F. C.; Govorov, A. O.; Liedl, T. DNA-Based Self-Assembly of Chiral Plasmonic Nanostructures with Tailored Optical Response. *Nature* **2012**, *483*, 311–314.

(136) Arteaga, O.; Sancho-Parramon, J.; Nichols, S.; Maoz, B. M.; Canillas, A.; Bosch, S.; Markovich, G.; Kahr, B. Relation between 2D/3D Chirality and the Appearance of Chiroptical Effects in Real Nanostructures. *Opt. Express* **2016**, *24*, 2242.

(137) Gansel, J. K.; Thiel, M.; Rill, M. S.; Decker, M.; Bade, K.; Saile, V.; von Freymann, G.; Linden, S.; Wegener, M. Gold Helix Photonic Metamaterial as Broadband Circular Polarizer. *Science* **2009**, *325*, 1513–1515.

(138) Helgert, C.; Pshenay-Severin, E.; Falkner, M.; Menzel, C.; Rockstuhl, C.; Kley, E.-B.; Tünnermann, A.; Lederer, F.; Pertsch, T. Chiral Metamaterial Composed of Three-Dimensional Plasmonic Nanostructures. *Nano Lett.* **2011**, *11*, 4400–4404.

(139) Wu, L.; Yang, Z.; Cheng, Y.; Lu, Z.; Zhang, P.; Zhao, M.; Gong, R.; Yuan, X.; Zheng, Y.; Duan, J. Electromagnetic Manifestation of Chirality in Layer-by-Layer Chiral Metamaterials. *Opt. Express* **2013**, *21*, 5239–5246.

(140) Larsen, G. K.; He, Y.; Wang, J.; Zhao, Y. Scalable Fabrication of Composite Ti / Ag Plasmonic Helices : Controlling Morphology and Optical Activity by Tailoring Material Properties. **2014**.

(141) Gibbs, J. G.; Mark, a. G.; Eslami, S.; Fischer, P. Plasmonic Nanohelix Metamaterials with Tailorable Giant Circular Dichroism. *Appl. Phys. Lett.* **2013**, *103*, 213101.

(142) Raman, C. V.; Krishnan, K. S. The Production of New Radiations by Light Scattering. Part I. *Proc. R. Soc. A Math. Phys. Eng. Sci.* **1929**, *122*, 23–35.

(143) Goulet, P. J. G.; Aroca, R. F. Distinguishing Individual Vibrational Fingerprints: Single-Molecule Surface-Enhanced Resonance Raman Scattering from One-to-One Binary Mixtures in Langmuir-Blodgett Monolayers. *Anal. Chem.* **2007**, *79*, 2728–2734.

(144) Palings, I.; Van den Berg, E.; Mathies, R. A.; Pardoen, J. A.; Winkel, C.; Lugtenburg, J. Assignment of Fingerprint Vibrations in the Resonance Raman Spectra of Rhodopsin, Isorhodopsin, and Bathorhodopsin: Implications for Chromophore Structure and Environment. *Biochemistry* **1987**, *26*, 2544–2556.

(145) Albrecht, M. G.; Creighton, J. A. Anomalously Intense Raman Spectra of Pyridine at a Silver Electrode. *J. Am. Chem. Soc.* **1977**, *99*, 5215–5217.

(146) Fleischmann, M.; Hendra, P. J.; McQuillan, A. J. Raman Spectra of Pyridine Adsorbed at a Silver Electrode. *Chem. Phys. Lett.* **1974**, *26*, 163–166.

(147) Campion, A.; Kambhampati, P. Surface-Enhanced Raman Scattering. *Chem. Soc. Rev.* **1998**, *27*, 240–249.

(148) Sharma, B.; Frontiera, R. R.; Henry, A.-I.; Ringe, E.; Van Duyne, R. P. SERS: Materials, Applications, and the Future. *Mater. Today* **2012**, *15*, 16–25.

(149) Fan, M.; Andrade, G. F. S.; Brolo, A. G. A Review on the Fabrication of Substrates for Surface Enhanced Raman Spectroscopy and Their Applications in Analytical Chemistry. *Anal. Chim. Acta* **2011**, *693*, 7–25.

(150) Zou, X.; Dong, S. Surface-Enhanced Raman Scattering Studies on Aggregated Silver Nanoplates in Aqueous Solution. *J. Phys. Chem. B* **2006**, *110*, 21545–21550.

(151) Schwartzberg, A. M.; Grant, C. D.; Wolcott, A.; Talley, C. E.; Huser, T. R.; Bogomolni, R.; Zhang, J. Z. Unique Gold Nanoparticle Aggregates as a Highly Active Surface-Enhanced Raman Scattering Substrate. *J. Phys. Chem. B* **2004**, *108*, 19191–19197.

(152) Ling, X.; Xie, L.; Fang, Y.; Xu, H.; Zhang, H.; Kong, J.; Dresselhaus, M. S.; Zhang,

J.; Liu, Z. Can Graphene Be Used as a Substrate for Raman Enhancement? *Nano Lett.* **2010**, *10*, 553–561.

(153) Wojcik, A.; Kamat, P. V. Reduced Graphene Oxide and Porphyrin. An Interactive Affair in 2-D. *ACS Nano* **2010**, *4*, 6697–6706.

(154) Wang, X.; Huang, P.; Feng, L.; He, M.; Guo, S.; Shen, G.; Cui, D. Green Controllable Synthesis of Silver Nanomaterials on Graphene Oxide Sheets via Spontaneous Reduction. *RSC Adv.* **2012**, *2*, 3816.

(155) Yu, X.; Cai, H.; Zhang, W.; Li, X.; Pan, N.; Luo, Y.; Wang, X.; Hou, J. G. Tuning Chemical Enhancement of SERS by Controlling the Chemical Reduction of Graphene Oxide Nanosheets. *ACS Nano* **2011**, *5*, 952–958.

(156) Zhang, Z.; Xu, F.; Yang, W.; Guo, M.; Wang, X.; Zhang, B.; Tang, J. A Facile One-Pot Method to High-Quality Ag-Graphene Composite Nanosheets for Efficient Surface-Enhanced Raman Scattering. *Chem. Commun. (Camb).* **2011**, *47*, 6440–6442.

(157) Murphy, S.; Huang, L.; Kamat, P. V. Reduced Graphene Oxide − Silver Nanoparticle Composite as an Active SERS Material. **2013**.

(158) Zhang, Y.; Liu, S.; Wang, L.; Qin, X.; Tian, J.; Lu, W.; Chang, G.; Sun, X. One-Pot Green Synthesis of Ag Nanoparticles-Graphene Nanocomposites and Their Applications in SERS, H_2O_2, and Glucose Sensing. *RSC Adv.* **2012**, *2*, 538.

(159) Zhou, Y.; Cheng, X.; Du, D.; Yang, J.; Zhao, N.; Ma, S.; Zhong, T.; Lin, Y. Graphene–silver Nanohybrids for Ultrasensitive Surface Enhanced Raman Spectroscopy: Size Dependence of Silver Nanoparticles. *J. Mater. Chem. C* **2014**, *2*, 6850.

(160) Ding, G.; Xie, S.; Liu, Y.; Wang, L.; Xu, F. Applied Surface Science Graphene Oxide-Silver Nanocomposite as SERS Substrate for Dye Detection : Effects of Silver Loading Amount and Composite Dosage. *Appl. Surf. Sci.* **2015**, *345*, 310–318.

(161) Liang, X.; You, T.; Liu, D.; Lang, X.; Tan, E.; Shi, J.; Yin, P.; Guo, L. Direct Observation of Enhanced Plasmon-Driven Catalytic Reaction Activity of Au Nanoparticles Supported on Reduced Graphene Oxides by SERS. *Phys. Chem. Chem. Phys.* **2015**, *17*, 10176–10181.

(162) Weisbuch, C.; Vinter, B. *Quantum Semiconductor Structures: Fundamentals and Applications*; Academic press, 2014.

(163) Miller, D. A. B. Optical Physics of Quantum Wells. *Quantum Dyn. Simple Syst.* **1996**, 239–266.

(164) Miller, D. A. B. Device Requirements for Optical Interconnects to Silicon Chips. *Proc. IEEE* **2009**, *97*, 1166–1185.

(165) Mukai, T.; Yamada, M.; Nakamura, S. Characteristics of InGaN-Based UV/Blue/Green/Amber/Red Light-Emitting Diodes. *Jpn. J. Appl. Phys.* **1999**, *38*, 3976–3981.

(166) Nakamura, S.; Senoh, M.; Iwasa, N.; Nagahama, S.; Yamada, T.; Mukai, T. Superbright Green InGaN Single-Quantum-Well-Structure Light-Emitting Diodes. *Jpn. J. Appl. Phys.* **1995**, *34*, L1332–L1335.

(167) Arif, R. A.; Zhao, H.; Ee, Y.-K.; Tansu, N. Spontaneous Emission and Characteristics of Staggered InGaN Quantum-Well Light-Emitting Diodes. *IEEE J. Quantum Electron.* **2008**, *44*, 573–580.

(168) Chow, W. W.; Koch, S. W. *Semiconductor-Laser Fundamentals: Physics of the Gain Materials*; Springer Science & Business Media, 2013.

(169) Zory, P. S. *Quantum Well Lasers*; Academic Press, 1993.

(170) Lien, D.-H.; Hsiao, Y.-H.; Yang, S.-G.; Tsai, M.-L.; Wei, T.-C.; Lee, S.-C.; He, J.-H. Harsh Photovoltaics Using InGaN/GaN Multiple Quantum Well Schemes. *Nano Energy* **2015**, *11*, 104–109.

(171) Jani, O.; Ferguson, I.; Honsberg, C.; Kurtz, S. Design and Characterization of

GaNInGaN Solar Cells. *Appl. Phys. Lett.* **2007**, *91*, 1–4.

(172) Chanyawadee, S.; Harley, R. T.; Taylor, D.; Henini, M.; Susha, A. S.; Rogach, A. L.; Lagoudakis, P. G. Efficient Light Harvesting in Hybrid CdTe Nanocrystal/bulk GaAs P-I-N Photovoltaic Devices. *Appl. Phys. Lett.* **2009**, *94*, 233502.

(173) Chanyawadee, S.; Harley, R. T.; Henini, M.; Talapin, D. V.; Lagoudakis, P. G. Photocurrent Enhancement in Hybrid Nanocrystal Quantum-Dot P-I-N Photovoltaic Devices. *Phys. Rev. Lett.* **2009**, *102*, 77402.

(174) Nizamoglu, S.; Sari, E.; Baek, J.-H.; Lee, I.-H.; Demir, H. V. Nonradiative Resonance Energy Transfer Directed from Colloidal CdSe/ZnS Quantum Dots to Epitaxial InGaN/GaN Quantum Wells for Solar Cells. *Phys. status solidi - Rapid Res. Lett.* **2010**, *4*, 178–180.

(175) Mueller, A. H.; Petruska, M. A.; Achermann, M.; Werder, D. J.; Akhadov, E. A.; Koleske, D. D.; Hoffbauer, M. A.; Klimov, V. I. Multicolor Light-Emitting Diodes Based on Semiconductor Nanocrystals Encapsulated in GaN Charge Injection Layers. *Nano Lett.* **2005**, *5*, 1039–1044.

(176) Demir, H. V.; Nizamoglu, S.; Mutlugun, E.; Ozel, T.; Sapra, S.; Gaponik, N.; Eychmüller, A. Tuning Shades of White Light with Multi-Color Quantum-Dot-Quantum-Well Emitters Based on Onion-like CdSe-ZnS Heteronanocrystals. *Nanotechnology* **2008**, *19*, 335203.

(177) Demir, H. V.; Nizamoglu, S.; Erdem, T.; Mutlugun, E.; Gaponik, N.; Eychmüller, A. Quantum Dot Integrated LEDs Using Photonic and Excitonic Color Conversion. *Nano Today* **2011**, *6*, 632–647.

(178) Nizamoglu, S.; Ozel, T.; Sari, E.; Demir, H. V. White Light Generation Using CdSe/ZnS Core–shell Nanocrystals Hybridized with InGaN/GaN Light Emitting Diodes. *Nanotechnology* **2007**, *18*, 65709.

(179) Chen, H. S.; Yeh, D. M.; Lu, C. F.; Huang, C. F.; Shiao, W. Y.; Huang, J. J.; Yang,

C. C.; Liu, I. S.; Su, W. F. White Light Generation with CdSe-ZnS Nanocrystals Coated on an InGaN-GaN Quantum-Well Blue/green Two-Wavelength Light-Emitting Diode. *IEEE Photonics Technol. Lett.* **2006**, *18*, 1430–1432.

(180) Decher, G. Fuzzy Nanoassemblies: Toward Layered Polymeric Multicomposites. *Science (80-.).* **1997**, *277*, 1232–1237.

(181) Decher, G.; Schlenoff, J. B. *Multilayer Thin Films: Sequential Assembly of Nanocomposite Materials: Second Edition*; Weinheim: Wiley-VCH, 2003; Vol. 1–2.

(182) Byrne, S. J.; Corr, S. A.; Rakovich, T. Y.; Gun'ko, Y. K.; Rakovich, Y. P.; Donegan, J. F.; Mitchell, S.; Volkov, Y. Optimisation of the Synthesis and Modification of CdTe Quantum Dots for Enhanced Live Cell Imaging. *J. Mater. Chem.* **2006**, *16*, 2896.

(183) Rogach, A. L.; Franzl, T.; Klar, T. A.; Feldmann, J.; Gaponik, N.; Lesnyak, V.; Shavel, A.; Eychmüller, A.; Rakovich, Y. P.; Donegan, J. F. Aqueous Synthesis of Thiol-Capped CdTe Nanocrystals: State-of-the-Art. *J. Phys. Chem. C* **2007**, *111*, 14628–14637.

(184) Cicek, N.; Nizamoglu, S.; Ozel, T.; Mutlugun, E.; Karatay, D. U.; Lesnyak, V.; Otto, T.; Gaponik, N.; Eychmüller, A.; Demir, H. V. Structural Tuning of Color Chromaticity through Nonradiative Energy Transfer by Interspacing CdTe Nanocrystal Monolayers. *Appl. Phys. Lett.* **2009**, *94*, 61105.

(185) Franzl, T.; Koktysh, D. S.; Klar, T. A.; Rogach, A. L.; Feldmann, J.; Gaponik, N. Fast Energy Transfer in Layer-by-Layer Assembled CdTe Nanocrystal Bilayers. *Appl. Phys. Lett.* **2004**, *84*, 2904–2906.

(186) Kim, D.; Okahara, S.; Nakayama, M.; Shim, Y. Experimental Verification of Förster Energy Transfer between Semiconductor Quantum Dots. *Phys. Rev. B* **2008**, *78*, 153301.

(187) Murphy, G. P.; Zhang, X.; Bradley, A. L. Temperature-Dependent Luminescent

Decay Properties of CdTe Quantum Dot Monolayers: Impact of Concentration on Carrier Trapping. *J. Phys. Chem. C* **2016**, *120*, 26490–26497.

(188) Constantine, C. A.; Gattás-Asfura, K. M.; Mello, S. V.; Crespo, G.; Rastogi, V.; Cheng, T.-C.; DeFrank, J. J.; Leblanc, R. M. Layer-by-Layer Biosensor Assembly Incorporating Functionalized Quantum Dots. *Langmuir* **2003**, *19*, 9863–9867.

(189) de Bastida, G.; Arregui, F. J.; Goicoechea, J.; Matias, I. R. Quantum Dots-Based Optical Fiber Temperature Sensors Fabricated by Layer-by-Layer. *IEEE Sens. J.* **2006**, *6*, 1378–1379.

(190) Akhavan, S.; Akgul, M. Z.; Hernandez-Martinez, P. L.; Demir, H. V. Plasmon-Enhanced Energy Transfer in Photosensitive Nanocrystal Device. *ACS Nano* **2017**, *11*, 5430–5439.

(191) Kniprath, R.; Rabe, J. P.; McLeskey, J. T.; Wang, D.; Kirstein, S. Hybrid Photovoltaic Cells with II–VI Quantum Dot Sensitizers Fabricated by Layer-by-Layer Deposition of Water-Soluble Components. *Thin Solid Films* **2009**, *518*, 295–298.

(192) De Girolamo, J.; Reiss, P.; Zagorska, M.; De Bettignies, R.; Bailly, S.; Mevellec, J.-Y.; Lefrant, S.; Travers, J.-P.; Pron, A. Layer-by-Layer Assembled Composite Films of Side-Functionalized poly(3-Hexylthiophene) and CdSe Nanocrystals: Electrochemical, Spectroelectrochemical and Photovoltaic Properties. *Phys. Chem. Chem. Phys.* **2008**, *10*, 4027.

(193) Liang, Z.; Dzienis, K. L.; Xu, J.; Wang, Q. Covalent Layer-by-Layer Assembly of Conjugated Polymers and CdSe Nanoparticles: Multilayer Structure and Photovoltaic Properties. *Adv. Funct. Mater.* **2006**, *16*, 542–548.

(194) Kim, B.-S.; Choi, J.-W. Polyelectrolyte Multilayer Microcapsules: Self-Assembly and toward Biomedical Applications. *Biotechnol. Bioprocess Eng.* **2007**, *12*, 323–332.

(195) Tang, Z.; Wang, Y.; Podsiadlo, P.; Kotov, N. A. Biomedical Applications of Layer-

by-Layer Assembly: From Biomimetics to Tissue Engineering. *Adv. Mater.* **2006**, *18*, 3203–3224.

(196) Hummers, W. S.; Offeman, R. E. Preparation of Graphitic Oxide. *J. Am. Chem. Soc.* **1958**, *80*, 1339–1339.

(197) Pendlebury, S. T.; Parbrook, P. J.; Mowbray, D. J.; Wood, D. A.; Lee, K. B. InGaN/GaN Quantum Wells with Low Growth Temperature GaN Cap Layers. *J. Cryst. Growth* **2007**, *307*, 363–366.

(198) O'Brien, M.; McEvoy, N.; Hallam, T.; Kim, H.-Y.; Berner, N. C.; Hanlon, D.; Lee, K.; Coleman, J. N.; Duesberg, G. S. Transition Metal Dichalcogenide Growth via Close Proximity Precursor Supply. *Sci. Rep.* **2014**, *4*, 7374.

(199) McAloney, R. A.; Sinyor, M.; Dudnik, V.; Goh, M. C. Atomic Force Microscopy Studies of Salt Effects on Polyelectrolyte Multilayer Film Morphology. *Langmuir* **2001**, *17*, 6655–6663.

(200) Swafford, L. A.; Weigand, L. A.; Bowers, M. J.; McBride, J. R.; Rapaport, J. L.; Watt, T. L.; Dixit, S. K.; Feldman, L. C.; Rosenthal, S. J. Homogeneously Alloyed CdS_XSe_{1-X} Nanocrystals: Synthesis, Characterization, and Composition/Size-Dependent Band Gap. *J. Am. Chem. Soc.* **2006**, *128*, 12299–12306.

(201) Yu, W. W.; Qu, L.; Guo, W.; Peng, X. Experimental Determination of the Extinction Coefficient of CdTe, CdSe, and CdS Nanocrystals. *Chem. Mater.* **2003**, *15*, 2854–2860.

(202) Lazarides, A. A.; Schatz, G. C. DNA-Linked Metal Nanosphere Materials: Structural Basis for the Optical Properties. *J. Phys. Chem. B* **2000**, *104*, 460–467.

(203) Ludwig, M.; Asher, S. A. Self-Absorption in Resonance Raman and Rayleigh Scattering: A Numerical Solution. *Appl. Spectrosc.* **1988**, *42*, 1458–1466.

(204) Hildebrandt, P.; Stockburger, M. Surface-Enhanced Resonance Raman Spectroscopy of Rhodamine 6G Adsorbed on Colloidal Silver. *J. Phys. Chem.* **1984**, *88*, 5935–5944.

(205) Grabolle, M.; Spieles, M.; Lesnyak, V.; Gaponik, N.; Eychmüller, A.; Resch-Genger, U. Determination of the Fluorescence Quantum Yield of Quantum Dots: Suitable Procedures and Achievable Uncertainties. *Anal. Chem.* **2009**, *81*, 6285–6294.

(206) Fedutik, Y.; Temnov, V.; Schöps, O.; Woggon, U.; Artemyev, M. Exciton-Plasmon-Photon Conversion in Plasmonic Nanostructures. *Phys. Rev. Lett.* **2007**, *99*, 136802.

(207) Akimov, a V; Mukherjee, a; Yu, C. L.; Chang, D. E.; Zibrov, a S.; Hemmer, P. R.; Park, H.; Lukin, M. D. Generation of Single Optical Plasmons in Metallic Nanowires Coupled to Quantum Dots. *Nature* **2007**, *450*, 402–406.

(208) Goodfellow, K. M.; Beams, R.; Chakraborty, C.; Novotny, L.; Vamivakas, A. N. Integrated Nanophotonics Based on Nanowire Plasmons and Atomically Thin Material. *Optica* **2014**, *1*, 149.

(209) Passaseo, A.; Esposito, M.; Cuscunà, M.; Tasco, V. Materials and 3D Designs of Helix Nanostructures for Chirality at Optical Frequencies. *Adv. Opt. Mater.* **2017**, *5*, 1601079.

(210) Schäferling, M.; Dregely, D.; Hentschel, M.; Giessen, H. Tailoring Enhanced Optical Chirality: Design Principles for Chiral Plasmonic Nanostructures. *Phys. Rev. X* **2012**, *2*, 31010.

(211) Kuzyk, A.; Schreiber, R.; Fan, Z.; Pardatscher, G.; Roller, E.-M.; Högele, A.; Simmel, F. C.; Govorov, A. O.; Liedl, T. DNA-Based Self-Assembly of Chiral Plasmonic Nanostructures with Tailored Optical Response. *Nature* **2012**, *483*, 311–314.

(212) Gibbs, J. G.; Mark, a. G.; Eslami, S.; Fischer, P. Plasmonic Nanohelix Metamaterials with Tailorable Giant Circular Dichroism. *Appl. Phys. Lett.* **2013**, *103*, 213101.

(213) Kristensen, A.; Yang, J. K. W.; Bozhevolnyi, S. I.; Link, S.; Nordlander, P.; Halas, N. J.; Mortensen, N. A. Plasmonic Colour Generation. *Nat. Rev. Mater.* **2016**, *2*, 16088.

(214) Kumar, K.; Duan, H.; Hegde, R. S.; Koh, S. C. W.; Wei, J. N.; Yang, J. K. W. Printing

Colour at the Optical Diffraction Limit. *Nat. Nanotechnol.* **2012**, *7*, 557–561.

(215) Lunz, M. Förster Resonant Energy Transfer in Nanocrystal Quantum Dot Structures, PhD Thesis, Trinity College Dublin, 2010.

(216) Crooker, S.; Hollingsworth, J.; Tretiak, S.; Klimov, V. Spectrally Resolved Dynamics of Energy Transfer in Quantum-Dot Assemblies: Towards Engineered Energy Flows in Artificial Materials. *Phys. Rev. Lett.* **2002**, *89*, 186802.

(217) Dalfovo, M. C.; Lacconi, G. I.; Moreno, M.; Yappert, M. C.; Sumanasekera, G. U.; Salvarezza, R. C.; Ibañez, F. J. Synergy between Graphene and Au Nanoparticles (Heterojunction) towards Quenching, Improving Raman Signal, and UV Light Sensing. *ACS Appl. Mater. Interfaces* **2014**, *6*, 6384–6391.

(218) Kasry, A.; Ardakani, A. A.; Tulevski, G. S.; Menges, B.; Copel, M.; Vyklicky, L. Highly Efficient Fluorescence Quenching with Graphene. *J. Phys. Chem. C* **2012**, *116*, 2858–2862.

(219) Chen, Z.; Berciaud, S.; Nuckolls, C.; Heinz, T. F.; Brus, L. E. Energy Transfer from Individual Semiconductor Nanocrystals to Graphene. *ACS Nano* **2010**, *4*, 2964–2968.

(220) Guo, C. X.; Yang, H. Bin; Sheng, Z. M.; Lu, Z. S.; Song, Q. L.; Li, C. M. Layered Graphene/Quantum Dots for Photovoltaic Devices. *Angew. Chemie Int. Ed.* **2010**, *49*, 3014–3017.

(221) Lin, Y.; Zhang, K.; Chen, W.; Liu, Y.; Geng, Z.; Zeng, J.; Pan, N.; Yan, L.; Wang, X.; Hou, J. G. Dramatically Enhanced Photoresponse of Reduced Graphene Oxide with Linker-Free Anchored CdSe Nanoparticles. *ACS Nano* **2010**, *4*, 3033–3038.

(222) Fleischmann, M. Raman Spectra of Pyridine Adsorbed at a Silver Electrode. *Chemical Physics Letters*, 1974, *26*, 2–5.

(223) Zhang, J.; Malicka, J.; Gryczynski, I.; Lakowicz, J. R. Surface-Enhanced Fluorescence of Fluorescein-Labeled Oligonucleotides Capped on Silver Nanoparticles. *J. Phys. Chem. B* **2005**, *109*, 7643–7648.

(224) Kulakovich, O.; Strekal, N.; Yaroshevich, A.; Maskevich, S.; Gaponenko, S.; Nabiev, I.; Woggon, U.; Artemyev, M. Enhanced Luminescence of CdSe Quantum Dots on Gold Colloids. *Nano Lett.* **2002**, *2*, 1449–1452.

(225) Zhang, Z.; Zhang, D.; Lin, H.; Chen, Y. Design and Fabrication of Graphene Fibers Based on Intermolecular Forces and Charge Properties in a Novel Acidic System. *RSC Adv.* **2016**, *6*, 100040–100045.

(226) Amendola, V.; Meneghetti, M. Size Evaluation of Gold Nanoparticles by UV−vis Spectroscopy. *J. Phys. Chem. C* **2009**, *113*, 4277–4285.

(227) Palik, E. D. *Handbook of Optical Constants of Solids*; 1st ed.; Academic Press, 1985; Vol. 1.

(228) Penzkofer, A.; Leupacher, W. Fluorescence Behavior of Highly Concentrated Rhodamine 6G Solutions. *J. Lumin.* **1987**, *37*, 61–72.

(229) Xie, L.; Ling, X.; Fang, Y.; Zhang, J.; Liu, Z. Graphene as a Substrate To Suppress Fluorescence in Resonance Raman Spectroscopy. *J. Am. Chem. Soc.* **2009**, *131*, 9890–9891.

(230) Kavitha, C.; Bramhaiah, K.; John, N. S.; Ramachandran, B. E. Low Cost, Ultra-Thin Films of Reduced Graphene oxide–Ag Nanoparticle Hybrids as SERS Based Excellent Dye Sensors. *Chem. Phys. Lett.* **2015**, *629*, 81–86.

(231) Sil, S.; Kuhar, N.; Acharya, S.; Umapathy, S. Is Chemically Synthesized Graphene "Really" a Unique Substrate for SERS and Fluorescence Quenching? *Sci. Rep.* **2013**, *3*, 3336.

(232) Fu, L.; Zhu, D.; Yu, A. Galvanic Replacement Synthesis of Silver Dendrites-Reduced Graphene Oxide Composites and Their Surface-Enhanced Raman Scattering Characteristics. *Spectrochim. Acta Part A Mol. Biomol. Spectrosc.* **2015**, *149*, 396–401.

(233) Clapp, A. R.; Medintz, I. L.; Mattoussi, H. Förster Resonance Energy Transfer

Investigations Using Quantum-Dot Fluorophores. *ChemPhysChem* **2006**, *7*, 47–57.

(234) Resch-Genger, U.; Grabolle, M.; Cavaliere-Jaricot, S.; Nitschke, R.; Nann, T. Quantum Dots versus Organic Dyes as Fluorescent Labels. *Nat. Methods* **2008**, *5*, 763–775.

(235) Grim, J. Q.; Manna, L.; Moreels, I. A Sustainable Future for Photonic Colloidal Nanocrystals. *Chem. Soc. Rev.* **2015**, *44*, 5897–5914.

(236) Huh, C.; Lee, K.-S.; Kang, E.-J.; Park, S.-J. Improved Light-Output and Electrical Performance of InGaN-Based Light-Emitting Diode by Microroughening of the P - GaN Surface. *J. Appl. Phys.* **2003**, *93*, 9383–9385.

(237) Bergman, D. J.; Stockman, M. I. Surface Plasmon Amplification by Stimulated Emission of Radiation: Quantum Generation of Coherent Surface Plasmons in Nanosystems. *Phys. Rev. Lett.* **2003**, *90*, 27402.

(238) Ferry, V. E.; Munday, J. N.; Atwater, H. A. Design Considerations for Plasmonic Photovoltaics. *Adv. Mater.* **2010**, *22*, 4794–4808.

(239) Atwater, H. A.; Polman, A. Plasmonics for Improved Photovoltaic Devices. *Nat. Mater.* **2010**, *9*, 865–865.

(240) Itzhakov, S.; Buhbut, S.; Tauber, E.; Geiger, T.; Zaban, A.; Oron, D. Design Principles of FRET-Based Dye-Sensitized Solar Cells with Buried Quantum Dot Donors. *Adv. Energy Mater.* **2011**, *1*, 626–633.

(241) Buhbut, S.; Itzhakov, S.; Oron, D.; Zaban, A. Quantum Dot Antennas for Photoelectrochemical Solar Cells. *J. Phys. Chem. Lett.* **2011**, *2*, 1917–1924.

(242) Bai, J.; Yang, C. C.; Athanasiou, M.; Wang, T. Efficiency Enhancement of InGaN/GaN Solar Cells with Nanostructures. *Appl. Phys. Lett.* **2014**, *104*, 51129.

(243) Mutlugün, E.; Nizamoğlu, S.; Demir, H. V. Highly Efficient Nonradiative Energy Transfer Using Charged CdSe/ZnS Nanocrystals for Light-Harvesting in Solution. *Appl. Phys. Lett.* **2009**, *95*, 33106.

(244) Lunz, M.; Bradley, A. L.; Chen, W.; Gun'ko, Y. K. Two-Dimensional Förster Resonant Energy Transfer in a Mixed Quantum Dot Monolayer: Experiment and Theory. *J. Phys. Chem. C* **2009**, *113*, 3084–3088.

(245) Franzl, T.; Klar, T. A.; Schietinger, S.; Rogach, A. L.; Feldmann, J. Exciton Recycling in Graded Gap Nanocrystal Structures. *Nano Lett.* **2004**, *4*, 1599–1603.

(246) Olutas, M.; Guzelturk, B.; Kelestemur, Y.; Gungor, K.; Demir, H. V. Highly Efficient Nonradiative Energy Transfer from Colloidal Semiconductor Quantum Dots to Wells for Sensitive Noncontact Temperature Probing. *Adv. Funct. Mater.* **2016**, *26*, 2891–2899.

(247) Prasai, D.; Klots, A. R.; Newaz, a K. M.; Niezgoda, J. S.; Orfield, N. J.; Escobar, C. a; Wynn, A.; Efimov, A.; Jennings, G. K.; Rosenthal, S. J.; *et al.* Electrical Control of near-Field Energy Transfer between Quantum Dots and Two-Dimensional Semiconductors. *Nano Lett.* **2015**, *15*, 4374–4380.

(248) Lee, Y. J.; Chiu, C. H.; Ke, C. C.; Lin, P. C.; Lu, T. C.; Kuo, H. C.; Wang, S. C. Study of the Excitation Power Dependent Internal Quantum Efficiency in InGaN/GaN LEDs Grown on Patterned Sapphire Substrate. *IEEE J. Sel. Top. Quantum Electron.* **2009**, *15*, 1137–1143.

(249) Higgins, L. J.; Karanikolas, V. D.; Marocico, C. A.; Bell, A. P.; Sadler, T. C.; Parbrook, P. J.; Bradley, A. L. Carrier Density Dependence of Plasmon-Enhanced Nonradiative Energy Transfer in a Hybrid Quantum Well-Quantum Dot Structure. *Opt. Express* **2015**, *23*, 1377.

(250) Ambacher, O.; Brunner, D.; Dimitrov, R.; Stutzmann, M.; Sohmer, A.; Scholz, F. Absorption of InGaN Single Quantum Wells Determined by Photothermal Deflection Spectroscopy. *Jpn. J. Appl. Phys.* **1998**, *37*, 745–752.

(251) Jordan, C.; Donegan, J. F.; Hegarty, J.; Roycroft, B. J.; Taniguchi, S.; Hino, T.; Kato, E.; Noguchi, N.; Ishibashi, A. Carrier-Density Dependence of the Photoluminescence

Lifetimes in ZnCdSe/ZnSSe Quantum Wells at Room Temperature. *Appl. Phys. Lett.* **1999**, *74*, 3359–3361.

(252) Kappei, L.; Szczytko, J.; Morier-Genoud, F.; Deveaud, B. Direct Observation of the Mott Transition in an Optically Excited Semiconductor Quantum Well. *Phys. Rev. Lett.* **2005**, *94*, 147403.

(253) Kos, Š.; Achermann, M.; Klimov, V.; Smith, D. Different Regimes of Förster-Type Energy Transfer between an Epitaxial Quantum Well and a Proximal Monolayer of Semiconductor Nanocrystals. *Phys. Rev. B* **2005**, *71*, 205309.

(254) Fouquet, J. E.; Siegman, A. E. Room-temperature Photoluminescence Times in a GaAs/$Al_XGa_{1-X}As$ Molecular Beam Epitaxy Multiple Quantum Well Structure. *Appl. Phys. Lett.* **1985**, *46*, 280–282.

(255) Fujiwara, K.; Tsukada, N.; Nakayama, T. Observation of Free Excitons in Room-temperature Photoluminescence of GaAs/AlGaAs Single Quantum Wells. *Appl. Phys. Lett.* **1988**, *53*, 675–677.

(256) Achermann, M.; Petruska, M. A.; Crooker, S. A.; Klimov, V. I. Picosecond Energy Transfer in Quantum Dot Langmuir−Blodgett Nanoassemblies. *J. Phys. Chem. B* **2003**, *107*, 13782–13787.

(257) Mendes, M. J.; Hernández, E.; López, E.; García-Linares, P.; Ramiro, I.; Artacho, I.; Antolín, E.; Tobías, I.; Martí, A.; Luque, A. Self-Organized Colloidal Quantum Dots and Metal Nanoparticles for Plasmon-Enhanced Intermediate-Band Solar Cells. *Nanotechnology* **2013**, *24*, 345402.

(258) Shur, M.; Gelmont, B.; Asif Khan, M. Electron Mobility in Two-Dimensional Electron Gas in AIGaN/GaN Heterostructures and in Bulk GaN. *J. Electron. Mater.* **1996**, *25*, 777–785.

(259) Thomas, S.; Thomas, R.; Zachariah, A. K.; Mishra, R. K. *Microscopy Methods in Nanomaterials Characterization*; Elsevier Science, 2017.

(260) Higgins, L. J.; Marocico, C. A.; Karanikolas, V. D.; Bell, A. P.; Gough, J. J.; Murphy, G. P.; Parbrook, P. J.; Bradley, A. L. Influence of Plasmonic Array Geometry on Energy Transfer from a Quantum Well to a Quantum Dot Layer. *Nanoscale* **2016**, *8*, 18170–18179.

(261) Radisavljevic, B.; Radenovic, a; Brivio, J.; Giacometti, V.; Kis, a. Single-Layer MoS_2 Transistors. *Nat. Nanotechnol.* **2011**, *6*, 147–150.

(262) Yin, Z.; Li, H. H.; Li, H. H.; Jiang, L.; Shi, Y.; Sun, Y.; Lu, G.; Zhang, Q.; Chen, X.; Zhang, H. Single-Layer MoS_2 Phototransistors. *ACS Nano* **2012**, *6*, 74–80.

(263) Lee, H. S.; Min, S.; Chang, Y.; Park, M. K.; Nam, T.; Kim, H.; Kim, J. H.; Ryu, S.; Im, S. MoS_2 Nanosheet Phototransistors with Thickness-Modulated Optical Energy Gap. *Nano Lett.* **2012**, *12*, 3695–3700.

(264) Zhang, W.; Huang, J.-K.; Chen, C.-H.; Chang, Y.-H.; Cheng, Y.-J.; Li, L.-J. High-Gain Phototransistors Based on a CVD MoS_2 Monolayer. *Adv. Mater.* **2013**, *25*, 3456–3461.

(265) Lopez-Sanchez, O.; Lembke, D.; Kayci, M.; Radenovic, A.; Kis, A. Ultrasensitive Photodetectors Based on Monolayer MoS_2. *Nat. Nanotechnol.* **2013**, *8*, 497–501.

(266) Mann, J.; Sun, D.; Ma, Q.; Chen, J. R.; Preciado, E.; Ohta, T.; Diaconescu, B.; Yamaguchi, K.; Tran, T.; Wurch, M.; *et al.* Facile Growth of Monolayer MoS_2 Film Areas on SiO2. *Eur. Phys. J. B* **2013**, *86*, 2–5.

(267) Yu, S. H.; Lee, Y.; Jang, S. K.; Kang, J.; Jeon, J.; Lee, C.; Lee, J. Y.; Kim, H.; Hwang, E.; Lee, S.; *et al.* Dye-Sensitized MoS_2 Photodetector with Enhanced Spectral Photoresponse. *ACS Nano* **2014**, *8*, 8285–8291.

(268) Kufer, D.; Nikitskiy, I.; Lasanta, T.; Navickaite, G.; Koppens, F. H. L.; Konstantatos, G. Hybrid 2D-0D MoS_2 -PbS Quantum Dot Photodetectors. *Adv. Mater.* **2015**, *27*, 176–180.

(269) Kufer, D.; Lasanta, T.; Bernechea, M.; Koppens, F. H. L.; Konstantatos, G. Interface

Engineering in Hybrid Quantum Dot–2D Phototransistors. *ACS Photonics* **2016**, *3*, 1324–1330.

(270) Li, H.; Zhang, Q.; Yap, C. C. R.; Tay, B. K.; Edwin, T. H. T.; Olivier, A.; Baillargeat, D. From Bulk to Monolayer MoS_2: Evolution of Raman Scattering. *Adv. Funct. Mater.* **2012**, *22*, 1385–1390.

(271) Lee, C.; Yan, H.; Brus, L. E.; Heinz, T. F.; Hone, J.; Ryu, S. Anomalous Lattice Vibrations of Single- and Few-Layer MoS_2. *ACS Nano* **2010**, *4*, 2695–2700.

(272) Sangwan, V. K.; Jariwala, D.; Kim, I. S.; Chen, K.-S.; Marks, T. J.; Lauhon, L. J.; Hersam, M. C. Gate-Tunable Memristive Phenomena Mediated by Grain Boundaries in Single-Layer MoS_2. *Nat. Nanotechnol.* **2015**, *10*, 403–406.

(273) Wu, C. C.; Jariwala, D.; Sangwan, V. K.; Marks, T. J.; Hersam, M. C.; Lauhon, L. J. Elucidating the Photoresponse of Ultrathin MoS_2 Field-Effect Transistors by Scanning Photocurrent Microscopy. *J. Phys. Chem. Lett.* **2013**, *4*, 2508–2513.

(274) Perea-López, N.; Lin, Z.; Pradhan, N. R.; Iñiguez-Rábago, A.; Laura Elías, A.; McCreary, A.; Lou, J.; Ajayan, P. M.; Terrones, H.; Balicas, L.; *et al.* CVD-Grown Monolayered MoS_2 as an Effective Photosensor Operating at Low-Voltage. *2D Mater.* **2014**, *1*, 11004.

(275) Klee, V.; Preciado, E.; Barroso, D.; Nguyen, A. E.; Lee, C.; Erickson, K. J.; Triplett, M.; Davis, B.; Lu, I.; Bobek, S.; *et al.* Superlinear Composition-Dependent Photocurrent in CVD-Grown Monolayer $MoS_{2(1-X)}Se_{2X}$ Alloy Devices. *Nano Lett.* **2015**, *15*, 2612–2619.

(276) Bube, R. H. A New Mechanism for Superlinear Photoconductivity with Relevance to Amorphous Silicon. *J. Appl. Phys.* **1993**, *74*, 5138–5143.

(277) Zhou, W.; Zou, X.; Najmaei, S.; Liu, Z.; Shi, Y.; Kong, J.; Lou, J.; Ajayan, P. M.; Yakobson, B. I.; Idrobo, J.-C. Intrinsic Structural Defects in Monolayer Molybdenum Disulfide. *Nano Lett.* **2013**, *13*, 2615–2622.

(278) Tongay, S.; Suh, J.; Ataca, C.; Fan, W.; Luce, A.; Kang, J. S.; Liu, J.; Ko, C.; Raghunathanan, R.; Zhou, J.; *et al.* Defects Activated Photoluminescence in Two-Dimensional Semiconductors: Interplay between Bound, Charged, and Free Excitons. *Sci. Rep.* **2013**, *3*, 2657.

(279) Bollinger, M. V.; Lauritsen, J. V.; Jacobsen, K. W.; Nørskov, J. K.; Helveg, S.; Besenbacher, F. One-Dimensional Metallic Edge States in MoS_2. *Phys. Rev. Lett.* **2001**, *87*, 196803.

(280) Zhang, J.; Yu, H.; Chen, W.; Tian, X.; Liu, D.; Cheng, M.; Xie, G.; Yang, W.; Yang, R.; Bai, X.; *et al.* Scalable Growth of High-Quality Polycrystalline MoS_2 Monolayers on SiO 2 with Tunable Grain Sizes. *ACS Nano* **2014**, *8*, 6024–6030.

(281) van der Zande, A. M.; Huang, P. Y.; Chenet, D. A.; Berkelbach, T. C.; You, Y.; Lee, G.; Heinz, T. F.; Reichman, D. R.; Muller, D. A.; Hone, J. C. Grains and Grain Boundaries in Highly Crystalline Monolayer Molybdenum Disulphide. *Nat. Mater.* **2013**, *12*, 554–561.

(282) Yu, Y.; Li, C.; Liu, Y.; Su, L.; Zhang, Y.; Cao, L. Controlled Scalable Synthesis of Uniform, High-Quality Monolayer and Few-Layer MoS_2 Films. *Sci. Rep.* **2013**, *3*, 1–6.

(283) Hur, J.-H.; Park, J.; Jeon, S. A Theoretical Modeling of Photocurrent Generation and Decay in Layered MoS_2 Thin-Film Transistor Photosensors. *J. Phys. D. Appl. Phys.* **2017**, *50*, 65105.

(284) Kufer, D.; Konstantatos, G. Highly Sensitive, Encapsulated MoS_2 Photodetector with Gate Controllable Gain and Speed. *Nano Lett.* **2015**, *15*, 7307–7313.

(285) Zhang, W.; Chuu, C.-P.; Huang, J.-K.; Chen, C.-H.; Tsai, M.-L.; Chang, Y.-H.; Liang, C.-T.; Chen, Y.-Z.; Chueh, Y.-L.; He, J.-H.; *et al.* Ultrahigh-Gain Photodetectors Based on Atomically Thin Graphene-MoS_2 Heterostructures. *Sci. Rep.* **2014**, *4*, 3826.

(286) Zhang, B. Y.; Liu, T.; Meng, B.; Li, X.; Liang, G.; Hu, X.; Wang, Q. J. Broadband

High Photoresponse from Pure Monolayer Graphene Photodetector. *Nat. Commun.* **2013**, *4*, 1811.

(287) Maity, P.; Debnath, T.; Ghosh, H. N. Slow Electron Cooling Dynamics Mediated by Electron–Hole Decoupling in Highly Luminescent CdS_XSe_{1-X} Alloy Quantum Dots. *J. Phys. Chem. C* **2015**, *119*, 10785–10792.

(288) Kioupakis, E.; Yan, Q.; Steiauf, D.; Van De Walle, C. G. Temperature and Carrier-Density Dependence of Auger and Radiative Recombination in Nitride Optoelectronic Devices. *New J. Phys.* **2013**, *15*.

(289) Zhang, Y. P.; Zhang, Z.-H.; Liu, W.; Tan, S. T.; Ju, Z. G.; Zhang, X. L.; Ji, Y.; Wang, L. C.; Kyaw, Z.; Hasanov, N.; *et al.* Nonradiative Recombination — Critical in Choosing Quantum Well Number for InGaN/GaN Light-Emitting Diodes. *Opt. Express* **2015**, *23*, A34.

(290) Lu, Z.; Lee, O.; Wong, J. C.; Salahuddin, S. Surface States in a Monolayer MoS_2 Transistor. *J. Mater. Res.* **2016**, *31*, 911–916.

(291) Graham, D.; Faulds, K.; Smith, W. E. Biosensing Using Silver Nanoparticles and Surface Enhanced Resonance Raman Scattering. *Chem. Commun.* **2006**, 4363.

(292) Le Ru, E. C.; Etchegoin, P. G. Quantifying SERS Enhancements. *MRS Bull.* **2013**, *38*, 631–640.

(293) Lin, Z.; Kerle, T.; Russell, T. P.; Schäffer, E.; Steiner, U. Structure Formation at the Interface of Liquid/Liquid Bilayer in Electric Field. *Macromolecules* **2002**, *35*, 3971–3976.

(294) Yeltik, A.; Guzelturk, B.; Ludwig Hernandez-Martinez, P.; Akhavan, S.; Volkan Demir, H. Excitonic Enhancement of Nonradiative Energy Transfer to Bulk Silicon with the Hybridization of Cascaded Quantum Dots. *Appl. Phys. Lett.* **2013**, *103*, 261103.

(295) Xia, J.; Huang, X.; Liu, L.-Z.; Wang, M.; Wang, L.; Huang, B.; Zhu, D.-D.; Li, J.-J.;

Gu, C.-Z.; Meng, X.-M. CVD Synthesis of Large-Area, Highly Crystalline $MoSe_2$ Atomic Layers on Diverse Substrates and Application to Photodetectors. *Nanoscale* **2014**, *6*, 8949.